AMORPHOUS SILICON OXYNITRIDE COATINGS FOR CRANIOFACIAL IMPLANTS STIMULATE OSTEOGENESIS VIA NRF2 ANTIOXIDANT ACTIVITY

by

NEELAM AHUJA

DISSERTATION

Submitted in partial fulfillment of the requirements

for the degree of Doctor of Philosophy at

The University of Texas at Arlington

December 2022

Arlington, Texas

Supervising Committee:

Dr. Venu Varanasi, Supervising Professor

Dr. Marco Brotto

Dr. Danial Trott

Dr. Rhonda Prisby

ABSTRACT

AMORPHOUS SILICON OXYNITRIDE COATINGS FOR CRANIOFACIAL IMPLANTS STIMULATE OSTEOGENESIS VIA NRF2 ANTIOXIDANT ACTIVITY

Neelam Ahuja, B.D.S, M.S

The University of Texas at Arlington

2022

Supervising Professor: Dr. Venu Varanasi

Craniomaxillofacial injuries and defects are functionally and socially debilitating. These defects require immediate attention, and most cases undergo reconstruction surgery to restore the lost tissues. Current treatment strategies such as autologous bone grafts and fixative titanium devices are well established to treat the craniofacial region. But, the limited supply of donor bone and secondary surgery limit the use of autologous bone grafts, and low bioactivity, poor osteointegration of the titanium devices, has led to an increased number of tissue engineering research for the development of newer biomaterials.

Bone defects especially in the craniofacial region can have a significant portion of bone tissue missing or lost and leaves the tissues ischemic, hypoxic and even contaminated. This leads to accumulation of reactive oxygen species, and the body's homeostatic mechanisms fails. The oxidative stress makes these defects complex and compromised. In this study, we aim to target to reduce the unwanted oxidative stress to improve healing rates in bone.

Prior studies have indicated the amorphous silicon oxynitride coatings created using plasma-enhanced chemical vapor deposition, shows leaching of the silicon ions which have a positive antioxidant effect and enhanced *in vitro* osteogenic biomarker expression. This study further investigates the bone defect healing for the silicon oxynitride coatings on titanium fixative devices in craniofacial region.

The highlights of the significance of each Chapter to the central theme of the Dissertation are described below.

CHAPTER 1: Introduction: This chapter gives a review on craniomaxillofacial injuries and defects, the current state of the art on treatment options for reconstruction, role of oxidative stress in bone healing, and the need for newer biomaterials. The chapter also states the Rationale and Aim for the proposed work, along with the clinical impact and benefit this research will achieve.

CHAPTER 2: A Comparative Study on Silicon Nitride, Titanium, and Poly-Ether Ether Ketone on Mouse Pre-Osteoblasts Cells: This study investigates silicon nitride, a ceramic, as a fixative device material for bone regeneration. We compare the biological response of silicon nitride to the current standard craniofacial biomaterials Titanium (metal) (Gold standard) and Polyether ether ketone (PEEK) (polymer). Results from this study conclude that silicon nitride and titanium have a comparative biological response. We learn the benefits of silicon nitride enhances wettability of the surface and increases bioactivity. However, the low tensile strength of silicon nitride makes it a less favorable material compared to titanium, especially in the craniofacial region.

CHAPTER 3: Silicon Oxynitrophosphide Nanoscale-Coating Enhances Antioxidant Marker - Induced Angiogenesis During *In Vivo* Cranial Bone Defect Healing: Due to the limitation seen in

Chapter 2, we study amorphous silicon nitride coatings for angiogenesis in cranial bone defect. We also investigated the coatings with ionic phosphorous as it enhances the vascular endothelial growth factor (VEGF) activity. The study results show upregulation of the antioxidant activity along with localized enhancement of the major angiogenic factors. In conclusion, silicon-based nano-layered coatings can reduce oxidative stresses by enhancing antioxidant activity, and support and differentiate endothelial cells.

CHAPTER 4: Increasing N/O Concentration in Bacteriostatic Silicon Oxynitride Coatings Enhances Osteogenic Transcription Via Nrf2 Antioxidant Activity: The amorphous nanolayered coating of silicon oxynitride is created using a plasma-enhanced chemical vapor deposition (PECVD) method. This *in vitro* study investigates and optimizes the highly tunable PECVD silicon oxynitride coatings for fixative devices to enhance maximal antioxidant activity as well as osteogenic activity under an oxidative stress condition. This study also examines the major transcription factor NRF2, which is involved in the antioxidant response against the oxidative stresses of the injury and is related to maintain bone cell homeostasis. Study results reveal the activation of the NRF2 antioxidant factor with silicon oxynitride coatings.

CHAPTER 5: *In Vivo* Analysis of Antioxidant Silicon Oxynitride- Titanium Coatings for Craniomaxillofacial Fixative Devices to Enhance Localized Bone Regeneration: This study evaluates the role of antioxidant silicon oxynitride coatings on titanium fixative devices for the application in craniomaxillofacial region. Results from the rat cranial defect surgery revealed more organized extracellular matrix and enhanced osteointegration with the silicon oxynitride coated devices compared to the uncoated. Similarly, the translational rabbit mandibular defect model revealed faster bone healing with a physiologic bone quality with the coated titanium plates and screw device. This study confirms our findings for the above studies.

CHAPTER 6: Overall Conclusions and Future Directions: This chapter concludes our findings and links the findings of our study results. Our findings show the activation of the antioxidant biomarkers in presence of the silicon oxynitride coatings and enhance angiogenic and osteogenic biomarkers. We conclude that the amorphous silicon oxynitride coatings has excellent outcomes *in vitro* and *in vivo* as potential coatings for pre-existing titanium fixative devices.

ACKNOWLEDGEMENTS

This endeavor would not have been possible without the support, guidance and mentorship of Dr. Venu Varanasi, my PhD supervisor. I would like to express my deepest gratitude to my defense committee, Dr. Marco Brotto, Dr. Rhonda Prisby and Dr. Daniel Trott, for providing expertise and making my work better. I also want to thank, Osteo Science Foundation Peter L. Geistlich Research Grant to support this work.

I would like to express my appreciation to Dr. Paul Fadel, Dr. Matthew Brothers, Department of Kinesiology and UTA College of Nursing and Health Innovation who helped in my academic journey. I am also grateful to Dr. Kamal Awad and Dr. Felipe A. do Monte for constantly motivating me and being a major part of this work.

Lastly, I want to recognize all our laboratory members Matthew Fiedler, Henry Tran, Sara Peper, Thy Vo, and Laureen Abbo Nono for their assistance and helpful suggestions. I would also like to thank UTA College of Nursing & Health Innovation Bone-Muscle Research Center (UTA-CONHI-BMRC) and Nanotechnology Research Center at Shimadzu center and the CCMB at UTA for their support.

.

DEDICATION

I want to dedicate this work to my parents, Poonam and Rajendra Singh Ahuja, for their unconditional love, support, and belief in me, which kept my spirits and motivation high during this whole process. I also want to dedicate my husband, Paramjeet Singh, who has been a constant source of encouragement and strength to complete my doctoral journey. I also want to greatly appreciate my brother, my best friend, and my biggest cheerleader, Arjun Ahuja. Lastly, I would be remiss in not mentioning my friend, Jasmine Tanna, for always being there.

TABLE OF CONTENTS

LIST OF TABLES

LIST OF FIGURES

CHAPTER 2

CHAPTER 3

CHAPTER 4

CHAPTER 1

GENERAL INTRODUCTION

1.1. CRANIOMAXILLOFACIAL BONE DEFECTS

Large bone defects affecting the craniomaxillofacial region can arise from high energy impact, trauma, blast injuries, congenital bone defects and resection of locally aggressive tumors (1). A significant number of these defects are sufficiently large and cannot spontaneously heal on its own. These defects are termed critical, as they require surgical intervention and planned reconstruction, to heal successfully. Overall, more than 400,000 patients present to the emergency room with facial fractures or large craniofacial defects require treatment each year, which costs over $1 billion of health care costs (2–4). Recent reports show that the incidence of craniomaxillofacial defects continues to rise by about 15% per year (5). Craniomaxillofacial defects, regardless of the cause, can affect function and esthetics which can be debilitating and socially incapacitating for a person. Large-sized bone defects are also biomedically and economically burdensome (6). These defects require three-dimensional structural support, including permanent protection to the underlying brain tissue, mechanical integrity, support jaw movement, facial esthetics along with faster healing rates. Thus, there is an urgent need to rapidly repair large craniomaxillofacial defects resulting from trauma or treatment of pathology.

The thickness and the stiffness, of the cranial and maxillofacial bone, vary according to different sites in the skull along with the related soft tissue making craniomaxillofacial region a complex structure to heal (7, 8). Another factor that affects the bone microenvironment healing is the various cell types. The angiogenic endothelial cells, bone-forming mesenchymal stem cells, osteoblasts and osteoclasts maintain bone homeostasis. The osteoblasts and osteoclasts work together for bone formation and bone resorption (bone remodeling) which maintains bone homeostasis, bone density, and strength. The osteocytes when mature, get incorporated in the bone matrix and become osteocytes. Osteocytes remain in the bone matrix and are mainly

responsible for bone turnover and adaptation (7, 9, 10). The endothelial cells also play an important role in homeostasis as it builds and maintains vascular network within the bone tissue.

An ideal biomaterial to enhance repair, regeneration and restoration of a large bone defect in the craniomaxillofacial region should be able to support various cell growth and mechanically support the bone defect.

1.2. CURRENT TREATMENT STRATEGIES

As mentioned above large-sized craniofacial bone defects require three-dimensional structural support, including permanent protection to the underlying brain tissue, mechanical integrity, support jaw movement, facial esthetics along with faster healing rates, which makes them difficult to restore. Current treatment strategies for repair and reconstruction include bone grafting, rigid fixation and other biomaterials are explained below.

1.2.1. Autografts

Bone grafts including autogenic and allogenic sources of bone are the gold standard for treating craniomaxillofacial bone defects (7, 11–13). Autograft is bone tissue taken from a secondary site from the patient's own body for replacing bone at the primary defect site. Iliac crest is one of the most common sites used for autogenic bone grafts. Smaller craniomaxillofacial defects show a very high success rate with autografts as it retains osteogenic and angiogenic cells, and show a favorable immunogenic response (7, 14). Despite the high success rate, there is limited bone availability for attaining the autogenic bone graft. Additionally, removing bone from a secondary area from the patient's body can lead to an additional surgery site, pain, vascular and nerve injury, secondary bone fracture, high chances of bone morbidity and longer healing times (7, 11).

1.2.2. Allografts and Xenografts

Allografts are bone grafts taken from a donor of the same species or a cadaver and Xenografts are bone grafts taken from a different species. These grafts overcome drawbacks of autografts such as the need for a secondary surgery, and increased chances of bone morbidity. Allografts and xenografts are required to undergo a series of processing such as decellularization and demineralization to minimize the immunologic response and disease transmission (7, 11). The vigorous pre-processing of these grafts can lead to a less osteogenic biomaterial, as it affects the extracellular matrix and collagen in the donor bone (7, 15, 16). There can also be a lot of variability between the different bone tissues that are being processed. Allograft and Xenograft, even after sterilization, can lead to high rate of infections and unfavorable immunologic reactions. The bone grafts also have limited mechanical strength for long-term stability in cases of critically large bone defects.

1.2.3. Metals

Metal fixative devices such as titanium are a popular choice of biomaterial to treat large bone defects. Large bone defects require reduction and fixation of the tissue grafts with a rigid fixative biomedical device (e.g., titanium (Ti)) or fixative device alone to bridge the defect gap, especially in the load-bearing bone to strengthen and structurally support the defects. Yet, conventional titanium lacks surface bioactivity, does not speed revascularization, has no antioxidant effect (17), and may fail due to aseptic loosening (18–20). Various surface modification techniques and coating modifications have been studied for titanium fixative devices to improve the metal-coating interface and prevent infection. However, the coatings have been unsuccessful due to thermal expansion mismatch at the coating-metal device interface (21–28), poor coating quality from high temperature (>700□C), reduced bioactivity (29, 30), or

reduction of osteogenic activity (31), resulting in immature bone healing and fibrous tissue attachment (32), and poor long-term stability (33).

1.2.4. Ceramics

Ceramics and hydroxyapatite-based materials have been widely used in dental clinics. Bioglass and Tricalcium phosphate is an alternative to allografts and autografts for bone regeneration (7, 34–36). These calcium and phosphorus-containing bioceramics have good biocompatibility and acceptable mechanical properties for defect stability. However, these materials are not as successful as the bone grafts due to their brittle nature, longer resorption times and high infection rates (7). Other ceramic materials such as nanosilicates and silicate nanoparticles have also been studied and show promising results in combination with metals and other biomaterials (7).

1.2.5. Polymers

Natural polymers derived from animals and plants (collagen-based biopolymers) have been studied to heal various soft and hard tissues. These polymers have tunable porosity and orientation which is beneficial for use in drug delivery applications. However, due to the poor mechanical properties, there has been limited applications for these biomaterials. Synthetic polymers such as polycaprolactone (PCL) and poly(lactic acid) (PLA) are FDA approved for tissue engineering applications are biodegradable, biocompatible with have tunable biomechanical properties (7, 37, 38). However, the synthetic biopolymers have longer than expected degradation rates and can produce cytotoxic degradation products.

Metals, ceramics and polymers have their associated benefits and drawbacks in craniofacial bone repair and regeneration. Studies combining two or more of these material approaches can overcome the drawbacks of the individual biomaterials.

1.3. OXIDATIVE STRESS AND BONE DEFECT HEALING

Large craniomaxillofacial defects, can often be associated with compromised wound healing resulting from deficient vascularization, hypoxia, wound contamination, or chemo/radiotherapy, complicating defect treatment. Studies have noted that compromised defects and injuries induced a delay in bone turnover rate (39, 40), and re-vascularization in adults (41) that imposed extended period of hospital stay and significantly delayed healing time (42). This delayed healing can be attributed to the factor of a marked increase in reactive oxygen species (ROS) (43), and prolonged inflammation (44). Prolonged oxidative stress causes damage to the nuclear acids and proteins causing irreparable cellular injury and restricting cell viability, growth, and proliferation (45). Additionally, intrinsic oxidative stresses due to an underlying systemic disease also impair the bone regenerating capacity by the production of oxidants and elimination of the protective antioxidant mechanisms (46–50). Elevating tissue-level antioxidant activity can reduce ROS and promote angiogenesis and osteogenesis needed for healing (44). A controlled ROS level has an important role in the regulation of many fundamental cellular processes in the body such as proliferation, differentiation, and repair (51, 52). However, increased ROS production causes structural damage and apoptosis of the genomic DNA of osteoblasts and osteoclasts disrupting the normal function (53). ROS activated lipid peroxidation-dependent lipoxygenase is associated with decreased osteoblastic activity and increased osteoclastic activity (54). With ROS being a major determinant of oxidative stress, controls the remodeling capacity of the bone (55). There is an intrinsic antioxidant system (such as glutathione peroxidase (GPX) and superoxide dismutase (SOD1)) that protects against cellular damage from oxidative stresses on the body. Physiologic factors such as age or pathological factors such as trauma leading to

critical defects lead to failure of the intrinsic protective antioxidant system against the high levels of ROS.

1.4. NEED FOR ANTIOXIDANT MATERIALS

The role of antioxidants in healing has been well established. Patients given exogenous or dietary antioxidants such as Vitamin E, Vitamin C, Carotenoids, and polyphenols improved bone health. Dietary or natural antioxidants after fracture had higher SOD1 activity, which reduced ROS and increased osteocalcin activity (43, 56), and lowered health care costs by lowering hospital stays (57). They reduce this barrier by electrochemically reducing ROS via increased antioxidant activity (e.g., nuclear erythroid factor 2 (NRF2), SOD1, and glutathione peroxidase (GPX)) (58, 59) and increasing the cation concentration thereby increased cation valence state (60). This leads to prompt treatment in compromised defects to limit inflammation and patient recovery time (61). Thus, antioxidants play a central role to lower ROS while inducing osteogenesis. Currently, we do not have any biomaterials that has an intrinsic antioxidant property. Further, an alternative approach of using targeted local delivery of small antioxidant molecules can intrinsically induce rapid cell recruitment, maintain viability, and provide surface to support healing. Yet, the exogenous approaches as well as small molecule delivery system are unable to overcome the challenge of healing large defects due to the large mass of strong bone that needs to be regenerated along with the need to stabilize the defects. **Thus, there is a great clinical need for novel fabrication methods and materials to improve fixative devices such as metal implants that not just provides structural support but also induces antioxidant activity that reduces oxidative stresses and accelerates bone healing.** Such biomaterials can

precisely target this mechanism to the wound healing environment and are vitally needed for volumetric bone repair.

1.5. PLASMA-ENHANCED CHEMICAL VAPOR DEPOSITION

Plasma-enhanced chemical vapor deposition (PECVD) is a method used to deposit thin films on substrates from a gas (vapor) state to a solid state. PECVD is widely used in the semiconductor industry and microelectronics applications. The PECVD technique uses plasma, instead of thermal energy in conventional CVD process, which leads the vacuum-based deposition at a relatively lower temperature (up to 400°C) (62). The plasma deposition creates a surface with free radicles and forms an amorphous coating and helps in evenly sputtering of the molecules which can maintain the surface morphology of the substrate. Further, the coatings are fabricated at relatively low temperature (< 400ºC), thus, thermal expansion mismatch between the implant substrate and coating layers are markedly reduced (63). The PECVD process is advantageous as the coating thickness, atom ratio, and interfacial formation onto a biomedical device are under our control. Furthermore, the thin films are formed relatively quickly (within 1 hour), and have high reliability and repeatability in manufacturing processes (63).

1.6. SILICON OXYNITRIDE

Silica (SiO_2) based biomaterials have been studied widely for their antibacterial properties (64, 65). Silica-/bioactive glass-based nanoparticles and surface modifications (30, 66–68) have been tested for their antioxidant properties. The Varanasi Laboratory used plasma-enhanced chemical vapor deposition for creating thin film Silicon Oxynitride (SiONx) coatings (69). This leads to an efficient stable coating layer of amorphous silica on an underlying metal

surface that The PECVD process led to a stable coating of amorphous silica on the substrate material and released Si^{4+} for several weeks (70). These implant coatings stimulated SOD1 activity and formed surface hydroxyapatite (HA) leading to osteogenesis in mouse osteoblast cells (71, 72). The amorphous SiONx materials are formed at a substrate temperature of 400 °C, chamber pressure of 900 mTorr, and ICP power of 30 W with a 13.56 MHz excitation frequency. The source gases used to create the SiONx-coatings were silane (SiH_4) diluted in argon (Ar), nitrous oxide (N_2O), nitrogen (N_2), and ammonia (NH_3) (70). The composition of the SiONx coating can be easily adjusted or tune according to the study requirements by controlling the gas flow in the PECVD chamber. This is an additional advantage of using the PECVD for biomedical devices. For example, the nitrogen-to-oxygen atom ratio is controlled by controlling the source gases NH_3 and N_2O under the reductive ionized gas environment (73). This leads to varying levels of tetrahedral and trigonal chemical bond structure depending on the N/O atom ratio within the films (73) which can change the surface charge and change the antioxidant activity of the coatings.

1.7. RATIONALE

As mentioned above, there is a crucial clinical need for novel fabrication methods and materials to improve fixative devices such as metal implants that provides structural support and also induce antioxidant activity that reduces oxidative stresses to accelerate bone healing. We rationalize that Silicon Oxynitride- titanium coatings induce antioxidant activity and reduces oxidative stresses through the NRF2 pathway. It has been established in the literature that NRF2 is a key transcriptional factor that is responsible for activating an antioxidant response reaction against the oxidative stresses (74). NRF2 has also been known to maintain homeostasis in bone

cells affecting bone healing rates suggesting the fact that NRF2 can promote fracture healing in the presence and absence of oxidative stresses, thereby implicating its role in bone healing after traumatic injury (45, 75). NRF2 is negatively regulated by its cytoplasmic antagonist Keap1 (Kelch-like erythroid cell-derived protein with cap 'n' collar homology-associated protein) leading to NRF2 ubiquitination and degradation by ubiquitin proteasome system (UPS) (76, 77).

Previous studies in our lab show that SiONx and Si^{4+} reduce ROS through cationic reduction, endothelial cell growth, and enhanced SOD1 activity while enhancing proliferation and differentiation of the mouse preosteoblast cells. Thus, the premise of our study is that oxidative stress, inflammation, and defect instability act as a large barrier for the rapid healing of severe bone loss. In contrast, SiONx-based coatings on fixative devices that release Si^{4+} will overcome this barrier by providing structural stability while inducing optimal antioxidant activity to lower ROS, and inflammation, and increase osteogenic activity to promote rapid defect healing.

In Chapter 2, we will first study a ceramic material, Silicon Nitride with a similar elemental composition to study the effect of osteogenic differentiation on its surface and compare the findings to the current gold standard for craniofacial reconstruction, Titanium and polyether ether ketone (PEEK).

In Chapter 3, we will investigate the silicon oxynitride coatings materials for its role in angiogenesis via reduction in oxidative stress and enhancing antioxidant expression.

In Chapter 4, we will optimize and uncover the antioxidant effect of SiONx coatings and its impact on healing, ROS management, and the role of NRF2 signaling to enhance osteogenesis.

Finally in Chapter 5, we will study the effect of SiONx coatings on a fixative device (titanium) *in vivo* on angiogenesis and osteogenesis. We will use rat cranial critical-sized defect

for a sub-critical sized defect model and Rabbit critical size defect for the load-bearing mandibular bone.

In our overall dissertation study design, the goal is to mechanically stabilize defects, boost antioxidant activity, and accelerate bone healing in compromised critical-sized defects.

1.8. IMPACT OF PROPOSED RESEARCH

As rationalized above, there is a critical need for antioxidant and structural support to promote bone healing. **Thus, a combined approach to fabricate biomaterials that structurally support and target antioxidant activity for oxidative stress and inflammation management to promote osteogenesis will constitute a major step toward the clinical translation of biomedical devices that hasten bone and vascular healing.**

1.9. REFERENCES

1. **Keating JF**, **Simpson AHRW**, **Robinson CM**. The management of fractures with bone loss. *J Bone Joint Surg Br* 87: 142–150, 2005. doi: 10.1302/0301-620x.87b2.15874.

2. **wwwPlasticSurgeryorg**. PLASTIC SURGERY STATISTICS REPORT 2017 Plastic Surgery Statistics Report [Online]. www.plasticsurgery.org.

3. **Erdmann D**, **Price K**, **Reed S**, **Follmar KE**, **Levin LS**, **Marcus JR**. A Financial Analysis of Operative Facial Fracture Management [Online]. *Plast Reconstr Surg* 121, 2008. https://journals.lww.com/plasreconsurg/Fulltext/2008/04000/A_Financial_Analysis_of_Operative_Facial_Fracture.32.aspx.

4. **Allareddy V**, **Allareddy V**, **Nalliah RP**. Epidemiology of facial fracture injuries. *J oral Maxillofac Surg Off J Am Assoc Oral Maxillofac Surg* 69: 2613–2618, 2011. doi: 10.1016/j.joms.2011.02.057.

5. **Roden KS**, **Tong W**, **Surrusco M**, **Shockley WW**, **Van Aalst JA**, **Hultman CS**. Changing characteristics of facial fractures treated at a regional, level 1 trauma center, from 2005 to 2010: an assessment of patient demographics, referral patterns, etiology of injury, anatomic location, and clinical outcomes. *Ann Plast Surg* 68: 461–466, 2012. doi: 10.1097/SAP.0b013e31823b69dd.

6. **Szpalski C**, **Barr J**, **Wetterau M**, **Saadeh PB**, **Warren SM**. Cranial bone defects: Current and future strategies. *Neurosurg Focus* 29: 1–11, 2010. doi: 10.3171/2010.9.FOCUS10201.

7. **Dewey MJ**, **Harley BAC**. Biomaterial design strategies to address obstacles in craniomaxillofacial bone repair. *RSC Adv* 11: 17809–17827, 2021. doi: 10.1039/D1RA02557K.

8. **McElhaney JH**, **Fogle JL**, **Melvin JW**, **Haynes RR**, **Roberts VL**, **Alem NM**.

Mechanical properties on cranial bone. *J Biomech* 3: 495–511, 1970. doi: 10.1016/0021-9290(70)90059-x.

9. **Aarden EM**, **Burger EH**, **Nijweide PJ**. Function of osteocytes in bone. *J Cell Biochem* 55: 287–299, 1994. doi: 10.1002/jcb.240550304.

10. **Teitelbaum SL**. Osteoclasts: what do they do and how do they do it? *Am. J. Pathol.* 170: 427–435, 2007.

11. **Elsalanty ME**, **Genecov DG**. Bone grafts in craniofacial surgery. *Craniomaxillofac Trauma Reconstr* 2: 125–134, 2009. doi: 10.1055/s-0029-1215875.

12. **Kruijt Spanjer EC**, **Bittermann GKP**, **van Hooijdonk IEM**, **Rosenberg AJWP**, **Gawlitta D**. Taking the endochondral route to craniomaxillofacial bone regeneration: A logical approach? *J cranio-maxillo-facial Surg Off Publ Eur Assoc Cranio-Maxillo-Facial Surg* 45: 1099–1106, 2017. doi: 10.1016/j.jcms.2017.03.025.

13. **Brown Baer PR**, **Wenke JC**, **Thomas SJ**, **Hale CRG**. Investigation of severe craniomaxillofacial battle injuries sustained by u.s. Service members: a case series. *Craniomaxillofac. Trauma Reconstr.* 5: 243–252, 2012.

14. **Pogrel MA**, **Podlesh S**, **Anthony JP**, **Alexander J**. A comparison of vascularized and nonvascularized bone grafts for reconstruction of mandibular continuity defects. *J oral Maxillofac Surg Off J Am Assoc Oral Maxillofac Surg* 55: 1200–1206, 1997. doi: 10.1016/s0278-2391(97)90165-8.

15. **Ghanaati S**, **Barbeck M**, **Booms P**, **Lorenz J**, **Kirkpatrick CJ**, **Sader RA**. Potential lack of "standardized" processing techniques for production of allogeneic and xenogeneic bone blocks for application in humans. *Acta Biomater* 10: 3557–3562, 2014. doi: 10.1016/j.actbio.2014.04.017.

16. **Bae HW**, **Zhao L**, **Kanim LEA**, **Wong P**, **Delamarter RB**, **Dawson EG**. Intervariability and intravariability of bone morphogenetic proteins in commercially available demineralized bone matrix products. *Spine (Phila Pa 1976)* 31: 1298–1299, 2006. doi: 10.1097/01.brs.0000218581.92992.b7.

17. **Iwai-Yoshida M**, **Shibata Y**, **Wurihan**, **Suzuki D**, **Fujisawa N**, **Tanimoto Y**, **Kamijo R**, **Maki K**, **Miyazaki T**. Antioxidant and osteogenic properties of anodically oxidized titanium. *J Mech Behav Biomed Mater* 13: 230–236, 2012. doi: 10.1016/j.jmbbm.2012.01.016.

18. **Jokstad A**. Common complications with implants and implant prostheses. *Evid Based Dent* 5: 70–71, 2004. doi: 10.1038/sj.ebd.6400267.

19. **MacInnes SJ**, **Gordon A**, **Wilkinson JM**. Risk factors for aseptic loosening following total hip arthroplasty. *Recent Adv Arthroplast* 10: 26975, 2012.

20. **Gita MK**, **Ravi CP V**. Mechanical complications with implants and implant prostheses. *Indian J Dent Adv* 3: 555–559, 2011.

21. **Bloyer DR**, **Gomez-Vega JM**, **Saiz E**, **Mcnaney JM**, **Cannon RM**, **Tomsia AP**. Fabrication and characterization of a bioactive glass coating on titanium implant alloys. *Acta Mater* 47: 4221–4224, 1999.

22. **Thomas KA**, **Kay JF**, **Cook SD**, **Jarcho M**. The effect of surface macrotexture and hydroxylapatite coating on the mechanical strengths and histologic profiles of titanium implant materials. *J Biomed Mater Res* 21: 1395–1414, 1987. doi: 10.1002/jbm.820211205.

23. **Dhert WJ**, **Klein CP**, **Wolke JG**, **Van der Velde EA**, **De Groot K**, **Rozing PM**. A mechanical investigation of fluorapatite, magnesiumwhitlockite, and hydroxylapatite plasma-sprayed coatings in goats. *J Biomed Mater Res* 25: 1183–1200, 1991.

24. **Wang BC**, **Lee TM**, **Chang E**, **Yang CY**. The shear strength and the failure mode of

plasma-sprayed hydroxyapatite coating to bone: the effect of coating thickness. *J Biomed Mater Res* 27: 1315–1327, 1993. doi: 10.1002/jbm.820271012.

25. **Yang C-Y**, **Wang BC**, **Chang WJ**, **Chang E**, **Wu JD**. Mechanical and histological evaluations of cobalt-chromium alloy and hydroxyapatite plasma-sprayed coatings in bone. *J Mater Sci Mater Med* 7: 167–174, 1996.

26. **Klein CPAT**, **Patka P V**, **Van der Lubbe HBM**, **Wolke JGC**, **De Groot K**. Plasma-sprayed coatings of tetracalciumphosphate, hydroxyl-apatite, and α-TCP on titanium alloy: An interface study. *J Biomed Mater Res* 25: 53–65, 1991.

27. **Hayashi K**, **Matsuguchi N**, **Uenoyama K**, **Kanemaru T**, **Sugioka Y**. Evaluation of metal implants coated with several types of ceramics as biomaterials. *J Biomed Mater Res* 23: 1247–1259, 1989.

28. **Foppiano S**, **Marshall SJ**, **Marshall GW**, **Saiz E**, **Tomsia AP**. Bioactive glass coatings affect the behavior of osteoblast-like cells. *Acta Biomater* 3: 765–771, 2007.

29. **Oku T**, **Suganuma K**, **Wallenberg LR**, **Tomsia AP**, **Gomez-Vega JM**, **Saiz E**. Structural characterization of the metal/glass interface in bioactive glass coatings on Ti-6Al-4V. *J Mater Sci Mater Med* 12: 413–417, 2001.

30. **Gomez-Vega JM**, **Saiz E**, **Tomsia AP**, **Marshall GW**, **Marshall SJ**. Bioactive glass coatings with hydroxyapatite and Bioglass particles on Ti-based implants. 1. Processing. *Biomaterials* 21: 105–111, 2000. doi: 10.1016/s0142-9612(99)00131-3.

31. **Tousi NS**, **Velten MF**, **Bishop TJ**, **Leong KK**, **Barkhordar NS**, **Marshall GW**, **Loomer PM**, **Aswath PB**, **Varanasi VG**. Combinatorial effect of Si4+, Ca2+, and Mg2+ released from bioactive glasses on osteoblast osteocalcin expression and biomineralization. *Mater Sci Eng C* 33: 2757–2765, 2013.

32. **van Oirschot BAJA**, **Alghamdi HS**, **Närhi TO**, **Anil S**, **Al Farraj Aldosari A**, **van den Beucken JJJP**, **Jansen JA**. In vivo evaluation of bioactive glass-based coatings on dental implants in a dog implantation model. *Clin Oral Implants Res* 25: 21–28, 2014.

33. **Roy M**, **Bandyopadhyay A**, **Bose S**. Induction Plasma Sprayed Nano Hydroxyapatite Coatings on Titanium for Orthopaedic and Dental Implants. *Surf Coat Technol* 205: 2785–2792, 2011. doi: 10.1016/j.surfcoat.2010.10.042.

34. **Tatara AM**, **Koons GL**, **Watson E**, **Piepergerdes TC**, **Shah SR**, **Smith BT**, **Shum J**, **Melville JC**, **Hanna IA**, **Demian N**, **Ho T**, **Ratcliffe A**, **van den Beucken JJJP**, **Jansen JA**, **Wong ME**, **Mikos AG**. Biomaterials-aided mandibular reconstruction using in vivo bioreactors. *Proc Natl Acad Sci U S A* 116: 6954–6963, 2019. doi: 10.1073/pnas.1819246116.

35. **Broggini N**, **Bosshardt DD**, **Jensen SS**, **Bornstein MM**, **Wang C-C**, **Buser D**. Bone healing around nanocrystalline hydroxyapatite, deproteinized bovine bone mineral, biphasic calcium phosphate, and autogenous bone in mandibular bone defects. *J Biomed Mater Res B Appl Biomater* 103: 1478–1487, 2015. doi: 10.1002/jbm.b.33319.

36. **Athanasiou VT**, **Papachristou DJ**, **Panagopoulos A**, **Saridis A**, **Scopa CD**, **Megas P**. Histological comparison of autograft, allograft-DBM, xenograft, and synthetic grafts in a trabecular bone defect: an experimental study in rabbits. *Med Sci Monit Int Med J Exp Clin Res* 16: BR24-31, 2010.

37. **Gredes T**, **Kunath F**, **Gedrange T**, **Kunert-Keil C**. Bone Regeneration after Treatment with Covering Materials Composed of Flax Fibers and Biodegradable Plastics: A Histological Study in Rats. *Biomed Res Int* 2016: 5146285, 2016. doi: 10.1155/2016/5146285.

38. **Athanasiou KA**, **Niederauer GG**, **Agrawal CM**. Sterilization, toxicity, biocompatibility and clinical applications of polylactic acid/polyglycolic acid copolymers. *Biomaterials* 17: 93–

102, 1996. doi: 10.1016/0142-9612(96)85754-1.

39. **Sandukji A**, **Al-Sawaf H**, **Mohamadin A**, **Alrashidi Y**, **Sheweita SA**. Oxidative stress and bone markers in plasma of patients with long-bone fixative surgery: role of antioxidants. *Hum Exp Toxicol* 30: 435–442, 2011. doi: 10.1177/0960327110374203.

40. **Hannemann A**, **Friedrich N**, **Spielhagen C**, **Rettig R**, **Ittermann T**, **Nauck M**, **Wallaschofski H**. Reference intervals for serum osteocalcin concentrations in adult men and women from the study of health in Pomerania. *BMC Endocr Disord* 13: 11, 2013. doi: 10.1186/1472-6823-13-11.

41. **Prasad G**, **Dhillon MS**, **Khullar M**, **Nagi ON**. Evaluation of oxidative stress after fractures. A preliminary study. *Acta Orthop Belg* 69 6: 546–51, 2003.

42. **Hwang K**, **You SH**. Analysis of facial bone fractures: An 11-year study of 2,094 patients. *Indian J Plast Surg* 43: 42–48, 2010. doi: 10.4103/0970-0358.63959.

43. **Sandukji A**, **Al-Sawaf H**, **Mohamadin A**, **Alrashidi Y**, **Sheweita SA**. Oxidative stress and bone markers in plasma of patients with long-bone fixative surgery: Role of antioxidants. *Hum Exp Toxicol* 30: 435–442, 2010. doi: 10.1177/0960327110374203.

44. **Wang Z**, **Ehnert S**, **Ihle C**, **Schyschka L**, **Pscherer S**, **Nussler NC**, **Braun KF**, **Van Griensven M**, **Wang G**, **Burgkart R**, **Stöckle U**, **Gebhard F**, **Vester H**, **Nussler AK**. Increased oxidative stress response in granulocytes from older patients with a hip fracture may account for slow regeneration. *Oxid Med Cell Longev* 2014: 819847, 2014. doi: 10.1155/2014/819847.

45. **Kubo Y**, **Wruck CJ**, **Fragoulis A**, **Drescher W**, **Pape HC**, **Lichte P**, **Fischer H**, **Tohidnezhad M**, **Hildebrand F**, **Pufe T**, **Jahr H**. Role of Nrf2 in Fracture Healing: Clinical Aspects of Oxidative Stress. *Calcif Tissue Int* 105: 341–352, 2019. doi: 10.1007/s00223-019-

00576-3.

46. **Hamada Y**, **Fujii H**, **Fukagawa M**. Role of oxidative stress in diabetic bone disorder. *Bone* 45: S35–S38, 2009.

47. **Dai K-R**, **Hao Y-Q**. Quality of healing compared between osteoporotic fracture and normal traumatic fracture. In: *Advanced Bioimaging Technologies in Assessment of the Quality of Bone and Scaffold Materials*. Springer, 2007, p. 531–541.

48. **Chakkalakal DA**, **Novak JR**, **Fritz ED**, **Mollner TJ**, **McVicker DL**, **Garvin KL**, **McGuire MH**, **Donohue TM**. Inhibition of bone repair in a rat model for chronic and excessive alcohol consumption. *Alcohol* 36: 201–214, 2005.

49. **Patel RA**, **Wilson RF**, **Patel PA**, **Palmer RM**. The effect of smoking on bone healing: a systematic review. *Bone Joint Res* 2: 102–111, 2013.

50. **Sies H**. Oxidative stress: oxidants and antioxidants. *Exp Physiol Transl Integr* 82: 291–295, 1997.

51. **Chavan SN**, **More U**, **Mulgund S**, **Saxena V**, **Sontakke AN**. Effect of supplementation of vitamin C and E on oxidative stress in osteoporosis. *Indian J Clin Biochem* 22: 101–105, 2007. doi: 10.1007/BF02913324.

52. **Mottaghi P**, **Nasri P**. Antioxidant and Bone; Protect Your Future: A Brief Review. *Iran J Public Health* 50: 1783–1788, 2021. doi: 10.18502/ijph.v50i9.7049.

53. **Mlakar SJ**, **Osredkar J**, **Prezelj J**, **Marc J**. The antioxidant enzyme GPX1 gene polymorphisms are associated with low BMD and increased bone turnover markers. *Dis Markers* 29: 71–80, 2010. doi: 10.3233/DMA-2010-0728.

54. **Gullberg B**, **Johnell O**, **Kanis JA**. World-wide projections for hip fracture. *Osteoporos Int a J Establ as result Coop between Eur Found Osteoporos Natl Osteoporos Found USA* 7:

407–413, 1997. doi: 10.1007/pl00004148.

55. **Jahanian E**, **Karimifar M**, **Rafieian-Kopaei M**. Antioxidants as a novel way to alleviate the adverse effects of oxidative stress in osteoporosis [Online]. *J parathyr dis* 4: 60–65, 2016. https://jparathyroid.com/Article/JPD_20160613105923.

56. **Pandey D**. *OXIDATIVE STRESS AND SOME ANTIOXIDANT PARAMETERS IN POSTMENOPAUSAL OSTEOPOROTIC WOMEN WITH FRACTURES: A CASE CONTROL STUDY KIRI/I OLAN POSTMENOPOZAL OSTEOPOROT‹K KADINLARDA OKS‹DAT‹F STRES VE BAZI ANT‹OKS‹DAN PARAMETRELER: B‹R OLGU KONTROL ÇALIfiMASI*. 2008.

57. **Fabian E**, **Gerstorfer I**, **Thaler HW**, **Stundner H**, **Biswas P**, **Elmadfa I**. Nutritional supplementation affects postoperative oxidative stress and duration of hospitalization in patients with hip fracture. *Wien Klin Wochenschr* 123: 88–93, 2011. doi: 10.1007/s00508-010-1519-6.

58. **Lean JM**, **Davies JT**, **Fuller K**, **Jagger CJ**, **Kirstein B**, **Partington GA**, **Urry ZL**, **Chambers TJ**. A crucial role for thiol antioxidants in estrogen-deficiency bone loss. *J Clin Invest* 112: 915–923, 2003. doi: 10.1172/JCI18859.

59. **Mathy-Hartert M**, **Hogge L**, **Sanchez C**, **Deby-Dupont G**, **Crielaard JM**, **Henrotin Y**. Interleukin-1β and interleukin-6 disturb the antioxidant enzyme system in bovine chondrocytes: a possible explanation for oxidative stress generation. *Osteoarthr Cartil* 16: 756–763, 2008. doi: https://doi.org/10.1016/j.joca.2007.10.009.

60. **Lü J-M**, **Lin PH**, **Yao Q**, **Chen C**. Chemical and molecular mechanisms of antioxidants: experimental approaches and model systems. *J Cell Mol Med* 14: 840–860, 2010. doi: 10.1111/j.1582-4934.2009.00897.x.

61. **Simunovic N**, **Devereaux PJ**, **Bhandari M**. Surgery for hip fractures: Does surgical delay affect outcomes? *Indian J Orthop* 45: 27–32, 2011. doi: 10.4103/0019-5413.73660.

62. **Sterling HF**, **Swann RCG**. Chemical vapour deposition promoted by r.f. discharge. *Solid State Electron* 8: 653–654, 1965. doi: https://doi.org/10.1016/0038-1101(65)90033-X.

63. **Franz G**. Plasma Enhanced Chemical Vapor Deposition of Organic Polymers. *Processes* 9, 2021. doi: 10.3390/pr9060980.

64. **Ferraris S**, **Corazzari I**, **Turci F**, **Cochis A**, **Rimondini L**, **Vernè E**. Antioxidant Activity of Silica-Based Bioactive Glasses. *ACS Biomater Sci Eng* 7: 2309–2316, 2021. doi: 10.1021/acsbiomaterials.1c00048.

65. **Ferraris S**, **Spriano S**. Antibacterial titanium surfaces for medical implants. *Mater Sci Eng C Mater Biol Appl* 61: 965–978, 2016. doi: 10.1016/j.msec.2015.12.062.

66. **Sanchez C**, **Julian B**, **Belleville P**, **Popall M**. Applications of hybrid organic-inorganic nanocomposites. *J Mater Chem* 15: 3559–3592, 2005. doi: 10.1039/B509097K.

67. **Chen J**, **Yang MS**, **Zhang SM**. Immobilization of antioxidant on nanosilica and the aging resistance behavior in polypropylene. *Compos Part A Appl Sci Manuf* 42: 471–477, 2011. doi: https://doi.org/10.1016/j.compositesa.2011.01.006.

68. **Catauro M**, **Papale F**, **Bollino F**, **Piccolella S**, **Marciano S**, **Nocera P**, **Pacifico S**. Silica/quercetin sol–gel hybrids as antioxidant dental implant materials. *Sci Technol Adv Mater* 16: 35001, 2015. doi: 10.1088/1468-6996/16/3/035001.

69. **Varanasi V**, **Aswath P**, **Maginot M**, **Lavrick N V**. Amorphous silicon oxide, amorphous silicon oxynitride, and amorphous silicon nitride thin films and uses thereof. Google Patents: 2021.

70. **Ilyas A**, **Odatsu T**, **Shah A**, **Monte F**, **Kim HKW**, **Kramer P**, **Aswath PB**, **Varanasi VG**. Amorphous silica: a new antioxidant role for rapid critical-sized bone defect healing. *Adv Healthc Mater* 5: 2199–2213, 2016.

71. **Ilyas A**, **Lavrik N V.**, **Kim HKW**, **Aswath PB**, **Varanasi VG**. Enhanced Interfacial Adhesion and Osteogenesis for Rapid "bone-like" Biomineralization by PECVD-Based Silicon Oxynitride Overlays. *ACS Appl Mater Interfaces* 7: 15368–79, 2015. doi: 10.1021/acsami.5b03319.

72. **Ilyas MA**, **Velton E**, **Shah A**, **Monte F**, **Kim HKW**, **Aswath PB**, **Varanasi VG**. Rapid Regeneration of Vascularized Bone by Nanofabricated Amorphous Silicon. *J Biomed Nanotechnol* 15: 1–15, 2019. doi: 10.1166/jbn.2019.2779.

73. **Varanasi VG**, **Ilyas A**, **Velten MF**, **Shah A**, **Lanford WA**, **Aswath PB**. Role of Hydrogen and Nitrogen on the Surface Chemical Structure of Bioactive Amorphous Silicon Oxynitride Films. *J Phys Chem B* 121: 8991–9005, 2017. doi: 10.1021/acs.jpcb.7b05885.

74. **Taguchi K**, **Motohashi H**, **Yamamoto M**. Molecular mechanisms of the Keap1–Nrf2 pathway in stress response and cancer evolution. *Genes to cells* 16: 123–140, 2011.

75. **Sun Y-X**, **Li L**, **Corry KA**, **Zhang P**, **Yang Y**, **Himes E**, **Mihuti CL**, **Nelson C**, **Dai G**, **Li J**. Deletion of Nrf2 reduces skeletal mechanical properties and decreases load-driven bone formation. *Bone* 74: 1–9, 2015.

76. **Wruck CJ**, **Götz ME**, **Herdegen T**, **Varoga D**, **Brandenburg L-O**, **Pufe T**. Kavalactones protect neural cells against amyloid β peptide-induced neurotoxicity via extracellular signal-regulated kinase 1/2-dependent nuclear factor erythroid 2-related factor 2 activation. *Mol Pharmacol* 73: 1785–1795, 2008.

77. **Canning P**, **Sorrell FJ**, **Bullock AN**. Structural basis of Keap1 interactions with Nrf2. *Free Radic Biol Med* 88: 101–107, 2015.

CHAPTER 2

A COMPARATIVE STUDY ON SILICON NITRIDE, TITANIUM, AND POLY-ETHER ETHER KETONE ON MOUSE PRE-OSTEOBLASTS CELLS

Neelam Ahuja[1 +], Kamal R. Awad[1 2 +,] Marco Brotto[1], Pranesh B Aswath[2], Venu Varanasi[1 2 *]

[1] Bone-Muscle Research Center, College of Nursing and Health Innovation, The University of Texas at Arlington, Texas 76019, USA; P: 817-272-2776/F: 817-272-5006.

[2] Department of Materials Science and Engineering, The University of Texas at Arlington, Texas 76019, USA; P: 817-272-2398/F: 817-272-2538.

[+] Co-first author: Kamal R. Awad and Neelam Ahuja

[*] Corresponding author.

Ahuja N, **Awad KR**, **Brotto M**, **Aswath PB**, **Varanasi V**. A comparative study on silicon nitride, titanium and polyether ether ketone on mouse pre-osteoblast cells. *Med DEVICES \& SENSORS* 4: e10139, 2021. doi: https://doi.org/10.1002/mds3.10139.

ABSTRACT

The current study provides more insights about the surface bioactivity of the silicon nitride (Si_3N_4) as a potential candidate for bone regeneration in craniofacial and orthopedic applications compared to conventional implantation materials. Current skeletal reconstructive materials like titanium and poly-ether ether ketone (PEEK) are limited by poor long-term stability, biocompatibility, and prolonged healing. Si_3N_4 is an FDA approved material for an intervertebral spacer in spinal fusion applications. It is a biocompatible and has anti-microbial properties. Here we hypothesize that Si_3N_4 to be an osteoconductive material and conducts the growth, differentiation of MC3T3-E1 cells for extracellular matrix deposition, mineralization, and eventual bone regeneration for craniofacial and orthopedic applications. MC3T3-E1 cells were used to study the osteoblastic differentiation and mineralization on sterile samples of Si_3N_4, titanium alloy, and PEEK. The samples were then analyzed for extracellular matrix deposition and mineralization by FTIR, Raman spectroscopy, SEM, EDX, Alizarin Red, qRT-PCR and ELISA. The *in vitro* study indicates the formation of collagen fibers and mineral deposition on all three sample surfaces. There was more profound and faster ECM deposition and mineralization on Si_3N_4 surface as compared to titanium and PEEK. The FTIR and Raman spectroscopy show formation of collagen and mineral deposition at 30 days for Si_3N_4 and titanium and not PEEK. The peaks shown by Raman for Si_3N_4 resemble closely to natural bone. Results also indicate the upregulation of osteogenic transcription factors such as RUNX2, SP7, collagen type I and Osteocalcin. The authors concluded that Si_3N_4 rapidly conducts mineralized tissue formation via extracellular matrix deposition and biomarker expression in mouse calvarial pre-osteoblasts cells. Thus, this study confirms that the bioactive Si_3N_4 could be a potential

material for craniofacial and orthopedic applications leading to rapid bone regeneration that resemble the natural bone structure.

Keywords: Silicon Nitride; MC3T3-E1 cells; collagen formation; Hydroxyapatite; titanium.

2.1. INTRODUCTION

Trauma, tumor resection, congenital defects, and various medical conditions result in craniomaxillofacial (CMF) and orthopedic bone defects, which affect either the bony contour or continuity, or both (1–3) Although autografts are the gold standard for healing small bone defects, they have limitations in larger defects due to limited bone volume availability at donor site, resorption of the graft, donor site morbidity, chances of infection at both the recipient and donor sites, increased surgical time, patient discomfort, and prolonged hospital stay (4–6). Further, allografts and xenografts have potential infectious and immunological risks (1, 7, 8). Various alloplastic materials have been developed and are in clinical use for bone replacement procedures (3, 4, 6). A useful reconstructive material/ fixative plate should have the ability to induce new bone formation while stabilizing the defect site without any growth of fibrous tissue at the bone/plate interface (Osseointegration) (9). Lastly, the reconstructive material should have a sufficient mechanical stability to withstand the implantation procedure and resist the collapse during the patient's normal activities (10).

In our previous study, we compared the use of three basic types of fixative implant/ reconstructive material (Polyether ether ketones (PEEK), Titanium (Ti6Al4V) and Silicon nitride (Si_3N_4) on their suitability to facilitate surface formation of Ca-P aggregates. Our goal in the prior work was to determine if a ceramic silicon nitride could produce possible non-cellular driven mineral formation to assess the potential to form a direct bond with Ca-P aggregates in a similar role as that of Ti-fixative plates. We found that such an effect was comparable with titanium and slightly elevated the potential (*in vitro*) growth of such aggregates on PEEK (11).

In the present study, we hypothesize that silicon nitride could be an osteoconductive material and enhance growth, differentiation, extracellular matrix (ECM), and mineral deposition

of the murine calvarial MC3T3-E1 pre-osteoblast cells. The authors tested this hypothesis by conducting a comparative study of the cellular response to the three surfaces: Ti6Al4V, Si_3N_4, and PEEK. *In vitro* cell culture studies were performed on the samples surface for 30 and 60 days using MC3T3-E1 cell line. At each time points, samples were collected and used to study the osteoblastic differentiation and mineralization on the sterile samples. The samples were then analyzed for extracellular matrix deposition and mineralization by FTIR, Raman spectroscopy, SEM, EDX, and Alizarin Red stain. For qRT-PCR and ELISA, the cells were grown, seeded, and differentiated using previously established protocol for 1, 3, 7 and 14 days. Then, qRT-PCR and ELISA studies were performed following our previously published protocol. The results were analyzed in a comparative way to clearly compare the surface activity of the Si_3N_4 to Ti6Al4V and PEEK as presented below.

2.2. MATERIALS AND METHODS

2.2.1. Sample Preparation

Samples of silicon nitride were provided and processed by Amedica Corporation (Salt Lake City, UT, USA) with physical properties as given previously (12). Disc of Ø12.7 x 2.5mm were prepared for further characterization and *in vitro* testing. PEEK (ASTM D6262, Ketron® PEEK 1000, Quadrant EPP USA, Inc., Reading PA, USA; distributed by McMaster-Carr, Santa Fe Springs, CA, USA) and a titanium alloy (ASTM F136, Ti6Al4V-ELI, distributed by Vincent Metals, Minneapolis, MN, USA) samples with the same diameter (Ø12.7 x 2.5mm) was used for comparison. The samples were immersed in 100% ethanol and ultrasonicated for 5 minutes to remove any possible surface debris. Sterilization was achieved as previously described (11) using gas sterilization with ethylene oxide for 12 hours and then vacuum desiccation was

performed for 24 hours to remove any residual absorbed ethylene oxide gas. Surface cleaning and sterilization were conducted at standard temperature and pressure (i.e., 25°C and 1 bar).

2.2.2. *In Vitro* Studies

In vitro cell study using murine calvarial MC3T3-E1 pre-osteoblast cells was accomplished to investigate cell differentiation and mineralization on each surface. The experimental studies were conducted at the Bone and Muscle Research Center and Department of Material Science and Engineering at University of Texas at Arlington. All characterizations were carried out at the Center for Characterization of Materials and Biology at the University of Texas at Arlington (CCMB, UTA).

Murine calvarial MC3T3-E1 pre-osteoblast cells (American Type Cell Culture Inc., Manassas, VA) were cultured using α-MEM supplemented with 10% fetal bovine serum (FBS) and 1% penicillin/ streptomycin (pen-strep) until 75-90% confluence in 75 sq. cm flasks (Corning Life Sciences Inc., Tewksbury, MA). These cells were used between passage 21-29 incubated at 37ºC, 100% relative humidity, and 5% CO2 (according to the manufacturer's specifications). Ethylene oxide sterilized samples of each test material (n=3) were washed twice with PBS, placed in 24 vacuum gas treated standard tissue culture well plates (Corning Life Sciences Inc., Tewksbury, MA), and seeded with 10^5 MC3T3-E1 cells for 24 hours. To study the osteoblastic differentiation and mineralization on the surface of the samples, the culture medium was replaced with differentiation medium after 24 hours of seeding, which consists of α-MEM supplemented with 10% FBS, 1% pen-strep enriched with 50 µg/ml ascorbic acid (Sigma Aldrich, Saint Louis, MO). The differentiating media was changed every 2 days and cells were cultured on the surface for 30 days to study ECM deposition and 60 days to study the mineralization. After 30 and 60 days, the samples were washed in PBS twice to remove non-

adherent cells and transferred to fresh well plates. The samples were fixed using 2% glutaraldehyde (Sigma Inc., St. Louis, MO) for 1 hour. The samples were then sequentially alcohol dehydrated using an ethanol-water mixture using sequential concentrations of alcohol (i.e., 25%, 50%, 75%, and 100%) to preserve the intact cellular structure on the sample surfaces. The samples were then analyzed using FT-IR, SEM, and Raman Spectroscopy and then stained with Alizarin red.

2.2.3. FT-IR and Raman Spectroscopy

FT-IR and Raman spectroscopy was conducted on all samples cultured for 30 days and 60 days to characterize the ECM formation and mineralization on the different surfaces. FT-IR analysis was performed using Thermo Nicolet 6700 FT-IR Spectrometer (Thermo Electron Corporation, Madison, WI, USA) with a smart attenuated total reflectance (ATR) accessory. The FT-IR absorbance spectra was collected over the range of 4000-500 cm^{-1}, with an aperture 150, 128 scans, and resolution of 4 cm^{-1}. Raman spectroscopy (DXR, Thermo Scientific Waltham, MA, USA) was conducted for Si_3N_4 and Ti6Al4V samples with a 780 nm excitation laser at 100 mW, 10x objective, and a 50 μm slit, whereas for PEEK using same excitation laser at 1 mW, 10x objective, and a 25 μm pinhole. Photo-bleaching for 4 minutes was used prior to spectra collection with a 10 s exposure time. Thirty-two spectra per location were recorded between 400-2000 cm^{-1}. Raman data from the surfaces of all samples after 60 days of the *in vitro* study revealed the ECM and mineralization composition. ECM composition can be revealed by the amide peaks and proline of collagen, the mineral content can be indicated by the presence of PO_4^{3-} symmetric stretching vibrational modes (Phosphate group of HA), and the Raman intensity is proportional to the mineralization content.

2.2.4. HR-SEM and EDS Analysis

High resolution scanning electron microscopy (HR-SEM) was used along with energy dispersive x-ray spectroscope (EDS) mapping to study the surface morphology of the ECM deposition and mineralization on Si_3N_4 and other samples. All samples were coated with silver using a sputter coated (CrC-100 sputter, Plasma Sciences Inc., Lorton, VA) for imaging using an Ultra HR-SEM (Hitachi S-4800 II FE SEM, Hitachi, Tokyo, Japan). Working distance of 10 mm under 20 kV were used and images were taken at different magnifications. EDS mapping of sample surfaces was observed with an EDS detector connected with a Hitachi S-3000N Variable Pressure SEM.

2.2.5. Alizarin Red Staining

Alizarin Red S staining was performed on the samples surface after 60 days of cell culture to detect calcium by forming Alizarin Red S-Calcium complex by chelation. 2% alizarin red solution (neutralized by 10% acetic acid and 10% ammonium hydroxide to pH 4.1- 4.3) was used to stain all samples for 15-30 minutes to be observed under the microscope for red-orange staining of calcium. The samples were washed to remove excess dye and dehydrated using acetone, and images were conducted using a digital microscope (VHX-6000, Keyence, Osaka, Japan).

2.2.6. qRT-PCR Analysis

Quantitative reverse transcriptase polymerase chain reaction (qRT-PCR) was used to study the gene expression of the MC3T3-E1 cells as previously described (13) on the surface of silicon nitride as compared to PEEK and titanium alloy. The cells were grown, seeded, and differentiated using the previously established protocol above for 1, 3, 7 and 14 days. Culture media was collected at each time point and stored at -80°C for further evaluation. qRT-PCR was

performed on all samples after days 1,3, and 7 using previously established protocol (13). Following cell lysing mRNA was extracted (RNeasy Mini Kit, Qiagen, Valencia, CA) and converted to cDNA (Reverse Transcription System, Promega, Madison, WI) based on manufacturer guidelines. Samples were tested for relative expression of runt-related transcription factor 2 (RUNX2, accession no. NM_009820.2), transcription factor SP7(SP7, accession no. AF184902.1), collagen type I, alpha 2 (Col1a2, accession no. NM_007743.2), and bone gamma carboxyglutamate protein (BGLAP, accession. NM_007541.3) using glyceraldehyde 3-phosphate dehydrogenase (GAPDH, accession no. NM_008084.2) as the internal housekeeping gene. Quantification of the relative gene expression was performed using delta−delta CT (Δ−Δ-CT) method.

2.2.7. ELISA

The cell culture media was collected at 1, 3, 7 and 14 days to evaluate the protein expression for different samples. The concentration for osteocalcin was determined using an enzyme-linked immunosorbent assay (ELISA) Kit (Elisa, Alfa Aesar, Ward Hill, MA) per manufacturer guidelines and previously described procedures (13). Samples were thawed and pipetted into the well plate along with kit standards. The plate was incubated and washed several times. Stop solution was added and the optical density was measured using a spectrophotometer at 450nm.

2.2.8. Statistical Analysis

Statistical analysis was performed using SPSS (IBM Corporation, Armonk, NY) and Microsoft excel (Microsoft Corporation, Redmond, WA) and all data is represented as mean ± standard deviation. Mean “average” is an important measure that incorporates the score from every subject in the research study, while the standard deviation is one of the most used

statistical measures to demonstrate data variability. Thus, mean, and standard deviation are best used when data are normally and symmetrically distributed (14). Paired T-test and One-way analysis of variance with post hoc Tukey 's test (between group comparisons) was used, and the p value was set to 0.05. * represents $p < 0.05$, ** for $p < 0.01$ and *** for $p < 0.001$.

2.3. RESULTS

2.3.1. FT-IR and Raman Spectroscopy

To identify the organic and inorganic components of the ECM environment on the surface of each sample, FT-IR analysis within 600-2000 cm^{-1} spectral range was performed. **Figure 2.1(a-c)** represents the FT-IR spectra of the samples seeded with MC3T3-E1 cells and cultured in differentiation media for 30 days. Both Si_3N_4 and Ti6Al4V samples exhibited peaks indicating the presence of collagen fibers and mineralization while the PEEK sample did not exhibit any significant peaks for the ECM environment. The spectra indicated several vibrational bands related to the ECM components such as ECM proteins (collagen), and P-O bonds of PO_4^{3-} mineral ions on Si_3N_4 and Ti6Al4V surfaces. The presence of ECM proteins on Si_3N_4 and Ti6Al4V surfaces is indicated by the presence of vibrational bands of amide I (peak a at 1637 cm^{-1}), amide II (peak b at 1532 cm^{-1}), and amide III (peak c at 1228 cm^{-1}). The stretching P-O bond (peak d) of PO_4^{3-} at 1030 cm^{-1} confirmed the mineral formation "inorganic components of the ECM" on Si_3N_4 and Ti6Al4V surfaces, and the presence of a single broad peak spanning by 900 - 1200 cm^{-1} which indicated the formation of amorphous calcium phosphate (ACP) (15). After 60 days of in-vitro cell culture, the FT-IR spectra revealed the presence of amide I, II, and III and the vibrational bands for P-O bond of PO_4^{3-} ions on the surface of all samples (Si_3N_4, Ti6Al4V, and PEEK), indicated in **figure 2.1 (d-f)**.

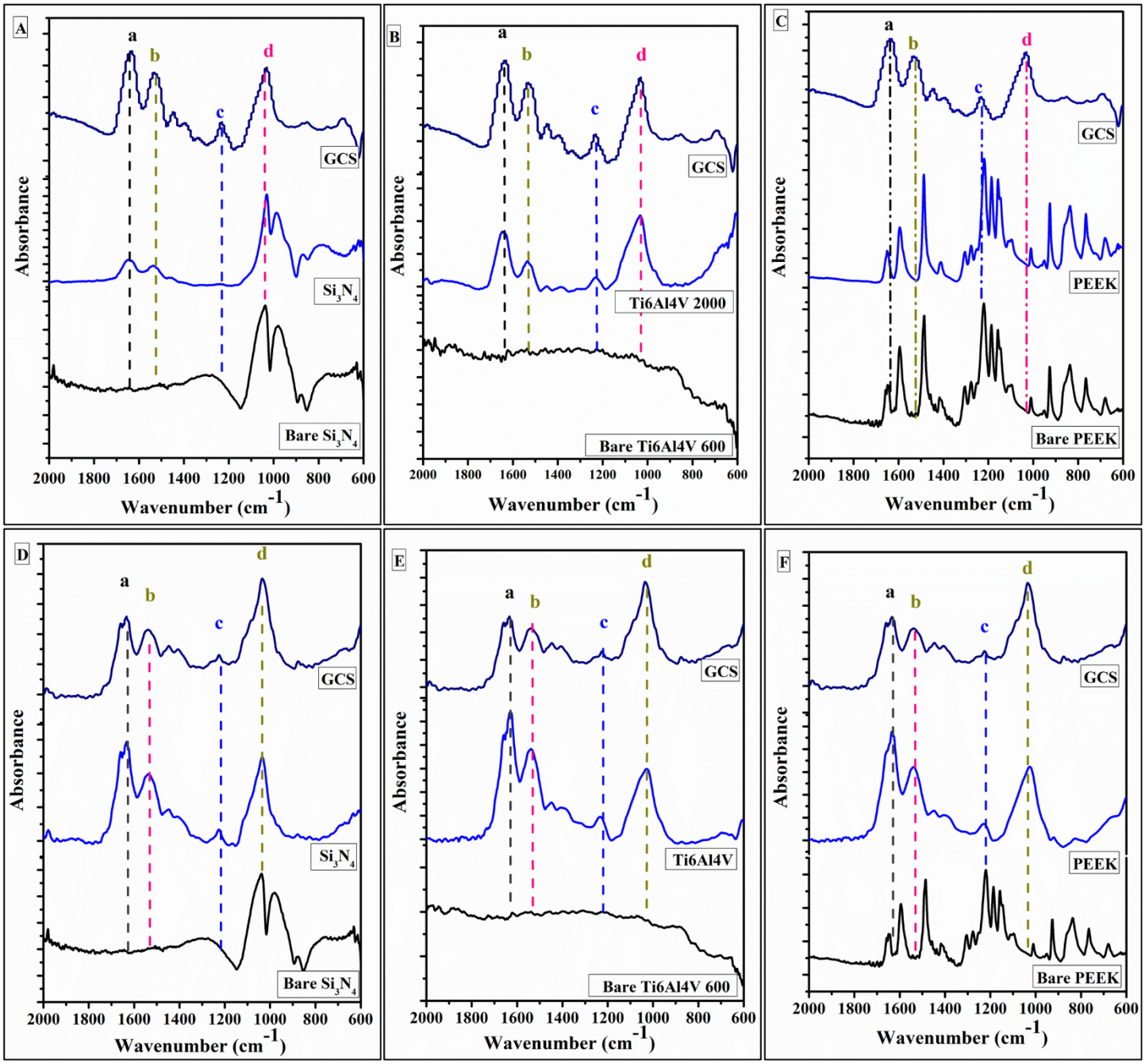

Figure 2.1: presents the FT-IR spectra of the of Si_3N_4, titanium alloy (Ti6Al4V), and PEEK samples showing the matrix deposition of MC3T3-E1 cells cultured in differentiating media for 30 days (a-c) and 60 days (d-e) of in vitro study. Peaks indicator (a→amide I, b→amide II, c→amide III, and d→P-O bond).

To gain more details about the composition of ECM and mineral formation on the samples after 60 days of the *in vitro* cell culture study, Raman analyses were conducted on the three different samples compared to the glass cover slip (GCS) as a control. **Figure 2.2** shows

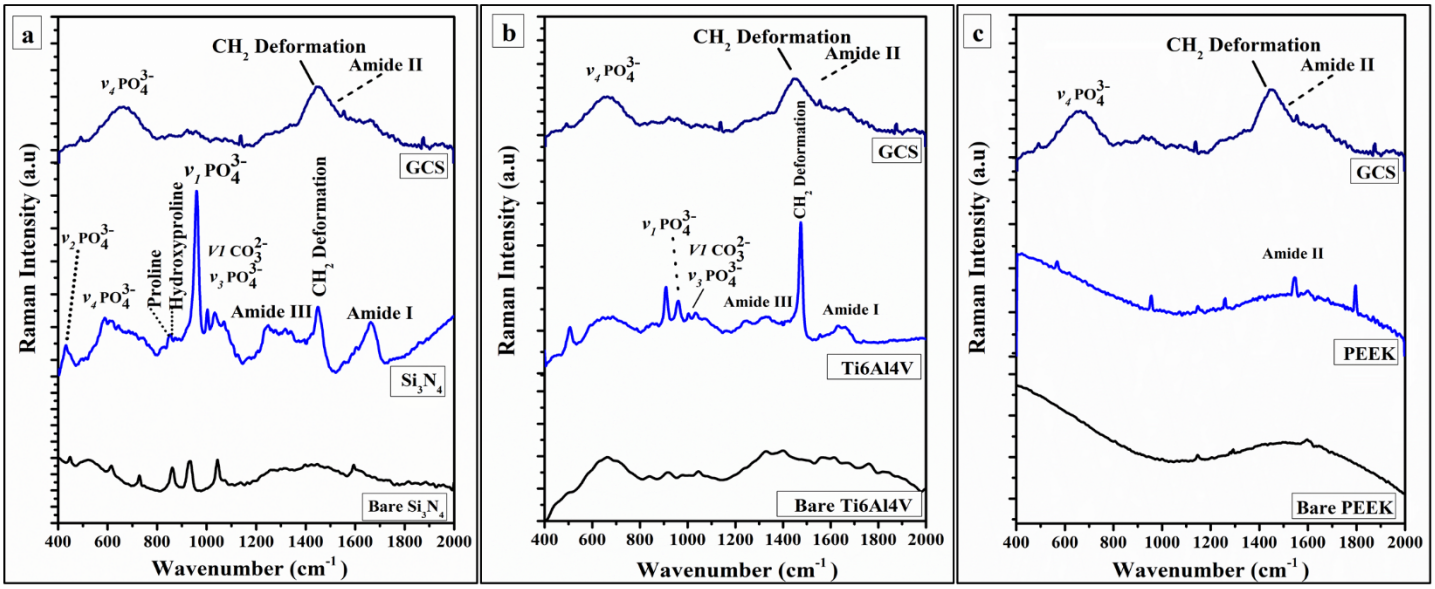

Figure 2.2: represents the Raman spectra of Si_3N_4, titanium alloy (Ti6Al4V), and PEEK samples showing the matrix deposition of MC3T3-E1 cells cultured in differentiating media for 60 days of the *in vitro* study.

the Raman spectra on the surface of each sample compared to the bare surface and GCS. After analyzing the Raman spectra for Si_3N_4, it is clear that Si_3N_4 surface displays peaks for amide I (1665 cm^{-1}), amide III (1255-1272 cm^{-1}) of collagen, and the four vibrational modes of phosphate group (symmetric stretching vibration of PO_4^{3-} of HA) at v_1:962 cm^{-1}, v_2:428 cm^{-1}, v_3:1044 cm^{-1}, and v_4:589 cm^{-1}. Additional functional groups indicated by peaks included a carbonate peak at 1033 cm^{-1}, collagen proline (853 cm^{-1}) and hydroxyproline at 872 cm^{-1}, as well as CH_2 deformation of proteins at 1446 cm^{-1}. Spectra results for Ti6Al4V samples only confirmed the presence of amide I and amide III of collagen, v_1 and v_3 modes of phosphate as well as the CH_2 deformation peak. The GCS control only displayed peaks for amide II, v_4- PO_4^{3-}, and CH_2 deformation peak, and PEEK only showed the amide II peak as indicated in **figure 2.2**.

2.3.2. HR-SEM and EDS Analysis

HR-SEM was used to capture the surface morphology and investigate the formation of collagen fibers and mineral on the different samples. **Figure 2.3** indicates the surface morphology of the samples after 30 days of the *in vitro* study. From **figure 2.3 (a)**, it should be

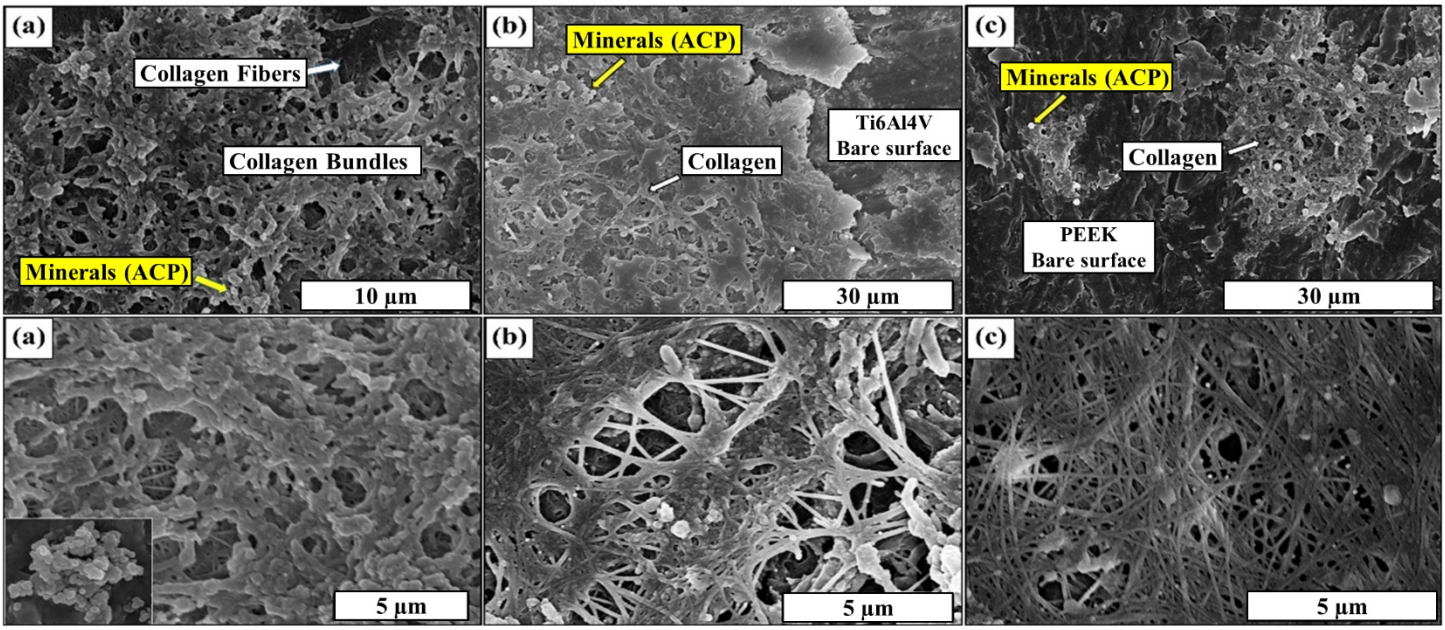

Figure 2.3: HR-SEM images at different magnification for (a) Si_3N_4, (b) Ti6Al4V, and c) PEEK samples showing the matrix deposition after 30 days of the *in vitro* study.

noted that the Si_3N_4 surface was completely covered with the collagen fibrils that turned into collagen bundles as indicated by the arrows. Furthermore, mineral (ACP) deposition was observed on the surface using high magnification imaging and confirmed the FT-IR and Raman results. HR-SEM images also confirmed the presence of collagen fibers and mineral deposition on the surface of Ti6Al4V samples (**Figure 2.3 b**). Although the high magnification images indicated that collagen fibers started to form collagen bundles on Ti6Al4V, the surface was not completely covered by the collagen fibers. Also, sparse deposition of ACP was detected on the surface of Ti6Al4V samples. On the other hand, SEM images of the PEEK samples revealed the presence of collagen fibrils, but no collagen bundles were detected. Moreover, the PEEK surface was not completely covered by collagen fibers. The poor ECM formations on the PEEK surfaces could be attributed to the low number of attached cells leading to low differentiation and poor ECM deposition. **Figure 2.4** presents the HR-SEM images at different magnifications for all samples to investigate the ECM mineralization after 60 days of the *in vitro* study. A "flower-

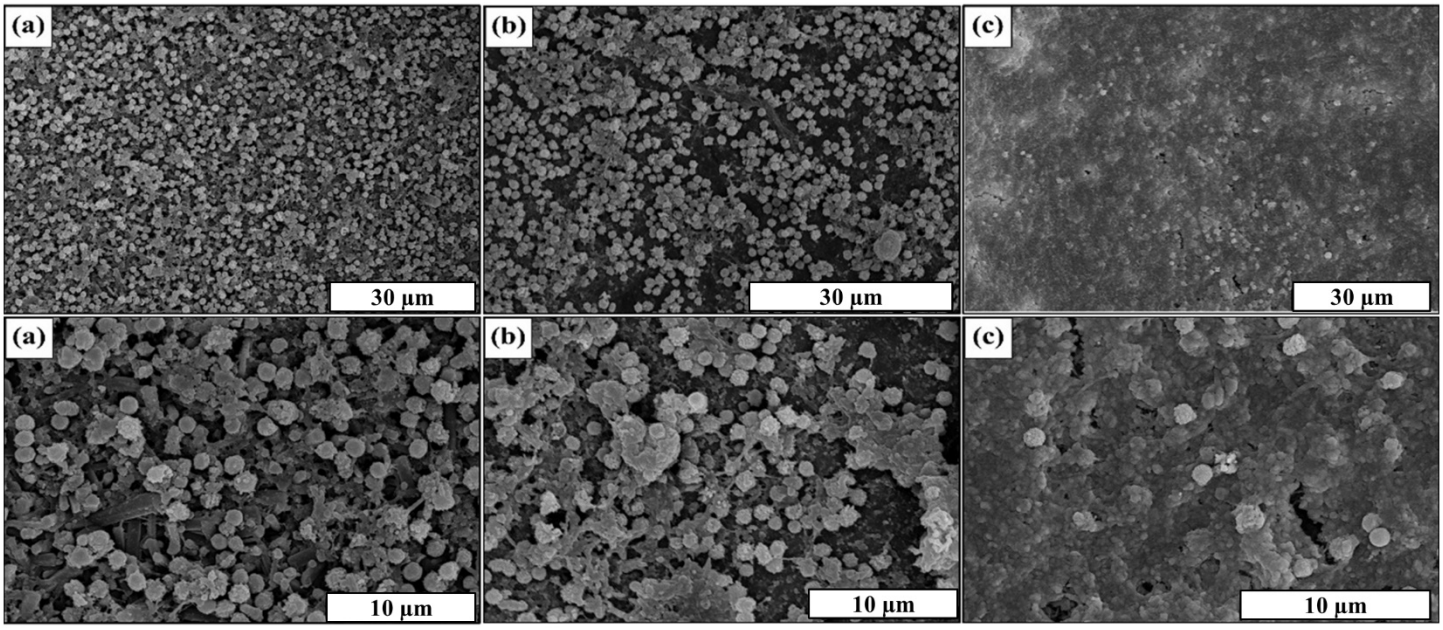

Figure 2.4: HR-SEM images at different magnification for (a) Si_3N_4, (b) Ti6Al4V, and (c) PEEK samples showing the matrix deposition after 60 days of the *in vitro* study.

like" porous ACP structure was deposited on Si_3N_4 and Ti6Al4V samples, covering the surfaces. Although mineral deposition on Ti6Al4V surfaces covered a comparable area to Si_3N_4 deposition, the later still has the highest coverage area as indicated in **figure 2.3a**. After 60 days PEEK sample surfaces were covered with collagen bundles while ACP deposition was sparse.

The energy dispersive X-ray spectroscopy (EDS) mapping was used to determine the surface morphology, composition, and element distribution of the mineral deposition. Regions of interest corresponding to ACP deposition were defined by mapping the surfaces and detecting the Ca, and P K edges. After 30 days of the *in vitro* study, only Ca and P deposition was observed on the surface of Si_3N_4 samples as shown in **figure 2.5 (a)**. This could be attributed to the high density of mineral deposition on the surface of Si_3N_4 compared to Ti6Al4V and PEEK samples. **Figure 2.5 (b-d)** presents the EDS mapping of the samples after 60 days which clearly identified the presence of mineral deposition on the surface of all samples, with high density deposition of Ca and P deposition on Si_3N_4 surfaces (**figure 2.5 b**).

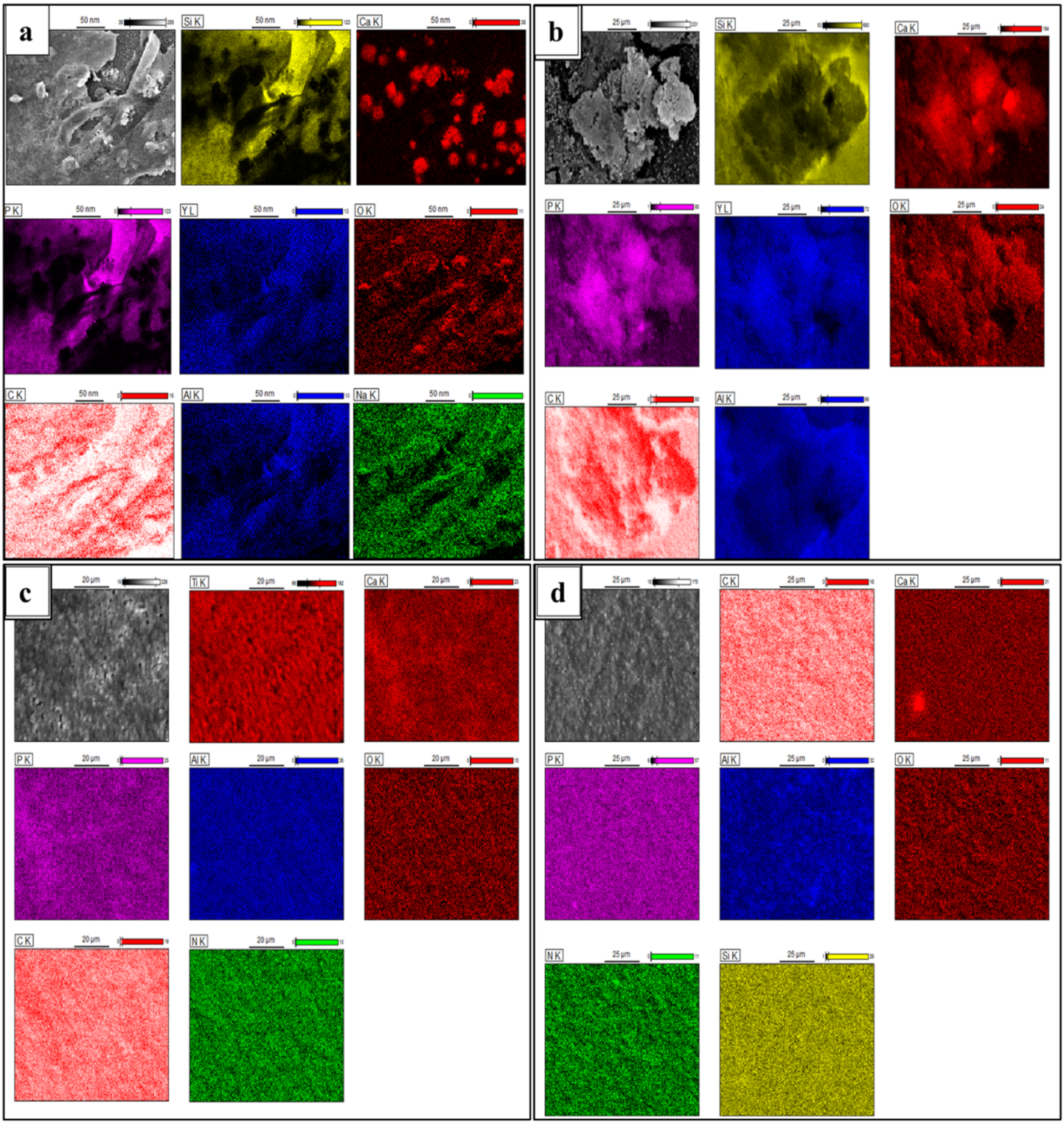

Figure 2.5: (a) EDS mapping of Si_3N_4 sample showing the matrix deposition after 30 days of in vitro study, (b-d) EDS mapping of (b) Si_3N_4, (c) Ti6Al4V, and (d) PEEK sample showing the matrix deposition after 60 days of the *in vitro* study.

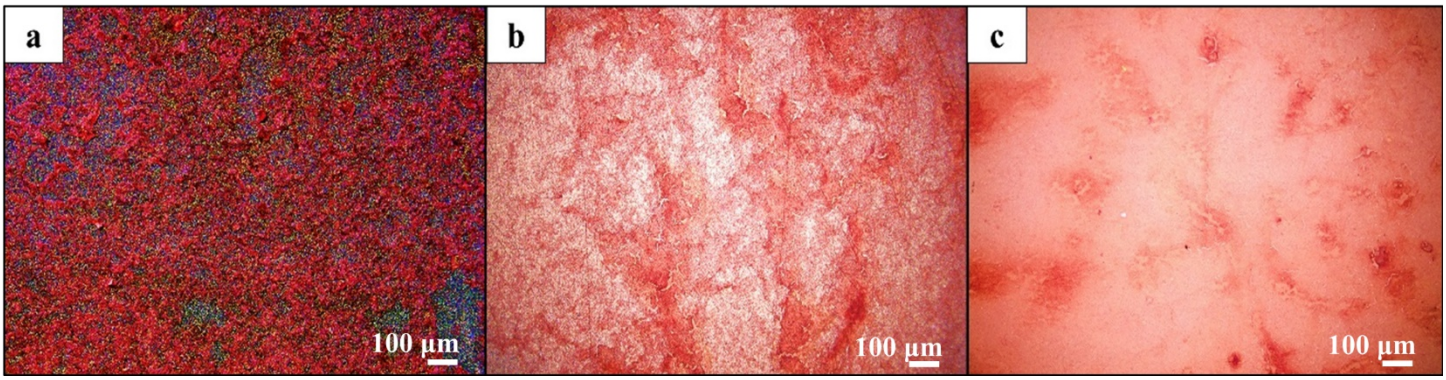

Figure 2.6: Alizarin red staining for calcium deposition on the surfaces a) Silicon Nitride, b) Titanium alloy, and c) PEEK.

2.3.3. Alizarin Red Staining

Alizarin Red S staining confirmed calcium deposition on the sample surfaces. Similar to the SEM results, a deep red-orange stain was observed on Si_3N_4 and Ti6Al4V indicating extracellular calcium deposition, shown in **figure 2.6**. Calcium deposition was observed on PEEK surfaces but with less intensity.

2.3.4. qRT-PCR and ELISA

qRT-PCR results indicated significantly higher relative expression of collagen I day 1 and day 3 of differentiation for titanium alloy and silicon nitride, shown in **figure 2.7-a**. There was an almost 4-fold increase of collagen I expression in silicon nitride samples compared to glass cover slip after 3 days. RUNX2 expression (**figure 2.7-b**) was significantly enhanced for Ti6Al4V at day 1, about 3-fold greater than RUNX2 expression in GCS samples, but there was no significant difference in the silicon nitride and GCS samples, despite a 2-fold increase compared to glass cover slip. There was a significant 2.5-fold increase in RUNX2 expression in both Ti6Al4V and Si_3N_4 samples after 3 and 7 days of differentiation compared to PEEK and glass cover slip. **Figure 2.7 (c)** shows the expression of Osterix determined (SP7) by qRT-PCR. There was a significant 2-fold increase in SP7 expression for Ti6Al4V and Si_3N_4 samples as compared to glass coverslip and PEEK. Osteocalcin (OCN) concentration, determined by

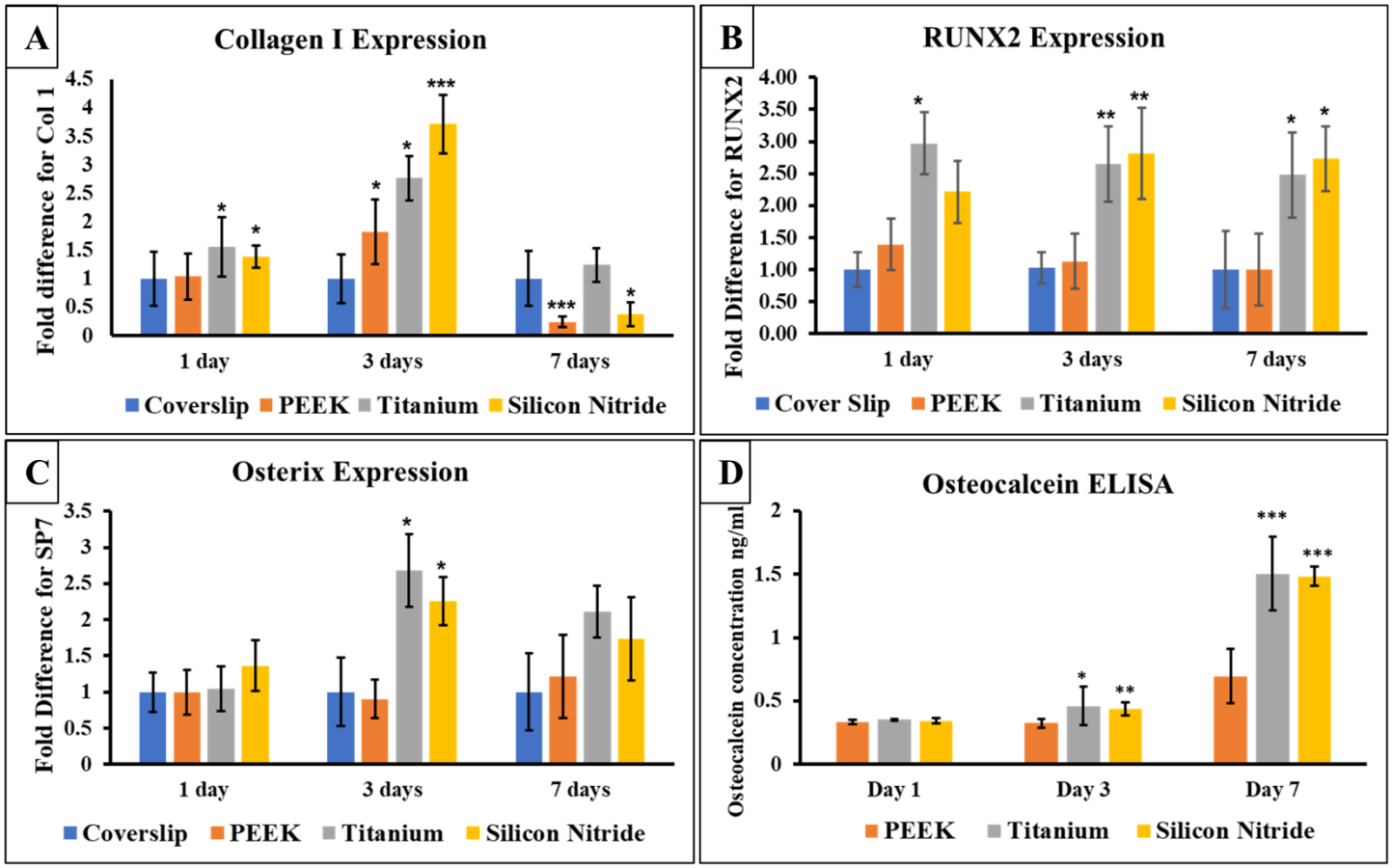

Figure 2.7: qRT-PCR results show the gene expression of (a) collagen I, (b) RUNX2, and (c) Osterix at 1, 3, and 7 days. (d) Osteocalcin (OCN) measured by ELISA.

ELISA, was significantly enhanced after 3 days of differentiation, and relatively increased after 7 days of culture for both Ti6Al4V and Si_3N_4 as shown in **figure 2.7 (d)**. All gene expression data as well as the ECM and mineralization analysis results were summarized as shown in **Table 2.1**.

2.4. DISCUSSION

Recent studies of silicon nitride have characterized its properties for protein adsorption, anti-microbial as well as osteointegration (16–18). These properties may be useful for orthopedic and craniofacial applications. In this study, we evaluated the osteoconductive nature of the silicon nitride as opposed to titanium and PEEK. We found evidence of ECM deposition and mineral formation on all three different surfaces i.e. Si_3N_4, Ti6Al4V, and PEEK after 30 and 60

Table 2.1: Summary of the ECM, Mineralization, qRT-PCR, and ELISA results on the different surfaces.

Results	**Silicon nitride**		**Ti alloy**		**PEEK**	
ECM and Mineralization	30 Days	60 Days	30 Days	60 Days	30 Days	60 Days
Amide I (1637 cm^{-1}, FTIR)	√	√	√	√	x	√
Amcide II (1532 cm^{-1}, FTIR)	√	√	√	√	x	√
Amide III (1228 cm^{-1}, FTIR)	√	√	√	√	x	√
P-O @PO_4^{3-} (1030 cm^{-1}, FTIR)	√	√	√	√	x	√
ACP @ (900 - 1200 cm^{-1}, FTIR)	√	√	√	√	x	√
V_1 CO_3^{2-} (Raman)	---	√	---	√	---	x
V_1 PO_4^{3-} and V_3 PO_4^{3-} (Raman)	---	√	---	√	---	x
V_2 PO_4^{3-} and V_4 PO_4^{3-} (Raman)	---	√	---	x	---	x
Proline and Hydroxyproline (Raman)	---	√	---	x	---	x

	Silicon nitride			**Ti alloy**			**PEEK**		
qRT-PCR and ELISA	1 Day	3 Days	7 Days	1 Day	3 Days	7 Days	1 Day	3 Days	7 Days
Collagen I expression (Fold difference)	1.38± 0.2	3.7± 0.5	0.37± 0.2	1.5± 0.5	2.7± 0.4	1.2± 0.3	1.0± 0.4	1.8± 0.5	0.24± 0.1
RUNX 2 expression (Fold difference)	2.2± 0.4	2.8± 0.7	2.7± 0.5	2.9± 0.4	2.6± 0.5	2.4± 0.6	1.3± 0.3	1.13± 0.4	1.0± 0.5
Osterix expression (Fold difference)	1.4± 0.35	2.2± 0.33	1.7± 0.5	1.04± 0.3	2.6± 0.5	2.11± 0.4	1.0± 0.3	0.9± 0.2	1.2± 0.6
Osteocalcin concentration (ng/ml)	0.34	0.43	1.48	0.35	0.45	1.5	0.33	0.32	0.69

days of *in vitro* study. It was noted that the relatively high densities of ECM and minerals were formed on the silicon nitride samples, confirmed by HR-SEM. Also, Si_3N_4 surfaces were completely covered by collagen bundles and ACP particles while slightly lower ECM coverage and minimal ACP deposition were observed on Ti6Al4V and PEEK surfaces. Bare Ti6Al4V and PEEK surfaces were observed in multiple SEM images. FT-IR and Raman spectroscopy supported SEM findings, revealing enhanced mineral deposition and extracellular matrix formation on the surfaces of Si_3N_4 surfaces compared to Ti6Al4V and PEEK.

FT-IR analysis revealed the presence of vibrational bands and P-O stretching typically exhibited by ECM proteins based on previously described in literature (15, 19). A significant single broad peak spanning 900– 1200 cm^{-1} (P-O peak) (refers to the formation of amorphous calcium phosphate (ACP) (15)) was observed, indicating the formation of either calcium phosphate or hydroxyapatite on the surface of Si_3N_4 and Ti6Al4V after just 30 days of *in vitro* study. It is important to note that the intensity of the P-O peak was relatively higher for Si_3N_4

surfaces compared to Ti6Al4V surfaces as shown in **figure 2.1(a, b)** indicating increased mineral content on Si_3N_4 surfaces compared to Ti6Al4V surfaces, which is confirmed by SEM findings. On the other hand, PEEK samples did not show any peaks related to ECM environment after 30 days as indicated in **figure 2.1(c)**. The absence of collagen and/or mineral formation on the PEEK surfaces could be attributed to the low surface energy, hydrophobic nature, and surface smoothness, leading to low protein adsorption and less cell attachment, resulting in little to no collagen or mineral deposition (20–23). After 60 days of culture FT-IR results indicated the presence of ECM and mineral on all three sample surfaces (Si_3N_4, Ti6Al4V, and PEEK) as seen in **Figure 2.1 (d-f)**. The intensity of amides and PO_4^{3-} peaks at 60 days increased relative to peak intensity at 30 days for Si_3N_4 and Ti6Al4V surfaces. Additionally, a shift in amide 1 peak position, represented by two closed peaks at 1659 and 1628 cm^{-1}, could be attributed to the presence of collagen/Ca^{2+} structure (24).

Interestingly, significant peaks for ECM and mineral content observed in the Raman spectra for Si_3N_4 surfaces were similar to previously established peaks found in the spectra of actual bone (25–27). The intensity of v_1- PO_4^{3-}peak accounts for the mineral content, and the full width at half maximum (FWHM) of that peak is proportional to the maturity of the crystals, representing the c-axis length (25). Thus, it is very important to note that the v_1-PO_4^{3-} peak intensity was greater for Si_3N_4 surfaces compared to Ti6Al4V surfaces. Also, FWHM was greater for Si_3N_4 compared to Ti6Al4V, confirming the formation of mature mineral crystals on the Si_3N_4 sample surface. The enhanced ECM and mineral formation on the silicon nitride surface can be attributed to its surface bioactivity and higher surface energy resulting in rapid and dense ECM and HA formation compared to the Ti6Al4V surface as reported. On the other hand, the spectra for PEEK samples only revealed peaks for amide II, and the spectra for GCS

samples displayed peaks for amide II, CH_2 deformation, and a broad peak for v_4- PO_4^{3-}, which can be attributed to the bio-inertness and hydrophobic properties of these surfaces. The results of FT-IR and Raman Spectroscopy suggest increased mineral deposition and dense extracellular matrix formation on Si_3N_4 surfaces, possibly due to enhanced MC3T3-E1 pre-osteoblast cell growth and differentiation.

EDS results confirmed the presence of Ca and P deposition on the surface of each sample that were previously indicated by the SEM images, FT-IR, and Raman spectroscopy. It is important to note the regions of high Ca and P deposition density compared to the main element's distribution of the sample. For example, on the Si_3N_4 sample, the increased density deposition of Ca and P slightly shield the Si_3N_4 surface, resulting in decreased displayed Si density in these regions.

To visualize the calcium mineral deposition on material surfaces Alizarin red staining was performed. SEM results, indicating that ECM and mineral formation are delayed on Ti6Al4V and PEEK surfaces compared to Si_3N_4 due to high density surface coverage of the ECM on Si_3N_4 surfaces, was confirmed by alizarin red staining. Low surface energy and lack of surface functional groups that act as precursors for collagenous ECM formation are likely main reasons for poor ECM deposition on Ti6Al4V and PEEK (21, 23, 28). On the contrary, increased cell attachment, growth, and proliferation and promotion of collagenous biomineral deposition observed on Si_3N_4 surfaces can be attributed to its hydrophilic nature, high surface energy, and presence of Si-O and Si-N surface bonding (29, 30).

Type 1 collagen is the most abundant extracellular matrix protein in bone and provides structural support, making it important for differentiation and organization of the bony tissues. Increased expression of collagen I induced by silicon nitride, signifies osteoblastic induction of

collagen synthesis in the extracellular matrix. α2β1 integrin mediator binds the collagenous matrix to the osteogenic cell membrane which induces the mitogen-activated protein kinases (MAPK) (31). These kinases phosphorylate and activate RUNX2 and OSX, bone specific transcription factors important for bone formation and mineralization (31, 32). These transcription factors bind to the promoter regions of certain downstream genes like osteocalcin, often used as a serum marker to detect osteoblastic activity and bone formation due to its role in osteoblastic maturation and hydroxyapatite nucleation (31, 33). Previous studies have shown that osteocalcin acts like a bridge between the bone matrix proteins and mineralization in the process of bone formation (34–36).

While the use of porous ceramic materials (i.e. Si_3N_4) in osteointegration applications is beneficial due to unique surface properties, some limitations could be arising due to the use of solid body ceramics for CMF applications. One of the main challenges is the lack of tensile strength to give the fixative plate some flexure when fixated into curved bony structures. Therefore, bulk ceramic or polymeric materials with low tensile strength (i.e. Si_3N_4 ~350-400 MPa, and PEEK~ 100-110 MPa) are not optimal for load bearing bone applications compared to tensile materials such as Ti-alloys (~ 920-980 MPa) (37). The benefits of Si_3N_4 surfaces relative to Ti6Al4V or PEEK in conjunction with limitations in tensile strength implies that Si_3N_4 may serve as a better coating material as opposed to a full body ceramic implanted into the bone. In this direction, we investigated Si_3N_4 and silicon oxynitride (SiOxNy) thin film coatings deposited using low temperature plasma enhanced chemical vapor deposition (PECVD) techniques (38–40). Currently, studies on the use of silicon oxynitride coatings which have demonstrated superior osteogenic properties compared to the materials studied here, are underway (38, 39, 41–43). Using these coatings, we can bring the unique surface properties of

Si_3N_4 and SiOxNy to the inert surface of reconstructive fixative materials (e.g. titanium plates). Furthermore, other biologically important elements such as phosphorus can be incorporated in the coatings for optimal biological activity (40), potentially aiding in the conduction of new bone on these fixative implant surfaces. Thus, the future research will focus on studying the viability of the amorphous SiONx/SiONPx-PECVD thin-films as potential coatings for Ti and bioinert implants materials for enhanced osteointegration and rapid bone regeneration.

2.5. CONCLUSION

In the current study, we report that silicon nitride surface has comparable mineralized tissue formation via extracellular matrix deposition and bone biomarker expression, in mouse calvarial pre-osteoblasts cells, to Ti6Al4V surface activity and superior to PEEK surface activity. The results revealed that there was ECM deposition and mineralization on silicon nitride surfaces. The FT-IR, Raman spectroscopy, and HR-SEM imaging results indicate formation of collagen and mineral deposition after 30 days on silicon nitride and titanium surfaces, but not PEEK surfaces, and the peaks displayed by the Raman spectra for silicon nitride resemble natural biomineral. Results from qRT PCR and ELISA assays included the upregulation of osteogenic transcription factors such as RUNX2, SP7, and collagen type I and Osteocalcin. While these results indicate that there are some advantages to the use of silicon nitride surfaces over Ti6Al4V and PEEK, they are counterbalanced by challenges associated with full body ceramics. We recommend investigation into the crystalline or amorphous form of silicon nitride as a coating for Ti6Al4V or PEEK for possible CMF applications.

2.6. ACKNOWLEDGEMENTS

The authors want to acknowledge the NIH/NIDCR for their support (1R56-DE027964-01A1-01), Texas STARs award, Departmental Start-up Funds, University of Texas at Arlington, College of Nursing and Health Innovation, Arlington, TX. The authors want to thank Dr. Bryan J. McEntire, and Ryan M. Bock of Amedica Corporation for their assistance in providing samples. We also want to acknowledge all our laboratory members Henry Tran, Sara Peper, Thy Vo for their support and helpful suggestions.

2.7. REFERENCES

1. Bone Grafts and Substitutes Market by Product (Allografts, Bone Grafts Substitutes, and Cell-based Matrices), by Application (Spinal Fusion, Long Bone, Foot & Ankle, Craniomaxillofacial, Joint Reconstruction, and Dental Bone Grafting). (2015-2023) [Online]. *Glob. Oppor. Anal. Ind. Forecast*: [date unknown]. https://www.alliedmarketresearch.com/bone-graft-substitutes-market.
2. Craniomaxillofacial Implants Market by Product (Mid Face Implants, Cranial or Neuro Implants, Man-dibular Orthognathic Implants, Distraction Systems, Bone Graft Substitutes, Thoracic Fixation Systems, Total TMJ Replacement Systems, Dural Repair Product. ([Online]. *Glob. Oppor. Anal. Ind. Forecast*: [date unknown]. https://www.alliedmarketresearch.com/craniomaxillofacial-implants-market.
3. **Neovius E**, **Engstrand T**. Craniofacial reconstruction with bone and biomaterials: review over the last 11 years. *J Plast Reconstr Aesthet Surg* 63: 1615–1623, 2010. doi: 10.1016/j.bjps.2009.06.003.
4. **Kwarcinski J**, **Boughton P**, **Ruys A**, **Doolan A**, **Van Gelder J**. Cranioplasty and Craniofacial Reconstruction: A Review of Implant Material, Manufacturing Method and Infection Risk. *Appl Sci* 7, 2017. doi: 10.3390/app7030276.
5. **Rogers GF**, **Greene AK**. Autogenous bone graft: basic science and clinical implications. *J Craniofac Surg* 23: 323–327, 2012. doi: 10.1097/SCS.0b013e318241dcba.
6. **Zanotti B**, **Zingaretti N**, **Verlicchi A**, **Robiony M**, **Alfieri A**, **Parodi PC**. Cranioplasty: Review of Materials. *J Craniofac Surg* 27: 2061–2072, 2016. doi: 10.1097/SCS.0000000000003025.
7. **Chiarello E**, **Cadossi M**, **Tedesco G**, **Capra P**, **Calamelli C**, **Shehu A**, **Giannini S**.

Autograft, allograft and bone substitutes in reconstructive orthopedic surgery. *Aging Clin Exp Res* 25 Suppl 1: S101-3, 2013. doi: 10.1007/s40520-013-0088-8.

8. **Grove, DPM JR**. Autograft, Allograft and Xenograft Options in the Treatment of Neglected Achilles Tendon Ruptures: A Historical Review with Illustration of Surgical Repair. *Foot Ankle J* 1, 2008. doi: 10.3827/faoj.2008.0105.0001.

9. **Albrektsson T**, **Johansson C**. Osteoinduction, osteoconduction and osseointegration. *Eur spine J Off Publ Eur Spine Soc Eur Spinal Deform Soc Eur Sect Cerv Spine Res Soc* 10 Suppl 2: S96-101, 2001. doi: 10.1007/s005860100282.

10. **Thrivikraman G**, **Athirasala A**, **Twohig C**, **Boda SK**, **Bertassoni LE**. Biomaterials for Craniofacial Bone Regeneration. *Dent Clin North Am* 61: 835–856, 2017. doi: 10.1016/j.cden.2017.06.003.

11. **Awad KR**, **Ahuja N**, **Shah A**, **Tran H**, **Aswath PB**, **Brotto M**, **Varanasi V**. Silicon nitride enhances osteoprogenitor cell growth and differentiation via increased surface energy and formation of amide and nanocrystalline HA for craniofacial reconstruction. *Med DEVICES SENSORS* 2: e10032, 2019. doi: 10.1002/mds3.10032.

12. **McEntire BJ**, **Lakshminarayanan R**, **Thirugnanasamb P**, **Seitz-Sampson JW**, **Bock RM**, **O'Brien D**. Processing and Characterization of Silicon Nitride Bioceramics. *Bioceram Dev Appl* 6: 1–9, 2016.

13. **Varanasi VG**, **Saiz E**, **Loomer PM**, **Ancheta B**, **Uritani N**, **Ho SP**, **Tomsia AP**, **Marshall SJ**, **Marshall GW**. Enhanced osteocalcin expression by osteoblast-like cells (MC3T3-E1) exposed to bioactive coating glass (SiO2-CaO-P2O5-MgO-K2O-Na2O system) ions. *Acta Biomater* 5: 3536–3547, 2009. doi: 10.1016/j.actbio.2009.05.035.

14. **Rodrigues CF de S**, **Lima FJC de**, **Barbosa FT**. Importance of using basic statistics

adequately in clinical research. *Brazilian J Anesthesiol (English Ed* 67: 619–625, 2017. doi: https://doi.org/10.1016/j.bjane.2017.01.011.

15. **Davies OG**, **Cox SC**, **Williams RL**, **Tsaroucha D**, **Dorrepaal RM**, **Lewis MP**, **Grover LM**. Annexin-enriched osteoblast-derived vesicles act as an extracellular site of mineral nucleation within developing stem cell cultures. *Sci Rep* 7: 12639, 2017. doi: 10.1038/s41598-017-13027-6.

16. **Pezzotti G**, **Oba N**, **Zhu W**, **Marin E**, **Rondinella A**, **Boschetto F**, **McEntire B**, **Yamamoto K**, **Bal BS**. Human osteoblasts grow transitional Si/N apatite in quickly osteointegrated Si(3)N(4) cervical insert. *Acta Biomater* 64: 411–420, 2017. doi: 10.1016/j.actbio.2017.09.038.

17. **Webster TJ**, **Patel AA**, **Rahaman MN**, **Sonny Bal B**. Anti-infective and osteointegration properties of silicon nitride, poly(ether ether ketone), and titanium implants. *Acta Biomater* 8: 4447–4454, 2012. doi: 10.1016/j.actbio.2012.07.038.

18. **Pezzotti G**, **Bock RM**, **Adachi T**, **Rondinella A**, **Boschetto F**, **Zhu W**, **Marin E**, **McEntire B**, **Bal BS**, **Mazda O**. Silicon nitride surface chemistry: A potent regulator of mesenchymal progenitor cell activity in bone formation. *Appl Mater Today* 9: 82–95, 2017. doi: https://doi.org/10.1016/j.apmt.2017.05.005.

19. **Megat Abdul Wahab R**, **Mohamed Rozali NA**, **Senafi S**, **Zainol Abidin IZ**, **Zainal Ariffin Z**, **Zainal Ariffin SH**. Impact of isolation method on doubling time and the quality of chondrocyte and osteoblast differentiated from murine dental pulp stem cells. *PeerJ* 5: e3180, 2017. doi: 10.7717/peerj.3180.

20. **Kurtz SM**, **Devine JN**. PEEK biomaterials in trauma, orthopedic, and spinal implants. *Biomaterials* 28: 4845–4869, 2007. doi: 10.1016/j.biomaterials.2007.07.013.

21. **Pelletier MH**, **Cordaro N**, **Punjabi VM**, **Waites M**, **Lau A**, **Walsh WR**. PEEK Versus Ti Interbody Fusion Devices: Resultant Fusion, Bone Apposition, Initial and 26-Week Biomechanics. *Clin spine Surg* 29: E208-14, 2016. doi: 10.1097/BSD.0b013e31826851a4.

22. **Torstrick FB**, **Safranski DL**, **Burkus JK**, **Chappuis JL**, **Lee CSD**, **Guldberg RE**, **Gall K**, **Smith KE**. Getting PEEK to Stick to Bone: The Development of Porous PEEK for Interbody Fusion Devices [Online]. *Tech Orthop* 32, 2017. https://journals.lww.com/techortho/Fulltext/2017/09000/Getting_PEEK_to_Stick_to_Bone__The_Development_of.5.aspx.

23. **Tsougeni K**, **Vourdas N**, **Tserepi A**, **Gogolides E**, **Cardinaud C**. Mechanisms of Oxygen Plasma Nanotexturing of Organic Polymer Surfaces: From Stable Super Hydrophilic to Super Hydrophobic Surfaces. *Langmuir* 25: 11748–11759, 2009. doi: 10.1021/la901072z.

24. **Zhang W**, **Huang Z-L**, **Liao S-S**, **Cui F-Z**. Nucleation Sites of Calcium Phosphate Crystals during Collagen Mineralization. *J Am Ceram Soc* 86: 1052–1054, 2003. doi: https://doi.org/10.1111/j.1151-2916.2003.tb03422.x.

25. **Ilyas A**, **Odatsu T**, **Shah A**, **Monte F**, **Kim HKW**, **Kramer P**, **Aswath PB**, **Varanasi VG**. Amorphous Silica: A New Antioxidant Role for Rapid Critical-Sized Bone Defect Healing. *Adv Healthc Mater* 5: 2199–2213, 2016. doi: 10.1002/adhm.201600203.

26. **Buchwald T**, **Kozielski M**, **Szybowicz M**. Determination of Collagen Fibers Arrangement in Bone Tissue by Using Transformations of Raman Spectra Maps. *Spectrosc An Int J* 27: 261487, 2012. doi: 10.1155/2012/261487.

27. **Draper ERC**, **Morris MD**, **Camacho NP**, **Matousek P**, **Towrie M**, **Parker AW**, **Goodship AE**. Novel assessment of bone using time-resolved transcutaneous Raman

spectroscopy. *J bone Miner Res Off J Am Soc Bone Miner Res* 20: 1968–1972, 2005. doi: 10.1359/JBMR.050710.

28. **Tsou H-K**, **Chi M-H**, **Hung Y-W**, **Chung C-J**, **He J-L**. In Vivo Osseointegration Performance of Titanium Dioxide Coating Modified Polyetheretherketone Using Arc Ion Plating for Spinal Implant Application. *Biomed Res Int* 2015: 328943, 2015. doi: 10.1155/2015/328943.

29. **Deng Y**, **Liu X**, **Xu A**, **Wang L**, **Luo Z**, **Zheng Y**, **Deng F**, **Wei J**, **Tang Z**, **Wei S**. Effect of surface roughness on osteogenesis in vitro and osseointegration in vivo of carbon fiber-reinforced polyetheretherketone-nanohydroxyapatite composite. *Int J Nanomedicine* 10: 1425–1447, 2015. doi: 10.2147/IJN.S75557.

30. **Gorth DJ**, **Puckett S**, **Ercan B**, **Webster TJ**, **Rahaman M**, **Bal BS**. Decreased bacteria activity on Si_3N_4 surfaces compared with PEEK or titanium. *Int J Nanomedicine* 7: 4829–4840, 2012. doi: 10.2147/IJN.S35190.

31. **Xiao G**, **Gopalakrishnan R**, **Jiang D**, **Reith E**, **Benson MD**, **Franceschi RT**. Bone morphogenetic proteins, extracellular matrix, and mitogen-activated protein kinase signaling pathways are required for osteoblast-specific gene expression and differentiation in MC3T3-E1 cells. *J bone Miner Res Off J Am Soc Bone Miner Res* 17: 101–110, 2002. doi: 10.1359/jbmr.2002.17.1.101.

32. **Artigas N**, **Ureña C**, **Rodríguez-Carballo E**, **Rosa JL**, **Ventura F**. Mitogen-activated protein kinase (MAPK)-regulated interactions between Osterix and Runx2 are critical for the transcriptional osteogenic program. *J Biol Chem* 289: 27105–27117, 2014. doi: 10.1074/jbc.M114.576793.

33. **Zoch ML**, **Clemens TL**, **Riddle RC**. New insights into the biology of osteocalcin. *Bone*

82: 42–49, 2016. doi: 10.1016/j.bone.2015.05.046.

34. **Hauschka P V**, **Carr SA**. Calcium-dependent alpha-helical structure in osteocalcin. *Biochemistry* 21: 2538–2547, 1982. doi: 10.1021/bi00539a038.

35. **Hoang QQ**, **Sicheri F**, **Howard AJ**, **Yang DSC**. Bone recognition mechanism of porcine osteocalcin from crystal structure. *Nature* 425: 977–980, 2003. doi: 10.1038/nature02079.

36. **Ritter NM**, **Farach-Carson MC**, **Butler WT**. Evidence for the formation of a complex between osteopontin and osteocalcin. *J Bone Miner Res* 7: 877–885, 1992. doi: https://doi.org/10.1002/jbmr.5650070804.

37. **Bal BS**, **Rahaman MN**. Orthopedic applications of silicon nitride ceramics. *Acta Biomater* 8: 2889–2898, 2012. doi: 10.1016/j.actbio.2012.04.031.

38. **Ahuja N**, **Awad K**, **Fiedler M**, **Aswath P**, **Brotto M**, **Varanasi V**. Preliminary study of in-situ 3D bioprinted nano-silicate biopolymer scaffolds for muscle repair in VML defects. *FASEB J* 34: 1, 2020. doi: https://doi.org/10.1096/fasebj.2020.34.s1.03514.

39. **AWAD KR**, **Ahuja N**, **Fiedler M**, **Huang J**, **Brotto L**, **Aswath P**, **Brotto M**, **Varanasi V**. Micro-patterned Bioactive Amorphous Silicon Oxynitride Enhances Adhesion, Growth, and Myotubes and Axon Alignment in Muscle and Nerve Cells. *FASEB J* 34: 1, 2020. doi: https://doi.org/10.1096/fasebj.2020.34.s1.02245.

40. **Monte F**, **Awad KR**, **Ahuja N**, **Kim H**, **Aswath P**, **Brotto M**, **Varanasi VG**. Amorphous Silicon Oxynitrophosphide Coated Implants Boost Angiogenic Activity of Endothelial Cells. .

41. **Varanasi VG**, **Ilyas A**, **Velten MF**, **Shah A**, **Lanford WA**, **Aswath PB**. Role of Hydrogen and Nitrogen on the Surface Chemical Structure of Bioactive Amorphous Silicon Oxynitride Films. *J Phys Chem B* 121: 8991–9005, 2017. doi:

10.1021/acs.jpcb.7b05885.

42. **Awad KR**, **Huang J**, **Brotto L**, **Aswath P**, **Brotto M**, **Varanasi V**. Patterned Silicon Oxynitride (SiONx) Scaffolds Enhance Alignment and Myogenic Differentiation of C2C12 Muscle Cells. *FASEB J* 33: 539.5-539.5, 2019. doi: https://doi.org/10.1096/fasebj.2019.33.1_supplement.539.5.

43. **Ilyas A**, **Lavrik N V**, **Kim HKW**, **Aswath PB**, **Varanasi VG**. Enhanced interfacial adhesion and osteogenesis for rapid "bone-like" biomineralization by PECVD-based silicon oxynitride overlays. *ACS Appl Mater Interfaces* 7: 15368–15379, 2015.

44. **Dimitriou R**, **Jones E**, **McGonagle D**, **Giannoudis P V**. Bone regeneration: current concepts and future directions. *BMC Med* 9: 66, 2011. doi: 10.1186/1741-7015-9-66.

45. **Nauth A**, **Schemitsch E**, **Norris B**, **Nollin Z**, **Watson JT**. Critical-Size Bone Defects: Is There a Consensus for Diagnosis and Treatment? [Online]. *J Orthop Trauma* 32, 2018. https://journals.lww.com/jorthotrauma/Fulltext/2018/03003/Critical_Size_Bone_Defects__Is_There_a_Consensus.2.aspx.

CHAPTER 3

SILICON OXYNITROPHOSPHIDE NANOSCALE-COATING ENHANCES ANTIOXIDANT MARKER -INDUCED ANGIOGENESIS DURING *IN VIVO* CRANIAL BONE DEFECT HEALING

Felipe A. do Monte [# 1, 2], Neelam Ahuja[# 3], Kamal R. Awad [3, 4], Zui Pan [3], Simon Young [5], Harry K.W. Kim [2, 6], Pranesh Aswath [4], Marco Brotto [3], and Venu G. Varanasi[* 3]

[1] Department of Bioengineering, University of Texas at Arlington, Texas 76019, USA

[2] Center for Excellence in Hip Disorders, Texas Scottish Rite Hospital, Texas 75219, USA

[3] Bone-Muscle Research Center, University of Texas at Arlington, Texas 76019, USA

[4] Department of Materials Science and Engineering, University of Texas at Arlington, Texas 76019, USA

[5] Department of Oral and Maxillofacial Surgery, The University of Texas Health Science Center at Houston, School of Dentistry, Houston, Texas 77054, USA

[6] Department of Orthopedic Surgery, University of Texas Southwestern Medical Center at Dallas, Dallas, Texas 75390, USA

[#] **Co-first author**

[*] **Corresponding author**

do Monte FA, **Ahuja N**, **Awad KR**, **Pan Z**, **Young S**, **Kim HKW**, **Aswath P**, **Brotto M**, **Varanasi VG**. Silicon Oxynitrophosphide Nanoscale-Coating Enhances Antioxidant Marker - Induced Angiogenesis During In Vivo Cranial Bone Defect Healing. *JBMR Plus* n/a: e10425, [date unknown]. doi: https://doi.org/10.1002/jbm4.10425.

ABSTRACT

Critical sized bone defects are challenging to heal due to the sudden and large volume of lost bone. Fixative plates are often used to stabilize defects, yet oxidative stress and delayed angiogenesis are contributing factors to poor biocompatibility and delayed bone healing. This study tests the angiogenic and antioxidant properties of amorphous silicon oxynitrophosphide (SiONPx) nanoscale coating material on endothelial cells to regenerate vascular tissue in vitro and in bone defects. In vitro studies evaluate the effect of SiONx and two different SiONPx compositions on human endothelial cells exposed to reactive oxygen species (e.g., H2O2) that simulates oxidative stress conditions. In vivo studies using adult male Sprague Dawley rats (~450 g) were performed to compare a bare plate, SiONPx-coated implant plate, and a sham control group using a rat standard sized calvarial defect. Results from this study showed that plates coated with SiONPx significantly reduced cell death, enhanced vascular tubule formation and matrix deposition by upregulating angiogenic and antioxidant expression (e.g. VEGFA, angiopoetin-1, SOD-1, NRF-2 and Cat-1). Moreover, endothelial cell markers (CD31) demonstrate a significant tubular structure on the SiONPx coating group compared to an empty and uncoated plate group. This reveals that atomic doping of phosphate into the nanoscale coating of SiONx produced markedly elevated levels of antioxidant and angiogenic markers that enhance vascular tissue regeneration. This study demonstrates that SiONPx or SiONx nanoscale coated materials enhance antioxidant expression, angiogenic marker expression, and reduce ROS levels needed for accelerating vascular tissue regeneration. These results further suggest that SiONPx nanoscale coating could be a promising candidate for titanium plate for rapid and enhanced cranial bone defect healing.

Keywords: Angiogenesis, amorphous silicon Oxynitrophosphide, antioxidants, bone healing, Oxidative stress.

3.1. INTRODUCTION

Loosening and failure of fixative implants in bone reconstruction surgeries is unfortunately common and can be attributed to a variety of factors like delayed healing and lack of osseointegration. Surgical revisions after these complications can be twice as expensive as the initial procedure and jeopardize functional and esthetic outcomes (1). Craniofacial, and orthopedic implant failure is defined as the inability of the implant/plate to osseointegrate with the surrounding host tissue due to a foreign body response and/or an opportunistic infection (2, 3). During the first few days of biomaterial implantation in the bone defect, the surrounding biological tissue can face severe and harmful oxidative stress conditions (2–4). High levels of oxidative stress can be deleterious to endothelial cells (5). Endothelial cell survival and proliferation is necessary for adequate new blood vessel formation and thus plays a vital role in bone regeneration (6). Therefore, to minimize complications, such as implant/plate-screw device loosening and failure, and improve healing rates, the material used for bone defect reconstruction must have innate antioxidant stimulus, as well as the ability to enhance angiogenesis. Silicon has been used in combination with nitrogen and/or oxygen for implant/ plate device composition and coating to enhance new bone formation and osseointegration (7–10).

A recent publication by our group showed that ionic Si is important for superoxide dismutase (SOD-1) activity (9). The enzyme SOD-1 plays a major role in metabolism of superoxide, which is the main reactive oxygen species produced in cell metabolism. Moreover, ionic silicon can enhance angiogenesis by upregulating hypoxia inducible factor-1 alpha (HIF-1a) and vascular endothelial growth factor A (VEGFA) in human umbilical vein endothelial cells (HUVECs) (11). Studies demonstrated that ionic phosphorus can enhance angiogenesis by upregulating VEGFA and inducing cell migration, matrix deposition, and capillary tubule

formation in HUVECs (12–14) Yet, there has not been any evidence linking biomaterials that release factors that can stimulate a key angiogenic marker, angiopoietin-1 (ang-1), under toxic oxidative stress conditions. Ang-1 is a key marker that, when expressed, prevents apoptosis in endothelial cells under critical survival conditions by activating the receptor tyrosine kinase Tie2 (15–18).

Previous work from our group demonstrated Plasma Enhanced Chemical Vapor Deposition (PECVD) coated silicon oxynitride (SiONx) and silicon oxynitrophosphide (SiONPx)-based fixative implants can upregulate ang-1 in HUVECs under standard *in vitro* growth conditions (no oxidative stress) (19). PECVD is a coating method that has proven to be useful for biomaterial manufacturing due to the use of relatively low temperature processing, ability to be manufactured onto 3D surfaces for clinically-relevant fixative implants, ability to enhance interfacial adhesion, form surface functional groups (hydroxyl and amide functional groups), and to allow surface patterning before coating, which enhances cell attachment and matrix deposition by mimicking the nano- and microstructure of an extracellular matrix (8, 9). In this study, we examine the use of PECVD SiONx or SiONPx based materials to enhance angiogenic properties of endothelial cells under deleterious oxidative stress conditions.
Here, we hypothesize that a PECVD amorphous SiONx or SiONPx nanoscale coating will increase the expression of both antioxidant (SOD-1, Cat-1, Nrf2) and angiogenic (CD31, ang-1) markers, and enhance vascular tubule formation while reducing reactive oxygen species (ROS) (4-HNE, H_2O_2). To test these hypotheses, we investigated the effect of PECVD nanoscale coatings formed by Si, O, N and P gas reagent sources on angiogenesis under a toxic oxidative stress environment induced by 0.6 mM H_2O_2, which was determined previously (20). *In vitro* experiments evaluated the effect on viability of HUVECs, matrix deposition, capillary tubule

formation, and gene expression of angiogenic and antioxidant markers on coated and uncoated surfaces. *In vivo* studies using adult male Sprague Dawley rats (~450 g) were used for this experiment to measure local and systemic levels of oxidative stress markers and local angiogenic markers. The *in vivo* study analyzed 4-Hydroxynonenal (4-HNE) levels in the blood serum, and CD31 and 4-HNE on a histological section after the fixative implants were placed in a rat standard sized calvarial defect.

3.2. EXPERIMENTAL SECTION

3.2.1. PECVD SiONx and SiONPx Coated Fixative Plate Preparation and Analysis of Surface Elemental Composition

In the current study to test the SiONx and SiONPx nanoscale-coating, 4 inches <100> test grade P-type silicon wafers (NOVA Electronic Materials, 1189 Porter Rd. Flower Mound, TX, USA) were used after standard cleaning procedures. The reasons for using silicon wafer as the base fixative implant substrate are the ease of fabrication process to form highly conformal, adherent, and uniform thin film overlays by PECVD, and ease of dicing the silicon wafer into appropriate plate size. The silicon wafers were immersed in piranha solution (3:1 mixture of sulfuric acid (H_2SO_4, 96%) and hydrogen peroxide (H_2O_2, 30%)) for 10 minutes, and then rinsed in deionized (DI) water for 1 minute. To remove the native oxide layer, the silicon wafers were immersed in hydrofluoric acid for 30-60 sec. Finally, the wafers were rinsed for three cleaning cycles under a continuous DI water purge, dried with N_2 gas and placed on a 200° C hot plate for five minutes (8, 9).

A TRION ORION II PECVD/LPECVD system (Trion Technology, Clearwater, FL) was used to deposit a 200nm uniform coating of SiONx and two different compositions of SiONPx

Table 3.1: The Three Steps and Flow Rates of the Different Gases Used for Processing SiON, SiONP1, and SiONP2 Implants

	SiH_4/Ar (15/85%)	PH_3/SiH_4/Ar (2/15/83%)	N_2O	N_2	NH_4	Ar	Time (sec)
Step 1	0	0	0	0	0	250	30
Step 2 ($SiON_x$)	24	0	155	225	50	0	226
Step 2 ($SiONP_x$)1 ($SiONP_x$)2	0	24	5 16	225	50	0	322
Step 3	0	0	0	0	0	250	30

Ar = Argon (carrier gas); N_2 = nitrogen; N_2O = nitrous oxide; NH_4 = ammonia; PH_3 = phosphine; SiH_4 = silane; SiON = silicon oxynitride; SiONP = silicon oxynitrophosphide.

overlays that have different O/N ratio as indicated in **Table 3.1**. All coatings were processed at a substrate temperature of 400°C, chamber pressure of 900 mTorr, an inductively coupled plasma ICP power of 30 W, and an applied excitation frequency of 13.56 MHz. Gas source and flow rate of each gas are also indicated in **Table 3.1**.

The refractive indices and film thicknesses were measured using ellipsometry at a wavelength of 632.8 nm (Gaertner LS300). The results of ellipsometry were confirmed using a reflectometer (Ocean Optics NC-UV-VIS TF Reflectometer).

Table 3.2: Energy-Dispersive X-Ray Spectroscopy Analysis of Atomic Surface Composition of SiON, SiONP1, and SiONP2 Coating

	EDS compositional data (at%)			
Sample	Si	O	N	P
SiON	52.5	35.1	12.3	0
SiONP1	61.8	7.3	30.5	0.28
SiONP2	58.7	14.2	26.8	0.27

EDS Compositional data in units of (at %). EDS = Energy-dispersive X-ray spectroscopy; SiON = silicon oxynitride; SiONP = silicon oxynitrophosphide.

High Resolution-Scanning electron microscopy (HR-SEM) (Hitachi S-3000N Variable Pressure) was used to image and analyze surface properties and verify film thickness of the coatings at a voltage of 20 KeV. SEM was also used to identify and measure the surface elemental composition of the PECVD coated plates using Energy Dispersive X-Ray Analysis

(EDX) apparatus at a voltage of 12 KeV. The surface elemental composition can be seen in **Table 3.2** and is explained in the results section.

3.2.2. *In Vitro* Study

Several factors were used to help design the experimental setup. Prior studies evaluated the protective effect of a drug on HUVECs under oxidative stress. The cells were exposed to H_2O_2 at toxic levels (> 0.5 mM) for 24-48 hours prior to treatment (21, 22). Further, a hypoxic condition of 1% O_2 can induce HUVECs autophagy (23). If the cells are also exposed to excessive time of low fetal bovine serum (malnutrition), this can induce phenotype changes in HUVECs (24). HUVECs cannot survive or maintain their phenotype if they are not supplemented with endothelial cells growth media (25). Thus, a 48 hour time limit of exposure of cells and ECM to H_2O_2 was implemented.

HUVECs (passage 2 to 4), endothelial cell growth medium 2 (EGM-2) (used for cell growth and subculture), and endothelial cell basal media 2 (EBM-2) (used for the proliferation and differentiation experiments) were acquired from Lonza®. The experiments were divided into 5 groups: I- glass cover slip (GCS), II- tissue culture plate (TCP), III- SiONx, IV- SiONPx1 (O: 7.3 at %), and V- SiONPx2 (O: 14.2 at %). Propidium Iodide fluorescent stain (dead cells), Calcein-AM (for live cells), Actin Staining 488 and DAPI Nuclei staining were used as fluorescent dyes on the fixed samples. Purified mouse anti-fibronectin (BD Bioscience, San Jose, CA) as a primary antibody and Goat anti-mouse with Alexa 488 was used as the secondary antibody for fibronectin immune staining. Quantitative data analysis of the images was conducted by ImageJ (26–28). Captured images were loaded onto ImageJ for Microsoft Windows for analysis. After loading, images were adjusted for brightness, contrast, and sharpness as needed. The images were then converted to 32-bit encoding. The threshold was then

adjusted until the entire extracellular matrix (ECM) was selected. Using the zoom or magnification function, minimize under or over selection of the ECM. Then, the ECM area was measured as a percentage of the total view. Several images were captured from different areas of each sample, and an average was recorded.

Hydrogen peroxide (H_2O_2) at a concentration of 0.6 mM was used to mimic an oxidative stress environment, the stock solution was acquired from Sigma-Aldrich 30% w/w in H_2O_2 with stabilizer. The H_2O_2 has been used previously for *in vitro* studies (29–31) as a major product of oxidative stress, mainly produced by swift conversion from superoxide (32–34). Based on previous publications, this specific H_2O_2 concentration has been demonstrated to be deleterious to live tissue (19, 20). Phosphate buffered saline (PBS) (Sigma-Aldrich, St. Louis, MO) and trypsin, buffer, and trypsin neutralizer (Lonza ®, Morristown, NJ), Angiopoietin 1 Human ELISA Kit (Invitrogen®, Waltham, MA) and HNE competitive ELISA kit (Cell Biolabs, Inc., San Diego, CA) were used for the *in vitro* experiments.

Cell viability under toxic H_2O_2: PECVD SiONx and SiONPx coated plates (square shape) with a dimension of 1.2x1.2 cm and glass cover slip (GCS) measured 1.5 cm diameter round were used for the experiment (4 samples per group). HUVECs were seeded on the plate surfaces (5000 cell/cm^2), placed in a 12 well plate with 100µL of EGM-2 according to the protocol described by Lonza® and allowed to attach on the surface for 1 hour (35, 36). After initial attachment 900 µL of EBM-2 + 10% FBS + H_2O_2 0.6 mM was added and cultured for 24 hours. MTS proliferation assay was performed on 4 samples/group for cell viability, and 3 samples per group were stained with propidium iodide for fluorescent imaging.

Matrix deposition under toxic H_2O_2: Cells were seeded as mentioned above along with the same media for mimicking an oxidative stress environment (4 samples per group). After 48

hours under oxidative stress, the media was changed to EBM-2 + 10% FBS without H_2O_2. Five days after initial cell seeding, the cells were fixed with 4% paraformaldehyde and immunostaining was conducted for fibronectin using the antibodies mentioned above. Three pictures from different areas were captured per sample using 10x magnification on a Zeiss Axion cell culture fluorescent microscope, and ImageJ was used for quantifying the area occupied by fibronectin.

Capillary tubule formation under toxic H_2O_2: All PECVD coated plates were cut to 0.5x0.5 cm in dimension (4 samples per group). All SiONx and SiONPx coated plates, GCS, and pipette tips were placed in a 48 well plate at 4° Celsius, 12 hours before the start of the experiment. Matrigel® without growth supplements was slowly thawed at 4° Celsius for 12 hours. First, 100 µL of Matrigel® was placed on the implant plates, GCS, and TCP, and then the well plate was placed inside the cell culture incubator at 37°C, 95% humidity and 5% CO_2 for 30 minutes. After 30 minutes, 100µL of EBM-2 + H_2O_2 was used to seed 60,000 cells/cm^2 on a bed of Matrigel® for each sample as mentioned in previously described protocol (36, 37). Finally, six hours after the initial cell seeding, 50 µL of Calcein AM 2µM diluted in EBM-2 was added to each well, and after 30 minutes 3 pictures from different areas in 10x magnification were captured per well. The total tube length was calculated using the Angiogenesis Analyzer Software (ImageJ plug-in).

Gene expression of angiogenic and oxidative stress markers on HUVECs under toxic hydrogen peroxide levels: The groups used in this experiment were: TCP, SiONx, SiONPx1 (O: 7.3at %) and SiONPx2 (O: 14.2at %). The cells were seeded on TCP and all three scaffolds (200,000 cells per well) in a 12 well plate, n= 4/group and EBM-2 + 10% FBS + H_2O_2 0.6mM was used as a conditioned medium. After 24 hours the cells were lysed using TRIzol and RNA was collected, precipitated in 70% ethanol, and the RNA solution was purified using a

miRNAeasy MINI KIT (50) from QIAGEN®. RNA sample concentration was normalized to 100µg/mL and cDNA conversion was made using a Goscript™ Reverse transcriptase kit from Promega Corporation. A 20µL reaction was prepared for reverse transcription polymerase chain reaction (RT-PCR) using TaqMan® Gene Expression Assay and the PCR machine (Life Technology) was set up with the standard protocol adjusted for 50 cycles. Results were expressed relative to the housekeeping gene 18S and compared to the control (TCP), and delta delta Ct method was used for calculations for fold change. All data is represented in fold change and statistical analysis were done using the delta-delta CT values. The following angiogenic and oxidative stress markers were studied; Angiogenic markers: Vascular endothelial growth factor A (VEGFA), Nesprin-2, and Angiopoietin 1 (ang-1); Oxidative stress markers: superoxide dismutase 1 (SOD-1), Catalase-1 (Cat-1), nitric oxide synthase 3 (NOS-3), Glutathione peroxidase 1 (GPX-1), and nuclear factor erythroid 2-related factor 2 (Nrf2) (**Table 3.3**).

Table 3.3: Gene Expression Assay TaqMan Identification

Gene	Assay identification
VEGFA	Hs00900055_m1
Ang-1	Hs00919202_m1
Nesprin-2 (SYNE2)	Hs00794881_m1
SOD-1	Hs00533490_m1
Cat-1 (CAT)	Hs00156308_m1
e-NOS (NOS3)	Hs01574665_m1
Nrf2	Hs00975961_g1

Ang-1 = Angiopoietin 1; Cat-1 = catalase 1; e-NOS = endothelial nitric oxide synthase; Nrf2 = nuclear factor erythroid 2-related factor 2; SOD-1 = superoxide dismutase 1; VEGFA = vascular endothelial growth factor A.

Angiopoietin-1 and 4-HNE levels in conditioned medium using enzyme-linked immunosorbent assay (ELISA): Using the same groups, sample size, and conditioned medium used for PCR (section 2.6), the culture media was collected before lysing the cells for RNA

extraction and placed in a 1.5 ml centrifuge tube with protease inhibitor (1:1000 dilution) and stored at –20°C. These supernatant media samples were then used for quantification of the protein concentration by bicinchoninic acid (BCA) assay and Ang1 ELISA. The data and comparison among groups were expressed in a bar graph showing the values relative to control (TCP). The 4-HNE was measured by competitive ELISA and expressed in a bar graph in µg/ml.

3.2.3. *In Vivo* Study

The establishment of a standardized defect is critical according to the study and also age/weight of the animal. For our study we choose the critical/standard sized calvarial defect model (6x4 mm) to study the effect of SiONPx coatings on angiogenesis which is widely used model to study cranial bone regeneration (38). These procedures are sensitive and technique dependent and require adequate training as well for reproducibility. The corrective use of blank defect (negative control) and sham (no bone defect) is also important as they serve as controls for an empty defect with no intervention and for the surgical method without creating the defect (39). In our study, we also observed the limitation of the plate fixation to the adjacent bony tissues, which were improved by the use of tissue bond (vetbond) and closely re-flapping the skin and suturing (40, 41). However, we did not re-approximate the periosteum to impose the more clinically relevant situation in which cranial injuries are accompanied by periosteum loss (42).

All surgical modalities, care and treatment plans followed the ethical use of animals' protocol approved by the Institutional Animal Care and Use Committee (IACUC) at The University of Texas at Arlington under IACUC protocol number A18.014. Materials used in the procedure were as follows: disposable surgical blades #15, gauze, dental bur #1 and #2, PBS,

templates made of silicon wafer (6 x 4mm), isoflurane, nalbuphine, suture (Vicryl 4-0), and other basic surgical tools.

Adult male Sprague Dawley rats (~450 g) were used for this experiment to measure local and systemic levels of oxidative stress markers and local angiogenic markers. The animals were randomly assigned for specific treatment. G-power software was used for sample size calculation with 80% power, $\alpha = 0.05$, and moderate effect size of 0.30. The animal study had 3 groups (n=3/group): I - sham, II – uncoated plate (silicon wafer with 2 nm natively grown SiO_2 surface), and III - 200 nm SiONPx2 (O: 14.2at %) coated plate. For group I (sham), all steps of the surgical procedure were done except creating the bone defect and implantation, thereby accounting for aspects of the surgical procedure. For Groups II and III (uncoated plate and coated plate, respectively), these materials were placed into rats that had two standard size calvarial defects measuring 6x4 mm on each side of median sagittal suture following the same technique used in a previous publication (9), despite the traditional description as 5 to 8 mm (38, 43–46). A 1 mm gap between the plate and bone side walls was made to determine the tissue regeneration on sample surfaces without conduction from the side walls of the defect.

Summary of the surgical procedure: Immediately before surgery, painkiller/sedative SR Buprenorphine 0.5/1mg/kg was injected subcutaneously. With the animal under anesthesia (2-3% isoflurane), an approximately 2.5 cm long incision was made on an imaginary line traced over the sagittal suture, from between the eyes to posterior, with a sterile blade. Then, the skin and periosteum were carefully elevated and spread to expose the two parietal bones. The two bone defects were created using a dental bur #1 and/or #2 of approximately the same dimensions of 6x4mm +/-1mm on either side of the midline while the surgical site and surrounding tissues was continuously irrigated with cold saline solution to prevent heating the surrounding bone and

keeping the soft tissue moist. The depth of the defect was carefully made, and the loosened bone was removed so as not to damage the dura. After cleaning the defect area, the plate was placed in the defect. The right side was empty (internal control) and the left side was implanted with SiONPx2 (O: 14.2at %) samples or silicon wafer samples (negative control). The skin was then sutured with Vicryl 4.0.

After the surgeries, rats were examined for signs of stress and any signs of pain or distress. Analgesia was administered to the animals for management of pain and distress after surgery if needed. 0.1ml of blood (from the rat tail vein) using a sterile syringe was extracted every week for further testing. The experimental end point was 2 weeks after the surgery, after which the animals underwent euthanasia (>90% CO_2 and monitored until the animal was deceased)

Detection of oxidative stress marker in blood serum : Blood was collected from rat tail vein (n=3/group), placed in a centrifuge tube and centrifuged at 5000 rpm for 10 minutes. The supernatant serum was stored in - 80°C until further use. The serum samples were used to measure 4-HNE by a competitive enzyme-linked immunosorbent assay (ELISA) kit acquired from Cell Biolabs, Inc. The animals were anesthetized using 2-3% isoflurane and blood was collected just before the surgery, at 1 week, and 2 weeks (just before euthanizing the animals).

Detection of angiogenic and oxidative stress markers (Serum analysis and histological analysis): Serum samples were used to measure Ang1 (ANG1-7 ELISA Kit (Rat) Cat #: OKDD01231), NRF2 (NFE2L2 ELISA Kit (Rat) Cat #: OKEH03531), and Hif1a (HIF1A ELISA Kit (Rat) Cat #: OKEH00594) by a competitive ELISA kit acquired from Aviva Systems Biology Corp (San Diego, CA) using manufacturer guidelines.

After euthanasia (2 weeks after surgery), the calvarial samples were harvested using a diamond saw preserving at least 5 mm of bone and tissue from the original defect and implanted samples. All sham samples had the sagittal suture and parietal bones preserved. The samples were fixed in 4% paraformaldehyde at 4°C for 5 days and decalcified by ethylenediaminetetraacetic acid (EDTA) for 1 week. Half of each sample was used for frozen section and half for plastic embedding.

Sanderson's staining: The samples embedded in plastic were polished and cleaned using polishing cloth and washed with tap water and ultrasonic cleaner. Later, the samples were stained with Sanderson's stain and counterstained with acid Fuchsin. Digital images were acquired using the 10x objective of a BIOQUANT OSTEOIMAGER (BIOQUANT Image Analysis Corp, Nashville, TN). These images were used to show the anatomic relationship between the bone defects and the implant plate.

Immunostaining (CD31 and 4-HNE): The samples were perfused with sucrose and embedded in an optimal cutting temperature compound for frozen sectioning and further immunostaining was conducted for CD31 (endothelial cell marker) and 4-HNE (oxidative stress marker). The frozen samples were cut at 10 μm thickness in a coronal plane to maintain the bone defects with and without plate in the same slide. The slides were washed with PBS and blocked with 10% goat serum. After blocking, the slides were washed again with PBS and the primary antibodies (Rabbit polyclonal 4-HNE (ab46545) 1:8000 and Rabbit polyclonal CD-31 (M20)TM 1:500) were placed on the slides and incubated overnight at 4°C. The slides were then introduced to the secondary antibodies Alexa Dye 594 Goat anti-Rabbit in 1:200 dilution, washed twice with PBS and mounted with a cover slip for microscopic evaluation. One slide per group was used as a negative control and was not exposed to the primary antibody. The pictures were captured from

the central area just above the implant plate or central fibrotic tissue (empty) of the defect in other to minimize presence of neovascularization from surrounding bone. We used a 20x objective on Zeiss Axion cell culture fluorescent microscope for acquisition of the images and captured 3 images per slide. The slides were obtained from three different areas (anterior, medium, and posterior). ImageJ software was used to calculate the amount of fluorescence in relation to the total area.

Immunostaining (Ang1, Hif1α and NRF2): The cut and polished plastic embedded samples were washed and then kept in xylene for two changes to remove the upper plastic layer for 1 min each. The samples were then washed in descending grade alcohol (100%, 90%, 75%, 50%, 25%, and 0%) to rehydrate the samples. The samples were then kept for antigen retrieval using testicular hyaluronidase method (47). Prewarmed testicular hyaluronidase solution was prepared using 47 ml of 0.1 M potassium phosphate and 3 ml of 0.1 M sodium phosphate with 0.025 g of testicular hyaluronidase (H3884; Sigma-Aldrich, St. Louis, MO) and the samples were kept in the solution for 30 mins at 37°C. The samples were then washed 3 times with PBS with 1% tween solution for 5 mins each and stained with primary antibodies Angiopoietin 1 Polyclonal Antibody (23302-1-AP; Proteintech North America, Rosemont, IL) in 1:500 dilution, Hif1α Polyclonal Antibody (PA1- 16601; Thermofisher Scientific, Waltham, MA) and NRF2/NFE2L2 Polyclonal Antibody (16396-1-AP; Proteintech North America, Rosemont, IL) in 1: 500 dilution overnight at 4°C, washed thrice again and stained with secondary antibodies Alexa Dye 594 Goat anti-Rabbit (red fluorescence) in 1:500 dilution and Alexa dye 488 Goat anti Rabbit (green fluorescence) (A-11008; ThermoFisher, Waltham, MA) in 1:500 dilution at room temperature for 1 hour. The samples were washed, mounted, and imaged. Image J software was used to calculate the percentage of fluorescence in relation to the total area.

3.2.4. Statistical Methods

The results were presented in box plots showing the mean, standard deviation, and significance levels. Normality tests were done before statistical analysis to confirm normal distribution. Student t-test was used for comparing the difference in means between the two groups at a significance level $p<0.05$. One-way ANOVA (Tukey's Pairwise) was used to compare means for more than two groups at a significance level $p<0.05$. OriginPro 2017, Past3 and Microsoft Excel 2016 Software were used for graphics and calculations.

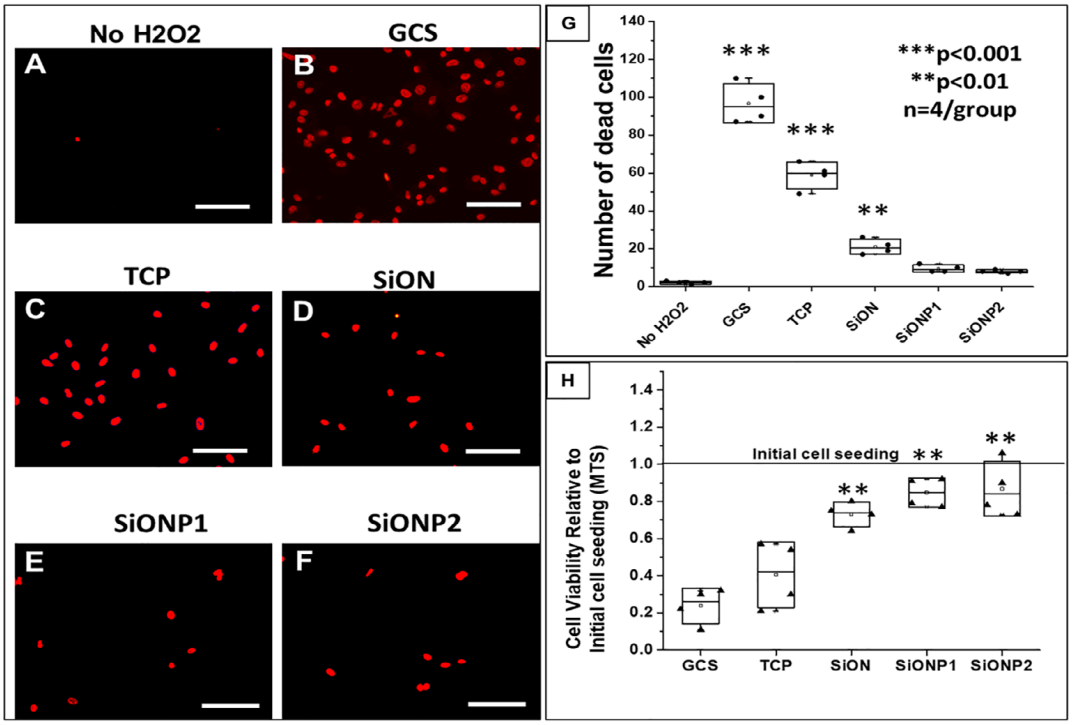

Figure 3.1 Effect of silicon oxynitride- (SiONx-) and silicon oxynitrophosphide- (SiONPx-plasma-enhanced chemical vapor deposition nanoscale implant coating on human umbilical vein endothelial cells under toxic levels of hydrogen peroxide (H_2O_2; 24 hours). Scale bar = 100 µm. (A–F) Propidium iodide (PI) staining shows dead cells (red stain). (G) Analysis after ANOVA (Tukey's pairwise) shows data from PI counting according to group. (H) Comparison of cell viability relative to the initial cell seeding among groups after MTS assay, the data were analyzed by ANOVA (Tukey's pairwise). GCS = glass cover slip; SiONP = silicon oxynitrophosphide; TCP = tissue culture plate. n = 4. ***$p < 0.001$ and **$p < 0.01$, all compared with No H_2O_2 group.

3.3. RESULTS

3.3.1. Cells Viability Under Toxic H_2O_2

Figure 3.1 shows the cells viability study using propidium iodide fluorescent stain and the data is presented by boxplots with the statistical significance for each group. We compared the study groups as follow: No H_2O_2, GCS, TCP, SiON, SiONPx1, and SiONPx2. The cells on the last five groups were exposed to toxic concentrations of H_2O_2. The SiONPx1 and SiONPx2 groups presented a reduced number of dead cells (red stain) and similar to No H_2O_2 group ($p>0.05$) as shown in **Figure 3.1(A-F)**. GCS and TCP showed a significantly increase in the number of dead cells compared to the other groups ($p<0.01$) **(Figure 3.1-G)**. Also, MTS assay was used to study the cell viability on the surface of the different study groups (GCS, TCP, SiONx, SiONPx1, and SiONPx2), and the data is presented in a boxplot at **Figure 3.1-H**. All groups were exposed to the same toxic concentration of H_2O_2 and relative to initial cell seeding. GCS and TCP showed a significant reduction in the number of viable cells, approximately 20% and 40%, respectively, compared to initial cell seeding ($p<0.001$). TCP presented almost 50% lower number of cells compared to SiONx, SiONPx1 and SiONPx2 ($p<0.01$). There was no significant difference among SiONx and SiONPx coating groups (SiONx, SiONPx1 and SiONPx2) ($p>0.05$) (**Figure 3.1-H**).

3.3.2. Matrix Deposition After Exposure to Toxic H_2O_2 Environment

Figure 3.2 presents the fibronectin deposition by HUVEC cells *in vitro*. The amount of fibronectin deposition was evaluated by fluorescent immunostaining, and the percentage of total area occupied by fibronectin is given in a boxplot (**Figure 3.2-F**). The GCS surface presented 3 times lower fibronectin deposition ($21.35 \pm 10.19\%$) than SiONx ($71.46 \pm 4.58\%$) and SiONPx1

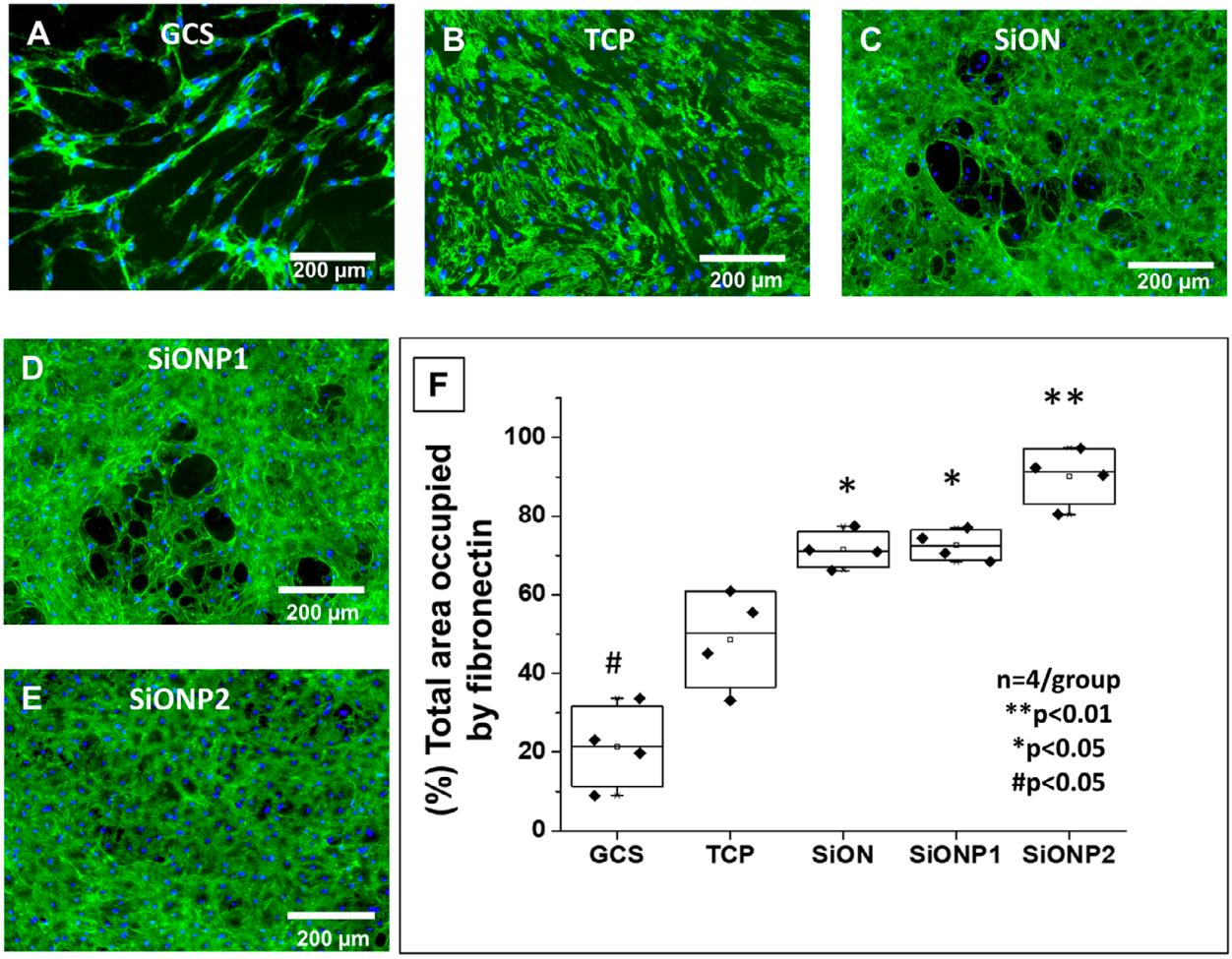

Figure 3.2 Fibronectin deposition by human umbilical vein endothelial cells (HUVECs) *in vitro*. (A–E) Fluorescent images after immunostaining for fibronectin deposition 5 days after HUVECs were exposed to toxic oxidative stress (0.6mM hydrogen peroxide). Scale bar = 200 µm. (F) Graph of data analysis after ANOVA (Tukey's pairwise) shows of percentage of area occupied by fibronectin after data collection using ImageJ. GCS = glass cover slip; SiON = silicon oxynitride; SiONP = silicon oxynitrophosphide; TCP = tissue culture plate. n = 4. **p < 0.01, *p < 0.05, and #p < 0.05, compared with TCP group.

(72.59 ± 3.84%) groups ($p<0.05$), and 4 times lower than SiONPx2 (90.11 ± 7.06%, $p<0.01$). The TCP surface also showed a significant reduction in fibronectin deposition (48.64 ± 12.29) compared to SiONx, SiONPx1 ($p<0.05$) and SiONPx2 ($p<0.01$) as presented at **Figure 3.2 (B-E)**. Fluorescent images showed significantly lower fibronectin deposition on the GCS surface than all other groups but had a tubular arrangement of the fibrous network. In contrast, TCP presented more fibronectin deposition than the GCS, with minimal tubular network formation of

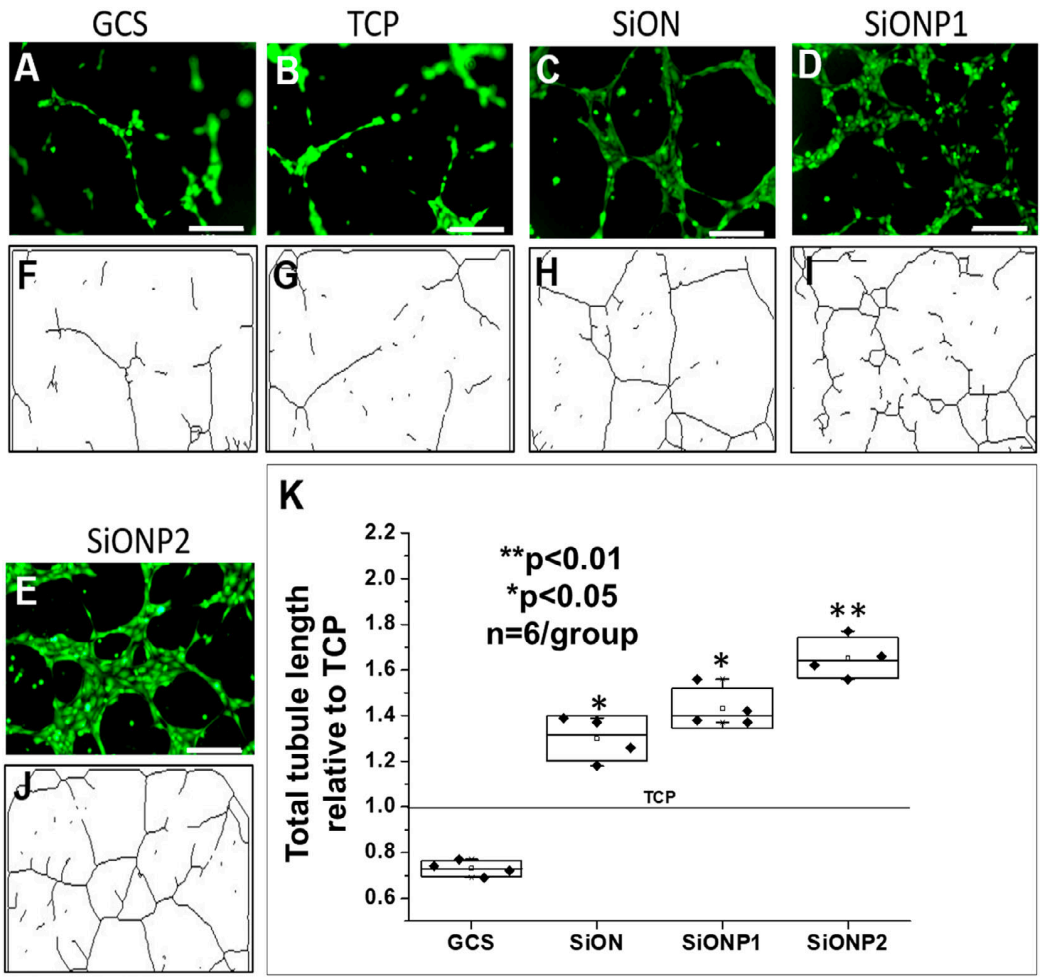

Figure 3.3 (A–E) Fluorescent images after calcein-AM staining of human umbilical vein endothelial cells (HUVECs) capillary tubule formation under toxic oxidative stress (0.6mM hydrogen peroxide). Scale bar = 200 μm. (F–J) Tree capillary network traced lines after analysis by angiogenesis analyzer (ImageJ plugin) software. (K) Graph of data analysis after ANOVA (Tukey's pairwise) shows comparison of total tubule length. GCS = glass cover slip; SiON = silicon oxynitride; SiONP = silicon oxynitrophosphide; TCP = tissue culture plate. n = 4. **p < 0.01 and *p < 0.05, compared with TCP group.

the fibers. SiONx, SiONPx1, and SiONPx2 surfaces had significantly more fibronectin deposition compared to GCS and TCP, along with marked enhancement in the tubular network structure on all SiONx and SiONPx-coated plates. SiONPx2 (O: 14.2 at %) produced the densest fibronectin structure along with tubular arrangement of fibers as compared to all groups (**Figure 3.2-E**).

3.3.3. Capillary Tubule Formation Under Toxic H_2O_2

Fluorescent images and tubular network lines traced on ImageJ software demonstrated improved tubular structure formation and length in HUVECs placed on PECVD SiONx and SiONPx coated materials compared to GCS and TCP (**Figure 3.3**). All SiONx and SiONPx groups presented a significantly enhanced total tubule length (SiONx coated plates showed 30% ($p<0.05$), SiONPx1 43% ($p<0.05$), and SiONPx2 65% improvement ($p<0.01$)) as compared to TCP. Conversely, GCS showed significant reduction in total tubule length compared to all other groups ($p<0.01$) (**Figures 3.3-B and 3.3-K**).

3.3.4. Angiopoietin-1 and 4-HNE Protein Adduct Levels in Conditioned Medium After Oxidative Stress (ELISA)

ELISA demonstrated that SiONx and SiONPx groups induced a marked increase in ang-1 production in HUVECs under toxic oxidative stress as compared to control (TCP) after 24 hours. The SiONx group showed 2-fold, SiONPx1 more than 6-fold, and SiONPx2 almost 5-fold

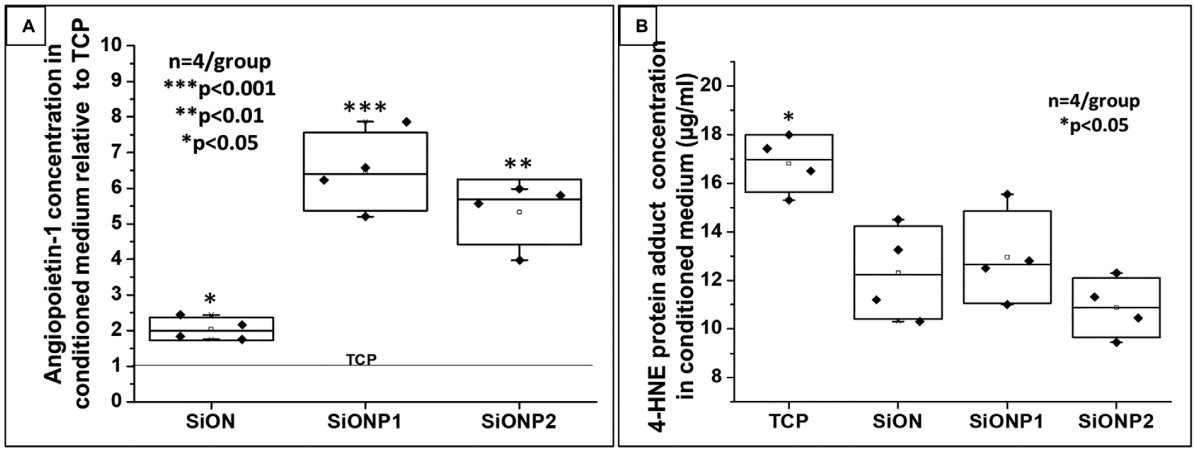

Figure 3.4 (A) ANG1 concentration in conditioned medium relative to TCP (control). ANOVA (Tukey's pairwise) was used for analysis and bicinchoninic acid assay was used to quantify the amount of ANG1 per µg of total protein on each sample. ***$p < 0.001$, **$p < 0.01$, and *$p < 0.05$, compared with TCP group. (B) 4-HNE protein adduct concentration in conditioned medium. Graph of data analysis after ANOVA (Tukey's pairwise). The conditioned medium was obtained from human umbilical vein endothelial cell culture after 24 hours in toxic oxidative stress induced by 0.6mM hydrogen peroxide. *$p < 0.05$, compared to each of the other groups. 4-HNE = 4-Hydroxynonenal; ANG1 = angiopoietin 1; SiON = silicon oxynitride; SiONP = silicon oxynitrophosphide; TCP = tissue culture plate. n = 4.

increase in the levels of ang-1 (**Figure 3.4-A**). There was no significant difference in 4-HNE protein adduct levels among the coated implant plate groups. However, all the SiONx and SiONPx coated groups showed significantly reduced levels of 4-HNE protein adduct as compared to TCP (control) ($p<0.05$) (**Figure 4-B**).

3.3.5. Gene Expression of Angiogenic and Oxidative Stress Markers on HUVECs Under Toxic Hydrogen Peroxide Levels

All angiogenic markers (VEGFA, NES-2, ang-1) were significantly overexpressed for SiONx and SiONPx coated plates compared to the control as shown in **Figure 3.5**. VEGFA (**Figure 3.5-A**) was expressed twice as much in HUVECs seeded on PECVD coated plates ($p<0.05$). Nesprin-2 (**Figure 3.5-B**) was overexpressed in SiONx (1.64 ± 0.11 times, $p<0.01$), SiONPx1 (1.44 ± 0.1 times, $p<0.01$), and SiONPx2 (1.67 ± 0.2 times, $p<0.01$) as compared to control. Ang-1 (**Figure 3.5-C**) was overexpressed in SiONx (1.47 ± 0.12 times, $p<0.05$),

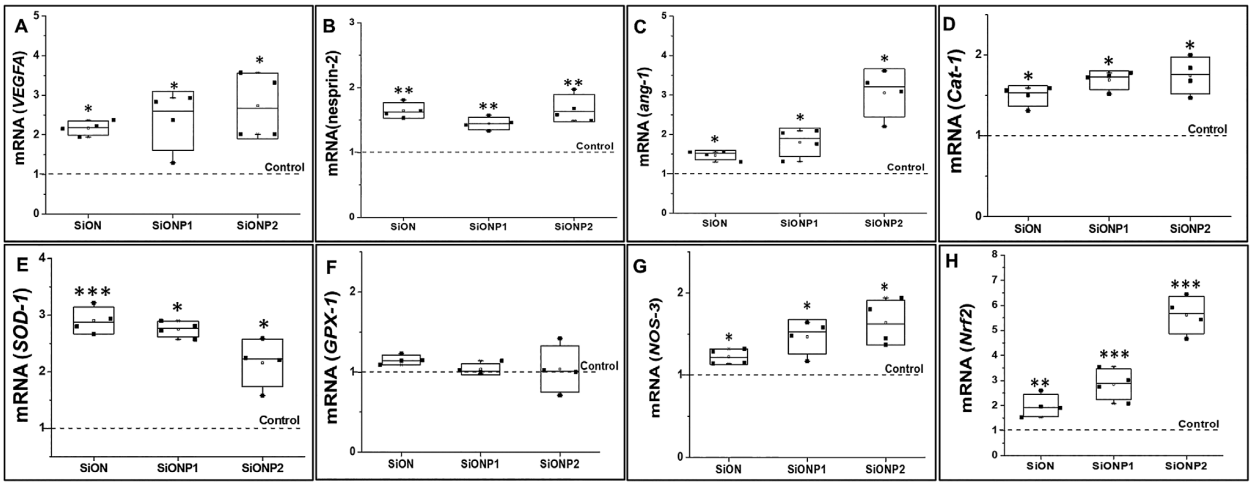

Figure 3.5 Human umbilical vein endothelial cell gene expression of angiogenic markers relative to 18S compared with control 24 hours under toxic oxidative stress (0.6mM hydrogen peroxide). (A) mRNA VEGFA. (B) mRNA nesprin-2. (C) mRNA angiopoietin-1. (D) mRNA Cat-1. (E) mRNA SOD-1. (F) mRNA GPX-1. (J) mRNA NOS-3. (H) mRNA Nrf2. ang-1 = Angiopoietin 1; Cat-1 = catalase 1; GPX-1 = glutathione peroxidase 1; NOS-3 = nitric oxide synthase 3; Nrf2 = nuclear factor erythroid 2-related factor 2; SiON = silicon oxynitride; SiONP = silicon oxynitrophosphide; SOD-1 = superoxide dismutase 1; VEGFA = vascular endothelial growth factor A. N = 4. ***$p < 0.01$ and *$p < 0.05$, compared with control.

SiONPx1 (1.79 ± 0.35 times, $p<0.05$), and SiONPx2 (O: 14.2 at %) (2.71±0.98 times, $p<0.05$) more than control.

Among all studied oxidative stress markers (Cat-1, SOD-1, GPX-1, Nrf2, NOS-3), GPX-1 (**Figure 3.5-F**) presented no significant difference compared to the control group. Cat-1 (**Figure 3.5-D**) was significantly overexpressed in SiONx (1.49 ± 0.12 times, $p<0.05$), SiONPx1 (1.69±0.11 times, $p<0.05$), and SiONPx2 (1.75 ± 0.23 times, $p<0.05$) than control. SOD-1 (**Figure 3.5-E**) expression was significantly more in SiONx (2.91 ± 0.24, times, $p<0.01$), SiONPx1 (2.76 ± 0.14, times, $p<0.05$), and SiONPx2 (2.16 ± 0.42, times, $p<0.05$) as compared to control. Also, NOS-3 (**Figure 3.5-G**) showed significant overexpression in SiONx (1.22 ±

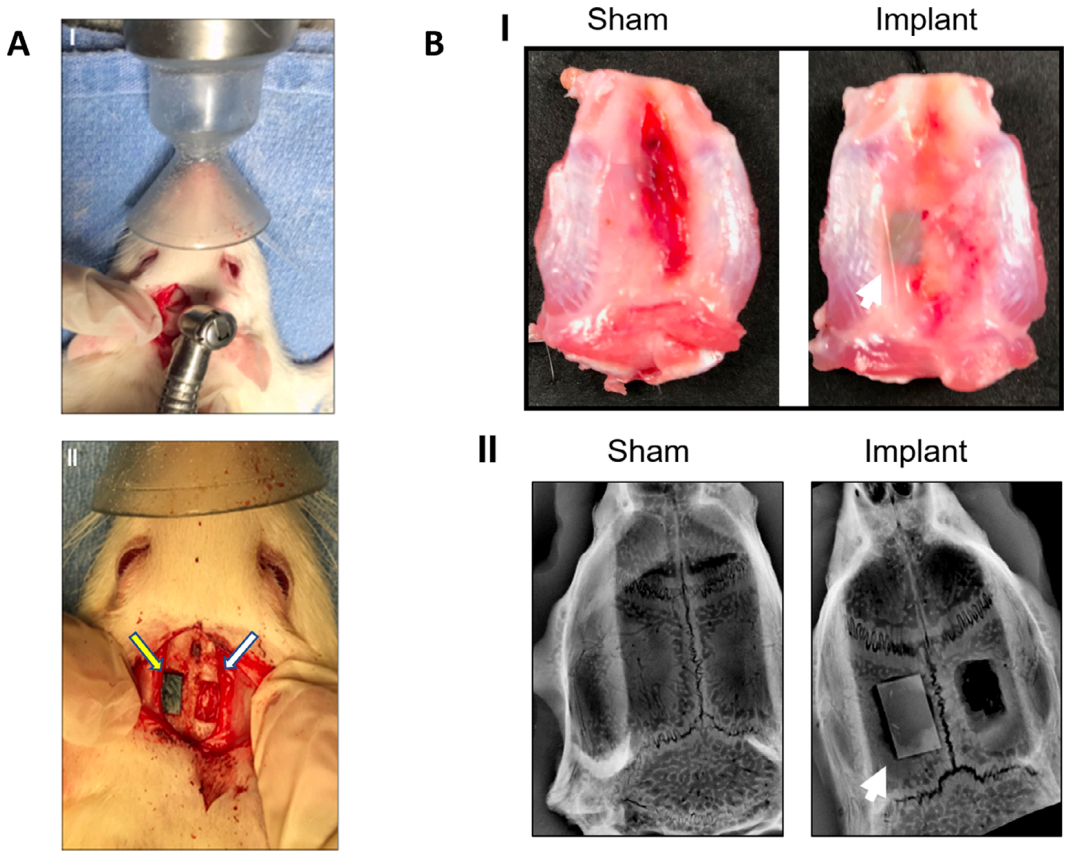

Figure 3.6 (A) Surgical procedure for material implantation. (I) Gross image of calvarial defect surgery with dental bur. (II) Gross image of the parietal bone bilateral calvarial defect (6 × 4 mm), implant on the left (yellow arrow) and empty on the right (white arrow). (B) Samples harvested from rat calvarium 15 days after surgery. (I) Gross image shows the macroscopic superior aspect of the calvaria. (II) An X-ray image with the sham (left) and calvarial defects and implant (right). The white arrow points to the implant. n = 3.

0.09-fold, p<0.05), SiONPx1 (1.46 ± 0.21 times, p<0.05), and SiONPx2 (1.64 ± 0.27 times, p<0.05) along with the other biomarkers. Nrf2 (**Figure 3.5-H**) was overexpressed in SiONx (1.99 ± 0.44, times, p<0.01), SiONPx1 (2.85 ± 0.61, times, p<0.001), and SiONPx2 (5.61 ± 0.75, times, p<0.001) as compared to control.

3.3.6. In Vivo Evaluation of PECVD-Coated Fixative Plates

Surgical procedures with coated and uncoated fixative implants are shown in **Figure 3.6-A**. During sample harvesting there was no macroscopic evidence of inflammation and all samples were well positioned inside the defect as verified by X-ray images in **Figure 3.6-B**. The animals were divided into 3 groups (n=3/group): Sham, Uncoated implant "Si bare wafer", and SiONPx2. Due to the most relevant results in the *in vitro* experiments, SiONPx2 plate was used in the *in vivo* studies. It is also important to mention that no adverse events were observed with the current model and the used biomaterials.

3.3.7. Serum Analysis (ELISA)

The bare silicon wafer control group showed a significant elevation in the 4-HNE serum concentration at 7 days after surgery (57.81±6.4 µg/ml) as compared to the pre-operative levels

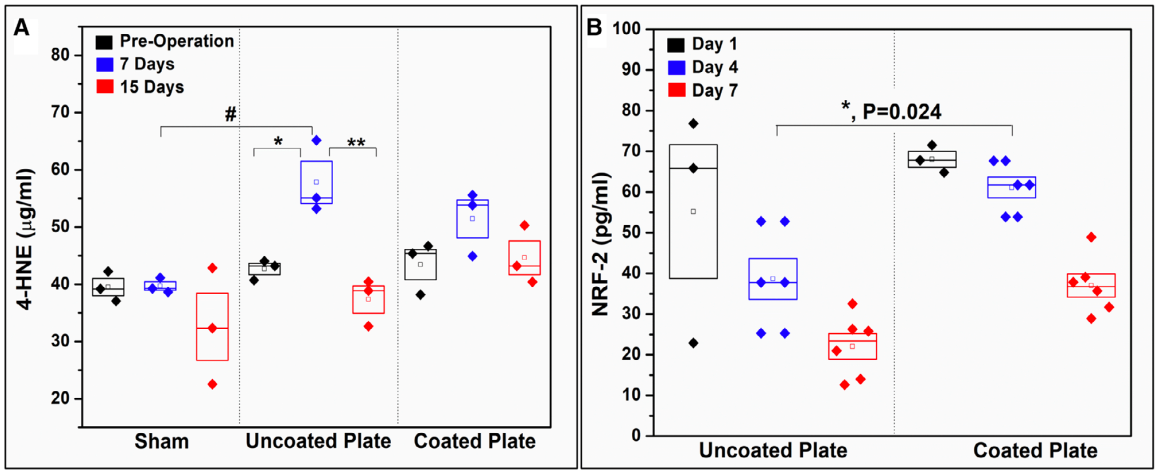

Figure 3.7 Bar graph shows 4-HNE protein adduct concentration in the rat serum presurgery, 7 days postsurgery, and 15 days postsurgery (competitive ELISA). *p < 0.05 (one-way ANOVA—Tukey's pairwise within the uncoated "bare" implant group) and #p < 0.05 (one-way ANOVA—Tukey's pairwise, same time point different groups).

(42.64±1.72 µg/ml), with a reduction at 15 days after surgery (37.32±4.11 µg/ml) ($p<0.05$). The 4-HNE serum concentration for the uncoated "bare" implant group was significantly higher at 7 days as compared to the sham (39.67±1.28 µg/ml) ($p<0.05$). The sham and SiONPx coated plate groups did not show any significant differences among the three time points within the same group ($p>0.05$) (**Figure 3.7-a**). We also see significant increased NRF2 activity in serum for SiONPx coated group as compared to the bare implant group (**Figure 3.7-b**).

3.3.8. Histological Analysis of Harvested Samples

Sanderson's staining: Sanderson's staining of coronally-sectioned calvaria are shown in **Figure 3.8** and shows areas used for capturing immunofluorescent images for CD31 and 4-HNE. The

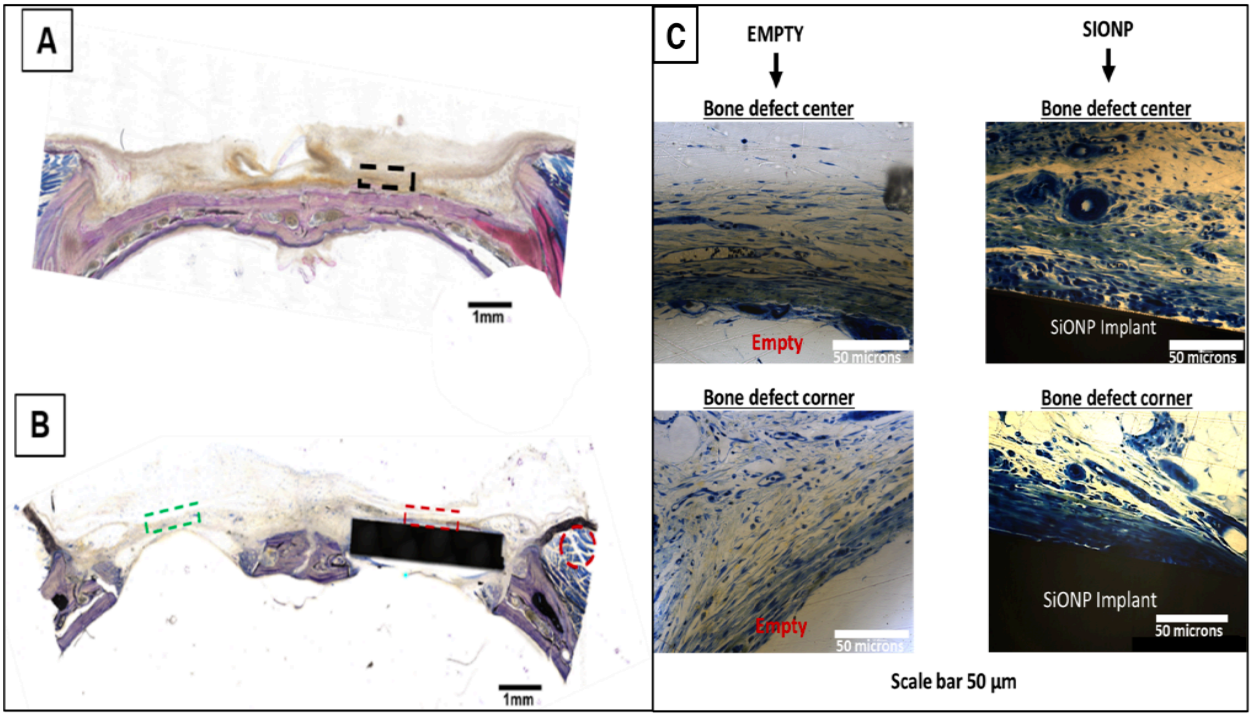

Figure 3.8 Bright field images acquired using the BIOQUANT Osteoimager showing coronal sections of rat calvaria after Sanderson's staining. Dotted rectangles represent the areas used for capturing immunofluorescent images. (A) The dotted black rectangular box is representative of a sham-operated animal. (B) The dotted green rectangular box indicates the location assessed for the empty standard-size calvarial defect, while the dotted red rectangular box indicates the location of the assessed implant-filled standard-size calvarial defect. The muscle is traced with a red circle. Scale bar = 1 mm. (C) Higher magnification images of empty defect (showing no vascular tissue formation) and coated implant surfaces (showing new vascular tissue formation). Uncoated surfaces did not exhibit any new vascular tissue formation, which matched that of empty defects. SiONP = silicon oxynitrophosphide.

coronal section of the sham-operated group is seen in **Figure 3.8-A** where the dotted black rectangular box represents the analyzed area. The surgical bone defect sample is shown in **Figure 3.8-B**, where the dotted green rectangular box represents the empty defect, the dotted red rectangular box represents the new tissue formed on the plates, and the dotted red circle represents the rat calvarial muscle area analyzed. **Figure 3.8-C** shows high magnification images of the cross section, where there is more vascular as well as osteoid formation on the SiONPx surface as compared to the empty defect.

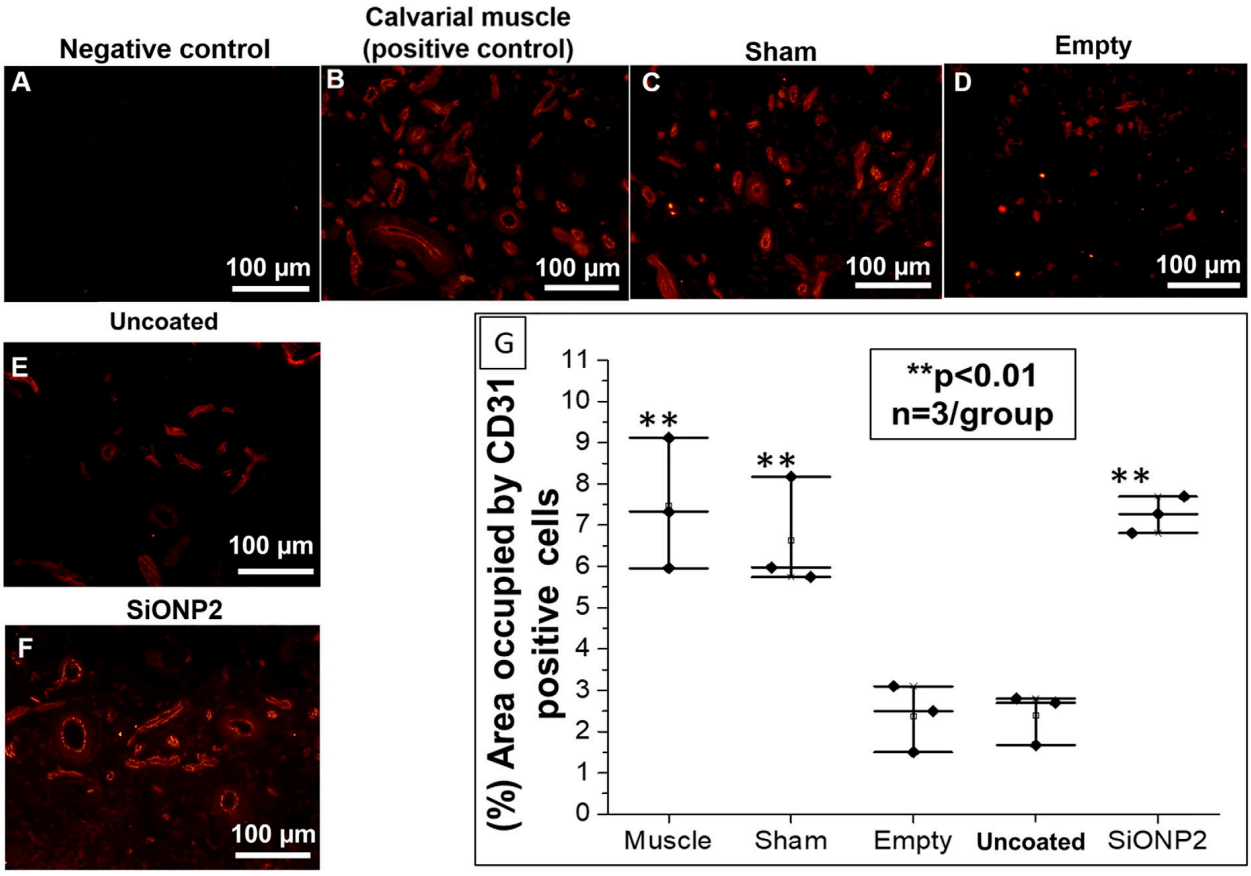

Figure 3.9 Immunofluorescence staining (Alexa Fluor 594) for CD31 15 days after implantation. Scale bar = 100 µm. (A) Negative staining control (no secondary antibody was used). (B) Calvarial muscle (positive control). (C) Sham (surgical procedure, no bone defects). (D) Empty defect. (E) Uncoated "bare" implant. (F) SiONP2. (G) Percentage area occupied by blood vessels and capillary network relative to sham. SiONP = silicon oxynitrophosphide. **p < 0.01, compared with empty and uncoated "bare" implant groups.

Immunostaining (CD31, Ang1, Hif1α NRF2 and 4-HNE): CD31 was used to compare samples collected from calvarial muscle, sham, empty, uncoated "bare" implant, and SiONPx2. And in the 4-HNE analyses, it was compared samples from empty, sham, uncoated implant and SiONPx2. Rats implanted with SiONPx demonstrated significantly more CD31 positive cells (2-fold increase), than empty and uncoated implant ($p<0.01$) groups. There was no significant difference when quantified among SiONPx2, muscle (positive control), and sham groups ($p>0.05$) (**Figure 3.9**).

Ang1 immunostaining (**Figure 3.10 (A-C)**) shows significantly higher expression of Ang1 on the SiONPx2 coated surface as compared to the uncoated group. There was a

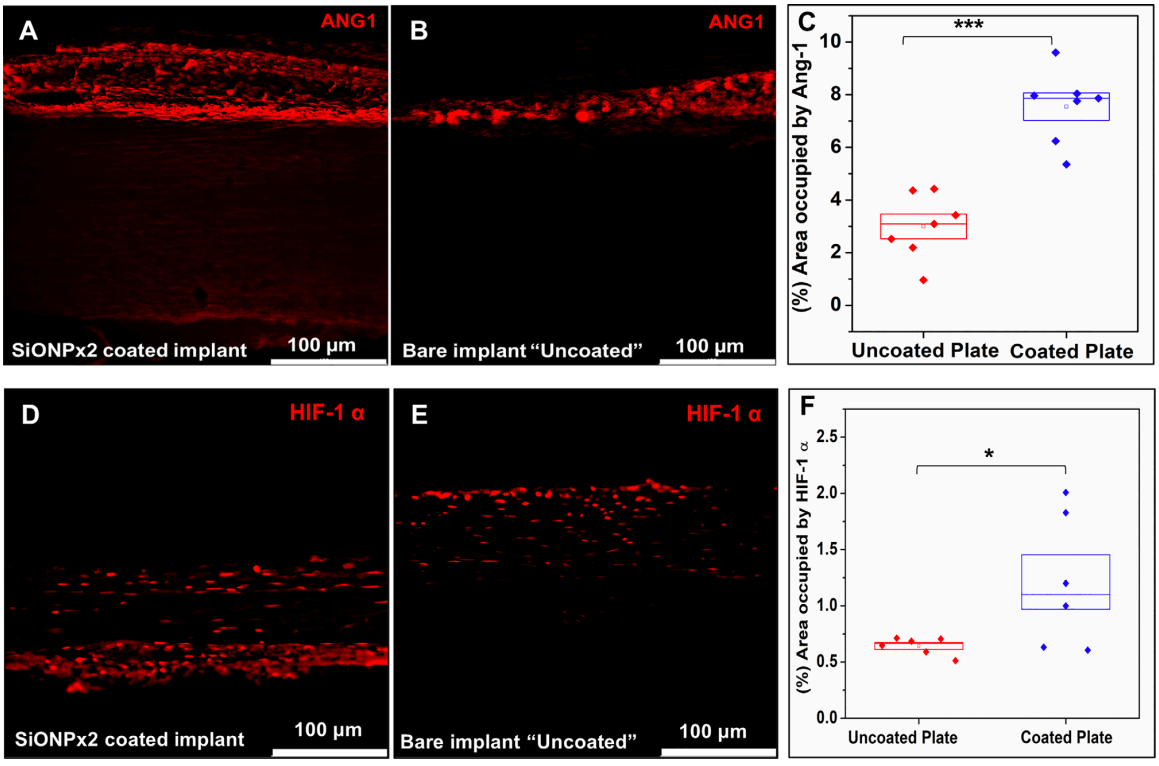

Figure 3.10 Immunofluorescence staining (Alexa Fluor 594) for Ang-1 and HIF-1α, 15 days after implantation. Scale bar 100 µm. (A) SiONPx2. (B) Uncoated "bare" implant. (C) Percentage of area occupied by Ang-1. Statistical difference, ***$p < 0.001$. (D) SiONPx2. (E) Uncoated "bare" implant. (F) Percentage of area occupied by HIF-1α. Statistical difference, *$p < 0.05$. Ang-1 = Angiopoietin-1; HIF-1α = hypoxia inducible factor-1 alpha; SiONP = silicon oxynitrophosphide.

significant difference of 2.5 fold between the coated and uncoated group ($p<0.001$). **Figure 3.10 (D-F)** shows the expression of Hif1α on the SiONPx coated and uncoated implant plates. Results

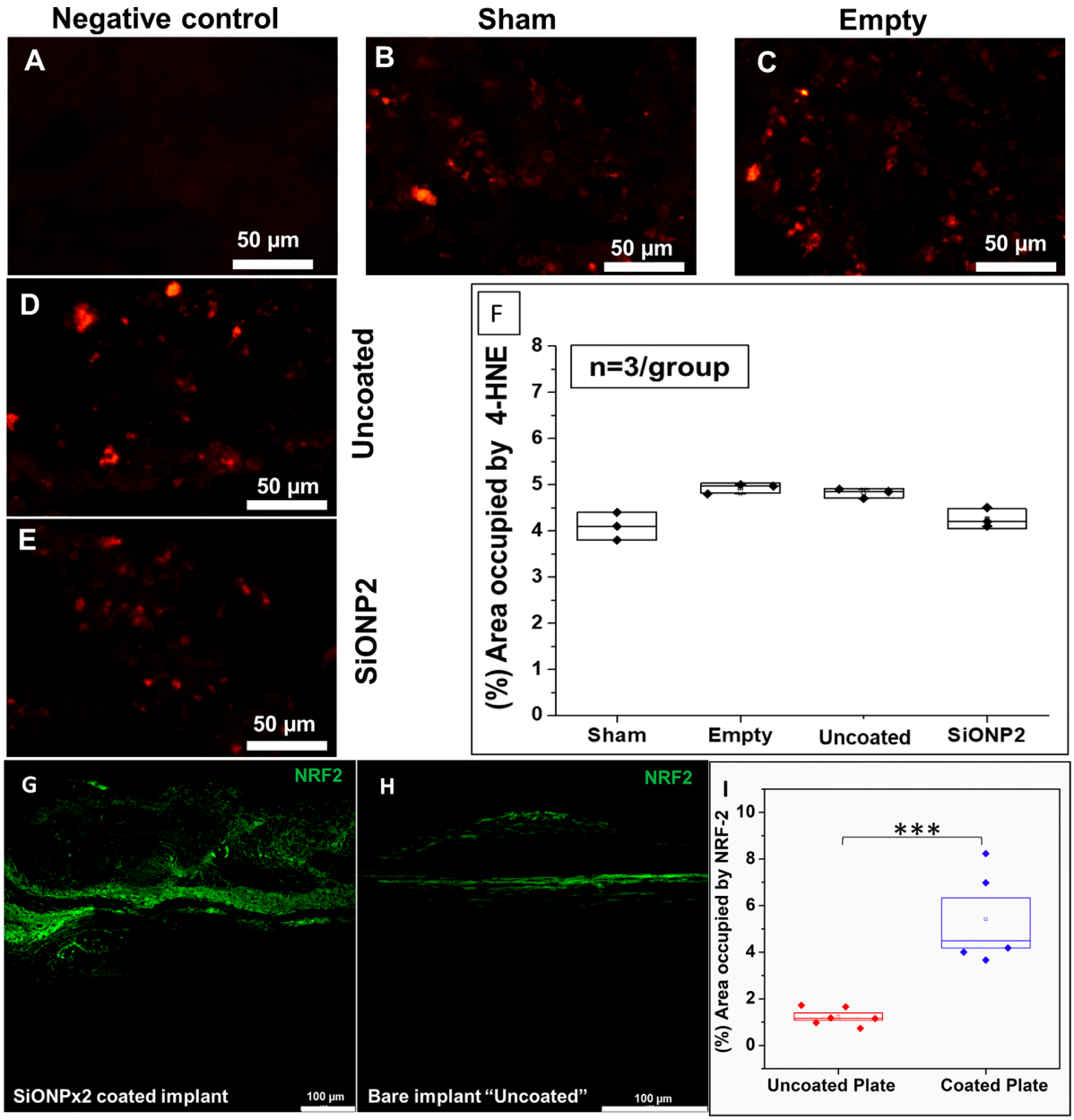

Figure 3.11 Immunofluorescence staining (Alexa Fluor 594) for 4-HNE and (Alexa Fluor 488) for NRF-2, 15 days after implantation. Scale bar = 50 µm. (A) Negative control. (B) Sham. (C) Empty defect. (D) Uncoated "bare" implant. (E) SiONP2. (F) Percentage of area occupied by 4-HNE. After one-way ANOVA-Tukey's pairwise, it was not detected difference among the studied groups ($p > 0.05$). (G) SiONPx2. (H) Bare implant. (I) Percentage of area occupied by NRF2. 4-HNE = 4-Hydroxynonenal; NRF2 = nuclear factor erythroid 2-related factor 2; SiONP = silicon oxynitrophosphide. Statistical difference, ***$p < 0.001$.

show significant difference ($p<0.05$) between the two groups.

The percentage of area occupied by 4-HNE tissue fluorescence signal shows no statistical difference among the groups ($p>0.05$) (**Figure 3.11 (A-F)**). The tissues surrounding the SiONPx coated plate showed 2-times more NRF2 expression (**Figure 3.11 (G-I)**) (significant difference) as compared to the uncoated plate group.

3.4. DISCUSSION

We demonstrated that SiONx and SiONPx groups could reduce cell death in HUVECs and improve proliferation as seen in **Figure 3.1**. The ions released and/or surface energy seem to have a protective effect on HUVECs, even when exposed to 0.6 mM H_2O_2. We could not find studies that correlate SiONx or SiONPx-based materials with a reduction of endothelial cell death, particularly under oxidative stress conditions. However, studies have reported that ionic silicon and silica based materials improve endothelial cells' proliferation by upregulating several angiogenic marker (11, 48–50). Our findings suggested that these biomaterials could accelerate tissue regeneration under unfavorable conditions, such as hypoxia and elevated reactive oxygen species present in large and complex bone defects.

In the following *in vitro* experiments, we detected a significant improvement in the length of the capillary tubule network and the fibronectin deposition in all PECVD coated SiONx and SiONPx implant plates, particularly with the SiONPx2 (O: 14.2 at %) group (**Figure 3.2-A**). Some previous studies have demonstrated silica-based materials can improve endothelial cells' capillary tubule formation (11, 50). However, none of these studies showed this effect under oxidative stress conditions, as observed in our experiments. Fibronectin is a glycoprotein that is produced by HUVECs and plays a major role in extracellular matrix formation during

angiogenesis. This protein regulates vascular remodeling, endothelial cell migration, survival, and elongation (28, 51, 52). In **Figures 3.2-C, D, E**, we can see that SiONx, SiONPx1, and SiONPx2 groups show enhanced fibronectin deposition in a circular shape with significantly higher density in the SiONPx groups.

We demonstrated that ang-1 production was enhanced in HUVECs exposed to SiONx, SiONPx1 and SiONPx2 (**Figure 3.4-A**). In addition, all PECVD coated groups presented a significant reduction of 4-HNE adduct (**Figure 3.4-B**). Ang-1 has been observed in previous literature to protect endothelial cells against apoptosis when they are under unfavorable survival conditions (15, 17). Moreover, this protein is important for endothelial cell migration, proliferation, and differentiation (18, 53). Another pertinent aspect is that ang-1 can induce osteoblastic differentiation, bone matrix deposition, and enhance bone mineral density (54, 55). The 4-HNE protein adduct is a product of lipid peroxidation and has been used to demonstrate oxidative stress levels *in vivo* and *in vitro*. Other molecules, such as Malondialdehyde (MDA) have been used to measure oxidative stress levels; however, MDA is less stable with a shorter half-life. Our results showed that the PECVD coated fixative implants reduced oxidative stress and enhanced ang-1 production, which could be preventing cell death as observed in our initial in vitro experiment (**Figure 3.1**).

The evaluation of angiogenic gene expression markers demonstrated that the mRNA levels of ang-1 were at least 2.5-fold enhanced in the SiONPx groups, and that finding corroborates with the protein level in the conditioned medium. VEGFA and Nesprin-2 mRNA levels were also enhanced in all groups with SiONx and SiONPx. VEGFA is a well-known major regulator of angiogenesis and can be stimulated by multiple factors (56, 57). Studies have demonstrated that ionic silicon released from the mesoporous silica and bioactive glasses can

enhance angiogenesis by upregulating VEGFA (11, 58). As mentioned above, ang-1 is relevant in angiogenesis and osteogenesis (15, 17, 18, 54, 55). Nesprin-2 is a large multi-domain protein that plays a dominant role in regulating endothelial cell shape and migration. This protein connects the nuclei to the cytoskeleton and regulates the architecture of both structures, controlling the angiogenic loop formation during pre-capillary tubular network organization (59).

Previously, a study reported that products of dissolution of calcium silicate can stimulate angiogenesis by inducing nitric oxide synthase upregulation (60). Nitric oxide can have an ambiguous role in angiogenesis under oxidative stress conditions. On one hand, high levels of superoxide can neutralize the angiogenic effect of NO by forming peroxydonitrite, which is a highly toxic molecule (61). On the other hand, authors reported that NO suppresses angiostatin, which is an inhibitor of angiogenesis (62). Lastly, NOS-3 and NO are associated with fracture healing modulation and are necessary for adequate bone formation (63, 64), which supports the use of SiONx and SiONPx in bone defects. Although these *in vitro* studies give us a great insight on the various factors that may be involved in enhanced angiogenesis for SiONx and SiONPx coated plates, they have a limitation that it cannot replicate the complex *in vivo* environment.

In the *in vivo* experiments we measured angiogenesis by CD31 and Ang1. We also measured Nrf2 activity and oxidative stress by 4-HNE immunofluorescent staining. In addition, 4-HNE was measured from blood samples collected before and after surgery. The SiONPx2 coated plate was used for the *in vivo* study as it presented the most relevant outcome in the *in vitro* experiments. SiONPx2 plates enhanced Ang1 expression and increased blood vessel density regenerated on the coating surface were similar to those seen in the evaluation of blood vessel density in cortical bone. In 2006, Kingsmill et al. studied the cortical vascular canals in human cranium and mandible based on quantitative calculations from digital backscattered

electron images (65). They reported that the mandible (labial aspect of the midline) has a high number of blood vessel canals (mean, 7.2/mm2) and a canal area of 7.5% compared to the parietal bone that has less blood vessel canals (mean, 5.9/mm2) and canal area of 5.5% (65). These results also support our *in vitro* observations and demonstrates that these coated plates can support and enhance angiogenesis in critical size bone defects. 4-HNE immune staining could not detect a difference between groups, likely due to lipid peroxidation product elimination or the adduction to other molecules by day 15. Studies have demonstrated that 4-HNE is unstable and can be difficult to detect after 10 days from the initial oxidative stress event (66, 67). After 7 days, the serum levels of 4-HNE adduct showed that animals implanted with SiONPx2 (O: 14.2 at %) in the left calvarial bone defect presented no difference compared to pre-operative levels. This observation suggests that the surfaces coated with SiONx and SiONPx by PECVD can reduce ROS and possibly improve and accelerate osseointegration of the biomaterial.

In general, all elements used in our study for the PECVD surface coating have been reported to facilitate angiogenesis (14, 68, 69). Among Si, N and P, Si is the most studied and supported in enhancing angiogenesis (11, 37, 38, 70, 71). As shown in **Table 3.2**, EDS analysis shows that the difference between SiONx, SiONPx1, and SiONPx2 (O: 14.2 at %) groups is mainly represented by Si, O and N at %, as P represents less than 1 at % of surface composition. However, the addition of P and the different N_2O flow rate between SiONPx1 and SiONPx2 (**Table 3.1**) played a role on the elemental surface composition of these two coatings. It seems that the elevated silicon at % can be responsible for the SiONPx1 and SiONPx2 outcome in enhancing angiogenesis and reducing the oxidative stress demonstrated in our *in vitro* studies. In terms of ionic surface composition, the different results observed in the SiONPx1 (O: 7.3at %), and SiONPx2 (O: 14.2 at %) groups can be attributed to oxygen content. The SiONPx2 group

presented twice more oxygen than the SiONPx1. Furthermore, despite not being part of this study, we have also demonstrated in a concurrent manuscript that SiONPx2 presented significantly reduced wettability compared to SiONPx1, which also can justify enhanced angiogenic effect of surfaces coated with SiONPx2 (19), as more hydrophilic surfaces enhance angiogenesis by improving cell attachment and proliferation (72, 73).

Antioxidant markers also play an important role in mitigating the effects of excessive ROS and oxidative stress. At the end of *in vitro* experiments, we measured the mRNA level of antioxidant enzymes and nitric oxide synthase. Our results showed that SOD-1 and Cat-1 were significantly up-regulated by PECVD coated surfaces. Moreover, NOS3 levels were significantly elevated in SiONPx groups. SOD-1 is an enzyme which catalyzes the conversion of superoxide, the main reactive oxygen species produced during cell metabolism, to hydrogen peroxide. Cat-1 is a potent antioxidant protein that accelerates the conversion of H_2O_2 in H_2O and O_2. Thus, the enhancement of SOD-1 and Cat-1 activity reduce oxidative stress and accordingly improve biocompatibility ad osseointegration (74). NOS-3 is an enzyme that participates in nitric oxide (NO) synthesis and is important for angiogenesis and tissue regeneration (75). Our group has reported the important role of ionic silicon in SOD-1 regulation within osteoblasts differentiated from MC3T3 cells (9).

Nrf2 is a latent protein that is a major transcriptional activator of genes coding for enzymatic antioxidants, such as catalase and superoxide dismutase, as well as a major anti-inflammatory signaling molecule that induced to express upon traumatic injury (76). A study showed that a Si-rich diet could reduce oxidative stress in the liver of aged rats by neutralizing peroxides generated from high cholesterol diets in a similar manner as hydroxytyrosol (77). This study showed that SOD1, CAT, and Nrf2 were able to recover to nominal levels as that of

rats not given cholesterol and shows the ability of Si ions to neutralize ROS and rescue normal function (77). Our results demonstrated for the first time that all plates coated with amorphous SiONx or SiONPx upregulated Nrf2. Perhaps this major regulator is playing a role in the antioxidant effect of SiONx and SiONPx in HUVECs. The superoxide dismutase enzyme has a cationic site formed by zinc and/or copper that by electrostatic interaction facilitates the bond between the enzyme and superoxide (O_2^-) (78–80). Using the same rationale, the Si^{4+} released from the plate coated with SiONx and SiONPx (9) can reduce oxidative stress by interacting with superoxide and preventing interaction with lipids, DNA, and proteins.

Finally, we speculate on the effect of these surfaces on antioxidant metalo-enzymes such as SOD1, CAT, and Nrf2. Antioxidant metalo-enzymes are activated by transition metal cations such as Cu^{2+}, Zn^{2+}, and Mg^{2+} due to their ability to present electrons in 3d orbital state for reaction with the enzymes (81, 82). This is required to overcome the spin orbital restriction associated with enzyme activity for this family of enzymes (83). We have demonstrated in prior work at SiONx and SiONPx induce spin orbit splitting in which 2p Si electrons transition to 3d theoretical orbitals when N is added to their structures (84, 85). We suggest that the added electron availability not only overcomes this spin restriction, the presence of the higher valance state Si^{4+} increases charge transfer to antioxidants as follows:

$$M^{(n+1)+}/SOD1 + 2nO_2^- + 2nH^+ = M^{(n+1)+}/SOD1 + nH_2O_2 + nO_2 \qquad \text{(Eq. 1)}$$

In Eq. 1, M represents transition metal cations such as Cu, Zn, and Mn and n = 1, 2, or 3. Eq. 1 present the overall reaction that has 2 steps. One step is the cation is reduced as it reduces superoxide. The other step involves the oxidation of the cation as superoxide is reduced (82). This means that the cation acts as a catalyst and as such conserves charge. For Si, the increased valence state of Si undergoes more moles of superoxide reduction. Antioxidants such as

glutathione peroxidase further dissociate the peroxide molecule into hydroxyl groups, which are further reduced by catalase (86). For Nrf2, which anchored in the cytoplasm through binding to Keap1, Si ions may dissociate Keap1 within the cytosol to release Nrf2, which then translocate into the nucleus as seen in **Figure 3.11 (G-I).** We will further investigate these reactions using metabolomics analysis to better understand the reaction efficiency of such reactions in future work to further elucidate this reaction mechanism.

3.5. CONCLUSION

In conclusion, our study demonstrated that fixative plates coated with SiONx and SiONPx sustained cellular viability, enhanced matrix deposition, and capillary tube formation in HUVECs under toxic oxidative stress. In addition, we demonstrated under the same conditions that these coatings upregulated ang-1, VEGFA, and antioxidant enzymes Nrf2, SOD1, and CAT. An *in vivo* experiment showed that the plates coated with SiONx and SiONPx, mainly SiONPx2, enhanced angiogenesis and reduced oxidative stress. These findings support the use of fixative implants coated with SiONx and SiONPx formed by Si (58.7 at %), O (14.2 at %), N (26.8 at %) and P (0.27 at %) in bone defect by creating a favorable environment for faster healing rates, and accordingly mitigation of implant loosening and failure. The use of a large skeletally mature animal like pigs, dogs, goats or sheep will provide future clinical relevance and efficacy of these fixative implant coatings for further translational use. Finally, the PECVD manufacturing cost, automation during fabrication, ability to coat all 3D and porous geometries, and relatively rapid manufacturing time make these nanoscale coatings highly viable for potential future clinical use.

3.6. ACKNOWLEDGMENTS

The authors would like to thank Dr. Olumide Aruwajoye, Dr. Suresh Adapala, Dr. Gen Kuroyanagi, Ila Oxendine, Yang Li, Reuel Cornelia, and Richard Banlaygas from the Center for Excellence in Hip Disorders, Texas Scottish Rite Hospital, for their assistance. We would like to thank the Brazilian Federal Government – Coordenacao de Aperfeicoamento de Pessoal de Nivel Superior (CAPES), for sponsoring the first author. We also would like to thank the Fulbright scholarships program and the National Research Centre at Egypt, for sponsoring the second author "Kamal Awad". We want to thank the Center for Nanotechnology and the C2MB at UTA. We would also like to thank the University of Texas STARS award and the National Institutes of Health (Grant Number 1R03DE023872-01, 1R56DE027964-01A1-01, NIH S10OD025230) for their support. We would also like to acknowledge our other lab members Thy Than Vo and Yan Chang for their time and contribution towards this manuscript.

The authors of the manuscript made the following contributions. Felipe A. do Monte and Neelam Ahuja serve as co-first author on the manuscript. Felipe A. do Monte, Neelam Ahuja, and Kamal R. Awad conducted all experiments under the supervision of the remaining authors. Felipe and Neelam act as co-first authors as they contributed equally including completion of experiments and revising the manuscript. Dr. Simon Young and Dr. Harry K.W. Kim provided clinical insight and access to cellular models for conducting studies for craniofacial and orthopaedic studies. Drs. Pranesh Aswath, Marco Brotto, Zui Pan and Venu G. Varanasi are the advisors and principal investigators on the respective grants along with Dr. Young and Dr. Kim that provided added resources and expertise eon the research. Dr. Aswath and Dr. Varanasi provided their patented SiONx and SiONPx coating fabrication method to Felipe Monte, Neelam Ahuja, and Kamal Awad to conduct the studies *in vitro* and *in vivo*. Dr. Brotto provided

molecular biological expertise in biomarker analysis given as figures in this study. Dr. Zui Pan provided expertise on immunofluorescence. All authors contributed to the written of the manuscript and accompanying revision.

3.7. REFERENCES

1. **Vanhegan IS**, **Malik AK**, **Jayakumar P**, **Ul Islam S**, **Haddad FS**. A financial analysis of revision hip arthroplasty. *J Bone Joint Surg Br* 94-B: 619–623, 2012. doi: 10.1302/0301-620X.94B5.27073.
2. **Pietropaoli D**, **Ortu E**, **Severino M**, **Ciarrocchi I**, **Gatto R**, **Monaco A**. Glycation and oxidative stress in the failure of dental implants: a case series. *BMC Res Notes* 6: 296, 2013. doi: 10.1186/1756-0500-6-296.
3. **Lindhe J**, **Meyle J**, **Group D of European Workshop on Periodontology**. Peri-implant diseases: Consensus Report of the Sixth European Workshop on Periodontology. *J Clin Periodontol* 35: 282–5, 2008. doi: 10.1111/j.1600-051X.2008.01283.x.
4. **Szpalski C**, **Barr J**, **Wetterau M**, **Saadeh PB**, **Warren SM**. Cranial bone defects: current and future strategies. *Neurosurg Focus* 29: E8, 2010. doi: 10.3171/2010.9.FOCUS10201.
5. **Liu Z**, **Liu Y**, **Xu Q**, **Peng H**, **Tang Y**, **Yang T**, **Yu Z**, **Cheng G**, **Zhang G**, **Shi R**. Critical role of vascular peroxidase 1 in regulating endothelial nitric oxide synthase Endothelial nitric oxide synthase Nitric oxide Asymmetricdimethylarginine Angiotensin II Oxidative stress. *Redox Biol* 12: 226–232, 2017. doi: 10.1016/j.redox.2017.02.022.
6. **Saran U**, **Piperni SG**, **Chatterjee S**. Role of angiogenesis in bone repair. *Arch Biochem Biophys* 561: 109–117, 2014. doi: 10.1016/j.abb.2014.07.006.
7. **Bock RM**, **McEntire BJ**, **Bal BS**, **Rahaman MN**, **Boffelli M**, **Pezzotti G**. Surface modulation of silicon nitride ceramics for orthopaedic applications. *Acta Biomater* 26: 318–330, 2015. doi: 10.1016/j.actbio.2015.08.014.
8. **Ilyas A**, **Lavrik N V.**, **Kim HKW**, **Aswath PB**, **Varanasi VG**. Enhanced Interfacial

Adhesion and Osteogenesis for Rapid “bone-like” Biomineralization by PECVD-Based Silicon Oxynitride Overlays. *ACS Appl Mater Interfaces* 7: 15368–79, 2015. doi: 10.1021/acsami.5b03319.

9. **Ilyas A**, **Odatsu T**, **Shah A**, **Monte F**, **Kim HKW**, **Kramer P**, **Aswath PB**, **Varanasi VG**. Amorphous Silica: A New Antioxidant Role for Rapid Critical-Sized Bone Defect Healing. *Adv Healthc Mater* 5: 2199–2213, 2016. doi: 10.1002/adhm.201600203.

10. **Awad KR**, **Ahuja N**, **Shah A**, **Tran H**, **Aswath PB**, **Brotto M**, **Varanasi V**. Silicon nitride enhances osteoprogenitor cell growth and differentiation via increased surface energy and formation of amide and nanocrystalline HA for craniofacial reconstruction. *Med DEVICES SENSORS* 2: e10032, 2019. doi: 10.1002/mds3.10032.

11. **Dashnyam K**, **Jin G-Z**, **Kim J-H**, **Perez R**, **Jang J-H**, **Kim H-W**, **JiPromoting angiogenesis with mesoporous microcarriers through a synergistic action of delivered silicon ion and VEGFn G-Z**, **Kim J-H**, **Perez R**, **Jang J-H**, **Kim H-W**. Promoting angiogenesis with mesoporous microcarriers through a synergistic action of delivered silicon ion and VEGF. *Biomaterials* 116: 145–157, 2017. doi: 10.1016/j.biomaterials.2016.11.053.

12. **Camalier CE**, **Yi M**, **Yu L-RR**, **Hood BL**, **Conrads KA**, **Lee YJ**, **Lin Y**, **Garneys LM**, **Bouloux GF**, **Young MR**, **Veenstra TD**, **Stephens RM**, **Colburn NH**, **Conrads TP**, **Beck GRJ**. An integrated understanding of the physiological response to elevated extracellular phosphate. *J Cell Physiol* 228: 1536–1550, 2013. doi: 10.1002/jcp.24312.

13. **Lin Y**, **Mckinnon KE**, **Ha SW**, **Beck GR**. Inorganic phosphate induces cancer cell mediated angiogenesis dependent on forkhead box protein C2 (FOXC2) regulated osteopontin expression. *Mol Carcinog* 54: 926–934, 2015. doi: 10.1002/mc.22153.

14. **Saghiri MA**, **Asatourian A**, **Orangi J**, **Sorenson CM**, **Sheibani N**. Functional role of inorganic trace elements in angiogenesis—Part I: N, Fe, Se, P, Au, and Ca. *Crit Rev Oncol* 96: 129–142, 2015. doi: 10.1016/j.critrevonc.2015.05.010.

15. **Harfouche R**, **Hasséssian HM**, **Guo Y**, **Faivre V**, **Srikant CB**, **Yancopoulos GD**, **Hussain SNA**. Mechanisms Which Mediate the Antiapoptotic Effects of Angiopoietin-1 on Endothelial Cells. .

16. **Abdel-Malak NA**, **Mofarrahi M**, **Mayaki D**, **Khachigian LM**, **Hussain SNA**. Early growth response-1 regulates angiopoietin-1-induced endothelial cell proliferation, migration, and differentiation. *Arterioscler Thromb Vasc Biol* 29: 209–16, 2009. doi: 10.1161/ATVBAHA.108.181073.

17. **Jin Kwak H**, **So J-N**, **Jae Lee S**, **Kim I**, **Young Koh G**. Angiopoietin-1 is an apoptosis survival factor for endothelial cells. *FEBS Lett* 448: 249–253, 1999. doi: 10.1016/S0014-5793(99)00378-6.

18. **Harel S**, **Mayaki D**, **Sanchez V**, **Hussain SNAA**. NOX2, NOX4, and mitochondrial-derived reactive oxygen species contribute to angiopoietin-1 signaling and angiogenic responses in endothelial cells. *Vascul Pharmacol* 92: 22–32, 2017. doi: 10.1016/j.vph.2017.03.002.

19. **Monte F**, **Awad KR**, **Ahuja N**, **Kim H**, **Aswath P**, **Brotto M**, **Varanasi VG**. Amorphous Silicon Oxynitrophosphide Coated Implants Boost Angiogenic Activity of Endothelial Cells. .

20. **Monte F**, **Cebe T**, **Ripperger D**, **Ighani F**, **Kojouharov H V**, **Chen BM**, **Kim HKW**, **Aswath PB**, **Varanasi VG**. Ionic silicon improves endothelial cells' survival under toxic oxidative stress by overexpressing angiogenic markers and antioxidant enzymes. *J Tissue*

Eng Regen Med 12: 2203–2220, 2018. doi: 10.1002/term.2744.

21. **Sui X**, **Xu Z**, **Xie M**, **Pei D**. Resveratrol Inhibits Hydrogen Peroxide-Induced Apoptosis in Endothelial Cells via the Activation of PI3K / Akt by miR-126. .

22. **He B**, **Fu G**, **Du X**, **Chu H**. Halofuginone protects HUVECs from H 2 O 2 -induced injury by modulating VEGF / JNK signaling pathway. 2, [date unknown]. doi: 10.1097/JCMA.0000000000000008.Copyright.

23. **Wu J**, **Lei Z**, **Yu J**. Hypoxia induces autophagy in human vascular endothelial cells in a hypoxia-inducible factor 1-dependent manner. *Mol Med Rep* 11: 2677–2682, 2015. doi: 10.3892/mmr.2014.3093.

24. **Lim YC**, **McGlashan SR**, **Cooling MT**, **Long DS**. Culture and detection of primary cilia in endothelial cell models. *Cilia* 4: 11, 2015. doi: 10.1186/s13630-015-0020-2.

25. **Kocherova I**, **Bryja A**, **Mozdziak P**, **Volponi AA**, **Piotrowska-kempisty H**, **Antosik P**, **Dyszkiewicz-konwi M**. Human Umbilical Vein Endothelial Cells (HUVECs) Co-Culture with Osteogenic Cells : From Molecular Communication to Engineering Prevascularised Bone Grafts. .

26. **Ferreira T**, **Rasband W**. ImageJ User Guide User Guide ImageJ. *Image J user Guid* 1.46r, 2012. doi: 10.1038/nmeth.2019.

27. **Chen Y**, **Yu Q**, **Xu CB**. A convenient method for quantifying collagen fibers in atherosclerotic lesions by imagej software. *Int J Clin Exp Med* 10: 14904–14910, 2017.

28. **Hielscher A**, **Ellis K**, **Qiu C**, **Porterfield J**, **Gerecht S**. Fibronectin deposition participates in extracellular matrix assembly and vascular morphogenesis. *PLoS One* 11: 1–27, 2016. doi: 10.1371/journal.pone.0147600.

29. **Zhu Y**, **Zhang Y-J**, **Liu W-W**, **Shi A-W**, **Gu N**. Salidroside Suppresses HUVECs Cell

Injury Induced by Oxidative Stress through Activating the Nrf2 Signaling Pathway. *Molecules* 21, 2016. doi: 10.3390/molecules21081033.

30. **Wei D-H**, **Deng J-L**, **Shi R-Z**, **Ma L**, **Shen J-M**, **Hoffman R**, **Hu Y-H**, **Wang H**, **Gao J-L**. Epimedin C protects H_2O_2-induced peroxidation injury by enhancing the function of endothelial progenitor HUVEC populations. .

31. **Gao S**, **Li S**, **Li Q**, **Zhang F**, **Sun M**, **Wan Z**, **Wang S**. Protective effects of salvianolic acid B against hydrogen peroxide-induced apoptosis of human umbilical vein endothelial cells and underlying mechanisms. *Int J Mol Med* 44: 457–468, 2019. doi: 10.3892/ijmm.2019.4227.

32. **Reuter S**, **Gupta SC**, **Chaturvedi MM**, **Aggarwal BB**. Oxidative stress, inflammation, and cancer: How are they linked? *Free Radic Biol Med* 49: 1603–1616, 2010. doi: 10.1016/j.freeradbiomed.2010.09.006.

33. **Jia C-H**, **Li M**, **Liu J**, **Zhao L**, **Lin J**, **Lai P-L**, **Zhou X**, **Zhang Y**, **Chen Z-G**, **Li H-Y**, **Liu A-L**, **Yang C-L**, **Gao T-M**, **Jiang Y**, **Bai X-C**. IKK-β mediates hydrogen peroxide induced cell death through p85 S6K1. *Cell Death Differ* 20: 248–58, 2013. doi: 10.1038/cdd.2012.115.

34. **Cui W**, **Leng B**, **Liu W**, **Wang G**. Suppression of Apoptosis in Human Umbilical Vein Endothelial Cells (HUVECs) by Klotho Protein is Associated with Reduced Endoplasmic Reticulum Oxidative Stress and Activation of the PI3K/AKT Pathway. *Med Sci Monit* 24: 8489–8499, 2018. doi: 10.12659/MSM.911202.

35. Clonetics ™ Endothelial Cell System. .

36. **Arnaoutova I**, **Kleinman HK**. In vitro angiogenesis: Endothelial cell tube formation on gelled basement membrane extract. *Nat Protoc* 5: 628–635, 2010. doi:

10.1038/nprot.2010.6.

37. **Keshaw H**, **Forbes A**, **Day RM**. Release of angiogenic growth factors from cells encapsulated in alginate beads with bioactive glass. *Biomaterials* 26: 4171–4179, 2005. doi: 10.1016/j.biomaterials.2004.10.021.

38. **Schmitz JP**, **Hollinger JO**. The critical size defect as an experimental model for craniomandibulofacial nonunions. [Online]. *Clin Orthop Relat Res* : 299–308, 1986. http://www.ncbi.nlm.nih.gov/pubmed/3084153.

39. **Robinson NB**, **Krieger K**, **Khan FM**, **Huffman W**, **Chang M**, **Naik A**, **Yongle R**, **Hameed I**, **Krieger K**, **Girardi LN**, **Gaudino M**. The current state of animal models in research: A review. *Int J Surg* 72: 9–13, 2019. doi: 10.1016/j.ijsu.2019.10.015.

40. **Gomes PS**, **Fernandes MH**. Rodent models in bone-related research: the relevance of calvarial defects in the assessment of bone regeneration strategies. *Lab Anim* 45: 14–24, 2011. doi: 10.1258/la.2010.010085.

41. **McGovern JA**, **Griffin M**, **Hutmacher DW**. Animal models for bone tissue engineering and modelling disease. *Dis Model Mech* 11, 2018. doi: 10.1242/dmm.033084.

42. **Garcia P**, **Histing T**, **Holstein J**, **Klein W**, **Laschke M**, **Matthys R**, **Ignatius A**, **Wildemann B**, **Lienau J**, **Peters A**, **Willie B**, **Duda G**, **Claes L**, **Pohlemann T**, **Menger M**. Rodent animal models of delayed bone healing and non-union formation: a comprehensive review. *Eur Cells Mater* 26: 1–14, 2013. doi: 10.22203/ecm.v026a01.

43. **Cooper GM**, **Mooney MP**, **Gosain AK**, **Campbell PG**, **Losee JE**, **Huard J**. Testing the critical size in calvarial bone defects: revisiting the concept of a critical-size defect. *Plast Reconstr Surg* 125: 1685–1692, 2010. doi: 10.1097/PRS.0b013e3181cb63a3.

44. **Porto GG**, **Vasconcelos BC do E**, **Andrade ES de S**, **Carneiro SC de AS**, **Frota MSM**.

Is a 5 mm rat calvarium defect really critical? *Acta Cir Bras* 27: 757–760, 2012. doi: 10.1590/S0102-86502012001100003.

45. **Lee JY**, **Musgrave D**, **Pelinkovic D**, **Fukushima K**, **Cummins J**, **Usas A**, **Robbins P**, **Fu FH**, **Huard J**. Effect of Bone Morphogenetic Protein-2-Expressing Muscle-Derived Cells on Healing of Critical-Sized Bone Defects in Mice. *J Bone Jt Surgery-American Vol* 83: 1032–1039, 2001. doi: 10.2106/00004623-200107000-00008.

46. **Chatzipetros E**, **Christopoulos P**, **Donta C**, **Tosios KI**, **Tsiambas E**, **Tsiourvas D**, **Kalogirou E-M**, **Tsiklakis K**. Application of nano-hydroxyapatite/chitosan scaffolds on rat calvarial critical-sized defects: A pilot study. *Med Oral Patol Oral Cir Bucal* 23: e625, 2018. doi: 10.4317/MEDORAL.22455.

47. **Akkiraju H**, **Bonor J**, **Nohe A**. An Improved Immunostaining and Imaging Methodology to Determine Cell and Protein Distributions within the Bone Environment. *J Histochem Cytochem Off J Histochem Soc* 64: 168–178, 2016. doi: 10.1369/0022155415626765.

48. **Li H**, **Chang J**. Bioactive silicate materials stimulate angiogenesis in fibroblast and endothelial cell co-culture system through paracrine effect. *Acta Biomater* 9: 6981–6991, 2013. doi: 10.1016/j.actbio.2013.02.014.

49. **Dashnyam K**, **El-Fiqi A**, **Buitrago JO**, **Perez RA**, **Knowles JC**, **Kim H-W**. A mini review focused on the proangiogenic role of silicate ions released from silicon-containing biomaterials. *J Tissue Eng* 8: 204173141770733, 2017. doi: 10.1177/2041731417707339.

50. **Zhai W**, **Lu H**, **Chen L**, **Lin X**, **Huang Y**, **Dai K**, **Naoki K**, **Chen G**, **Chang J**. Silicate bioceramics induce angiogenesis during bone regeneration. *Acta Biomater* 8: 341–349, 2012. doi: 10.1016/j.actbio.2011.09.008.

51. **Chiang HY**, **Korshunov VA**, **Serour A**, **Shi F**, **Sottile J**. Fibronectin is an important

regulator of flow-induced vascular remodeling. *Arterioscler Thromb Vasc Biol* 29: 1074–1079, 2009. doi: 10.1161/ATVBAHA.108.181081.

52. **Kiyonaga H**, **Doi Y**, **Karasaki Y**, **Arashidani K**, **Itoh H**, **Fujimoto S**, **Kiyonaga H**, **Itoh H**, **Doi Y**, **Fujimoto S**, **Karasaki Y**, **Arashidani K**. Expressions of endothelin-1, fibronectin, and interleukin-1$α$ of human umbilical vein endothelial cells under prolonged culture [Online]. *Med Electron Microsc* 34: 41–53, 2001. http://download.springer.com.ezproxy.uta.edu/static/pdf/392/art%253A10.1007%252Fs007950100003.pdf?originUrl=http%3A%2F%2Flink.springer.com%2Farticle%2F10.1007%2Fs007950100003&token2=exp=1490272151%7B~%7Dacl=%2Fstatic%2Fpdf%2F392%2Fart%25253A10.1007%25252F.

53. **Abdel-Malak NA**, **Srikant CB**, **Kristof AS**, **Magder SA**, **Di Battista JA**, **Hussain SNA**. Angiopoietin-1 promotes endothelial cell proliferation and migration through AP-1-dependent autocrine production of interleukin-8. *Blood* 111: 4145–54, 2008. doi: 10.1182/blood-2007-08-110338.

54. **Suzuki T**, **Miyamoto T**, **Fujita N**, **Ninomiya K**, **Iwasaki R**, **Toyama Y**, **Suda T**. Osteoblast-specific Angiopoietin 1 overexpression increases bone mass. .

55. **Park S-H**, **Lee J**, **Kang M-A**, **Moon YJ**, **Wang S Il**, **Kim KM**, **Park B-H**, **Jang KY**, **Kim JR**. Potential of L-thyroxine to differentiate osteoblast-like cells via Angiopoietin1. .

56. **Ferrara N**, **Gerber H-P**, **LeCouter J**. The biology of VEGF and its receptors. *Nat Med* 9: 669–676, 2003. doi: 10.1038/nm0603-669.

57. **Shibuya M**. Vascular endothelial growth factor and its receptor system: physiological functions in angiogenesis and pathological roles in various diseases. *J Biochem* 153: 13–19, 2013. doi: 10.1093/jb/mvs136.

58. **Zhao S**, **Li L**, **Wang H**, **Zhang Y**, **Cheng X**, **Zhou N**, **Rahaman MN**, **Liu Z**, **Huang W**, **Zhang C**. Wound dressings composed of copper-doped borate bioactive glass microfibers stimulate angiogenesis and heal full-thickness skin defects in a rodent model. *Biomaterials* 53: 379–391, 2015. doi: 10.1016/j.biomaterials.2015.02.112.

59. **King SJ**, **Nowak K**, **Suryavanshi N**, **Holt I**, **Shanahan CM**, **Ridley AJ**. Nesprin-1 and nesprin-2 regulate endothelial cell shape and migration. *Cytoskeleton* 71: 423–434, 2014. doi: 10.1002/cm.21182.

60. **Chou MY**, **Kao CT**, **Hung CJ**, **Huang TH**, **Huang SC**, **Shie MY**, **Wu BC**. Role of the P38 pathway in calcium silicate cement-induced cell viability and angiogenesis-related proteins of human dental pulp cell in vitro. *J Endod* 40: 818–824, 2014. doi: 10.1016/j.joen.2013.09.041.

61. **Förstermann U**, **Sessa WC**. Nitric oxide synthases: regulation and function. *Eur Heart J* 33: 829–37, 837a-837d, 2012. doi: 10.1093/eurheartj/ehr304.

62. **Matsunaga T**, **Weihrauch DW**, **Moniz MC**, **Tessmer J**, **Warltier DC**, **Chilian WM**. Angiostatin inhibits coronary angiogenesis during impaired production of nitric oxide. *Circulation* 105: 2185–2191, 2002. doi: 10.1161/01.CIR.0000015856.84385.E9.

63. **Diwan AD**, **Wang MINX**, **Jang D**, **Zhu WEI**, **Murrell GAC**. Nitric Oxide Modulates Fracture Healing. *J Bone Miner Res* 15: 342–351, 2000. doi: 10.1359/jbmr.2000.15.2.342.

64. **Zhu W**, **Diwan a D**, **Lin JH**, **Murrell G a**. Nitric oxide synthase isoforms during fracture healing. *J Bone Miner Res* 16: 535–40, 2001. doi: 10.1359/jbmr.2001.16.3.535.

65. **Kingsmill VJ**, **Gray CM**, **Moles DR**, **Boyde A**. Cortical Vascular Canals in Human Mandible and Other Bones. *J Dent Res* 86: 368–372, 2007. doi: 10.1177/154405910708600413.

66. **Dong Hyun Kim, Seung Jun Kwack, Kyung Sik Yoon JSC& B-M**, **Lee**. 4-Hydroxynonenal: A Superior Oxidative Biomarker Compared to Malondialdehyde and Carbonyl Content Induced by Carbon Tetrachloride in Rats. .

67. **Spickett CM**. The lipid peroxidation product 4-hydroxy-2-nonenal: Advances in chemistry and analysis. *Redox Biol* 1: 145–152, 2013. doi: 10.1016/j.redox.2013.01.007.

68. **Saghiri MA**, **Asatourian A**, **Orangi J**, **Sorenson CM**, **Sheibani N**. Functional role of inorganic trace elements in angiogenesis-Part II: Cr, Si, Zn, Cu, and S. *Crit Rev Oncol Hematol* 96: 143–155, 2015. doi: 10.1016/j.critrevonc.2015.05.011.

69. **Saghiri MA**, **Orangi J**, **Asatourian A**, **Sorenson CM**, **Sheibani N**, **Saghiri MA**. Functional Role of Inorganic Trace Elements in in Angiogenesis Part III: (Ti, Li, Ce, As, Hg, Va, Nb and Pb) HHS Public Access. *Crit Rev Oncol Hematol* 98: 290–301, 2016. doi: 10.1016/j.critrevonc.2015.10.004.

70. **Haro Durand LA**, **Vargas GE**, **Vera-Mesones R**, **Baldi A**, **Zago MP**, **Fanovich MA**, **Boccaccini AR**, **Gorustovich A**. In vitro human umbilical vein endothelial cells response to ionic dissolution products from lithium-containing 45S5 bioactive glass. *Materials (Basel)* 10, 2017. doi: 10.3390/ma10070740.

71. **Day RM**. Bioactive glass stimulates the secretion of angiogenic growth factors and angiogenesis in vitro. *Tissue Eng* 11: 768–777, 2005. doi: 10.1089/ten.2005.11.768.

72. **Chaiwong SS and JSL and SBJ and DHS and LDY and JGH and C**. Wettability Effect of PECVD-SiO x Films on Poly(lactic acid) Induced by Oxygen Plasma on Protein Adsorption and Cell Attachment. *J Phys Conf Ser* 423: 12042, 2013. doi: 10.1088/1742-6596/423/1/012042.

73. **Arima Y**, **Iwata H**. Effect of wettability and surface functional groups on protein

adsorption and cell adhesion using well-defined mixed self-assembled monolayers. *Biomaterials* 28: 3074–3082, 2007. doi: 10.1016/j.biomaterials.2007.03.013.

74. **Mouthuy PA**, **Snelling SJB**, **Dakin SG**, **Milković L**, **Gašparović AČ**, **Carr AJ**, **Žarković N**. Biocompatibility of implantable materials: An oxidative stress viewpoint. *Biomaterials* 109: 55–68, 2016.

75. **Aicher A**, **Heeschen C**, **Mildner-Rihm C**, **Urbich C**, **Ihling C**, **Technau-Ihling K**, **Zeiher AM**, **Dimmeler S**. Essential role of endothelial nitric oxide synthase for mobilization of stem and progenitor cells. *Nat Med* 9: 1370–1376, 2003. doi: 10.1038/nm948.

76. **Gallorini M**, **Petzel C**, **Bolay C**, **Hiller K-A**, **Cataldi A**, **Buchalla W**, **Krifka S**, **Schweikl H**. Activation of the Nrf2-regulated antioxidant cell response inhibits HEMA-induced oxidative stress and supports cell viability. *Biomaterials* 56: 114–128, 2015. doi: 10.1016/j.biomaterials.2015.03.047.

77. **Santos-López JA**, **Garcimartín A**, **Merino P**, **López-Oliva ME**, **Bastida S**, **Benedí J**, **Sánchez-Muniz FJ**. Effects of Silicon vs. Hydroxytyrosol-Enriched Restructured Pork on Liver Oxidation Status of Aged Rats Fed High-Saturated/High-Cholesterol Diets. *PLoS One* 11: e0147469, 2016. doi: 10.1371/journal.pone.0147469.

78. **Desideri A**, **Polticelli F**, **Falconi M**, **Sette M**, **Ciriolo MR**, **Paci M**, **Rotilio G**. Electrostatic recognition in redox copper proteins: a 1H NMR study of the protonation behavior of His 19 in oxidized and reduced Cu,Zn superoxide dismutase. *Arch Biochem Biophys* 301: 244–250, 1993. doi: 10.1006/abbi.1993.1140.

79. **Fisher CL**, **Hallewell RA**, **Roberts VA**, **Tainer JA**, **Getzoff ED**. Probing the structural basis for enzyme-substrate recognition in Cu,Zn superoxide dismutase. *Free Radic Res*

Commun 12-13 Pt 1: 287–296, 1991.

80. **Shi Y**, **Mowery RA**, **Shaw BF**. Effect of metal loading and subcellular pH on net charge of superoxide dismutase-1. *J Mol Biol* 425: 4388–4404, 2013. doi: 10.1016/j.jmb.2013.07.018.

81. **Hippeli S**, **Elstner EF**. Transition metal ion-catalyzed oxygen activation during pathogenic processes. *FEBS Lett* 443: 1–7, 1999. doi: 10.1016/S0014-5793(98)01665-2.

82. **Brazier MW**, **Wedd AG**, **Collins SJ**. Antioxidant and Metal Chelation-Based Therapies in the Treatment of Prion Disease. *Antioxidants (Basel, Switzerland)* 3: 288–308, 2014. doi: 10.3390/antiox3020288.

83. **Riley PA**. Free Radicals in Biology: Oxidative Stress and the Effects of Ionizing Radiation. *Int J Radiat Biol* 65: 27–33, 1994. doi: 10.1080/09553009414550041.

84. **Ilyas MA**, **Velton E**, **Shah A**, **Monte F**, **Kim HKW**, **Aswath PB**, **Varanasi VG**. Rapid Regeneration of Vascularized Bone by Nanofabricated Amorphous Silicon. *J Biomed Nanotechnol* 15: 1–15, 2019. doi: 10.1166/jbn.2019.2779.

85. **Varanasi VG**, **Ilyas A**, **Velten MF**, **Shah A**, **Lanford WA**, **Aswath PB**. Role of Hydrogen and Nitrogen on the Surface Chemical Structure of Bioactive Amorphous Silicon Oxynitride Films. *J Phys Chem B* 121: 8991–9005, 2017. doi: 10.1021/acs.jpcb.7b05885.

86. **Kurutas EB**. The importance of antioxidants which play the role in cellular response against oxidative/nitrosative stress: current state. *Nutr J* 15: 71, 2016. doi: 10.1186/s12937-016-0186-5.

CHAPTER 4

INCREASING N/O CONCENTRATION IN BACTERIOSTATIC SILICON OXYNITRIDE COATINGS ENHANCES OSTEOGENIC TRANSCRIPTION VIA NRF2 ANTIOXIDANT ACTIVITY

Neelam Ahuja [1], Kamal Awad [1, 2], Marco Brotto [1], Su Yang [3], He Dong [3], Pranesh Aswath [2], Simon Young [4], Venu Varanasi [1 *]

[1] Bone-Muscle Research Center, College of Nursing and Health Innovation, University of Texas at Arlington.

[2] Department of Material Science and Engineering, University of Texas at Arlington.

[3] Department of Chemistry, University of Texas at Arlington.

[4] Department of Oral and Maxillofacial Surgery, University of Texas Health Science Center at Houston

[*] **Corresponding author**

ABSTRACT

Background: Compromised and complicated bone defects often have prolonged and delayed healing due to lack of bioactivity of the fixative device, secondary infections, and associated oxidative stress. Here, we propose amorphous silicon oxynitride (SiONx) as coatings for the fixative devices to improve bioactivity, bacteriostasis, and reduce oxidative stress to heal large bone. We aim to study the effect of increasing the nitrogen to oxygen ratio in the SiONx to fine tune the cellular activity and the antioxidant effect against the oxidative stress conditions. We further propose that SiONx induces the antioxidant activity by the NRF2 pathway.

Methods: Five compositions of SiONx were fabricated as thin film plasma enhanced chemical vapor deposition (PECVD) coatings onto implant surfaces by changing the N_2O flow rate (N/O ratio for gas flow of N_2O = 0 sccm to N_2O = 160 sccm). *In vitro* studies involved human mesenchymal stem cells (MSC) to study the effect of SiONx coatings on osteogenesis with and without toxic oxidative stress conditions (0.2mM H_2O_2 in culture media). Additionally, bacterial growth was studied on SiONx surfaces using Methicillin-Resistant Staphylococcus Aureus (MRSA) colonies. We evaluated the samples for cell proliferation (MTS, Live/Dead assay), osteogenic differentiation, and antioxidant activity (PCR, ELISA, immunohistochemistry). Studies were conducted for 1-7 days, and all studies were repeated to yield n = 9 per group. We performed NRF2 siRNA transfection for the hMSCs (NRF2-KD) to study the antioxidant response to silicon ions.

Results: SiONx implant surfaces showed a >4-fold decrease in bacterial growth vs control. Increasing the N/O ratio in SiONx implants increased the alkaline phosphatase activity >1.5 times and > 2-fold for other osteogenic markers (osteocalcin, RUNX2, and osterix) under normal conditions. Increasing the N/O ratio in SiONx showed increased protective effects and improved

cell viability against the toxic oxidative stress conditions for the MSCs. There was a significant increase in osteocalcin activity compared to the uncoated group along with increased antioxidant activity, under oxidative stress conditions. In NRF2-KD cells, the enhancing effect of Si ions that release from SiONx films was inhibited, thereby, illustrating the role of NRF2 signaling that is involved in Si upregulation of osteogenic activity.

Conclusions: SiONx coatings displayed bacteriostatic properties and enhanced bone healing under conditions of toxic oxidative stress by enhancing antioxidant NRF2 activity that induced ROS reduction and robust osteogenic marker expression leading to rapid bone regeneration. N-doping onto a fixative device/ biomaterial surface can enhance osteogenic differentiation and pro-oxidant reduction via enhanced NRF2 activity. These results indicate the potential for inducing *in vivo* bone regeneration in a challenging oxidative stress environment.

Keywords: silicon oxynitride, reactive oxygen species, plasma-enhanced chemical vapor deposition, antioxidant activity, osteogenic differentiation

4.1. INTRODUCTION

High-energy traumatic bone injuries, infections requiring surgical debridement, and large tumor resections result in large bone defects that are often associated with compromised wound healing resulting from deficient vascularization, hypoxia, wound contamination, or chemoradiotherapy (1, 2). These factors further complicate the defect healing process by the accumulation of reactive oxygen species (ROS) and prolonged inflammation which may not be eliminated by the protective antioxidant mechanisms in the body (3–5). This accumulation of excessive toxic radicals of ROS leads to oxidative stress which increases the osteoclastic activity and disrupts the remodeling process of the bone (4, 6). Prolonged oxidative stress causes damage to the nuclear acids and proteins causing irreparable cellular injury, restricting cell viability, growth, and proliferation. Exogenous or dietary antioxidants have been shown to reduce ROS and increase osteocalcin activity via increased antioxidant activity (3, 7–9) (e.g., nuclear erythroid factor 2 (NRF2), superoxide dismutase (SOD1), and glutathione peroxidase (GPX)). Yet, these exogenous approaches are unable to overcome the challenge of spontaneous healing and completely regenerating the large bone defects (10). Further, an alternative approach of using local delivery of small molecule antioxidant agents in biomaterials can intrinsically induce rapid cell recruitment, maintain viability, and provide the needed surface to support healing. Thus, antioxidants play a central role to lower ROS while inducing angiogenesis and osteogenesis to spur bone and vascular regeneration needed for healing bone defects.

Current treatment options for large and compromised bone defects use fixative implants such as titanium for functional reconstruction (1), yet these materials lack bioactivity along with antioxidant properties (11, 12) and sometimes lead to microbial biofilm formation causing infection (13). This leads to poor osteointegration, implant loosening, and failure, further

compromising the defect healing (14, 15). Various coating materials used to improve the above problems have failed due to thermal expansion mismatch (16–19), poor coating quality from high-temperature fabrication (>700ºC), reduced bioactivity (20, 21), or reduction of osteogenic activity (22), resulting in immature bone healing and fibrous tissue attachment (23), and poor long-term stability (24). New biomaterials or coatings on already existing biomaterials/ fixative materials that can precisely target antioxidant mechanisms to the wound healing environment are vitally needed for volumetric bone repair.

Our previous studies have shown that SiONx coatings induce antioxidant activity that reduces ROS and inflammation resulting in early bone tissue regeneration (25, 26). Also, silica (SiO_2) based nanoparticles/surface modifications have been studied widely for their antibacterial properties (27). SiONx is an amorphous material with varying levels of tetrahedral and trigonal chemical bond structure depending on the N/O atom ratio within the films. This ratio is controlled by the formation of the material from source gases NH_3 and N_2O, respectively, under a reductive ionized gas environment (28). This is advantageous as the coating thickness, atom ratio, and interfacial formation onto a biomedical device are under our control. Further, these materials can be fabricated at relatively low temperature (< 400ºC), thus, thermal expansion mismatch between the implant substrate and coating layers are markedly reduced and the film can be formed relatively quickly (within 1 hour) so that these factors are not an added burden to the "made-to-order" or "patient defect tailored" manufacturing process. The SiONx nanolayered coatings on the biomedical device will lead to a targeted delivery of the antibacterial as well as the antioxidant properties at the defect/injury site. Hence, we aim to study SiONx surface and Si ion release effect on bacterial growth as well as MSCs proliferation and differentiation *in vitro* with and without oxidative stress conditions. To achieve our aim, we use increasing nitrogen to

oxygen atom ratio (N/O) in the Si-O-N composition as the independent variable. We will use the atom ratio which essentially describes the solid-state substitution of O for N as it is added into the material. The N/O ratio is dictated by the NH_3/ N_2O gas flow in PECVD. The N/O ratio affects the local surface dipole that plays a role in the oxidative state (or valence state) of the surface. Subsequently, cells exposed to these surfaces with differing oxidative states can have differences in viability and proliferation due to the ability of the surface to potentially affect how the cell interacts with its local environment.

Here, we study the effect of increasing nitrogen (N) dose in SiONx surface coatings on bacteriostatic capacity, antioxidant activity, ROS, and osteogenesis. We aim to study this effect to maximize the antioxidant activity for maximal oxidative stress reduction. We further propose that SiONx induces antioxidant activity and reduces oxidative stresses through the NRF2 pathway. It has been established in the literature that NRF2 is a key transcriptional factor that is responsible for activating an antioxidant response reaction against the oxidative stresses (29–31). NRF2 can be promoted by a traumatic injury or fracture which creates an oxidative stress response and regulates the bone healing rates. We will uncover the role of NRF2 signaling pathway in the SiONx antioxidant activity and osteogenesis.

4.2. MATERIALS AND METHODS

4.2.1. Fabrication of the Coatings

Silicon oxynitride (SiONx) thin film coating was fabricated according to our previously published methods (26, 32). Briefly, the surface was prepared for the coatings using standard cleaning procedures using piranha solution (3:1 mixture of sulfuric acid (H_2SO_4, 96%) and hydrogen peroxide (H_2O_2, 30%)) for 10 minutes, and then rinsed in deionized (DI) water for 1

minute. Then, TRION ORION II PECVD/LPECVD system (Trion Technology, Clearwater, FL) was used to deposit a 1000 nm thin film coating of SiONx on silicon wafer. Increasing the N_2O gas flow rate will increase the oxygen incorporation in the coatings over nitrogen content. Thus, five different chemistries of SiONx were fabricated based on changing the N_2O flow rate. The refractive index (N) of the deposited coatings were measured and used to distinguish the coatings in this study. Refractive index values ranged from N = 2 for N_2O = 0 sccm to N = 1.45 for N_2O = 160 sccm. The study groups were as follows: 1) Positive control (Tissue culture plate surface), 2) N = 1.45, 3) N = 1.57, 4) N = 1.65, 5) N = 1.82 and 6) N = 2. The composition of the coatings, exact flow rate and refractive index of each coating is provided in **Table 4.1**.

Table 4.1: Gas Flow Rates, deposition rate, and refractive index for Silicon Oxynitride (Si-O-N) Layers Deposited by PECVD.

Sample	**Gas flow rate (sccm)**				**Deposition Rate (nm/min)**	**Refractive index (N)**
	15% SiH_4/Ar	**N_2O**	**N_2**	**NH_3**		
1	24	160	225	50	62.5	1.45
2	24	155	225	50	59.5	1.57
3	24	16	225	50	44.5	1.65
4	24	3	225	50	41.0	1.82
5	24	0	225	50	36.5	2.0

4.2.2. Bacteriological Analysis

Methicillin-resistant Staphylococcus aureus (MRSA) bacterial assays were conducted to study the bacterial growth on the implant surfaces. For each experiment, a single colony from the inoculation plate was used with Mueller Hinton Broth (MHB) as the medium. A total of 105 colony-forming unit/mL (CFU/mL) were seeded onto the material surface with an inoculation

loop and the samples were dried of all liquid and then incubated at 37 °C for 12, 24, or 48 hrs. Live/dead bacteria assay kit was used to stain the bacteria on the surfaces for 15 min at room temperature, washed with PBS and imaged under EVOS M5000 Imaging System. ImageJ software was used to further analyze the results.

4.2.3. *In Vitro* Studies

Human bone marrow mesenchymal stem cells (MSCs) were obtained from Lonza (Lonza Walkersville Inc., MD, USA). All cells were authenticated, performance assayed, and tested negative for mycoplasma, according to the provider. MSCs (Passage 2-4) were grown according to Lonza protocol in MSCGM BulletKitTM (Lonza, PT-3238 & PT-4105) specific growth medium, at 37°C and 5% CO_2 in a completely humidified incubator. For studying the effect of increasing nitrogen concentration in the coatings, the following groups (n = 4) were used for all in vitro studies, I- Tissue culture plate (TCP), II- SiONx N = 1.45, III- SiONx N = 1.57, IV- SiONx N = 1.65, V- SiONx N = 1.82 and VI- SiONx N = 2. Cells (5000-6000 cells/cm^2) were seeded on TCP as control and SiONx with different refractive indices and allowed to grow for 7 days.

In vitro cytotoxicity studies were performed according to ISO 10993-5 "biological evaluation of medical devices-part 5: tests for *in vitro* cytotoxicity". Cytotoxicity, cell adhesion, viability and proliferation were studied at 1, 4 and 7 days. MTS-CellTiter 96® AQueous One Solution Cell Proliferation Assay, (Promega, Madison, WI, USA) was used for quantitative analysis of cell growth and proliferation and LIVE/DEAD™ Viability/Cytotoxicity Stain Kit (Thermo Fischer Scientific Inc. Waltham, MA, USA) was used for qualitative analysis of cell adhesion and viability on the tested surfaces. Both assays were performed according to manufacturer's instructions and our previously published protocols (33). The colorimetric

absorbance of the MTS assay was determined using a microplate reader (SpectraMax® i3, Molecular Devices, CA) at 490 nm. Live/dead fluorescent images were then taken using a DMi8 inverted Leica microscope (Leica Microsystems Inc., IL, USA), with green fluorescent calcein-AM for live cells and red-fluorescent ethidium homodimer-1 for dead cells.

To induce osteogenic differentiation of the MSCs, hMSC differentiation BulletKit™ – osteogenic was acquired from Lonza, PT-3002 which contains osteogenic differentiation basal medium and hMSC osteogenic SingleQuots™. All groups as above were used for all differentiation studies including TCP as control and SiONx with different refractive indices. Differentiation studies were conducted for 7 days, with media collected for analysis at Day 1, 4, and 7.

To study the effect of SiONx on osteogenic differentiation of MSCs, Alkaline Phosphatase (ALP) Kit (Colorimetric) (Abcam, Waltham, MA) was used to quantify the ALP activity in the collected media for differentiated MSCs after 1, 4 and 7 days.
At 7 days of differentiation, RNA was collected from the differentiated MSCs, purified using miRNAeasy MINI KIT from QIAGEN ® and converted to cDNA using Goscript™ Reverse transcriptase kit from Promega Corporation. Reverse transcription polymerase chain reaction (rtPCR) was performed using TaqMan® Gene Expression Assay with the standard protocol adjusted for 40 cycles. Results were expressed relative to the housekeeping gene GAPDH and compared to the control (TCP), and delta delta Ct method was used for gene expression calculations. Osteogenic markers: RUNX2 (Runt-related transcription factor- 2), BGLAP (Osteocalcin, also OCN), ALP (Alkaline Phosphatase), SP7 (Osterix) were performed.

For detection of OCN by immunohistochemistry, at 7 days of differentiation, the cell culture well plates were washed with PBS, fixed and blocked with 10% goat serum. After

blocking, the primary antibodies (Rabbit polyclonal OCN 1:500) were placed on the slides and incubated overnight at 40°C. Then secondary antibodies Alexa Dye 594 Goat anti Rabbit in 1:200 dilution was introduced and incubated for 1-2 hours, washed twice with PBS, stained with DAPI for 15-20 mins at room temperature and evaluated under DMi8 inverted Leica microscope (Leica Microsystems Inc., IL, USA).

4.2.4. *In Vitro* Analysis Under Oxidative Stress

Hydrogen peroxide (H_2O_2) was used to induce oxidative stress to the cells. H_2O_2 has been used in various *in vitro* studies as a major product of oxidative stress, mainly produced by swift conversion from superoxide. A preliminary study was conducted using different H_2O_2 concentrations ranging from 0-1mM to determine the optimal amount of H_2O_2 to mimic an oxidative stress environment deleterious for the cells. The stock solution was acquired from Sigma-Aldrich 30% w/w of H_2O_2 with a stabilizer. Based on our study, we determined 0.2mM concentration of H_2O_2 to be deleterious for the MSCs.

All cell culture studies stated above including the cell viability and proliferation (MTS and Live/Dead assay) along with differentiation studies (ALP assay, PCR, IHC) were repeated under oxidative stress conditions by introducing 0.2mM of H_2O_2 to the cell culture environment. Additionally, antioxidant markers: nuclear factor erythroid 2-related factor 2 (NRF2) and KEAP1 were performed for the oxidative stress study.

4.2.5. *In Vitro* Knockdown Study

We acquired human NRF2 siRNA from Santa Cruz Biotechnology, Inc (SC-37030) to knockdown NRF2 (NRF2-KD) in the MSCs. We followed the manufacturer's protocol to perform NRF2 siRNA transfection. We seeded the MSCs in a 6-well plate as mentioned above and incubated until the cells are 60-80% confluent. We prepared the transfection solutions-

Solution A: For each transfection, 6ul siRNA duplex into 100 µl siRNA Transfection Medium (sc-36868) and Solution B: For each transfection, 6 µl of siRNA Transfection Reagent (sc-29528) into 100 µl siRNA Transfection Medium (sc-36868). Solution A and Solution B were mixed gently, and the mixture was incubated for 15-30 mins at room temperature. The solution was then mixed with 0.8ml of siRNA Transfection Medium to the Transfection solution made above (A+B). We washed the seeded cells twice and then incubated at 37°C with the siRNA Transfection Reagent for 6-7 hours. After transfection, the reagent was removed, replaced with normal growth medium, and allowed to grow for 4 days. The cells were collected for PCR analysis. Along with the siRNA transfection, we also performed an internal control for the siRNA transfection which included a scrambled sequence that will not lead to the specific degradation of any known cellular mRNA.

4.2.6. Statistical Methods, Data Analysis and Reporting

The results were presented in box plots showing the mean, standard deviation and significance levels. One-way ANOVA (Tukey's Pairwise) was used to compare means for more than two groups at a significance level $p < 0.05$. ImageJ was used for image analysis. OriginPro 2017, Past3 and Microsoft Excel 2016 Software were used for graphics and calculations.

4.3. RESULTS

4.3.1. Bacteriostatic Effect:

We studied the bacterial growth and adherence of MRSA on the various SiONx chemistries compared to the titanium surface (control). **Figures 4.1** presents the quantitative analysis of the live bacteria of MRSA on SiONx coated surfaces compared to titanium after 12, 24, and 48 hours calculated by ImageJ software. All SiONx coated samples presented a

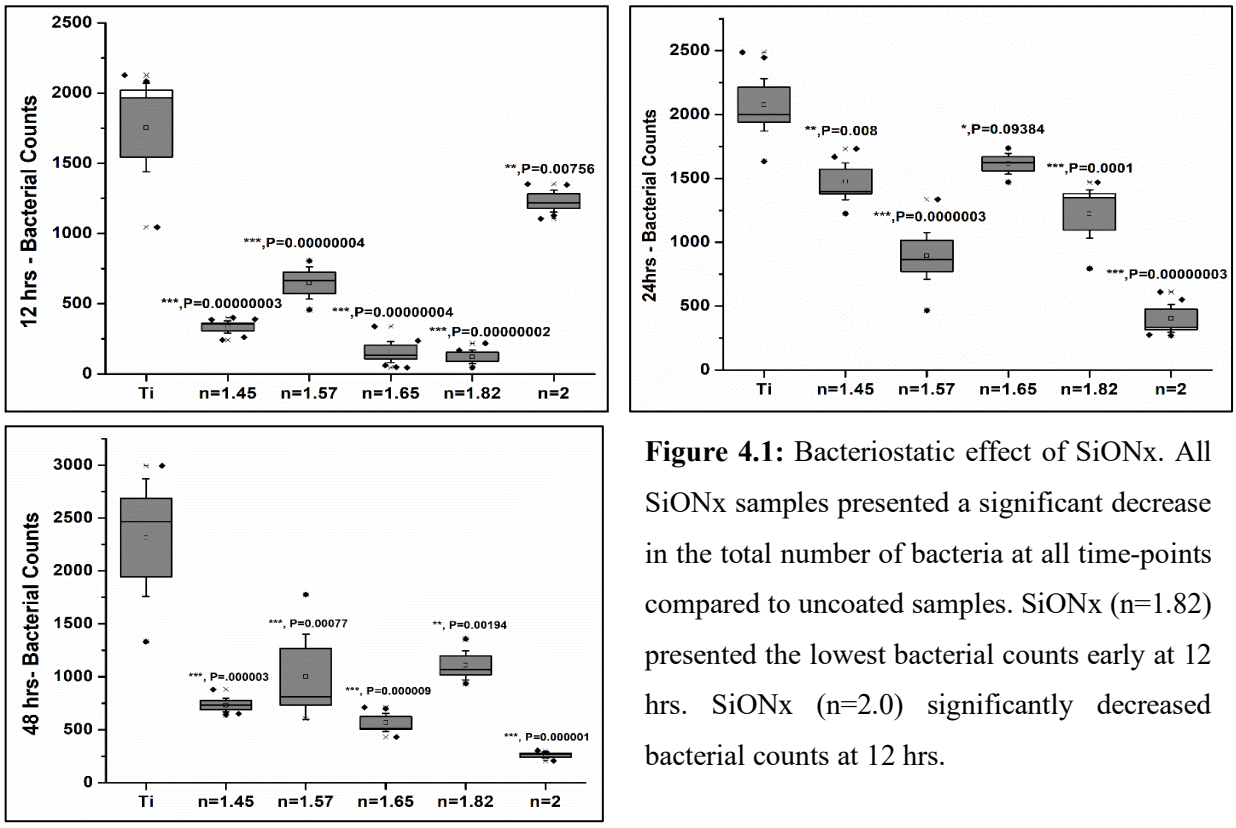

Figure 4.1: Bacteriostatic effect of SiONx. All SiONx samples presented a significant decrease in the total number of bacteria at all time-points compared to uncoated samples. SiONx (n=1.82) presented the lowest bacterial counts early at 12 hrs. SiONx (n=2.0) significantly decreased bacterial counts at 12 hrs.

significant decrease in cell viability and proliferation, seen with decrease in the green stain (live bacteria) and increase in red stain (dead bacteria) shown in **Figure 4.2** at 48 hours (Supplemental Figure. 4.8.1 and 4.8.2 represents bacterial Live/Dead stain at 12 and 24 hours, respectively). High N/O ratio SiONx (N = 2.0) surface presented a significant decrease in bacterial counts at 12 hours and the lowest bacterial counts amongst all SiONx groups after 24 and 48 hours. This suggests bacteriostatic effect on the SiONx coated surfaces inhibiting the bacterial growth and proliferation compared to titanium.

4.3.2. Cell Viability and Proliferation Under Normal Conditions

We studied the cell viability, growth and proliferation of the MSCs on the various SiONx chemistries to evaluate the effect of increasing nitrogen content relative to oxygen while keeping silicon content fixed in the coatings. We performed MTT assay for quantitative analysis along with qualitative Live/Dead fluorescent (Calcein AM and Ethidium homodimer) at 1, 4 and 7

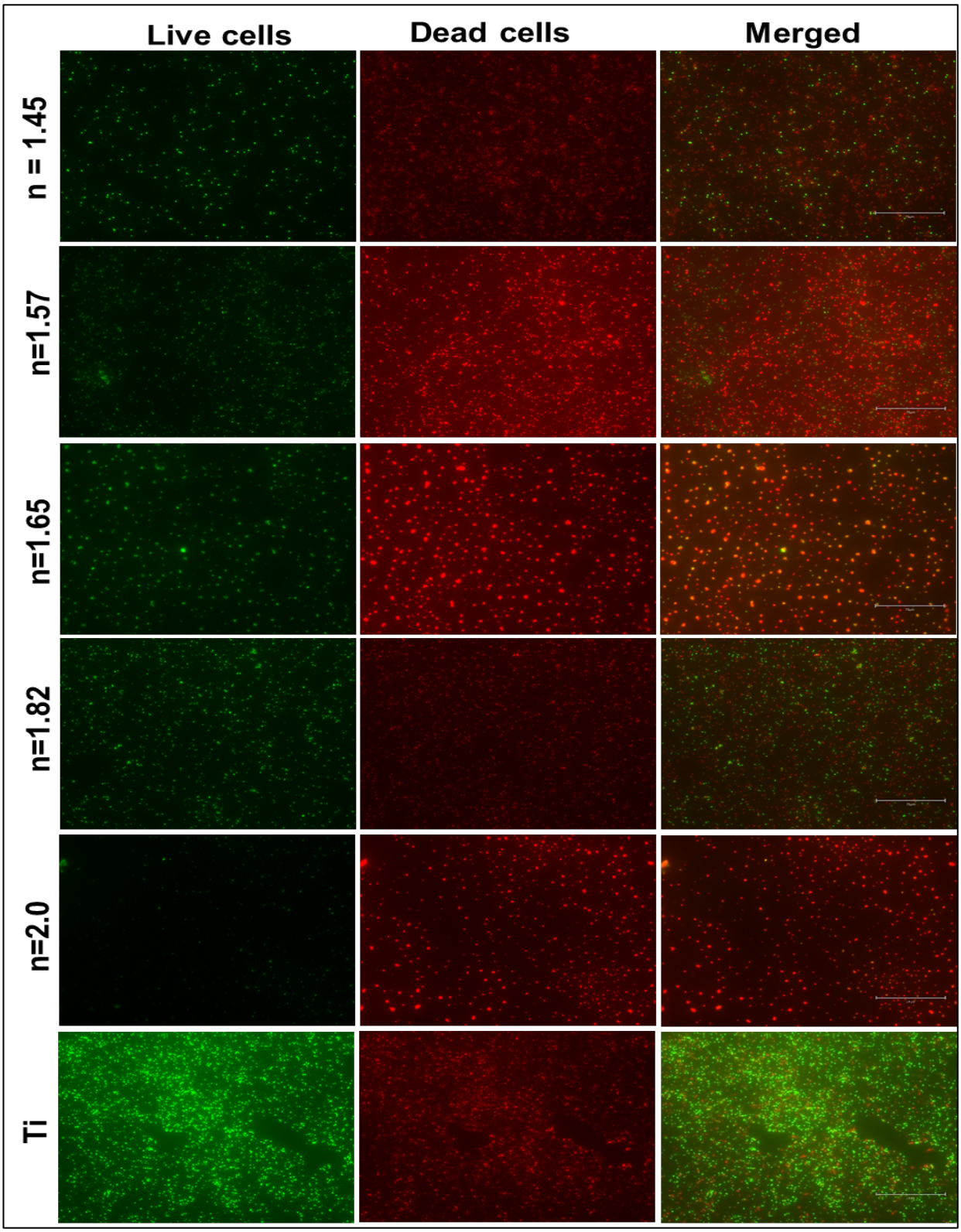

Figure 4.2: Bacteriostatic effect of SiONx coatings. Fluorescence images show the live (green) and dead bacteria (red) on the different SiONx surfaces compared to Ti implants after 48 hours.

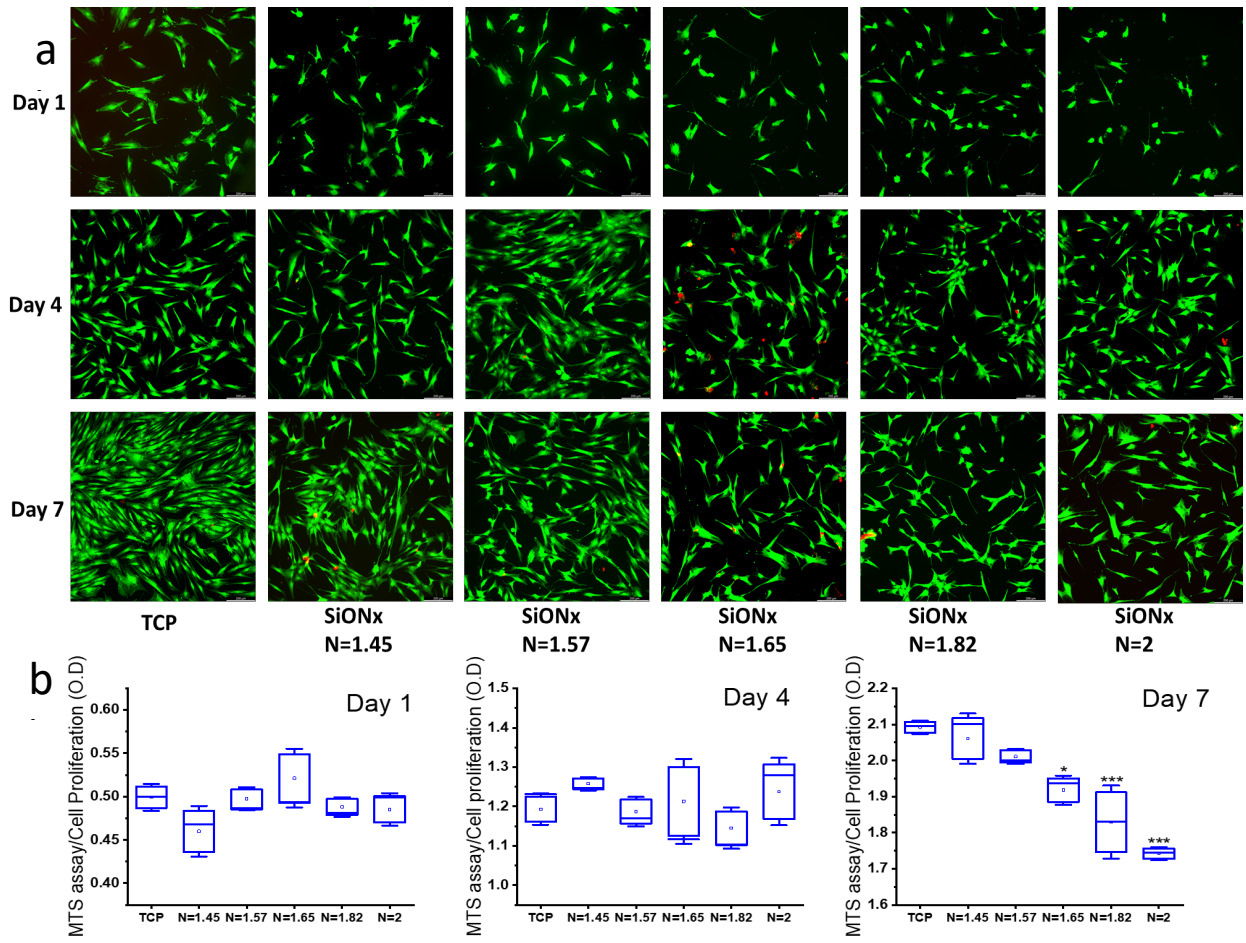

Figure 4.3. Cell Viability and Proliferation assay evaluated by (a) fluorescent Live (Calcein AM) (green stain) and Dead (Ethidium homodimer) (red stain) along with quantitative evaluation by (b) MTS assay at Day 1, 4 and 7 of seeding on the various SiONx surface chemistries.

days of seeding on the various SiONx surfaces (**Figure 4.3**). There are no significant differences between the groups along with the positive control (TCP surface) at Day 1 and 4 of cell proliferation under normal conditions suggesting normal growth. However, we see decreasing cellular proliferation in increased N/O ratio surfaces at 7 days, this can be attributed to detachment of the MSCs on the un-patterned base silicon wafer surface.

4.3.3. Osteogenic Differentiation with Increasing N/O Ratio in SiONx Surfaces

We studied the alkaline phosphatase (ALP) activity by ELISA (**Figure 4.4**) using the cell culture supernatant of the seeded MSCs undergoing osteogenic differentiation at 1, 4 and 7 days

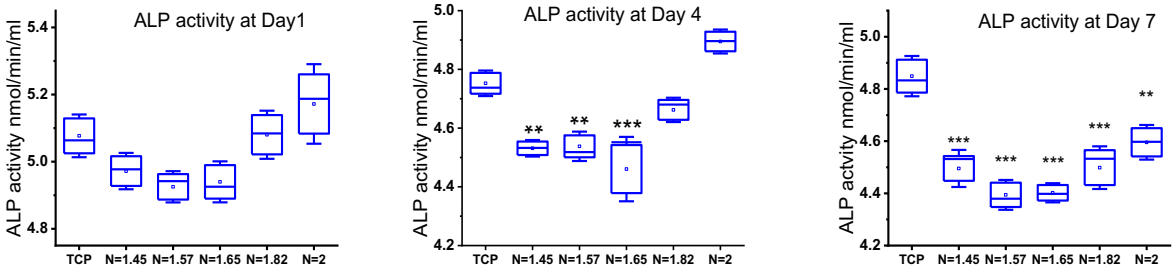

Figure 4.4. Alkaline Phosphatase assay at Day 1, 4 and 7 of osteogenic differentiation in MSCs on the different SiONx chemistries. The ALP activity is not significantly different in SiONx N= 1.82 and N=2 when compared to control at Day 1 and 4.

on various SiONx chemistries. The ALP activity is not significantly different in SiONx N = 1.82 and N = 2 when compared to control (TCP) at Day 1 and 4. At Day 7, there is significantly less ALP activity in the media supernatant of the SiONx samples as compared to the control, this can be due to the decrease in the cellular numbers as seen above. However, there is a significant

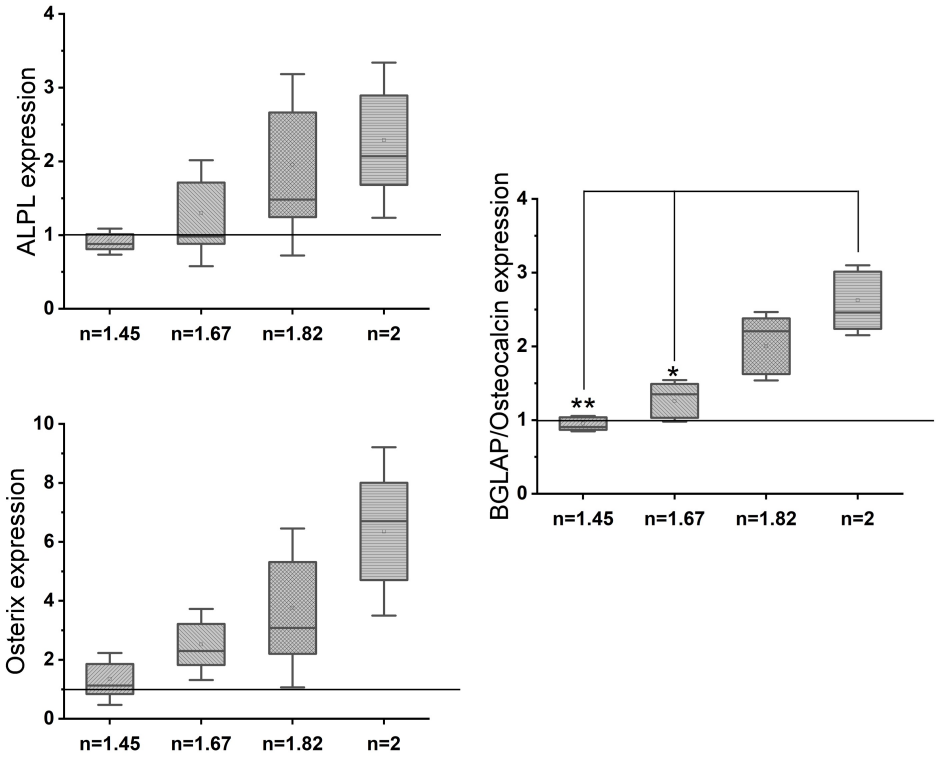

Figure 4.5. Gene expression analysis (rt-PCR) shows significant upregulation of osteogenic markers in SiONx as compared to baseline control. The increase in the N/O ratio increases the osteogenic marker expression.

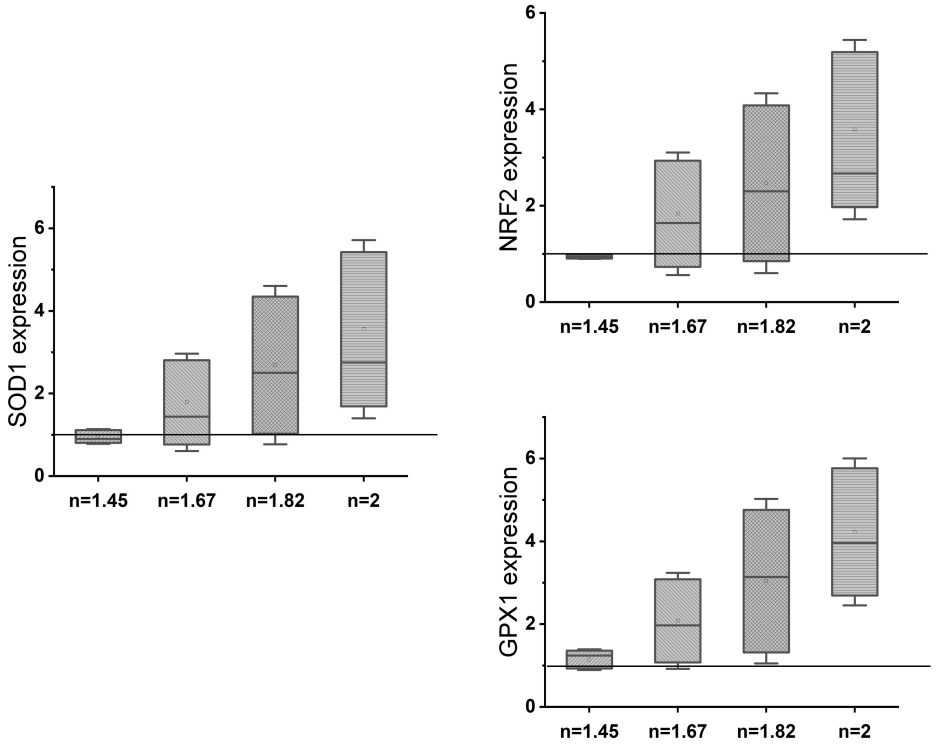

Figure 4.6. Gene expression analysis (rt-PCR) shows an upregulation of antioxidant markers in SiONx as compared to baseline control. The increase in the N/O ratio increases the antioxidant marker expression.

increase in ALP activity as the SiONx nitrogen content is increased relative to oxygen at Day 7 (with maximum activity shown in N = 2 SiONx group).

Gene expression analysis (rt-PCR) (**Figure 4.5**) shows there is an upregulation of osteogenic markers (Osteocalcin, ALPL and Osterix) with the increasing N/O ratio in the SiONx as compared to the control. There is >2-3X upregulation of osteogenic markers in SiONx N= 1.82 and N = 2 as compared to control and the other SiONx chemistries. We also see a similar upregulation of the antioxidant markers (**Figure 4.6**) (SOD1, NRF2 and GPX1) with increasing the N/O ratio in the SiONx as compared to the control. Although there is 2x upregulation in the antioxidant activity, no significant differences were found from the baseline (Except GPX1 for SiONx N=2).

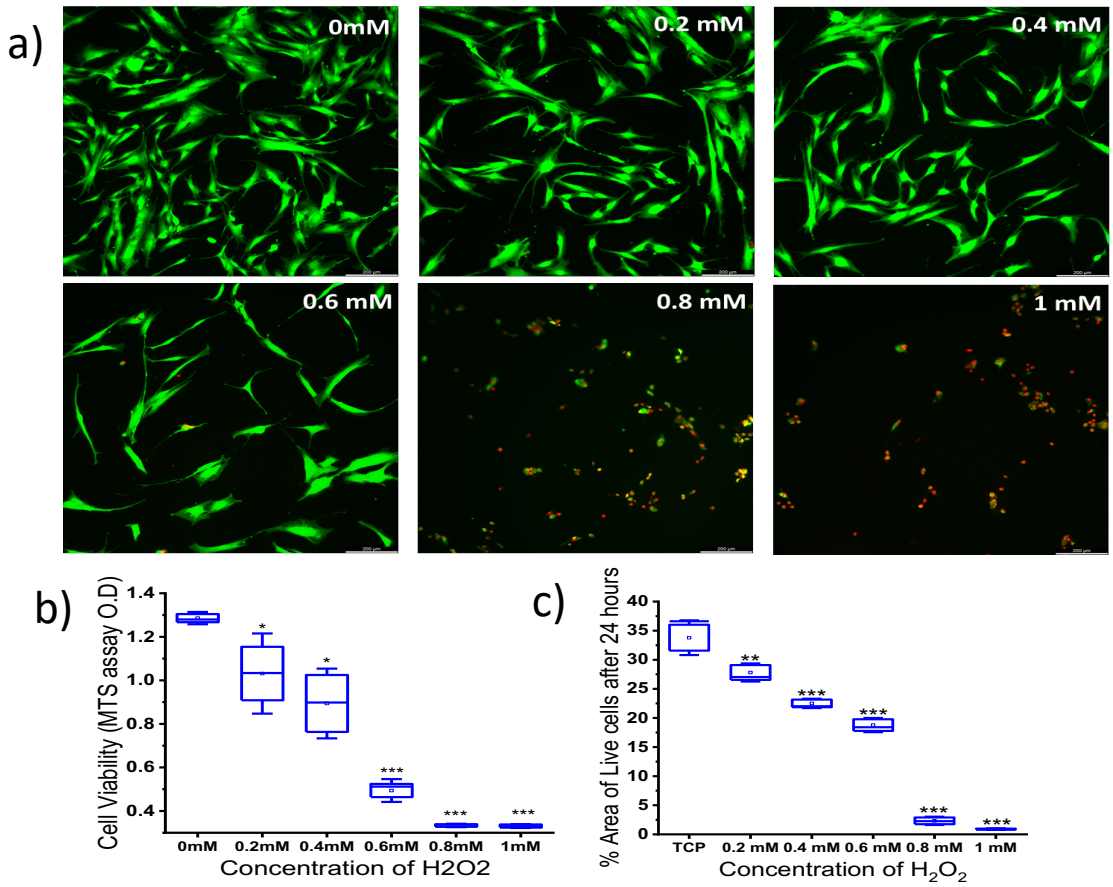

Figure 4.7. Cell viability tested under various concentrations of Hydrogen peroxide by Live/Dead assay (a), MTS assay (b) and quantification of Live cells by Image J (c). We use 0.2mM concentration of Hydrogen peroxide for our further studies.

4.3.4. Determining Minimal H_2O_2 Concentration for Inducing Oxidative Stress in MSCs

To determine the minimal concentration of H_2O_2 to deleterious effect the growth of the MSCs, we tested the cell viability (MTT and Live/Dead assay) with various H_2O_2 concentrations added in the culture media ranging between 0-1mM (specific groups 0mM- no H_2O_2 (control), 0.2mM, 0.4mM, 0.6mM, 0.8mM and 1mM). **Figure 4.7** shows significant lower number of live cells (15-20% less) in even low concentrations of hydrogen peroxide (0.2mM and 0.4mM). There was more than 60% reduction in cell survival at 0.6mM and almost all the cells died at concentrations higher than and at 0.8mM. We removed the oxidative stress medium after 24 hours and survived the cells in normal growth medium for 3 days. We observed that even after the removal of the initial oxidative stress, there was a sustained insult on the cell survival. Hence,

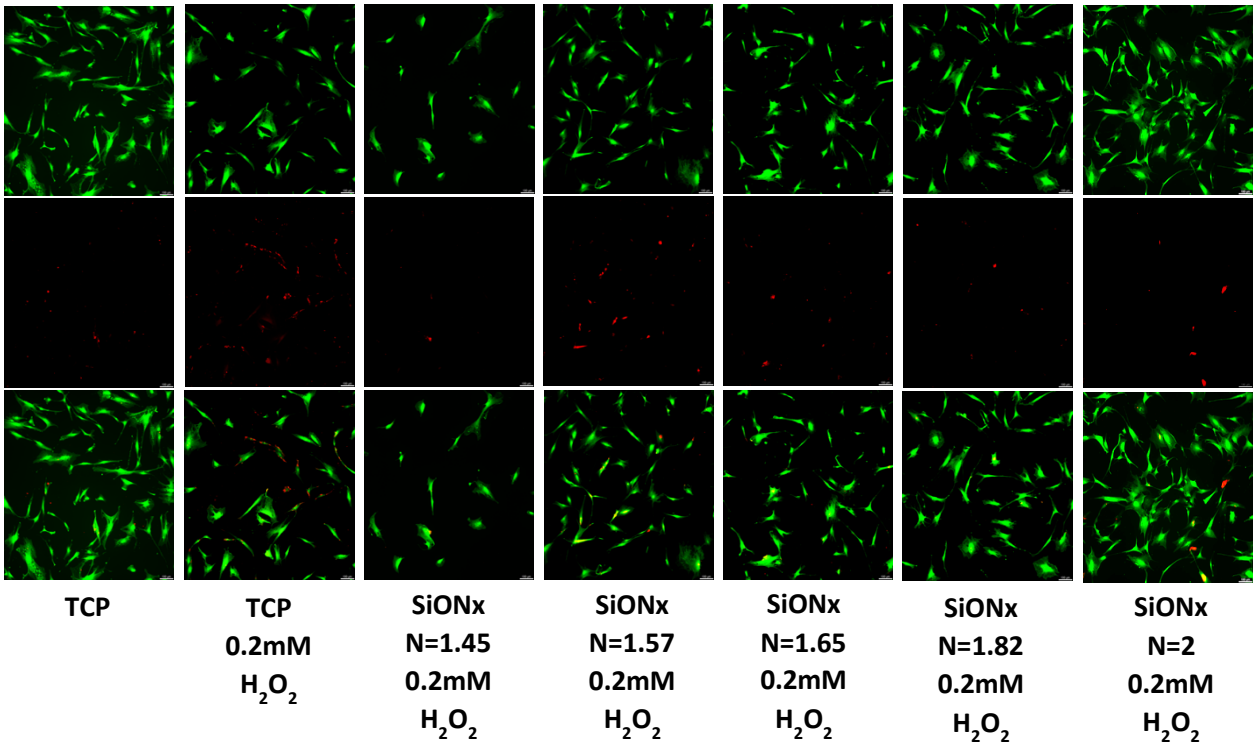

Figure 4.8. Cell Proliferation on various SiONx chemistries under toxic oxidative stress. Green (stained by Calcein AM) represents the live cells and Red (stained by Ethidium homodimer) represents the dead cells

we choose 0.2mM as our final concentration as there was significant effect of the toxic oxidative stress environment and on further growing the cells after the initial insult, we had more than 60% cell survival rate (Supplemental Figure 4.8.3).

4.3.5. Effect of Increasing Nitrogen Concentration in SiONx Chemistry on Cell Proliferation and Differentiation Under Oxidative Stress Conditions

We further analyzed the effect of cell viability and growth by MTT assay and Live/Dead staining on MSCs when seeded on the various SiONx chemistries under toxic oxidative conditions. **Figure 4.8** shows increasing the nitrogen content relative to the oxygen (when silicon is kept constant) has a protective effect on the MSCs against the toxic oxidative stress, showing

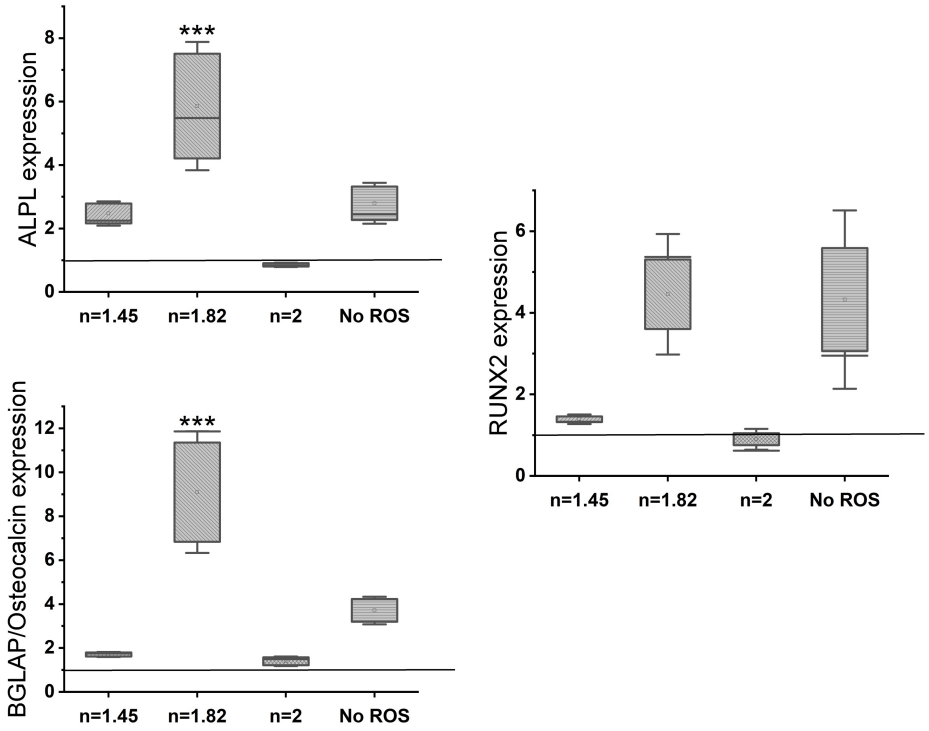

Figure 4.9. Gene expression analysis (rt-PCR) shows a significant upregulation of osteogenic markers in SiONx n= 1.82 as compared to baseline control in an oxidative stress environment. The osteogenic marker expression is not significantly different from the baseline with no oxidative stress environment.

significantly more (2X) cells on N = 2 as compared to N = 1.45 and N = 1.57 and not significantly different from cells with no hydrogen peroxide introduced in the environment. On differentiating the MSCs in an osteogenic medium for 7 days after the initial oxidative stress environment, PCR analysis reveal, there is an increase in the upregulation in RUNX2 (**Figure. 4.9**) in SiONx N=1.82 when compared the baseline with oxidative stress as well as other SiONx chemistries and was comparative to the control with no oxidative stress. There is also a significant upregulation in ALPL and Osteocalcin with SiONx N=1.82 compared to the baseline with/without and other SiONx chemistries (**Figure 4.9**). Fluorescent microscopy also reveals significantly enhanced osteocalcin (OCN) activity (**Figure. 4.10**) on the SiONx surface. Antioxidant markers are significantly overexpressed (SOD1, NRF2 and GPX1) in SiONx N=

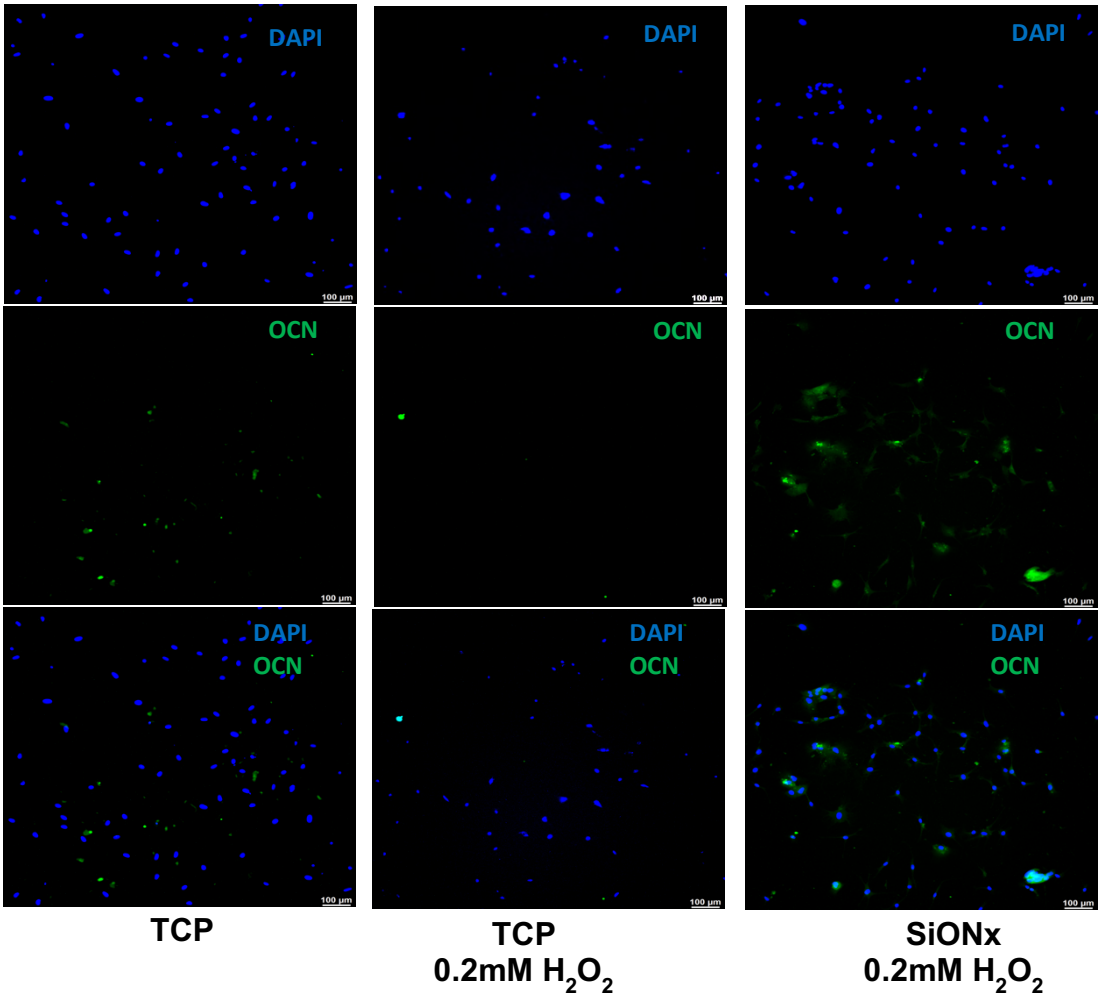

Figure 4.10. IHC staining representing DAPI and Osteocalcin on MSCs after 7 days of osteogenic differentiation. There is overexpression of the osteogenic marker on the SiONx surface when compared to the control.

1.82 which correlated to the overexpression of the oxidative markers in the same groups when compared to the baseline with oxidative stress and other SiONx chemistries as well as the control group with no oxidative stress involved (**Figure 4.11**). Keap1 marker expression shows expression compared to the control with no oxidative stress, however no significant differences are observed within the groups. There was also an increased expression in the antioxidant NRF2 activity (**Figure 4.12**) on the SiONx surface compared to the control.

We observed more than 70% transfection with NRF2 siRNA at 6 hours of incubation. We grew the MSCs in normal growth media for 4 days post transfection and added 0.5mM of Si ions

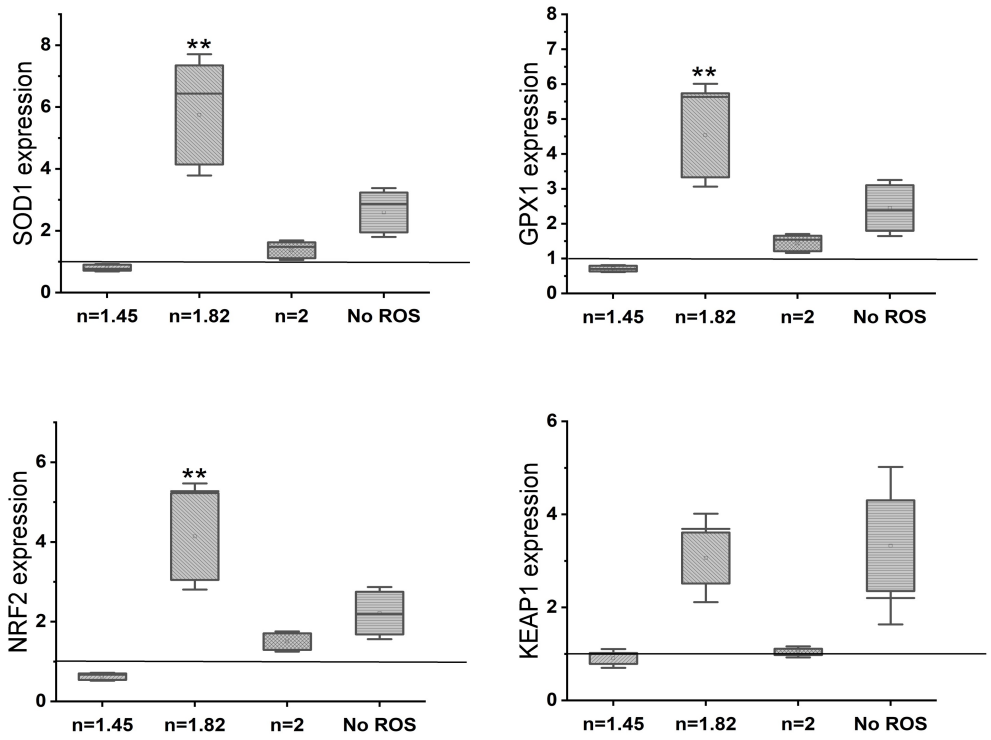

Figure 4.11. Gene expression analysis (rt-PCR) shows a significant upregulation of antioxidant markers in SiONx n= 1.82 as compared to baseline control in an oxidative stress environment.

to study the effect of silicon on NRF2 and antioxidant activity. rtPCR analysis after NRF2 KD reveals that the NRF2 activity remains suppressed even after the addition of Si ions (**Figure 4.13**). Antioxidant expression reveals that with no transfection, there is a 2X increase in the SOD1 and GPX1 expression (**Figure 4.13**). There is a similar effect in the control transfection group (scrambled sequence with no effect on mRNA), although when NRF2 is knockdown there is no increase in the antioxidant expression compared to the baseline (**Figure 4.13**). There are no significant differences between the no transfection group and the NRF2.

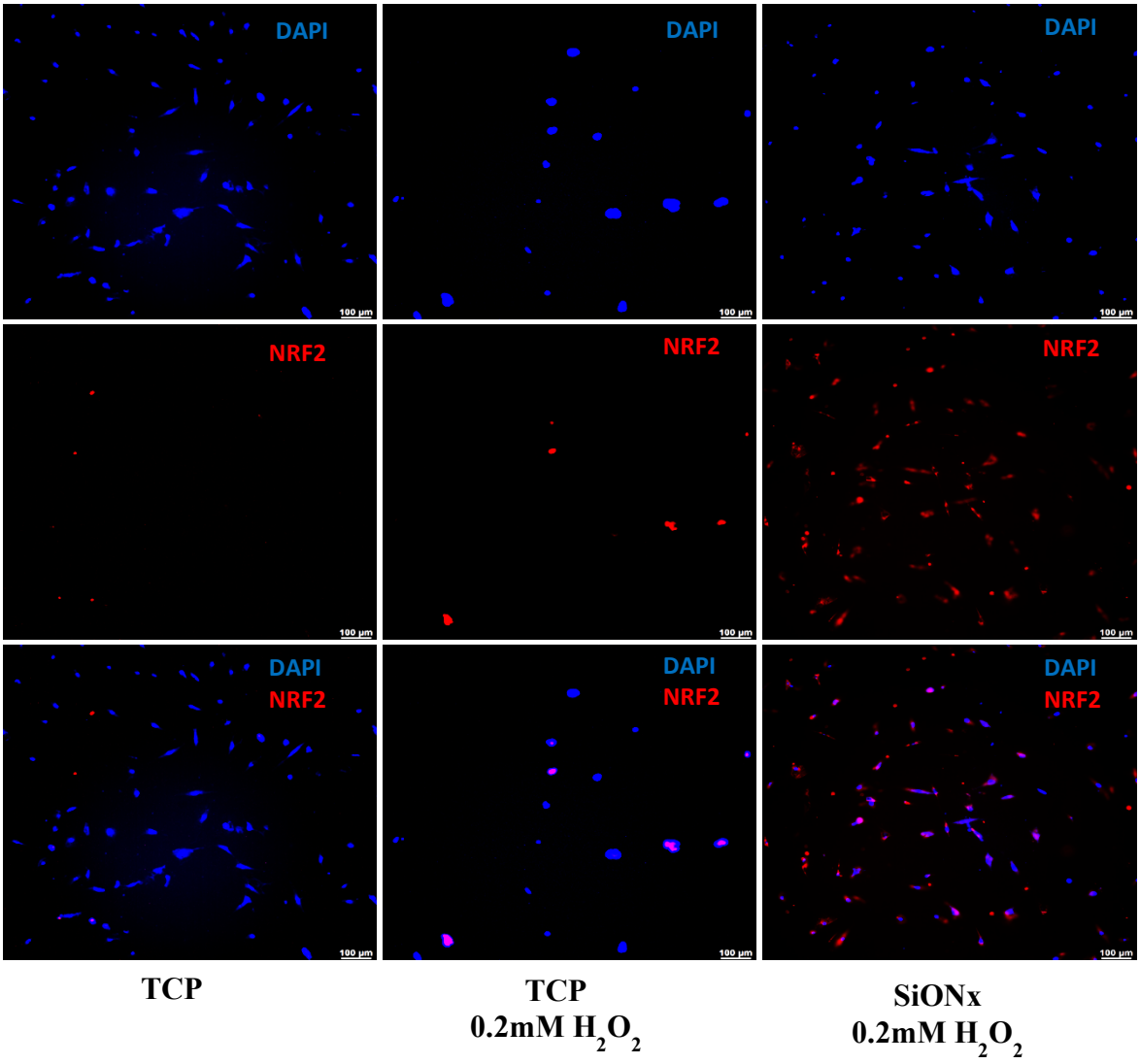

Figure 4.12. IHC staining representing DAPI and NRF2 on MSCs after 7 days of osteogenic differentiation. There is significant increase in the antioxidant NRF2 activity on the SiONx surface when compared to the control.

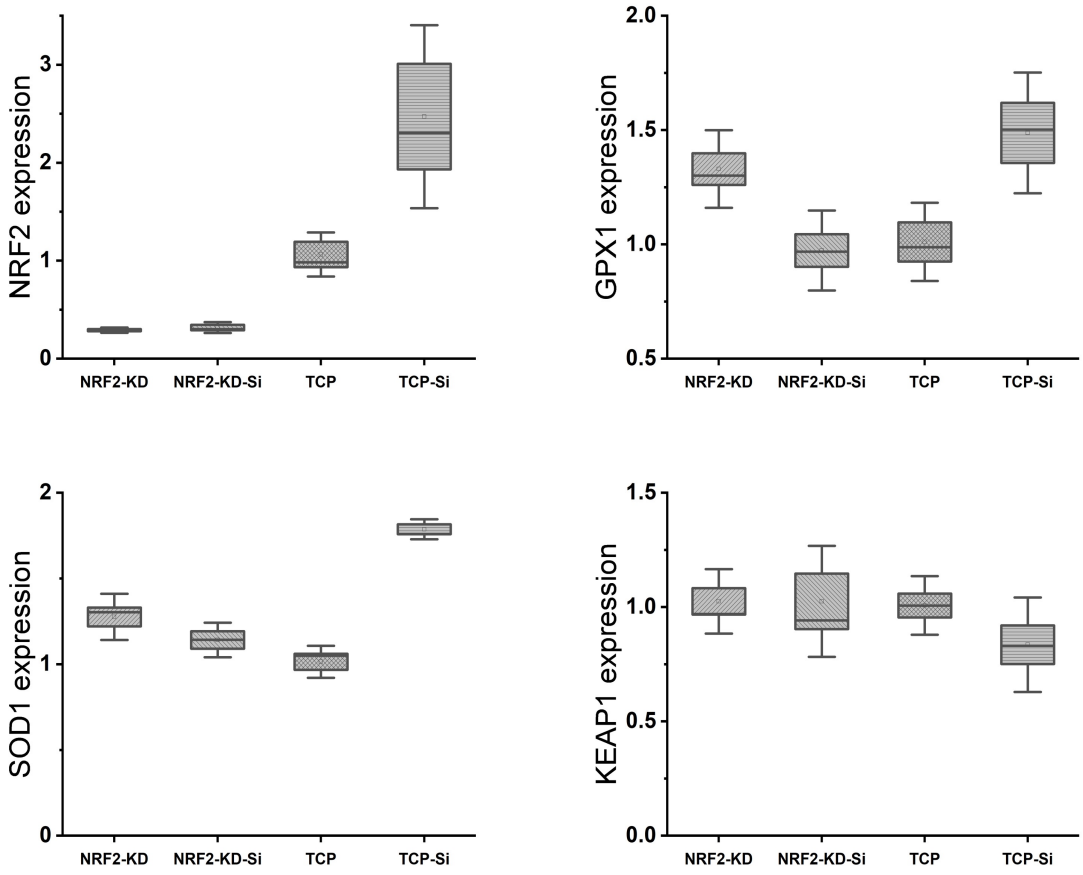

Figure 4.13. The NRF2-KD blocks the Si ion protective effect on the antioxidant expression.

4.4. DISCUSSION

In this study, we investigated the effect of increasing nitrogen dose in SiONx surface coatings on bacterial culture and *in vitro* mesenchymal stem cells' viability, proliferation, and osteogenic capacity. In addition, we also studied the effect of the coatings on MSCs under hydrogen peroxide to induce cellular-level oxidative stress.

Our results indicate that SiONx coatings have a bacteriostatic effect inhibiting bacterial growth and proliferation (**Figure 4.1** and Supplemental Figure 1) on its surface as compared to a regular titanium surface. MRSA is the most common bacterial infections related to bone and joint injuries along with most hospital acquired infections. As these SiONx PECVD based

coatings are amorphous (26), they have an ability to dissolve in the physiological environment and release Si, O, and N ions. The released Si-bonds can attribute to changes in the bacterial structure and also activate some superoxide radicals resulting in bacterial death (27, 34). The increasing nitrogen content in the SiONx chemistry leads to the formation of highly oxidative protonated radicals, which will then result in bacterial inactivation. This can explain the pronounced effect of high nitrogen content SiONx coatings that inhibited the bacterial growth compared to the Ti surface. Thus, the presented data suggest a possible antibacterial/bacteriostatic effect of SiONx coatings compared to the Ti implants that showed a massive bacterial growth on its surface.

Reactive oxygen species (ROS) have been proven to play a role in aging, number of pathological conditions as well as traumatic injuries (35, 36). The role of ROS in bone metabolism is dual, considering its effects under physiological or pathological conditions (4, 37). Under physiological conditions, the production of ROS by osteoclasts helps accelerate the destruction of calcified tissue, thus assisting in bone remodeling. In pathological conditions such as when bone fractures, the radical generation is remarkably high (4, 5, 38). Inhibition of the antioxidant enzymes activities, such as superoxide dismutase and glutathione peroxidase, was found to increase superoxide production by the osteoclasts, leading to a delayed bone remodeling process (5, 38). Therefore, oxidative stress is an important mediator of bone remodeling and healing along with the compensatory antioxidant mechanism which helps restore the physiologic process (8). It can be concluded that increased free radical production overwhelms the natural antioxidants defense mechanisms, subjecting individuals to hyperoxidant stress and thus leading to delayed bone healing. In addition, administration of antioxidants might help in the acceleration of healing of fractured bones to some extent, but does not guarantee a full

physiologic recovery in cases of large and compromised bone defects. Thus, preparing biomaterials that can treat the defect by reducing ROS and stimulating osteogenesis within the bone defect can greatly improve the efficacy of such treatments to repair the lost bone.

Our previous studies have found reduction in the lipid peroxidation on the SiONx coated implants along with increase in the angiogenic activity (25). Silicon oxynitride chemical structure contains a range of bonding that is tetrahedral with low N/O ratio and trigonal with high N/O ratio in general. The RBM is valid for low N/O ratio while the RMM is valid for high N/O. We also showed that the increase in N/O ratio results in a lowering of the energy needed for 2p to 3d electron transitions. The presence of 3d electron orbits is what is needed to stimulate antioxidant activity, which is spin orbit restricted and only become activated by transition metals with readily available 3d electrons (Zn, Cu, Mn, Fe). More fundamentally, the increase in N/O ratio changes the partial charge and surface dipole that affects how the surface will share electrons with attached cellular membranes in which biomolecules depend on the energy state of these surface electrons.

Under normal physiologic in vitro conditions, we observed no significant differences in the various SiONx coated surfaces as compared to a cell culture treated surface as a positive control indicating favorable cellular viability and proliferation on the coated surfaces (**Figure 4.3**). Increasing the N/O ratio had a positive impact on the MSC osteogenic differentiation seen by the increase in ALP activity (**Figure 4.4**) and various other markers (**Figure 4.5** and **4.6**). When oxidative stresses were introduced to the physiologic cell culture environment, we observed significant differences in the viability and proliferation of the mesenchymal stem cells with the increasing N/O ratio in SiONx. Increasing the N/O ratio resulted an increasing protective phenomenon (attributed to the change in charge) towards the mesenchymal stem cells

with no significant differences in cell numbers when compared to cell grown in a normal physiologic environment (**Figure 4.8**). Under oxidative stress conditions, we see an upregulation of the osteogenic marker and antioxidant markers with SiONx N=1.82 group compared to the other groups. This upregulation was similar to the control with no oxidative stress conditions or even significantly higher for osteogenic markers such as ALPL and Osteocalcin. As previously studied by our lab (28), we have seen that the Si-H and N-H bonds increase with the increase in N content for the Si-O-N and the increased nitrogen content reduces the partial charge of constituent elements and changes the bonding structure from random bonding to random mixing. We observe that SiONx with the refractive index of N= 1.82 in our group enhances bioactivity and maximizes the antioxidant effect against the oxidative stresses, exhibiting [Si-Si]-[Si-O]-[Si-N] bonds as compared to SiONx N=2 (which is basically very nitrogen-rich, SiNx).

Studies have shown that NRF2 is a key transcription factor that maintains homeostasis in the bone cells, especially against oxidative stresses (29, 39). These studies indicate the antioxidant pathway activation of NRF2 against detrimental oxidative stress along with improvement in the bone healing of fractures. NRF2 has also known to be of crucial importance in the reduction of degenerative bone diseases (35, 40). In physiological conditions NRF2 is negatively regulated by its cytoplasmic antagonist KEAP1, however ROS can deactivate KEAP1 to prevent NRF2 degradation (25, 40). This leads to translocation of the NRF2 to bind to ARE which encodes antioxidant enzymes and cytoprotective proteins (29). Our previous studies show the expression of several antioxidants including SOD1 and GPX on the endothelial cell lines (25). In this study, we show overexpression of NRF2 under oxidative stress conditions for SiONx (**Figure 4.11** and **4.12**) along with other antioxidant markers. When we block the NRF2

(NRF2-KD), we do not see the upregulation of the antioxidant markers with the silicon ions as before (**Figure 4.13**). This indicates our rationale, SiONx induces the antioxidant properties through the NRF2 pathway, to be true. We think that this overexpression of NRF2 activity and relatively unaffected KEAP1 activity (normalized to the cell number) (**Figure 4.13** and Supplemental Figure. 4.8.4) indicates the activation of the NRF2-ARE pathway to induce antioxidant enzymes and cytoprotective proteins along with enhancing osteogenic capacity in the MSCs.

Complicated bone defects as they are presented clinically can originate from a myriad of situations. The complicating factor in all these situations is the "hidden" aspect of oxidative stress that can manifest as a result from the patient's own biological condition, such as diabetes or aging. Thus, preparing biomaterials that can treat the defect by reducing ROS and stimulating osteogenesis for MSCs within the bone defect can greatly improve the efficacy of such treatments to repair the lost bone.

4.5. CONCLUSION

In conclusion, we observed that SiONx coatings displayed bacteriostatic properties and supported mesenchymal stem cell viability and proliferation. Increasing the nitrogen to oxygen ratio while keeping the silicon content constant did show enhancement of the osteogenic capacity in normal physiologic conditions. There was a protective antioxidant effect by the activation of the NRF2 overexpression of the SiONx coatings with maximum N/O ratio under conditions of toxic oxidative stress that induced ROS reduction and robust osteogenic marker expression leading to enhanced osteogenic capacity.

4.6. ACKNOWLEDGEMENTS

The authors want to acknowledge National Institutes of Health /National Institute of Dental and Craniofacial Research (1R56DE027964-01A1-01), the Osteo Science Foundation Peter L. Geistlich Research Grant, Texas STARs award, Departmental Start-up Funds, University of Texas at Arlington (UTA) College of Nursing and Health Innovation, Arlington, TX, for their generous support for this study. The authors would also like to thank UTA College of Nursing & Health Innovation Bone-Muscle Research Center (UTA-CONHI-BMRC) and Nanotechnology Research Center at Shimadzu center at UTA for their support. Lastly, we want to acknowledge Ms. Laureen Abbo Nono, summer intern student at the Varanasi laboratory, for her contribution towards this study.

4.7. REFERENCES

1. **Dimitriou R**, **Jones E**, **McGonagle D**, **Giannoudis P V**. Bone regeneration: current concepts and future directions. *BMC Med* 9: 66, 2011. doi: 10.1186/1741-7015-9-66.
2. **Nauth A**, **Schemitsch E**, **Norris B**, **Nollin Z**, **Watson JT**. Critical-Size Bone Defects: Is There a Consensus for Diagnosis and Treatment? [Online]. *J Orthop Trauma* 32, 2018. https://journals.lww.com/jorthotrauma/Fulltext/2018/03003/Critical_Size_Bone_Defects__Is_There_a_Consensus.2.aspx.
3. **Sandukji A**, **Al-Sawaf H**, **Mohamadin A**, **Alrashidi Y**, **Sheweita SA**. Oxidative stress and bone markers in plasma of patients with long-bone fixative surgery: role of antioxidants. *Hum Exp Toxicol* 30: 435–442, 2011. doi: 10.1177/0960327110374203.
4. **Banfi G**, **Iorio EL**, **Corsi MM**. Oxidative stress, free radicals and bone remodeling. *Clin Chem Lab Med* 46: 1550–1555, 2008. doi: 10.1515/CCLM.2008.302.
5. **Sheweita SA**, **Khoshhal KI**. Calcium metabolism and oxidative stress in bone fractures: role of antioxidants. *Curr Drug Metab* 8: 519–525, 2007. doi: 10.2174/138920007780866852.
6. **Wang Z**, **Ehnert S**, **Ihle C**, **Schyschka L**, **Pscherer S**, **Nussler NC**, **Braun KF**, **Van Griensven M**, **Wang G**, **Burgkart R**, **Stöckle U**, **Gebhard F**, **Vester H**, **Nussler AK**. Increased oxidative stress response in granulocytes from older patients with a hip fracture may account for slow regeneration. *Oxid Med Cell Longev* 2014: 819847, 2014. doi: 10.1155/2014/819847.
7. **Lean JM**, **Davies JT**, **Fuller K**, **Jagger CJ**, **Kirstein B**, **Partington GA**, **Urry ZL**, **Chambers TJ**. A crucial role for thiol antioxidants in estrogen-deficiency bone loss. *J Clin Invest* 112: 915–923, 2003. doi: 10.1172/JCI18859.

8. **Zhou Q**, **Zhu L**, **Zhang D**, **Li N**, **Li Q**, **Dai P**, **Mao Y**, **Li X**, **Ma J**, **Huang S**. Oxidative Stress-Related Biomarkers in Postmenopausal Osteoporosis: A Systematic Review and Meta-Analyses. *Dis Markers* 2016: 7067984, 2016. doi: 10.1155/2016/7067984.

9. **Mathy-Hartert M**, **Hogge L**, **Sanchez C**, **Deby-Dupont G**, **Crielaard JM**, **Henrotin Y**. Interleukin-1beta and interleukin-6 disturb the antioxidant enzyme system in bovine chondrocytes: a possible explanation for oxidative stress generation. *Osteoarthr Cartil* 16: 756–763, 2008. doi: 10.1016/j.joca.2007.10.009.

10. **Simunovic N**, **Devereaux PJ**, **Bhandari M**. Surgery for hip fractures: Does surgical delay affect outcomes? *Indian J Orthop* 45: 27–32, 2011. doi: 10.4103/0019-5413.73660.

11. **Iwai-Yoshida M**, **Shibata Y**, **Wurihan**, **Suzuki D**, **Fujisawa N**, **Tanimoto Y**, **Kamijo R**, **Maki K**, **Miyazaki T**. Antioxidant and osteogenic properties of anodically oxidized titanium. *J Mech Behav Biomed Mater* 13: 230–236, 2012. doi: 10.1016/j.jmbbm.2012.01.016.

12. **Xue T**, **Attarilar S**, **Liu S**, **Liu J**, **Song X**, **Li L**, **Zhao B**, **Tang Y**. Surface Modification Techniques of Titanium and its Alloys to Functionally Optimize Their Biomedical Properties: Thematic Review. *Front Bioeng Biotechnol* 8: 603072, 2020. doi: 10.3389/fbioe.2020.603072.

13. **Schmidt AH**, **Swiontkowski MF**. Pathophysiology of infections after internal fixation of fractures. *J Am Acad Orthop Surg* 8: 285–291, 2000. doi: 10.5435/00124635-200009000-00002.

14. **Flemming H-C**, **Wingender J**. The biofilm matrix. *Nat Rev Microbiol* 8: 623–633, 2010. doi: 10.1038/nrmicro2415.

15. **Arciola CR**, **Campoccia D**, **Montanaro L**. Implant infections: adhesion, biofilm

formation and immune evasion. *Nat Rev Microbiol* 16: 397–409, 2018. doi: 10.1038/s41579-018-0019-y.

16. **Thomas KA**, **Kay JF**, **Cook SD**, **Jarcho M**. The effect of surface macrotexture and hydroxylapatite coating on the mechanical strengths and histologic profiles of titanium implant materials. *J Biomed Mater Res* 21: 1395–1414, 1987. doi: 10.1002/jbm.820211205.

17. **Bloyer DR**, **Gomez-Vega JM**, **Saiz E**, **Mcnaney JM**, **Cannon RM**, **Tomsia AP**. Fabrication and characterization of a bioactive glass coating on titanium implant alloys. *Acta Mater* 47: 4221–4224, 1999.

18. **Hayashi K**, **Matsuguchi N**, **Uenoyama K**, **Kanemaru T**, **Sugioka Y**. Evaluation of metal implants coated with several types of ceramics as biomaterials. *J Biomed Mater Res* 23: 1247–1259, 1989. doi: 10.1002/jbm.820231103.

19. **Wang BC**, **Lee TM**, **Chang E**, **Yang CY**. The shear strength and the failure mode of plasma-sprayed hydroxyapatite coating to bone: the effect of coating thickness. *J Biomed Mater Res* 27: 1315–1327, 1993. doi: 10.1002/jbm.820271012.

20. **Oku T**, **Suganuma K**, **Wallenberg LR**, **Tomsia AP**, **Gomez-Vega JM**, **Saiz E**. Structural characterization of the metal/glass interface in bioactive glass coatings on Ti-6Al-4V. *J Mater Sci Mater Med* 12: 413–417, 2001. doi: 10.1023/a:1011296903316.

21. **Gomez-Vega JM**, **Saiz E**, **Tomsia AP**, **Marshall GW**, **Marshall SJ**. Bioactive glass coatings with hydroxyapatite and Bioglass particles on Ti-based implants. 1. Processing. *Biomaterials* 21: 105–111, 2000. doi: 10.1016/s0142-9612(99)00131-3.

22. **Saffarian Tousi N**, **Velten MF**, **Bishop TJ**, **Leong KK**, **Barkhordar NS**, **Marshall GW**, **Loomer PM**, **Aswath PB**, **Varanasi VG**. Combinatorial effect of Si4+, Ca2+, and

Mg2+ released from bioactive glasses on osteoblast osteocalcin expression and biomineralization. *Mater Sci Eng C Mater Biol Appl* 33: 2757–2765, 2013. doi: 10.1016/j.msec.2013.02.044.

23. **van Oirschot BAJA**, **Alghamdi HS**, **Närhi TO**, **Anil S**, **Al Farraj Aldosari A**, **van den Beucken JJJP**, **Jansen JA**. In vivo evaluation of bioactive glass-based coatings on dental implants in a dog implantation model. *Clin Oral Implants Res* 25: 21–28, 2014. doi: 10.1111/clr.12060.

24. **Roy M**, **Bandyopadhyay A**, **Bose S**. Induction Plasma Sprayed Nano Hydroxyapatite Coatings on Titanium for Orthopaedic and Dental Implants. *Surf Coat Technol* 205: 2785–2792, 2011. doi: 10.1016/j.surfcoat.2010.10.042.

25. **do Monte FA**, **Ahuja N**, **Awad KR**, **Pan Z**, **Young S**, **Kim HKW**, **Aswath P**, **Brotto M**, **Varanasi VG**. Silicon Oxynitrophosphide Nanoscale-Coating Enhances Antioxidant Marker -Induced Angiogenesis During In Vivo Cranial Bone Defect Healing. *JBMR Plus* n/a: e10425, [date unknown]. doi: https://doi.org/10.1002/jbm4.10425.

26. **Ilyas A**, **Odatsu T**, **Shah A**, **Monte F**, **Kim HKW**, **Kramer P**, **Aswath PB**, **Varanasi VG**. Amorphous Silica: A New Antioxidant Role for Rapid Critical-Sized Bone Defect Healing. *Adv Healthc Mater* 5: 2199–2213, 2016. doi: 10.1002/adhm.201600203.

27. **Tian B**, **Liu Y**. Antibacterial applications and safety issues of silica-based materials: A review. *Int J Appl Ceram Technol* 18: 289–301, 2021. doi: https://doi.org/10.1111/ijac.13641.

28. **Varanasi VG**, **Ilyas A**, **Velten MF**, **Shah A**, **Lanford WA**, **Aswath PB**. Role of Hydrogen and Nitrogen on the Surface Chemical Structure of Bioactive Amorphous Silicon Oxynitride Films. *J Phys Chem B* 121: 8991–9005, 2017. doi:

10.1021/acs.jpcb.7b05885.

29. **Kubo Y**, **Wruck CJ**, **Fragoulis A**, **Drescher W**, **Pape HC**, **Lichte P**, **Fischer H**, **Tohidnezhad M**, **Hildebrand F**, **Pufe T**, **Jahr H**. Role of Nrf2 in Fracture Healing: Clinical Aspects of Oxidative Stress. *Calcif Tissue Int* 105: 341–352, 2019. doi: 10.1007/s00223-019-00576-3.

30. **Taguchi K**, **Motohashi H**, **Yamamoto M**. Molecular mechanisms of the Keap1–Nrf2 pathway in stress response and cancer evolution. *Genes to cells* 16: 123–140, 2011.

31. **Sun Y-X**, **Li L**, **Corry KA**, **Zhang P**, **Yang Y**, **Himes E**, **Mihuti CL**, **Nelson C**, **Dai G**, **Li J**. Deletion of Nrf2 reduces skeletal mechanical properties and decreases load-driven bone formation. *Bone* 74: 1–9, 2015.

32. **Varanasi V**, **Aswath P**, **Maginot M**, **Lavrick N V**. Amorphous silicon oxide, amorphous silicon oxynitride, and amorphous silicon nitride thin films and uses thereof. Google Patents: 2021.

33. **Awad K**, **Ahuja N**, **Fiedler M**, **Peper S**, **Wang Z**, **Aswath P**, **Brotto M**, **Varanasi V**. Ionic Silicon Protects Oxidative Damage and Promotes Skeletal Muscle Cell Regeneration. *Int J Mol Sci* 22, 2021. doi: 10.3390/ijms22020497.

34. **Pezzotti G**, **Bock RM**, **McEntire BJ**, **Jones E**, **Boffelli M**, **Zhu W**, **Baggio G**, **Boschetto F**, **Puppulin L**, **Adachi T**, **Yamamoto T**, **Kanamura N**, **Marunaka Y**, **Bal BS**. Silicon Nitride Bioceramics Induce Chemically Driven Lysis in Porphyromonas gingivalis. *Langmuir* 32: 3024–3035, 2016. doi: 10.1021/acs.langmuir.6b00393.

35. **Reuter S**, **Gupta SC**, **Chaturvedi MM**, **Aggarwal BB**. Oxidative stress, inflammation, and cancer: How are they linked? *Free Radic Biol Med* 49: 1603–1616, 2010. doi: 10.1016/j.freeradbiomed.2010.09.006.

36. **Förstermann U**, **Sessa WC**. Nitric oxide synthases: regulation and function. *Eur Heart J* 33: 829–37, 837a-837d, 2012. doi: 10.1093/eurheartj/ehr304.

37. **Basu S**, **Michaëlsson K**, **Olofsson H**, **Johansson S**, **Melhus H**. Association between Oxidative Stress and Bone Mineral Density. *Biochem Biophys Res Commun* 288: 275–279, 2001. doi: https://doi.org/10.1006/bbrc.2001.5747.

38. **Nielsen F**, **Mikkelsen BB**, **Nielsen JB**, **Andersen HR**, **Grandjean P**. Plasma malondialdehyde as biomarker for oxidative stress: reference interval and effects of life-style factors. *Clin Chem* 43: 1209–1214, 1997.

39. **Lippross S**, **Beckmann R**, **Streubesand N**, **Ayub F**, **Tohidnezhad M**, **Campbell G**, **Kan YW**, **Horst F**, **Sönmez TT**, **Varoga D**, **Lichte P**, **Jahr H**, **Pufe T**, **Wruck CJ**. Nrf2 Deficiency Impairs Fracture Healing in Mice. *Calcif Tissue Int* 95: 349–361, 2014. doi: 10.1007/s00223-014-9900-5.

40. **Sies H**. Hydrogen peroxide as a central redox signaling molecule in physiological oxidative stress: Oxidative eustress ☆. *Redox Biol* 11: 613–619, 2017. doi: 10.1016/j.redox.2016.12.035.

4.8. SUPPLEMENTAL FIGURES

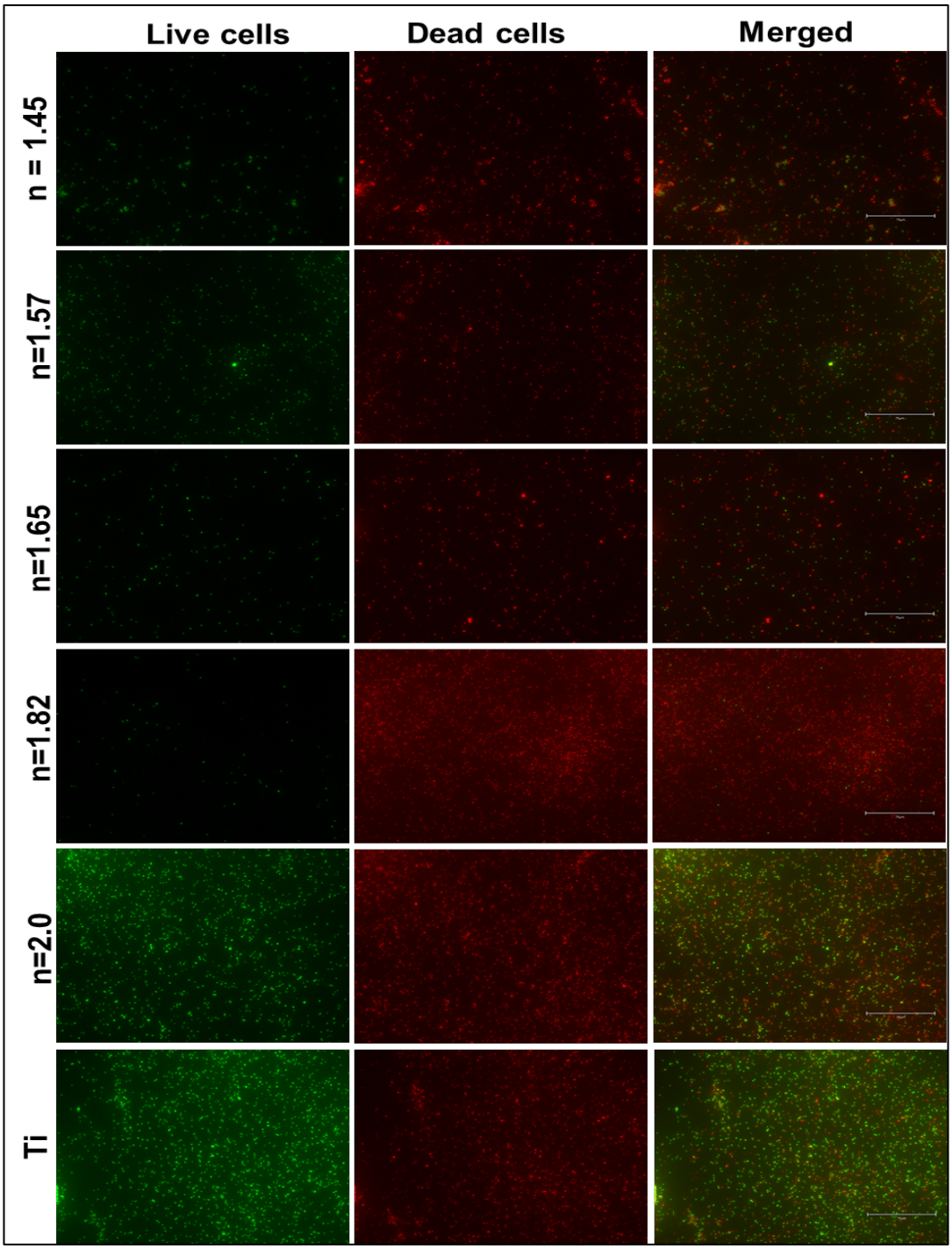

Supplemental Figure 4.8.1: Bacteriostatic effect of SiONx coatings verse Ti implants. Fluorescence images show the live (green) and dead bacteria (red) on the different SiONx surfaces compared to Ti implant after 12 hours.

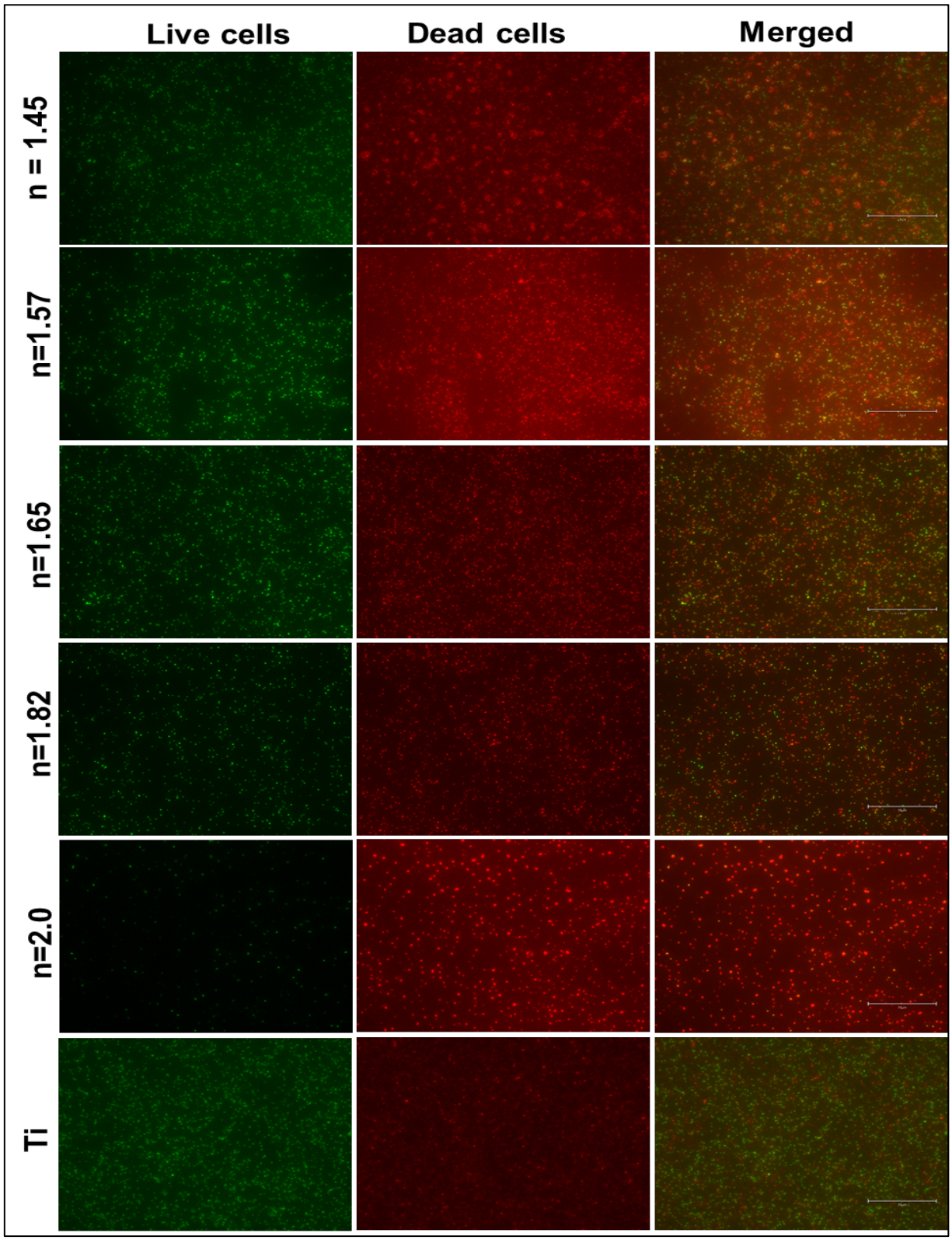

Supplemental Figure 4.8.2: Bacteriostatic effect of SiONx coatings verse Ti implants. Fluorescence images show the live (green) and dead bacteria (red) on the different SiONx surfaces compared to Ti implant after 24 hours.

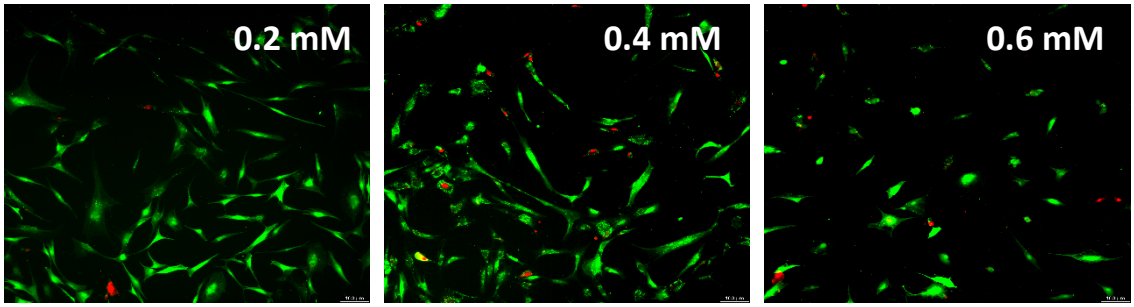

Supplemental Figure 4.8.3. Live/Dead assay performed after 4 days of an initial 24-hour insult using various concentrations of Hydrogen peroxide to study the sustained toxic effects of H_2O_2 on MSCs.

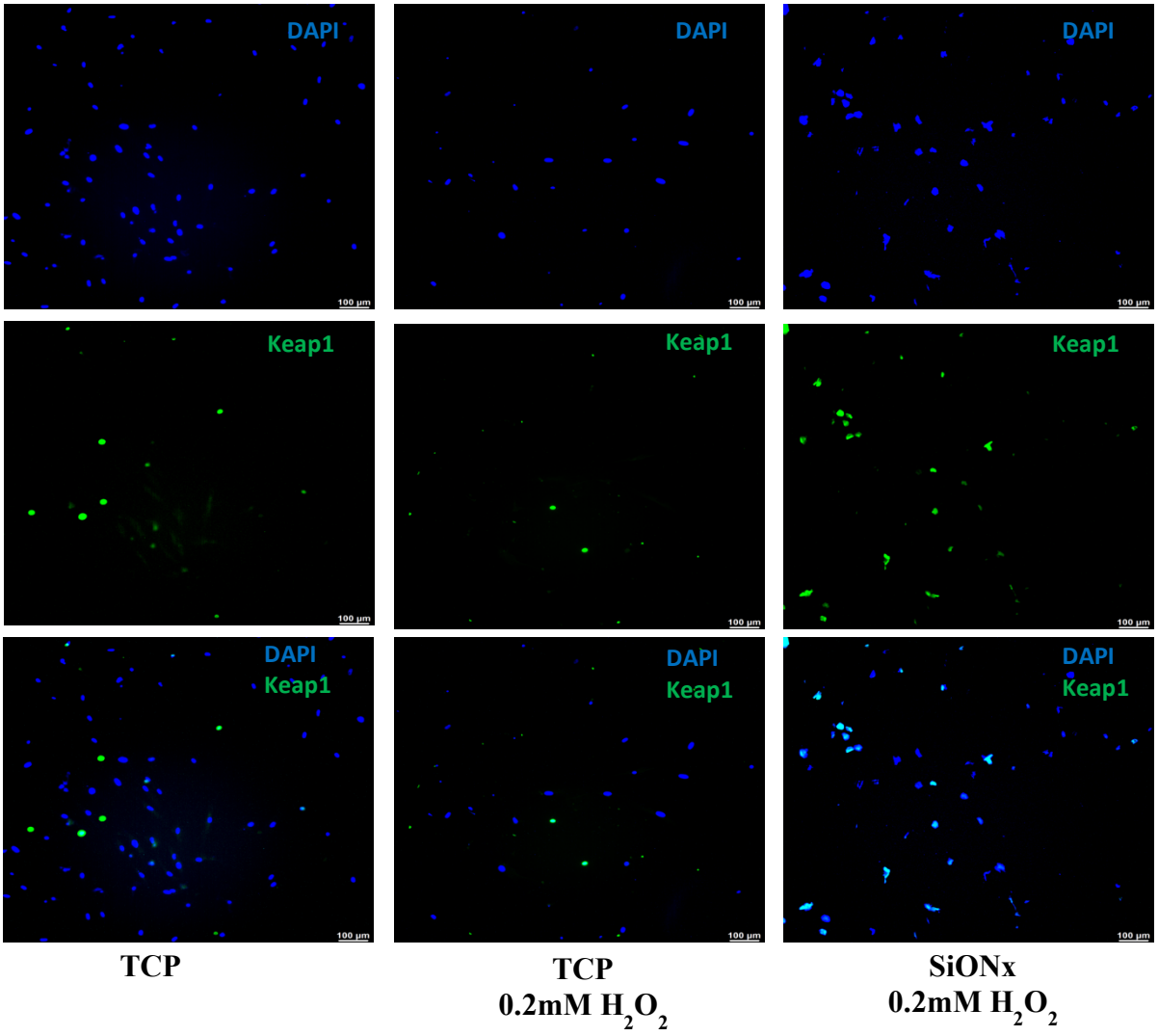

Supplemental Figure 4.8.4. IHC staining representing DAPI and Keap1 on MSCs after 7 days of osteogenic differentiation. There is no significant difference in the Keap1 activity on the SiONx surface when compared to the control.

CHAPTER 5

IN VIVO ANALYSIS OF ANTIOXIDANT SILICON OXYNITRIDE- TITANIUM COATINGS FOR CRANIOMAXILLOFACIAL FIXATIVE DEVICES TO ENHANCE LOCALIZED BONE REGENERATION

Neelam Ahuja [1], Kamal Awad [1, 2], Marco Brotto [1], Pranesh Aswath [2], Simon Young [3], Antonios Mikos [4], Venu Varanasi [1 *]

[1] Bone-Muscle Research Center, College of Nursing and Health Innovation, University of Texas at Arlington.

[2] Department of Material Science and Engineering, University of Texas at Arlington.

[3] Department of Oral and Maxillofacial Surgery, University of Texas Health Science Center at Houston

[4] Department of Bioengineering and Chemical and Biomolecular Engineering, Rice University, Houston

[*] **Corresponding author**

ABSTRACT

Large and morphologically complex bone defects are challenging to heal due to the inability of the defect to spontaneously regenerate. Even with the use of medical devices such as titanium plates and implants, these defects still have a longer than desired healing time. In this study, we use silicon oxynitride coatings to demonstrate their potential to increase healing rates by local stimulation of biomarkers important for rapid bone regeneration. These materials were tested in critical-sized bone defects in rat calvaria and rabbit mandible that simulate large bone defects with challenges to bone regeneration. We compare the SiONx-coated fixative devices to uncoated implants/fixative titanium devices, which is a gold standard for craniofacial and orthopedic applications. In this study, we demonstrated the ability of SiONx coatings to stimulate the healing response of new bone formation in large bone defects and enhanced osteointegration. Results from micro-CT showed elevated amount of newly formed bone vs bare or empty treated defects in both animal models. Histological evaluation showed the presence of antioxidant and osteogenic biomarkers at a level higher than for uncoated group. Silicon Oxynitride coatings reveal the potential to promote rapid bone regeneration via several key antioxidant and osteogenic markers. These results suggest the ability for these coatings to heal large traumatic bone defects.

Keywords: silicon oxynitride, alkaline phosphatase, nuclear erythroid factor 2, reactive oxygen species

5.1. INTRODUCTION

Nearly 178 million people globally undergo a surgical procedure including craniomaxillofacial surgeries to treat bone defects and fractures in a year (1–3). A significant number of these defects are sufficiently large and cannot heal by the body's innate capacity. These defects are termed critical-sized defects (CSDs) as they require planned reconstruction and secondary surgery (4). Due to the various drawbacks and limited availability of autogenous bone grafts, biomedical devices such as titanium (Ti) fixative devices in the form of plates or mesh implants are required to stabilize the defect and maintain the defect contour (4,5). Titanium, due to its excellent physical properties and biocompatibility, has been considered the gold standard in orthopedic and dental implant applications (6,7). Titanium surface spontaneously forms a thin oxide layer when exposed to air, which prevents corrosion and further oxidation (8). However, the Ti surface has limited surface bioactivity. This intrinsic property limits strong bone-implant interfacial bonding limiting long-term bone-implant adhesion and increased potential for implant failure (9,10). Previously, various surface modification techniques have been applied to Ti devices to improve surface biological properties and improved bone-implant adhesion (10). Certain surface modifications such as sandblasting, large grit, and acid-etching treatments enhance implant mechanical fixation due to increased surface area for bony contact (11). However, these modifications increase surface roughness can lead to biofilm accumulation and enhance bacterial growth (12). Other surface modification techniques such as glow discharge, electrolytic plasma, and photocatalytic materials enhance bioactivity without affecting the surface topography or roughness (13). These surface techniques enhanced bioactivity, and antimicrobial properties and are being widely used (13–15). However, these techniques can result in cell cytotoxicity and short term-efficiency.

Large bone injuries cause an accumulation of free radicals in the damaged tissue which increases the generation of reactive oxygen species (ROS) and limit the healing process (16). ROS can manifest as superoxide anion (O_2^-), hydrogen peroxide (H_2O_2), and hydroxyl radical (OH^-). This ROS causes lipid peroxidation, which is highly reactive, causes the most oxidative damage to the cells leading to apoptosis of genomic DNA in osteoblasts and osteoclasts (16–18). Lipid peroxidation can be detected in the serum (increased levels of serum malondialdehyde [MDA]) and is also a measure of osteoclastic activity, which leads to resorption and remodeling in early stages but lead to poor bone quality and delayed healing at later stages (2-3 weeks after the injury) (19). Also, excessive oxidative stresses can also be accompanied by prolonged inflammatory responses which can add to the healing rates (17,18). Metal implant devices are typically surface chemically inert and cannot reduce ROS levels on their own. In this study, we propose the use of a coating, silicon oxynitride, that may have the ability to reduce ROS through the stimulation of antioxidant markers that in turn are involved in osteogenic healing.

Silicon Oxynitride (SiONx) is a commonly used dielectric that has been used in many applications including semiconductors, photovoltaics, and fuel cells used for high current density producing devices. We use a plasma enhanced chemical vapor deposition (PECVD) for fabricating the SiONx amorphous coatings under source gases NH_3 and N_2O, which creates the advantage of ion leaching, control of coating thickness and better interfacial formation (20–22). Further, PECVD coatings are fabricated at relatively low temperature (< 400°C), thus, avoiding the thermal expansion mismatch between the implant substrate and coating layers along with faster and controlled manufacturing process. Finally, these coatings are amorphous in nature and release Si ions (Si^{4+}). The amorphous surface allows for the formation of covalent structures of

hydroxyapatite to form at a rapid rate (within hours) (22, 23) and the Si^{4+} cation has the potential to induce antioxidant responses while also quenching ROS thereby potentially overcoming the challenge to rapid MSC osteogenesis and long-term bone-implant bonding. In this study, we tested our newly developed plasma enhanced chemical vapor deposition (PECVD) coatings as potential surface coatings for Ti implants.

In our prior work, we noted the positive benefits of using these coatings on the formation of vascular tissue (23–25). The formation of the vascular tissue during bone healing is vital for the regeneration process to be sustained. It was found in this work that silicon oxynitride enhanced the expression of key angiogenic makers such as angiopoietin, vascular endothelial growth factor A, and hypoxia-inducing factor 1A (25). This shows promise in inducing the faster regeneration of new bone and that will be investigated in this work.

We also found that the coatings had an effect on reducing ROS through their release of ionic Si, *in vitro* (23). In this study, we will characterize ROS, antioxidant, and osteogenic markers in regenerated bone layers. The goal of this study is to identify key biomarkers of bone regeneration that lead to spontaneous and rapid healing of large bone defects. We use the Sprague Dawley rat cranial model for our sub-critical sized bone defect to study the bone regeneration as these studies cannot be replicated in cell culture and minimize the utilization of larger animal models. We then study the rabbit mandibular critical-sized defect model as it is a more translational model. In this study, our aim is to evaluate antioxidant and osteogenic markers that play a key role in the rapid bone regeneration process as a result of coated and uncoated implant treatment.

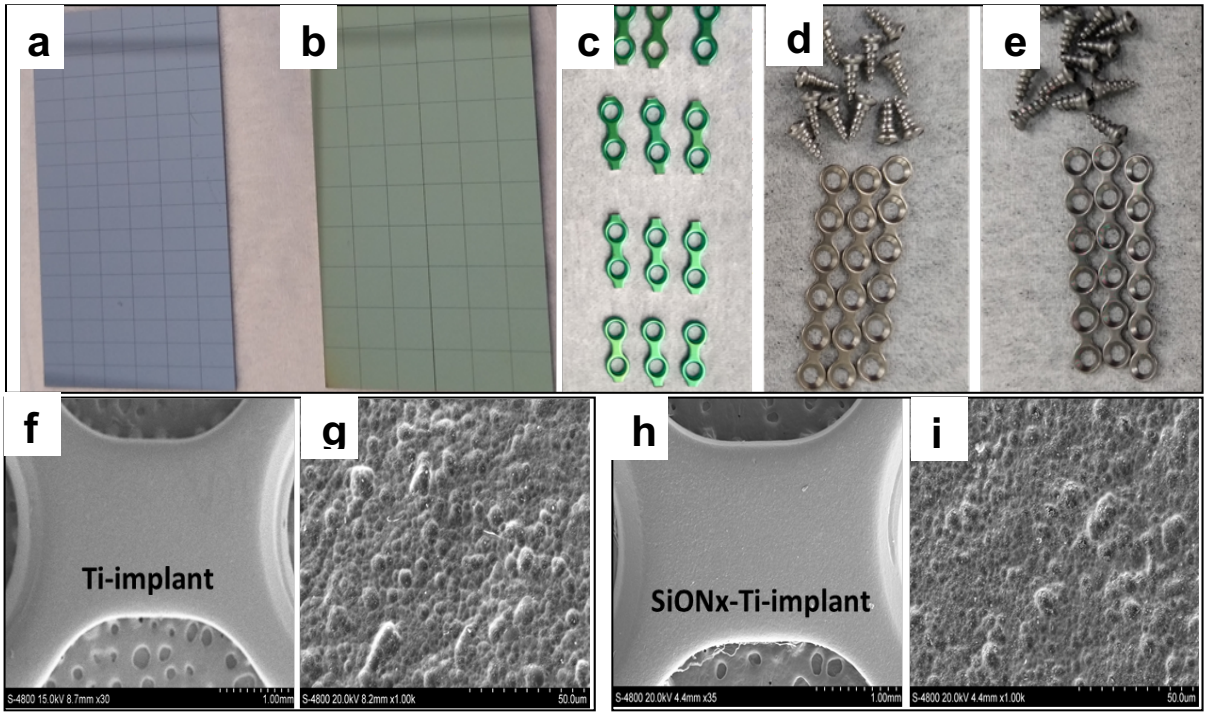

Figure. 5.1: Silicon wafer (a) and titanium plate and screws (c, d, f, g) were coated with SiONx using plasma enhanced chemical vapor deposition (b, e, h, i). SEM images show no surface characteristic differences between the titanium plate (f, g) and SiONx coated plate (h, i).

5.2. METHODS

5.2.1. Study Design

Plasma-Enhanced Chemical Vapor Deposition (PECVD) is used in this study to fabricate silicon oxynitride on simulated biomedical device surfaces (**Figure 5.1**). The coated and uncoated materials were then implanted into large cranial bone defects and studied for their effect on local tissue biomarkers. Methods such as immunohistochemical staining and enzyme-linked immunosorbent assay are used to characterize the healing response. Micro-computed tomography (Micro-CT) and various x-ray methods (x-ray diffraction, x-ray absorbance spectroscopy) are used to identify the bone mineral that is formed.

5.2.2. Plasma-Enhanced Chemical Vapor Deposition (PECVD)

Silicon oxynitride (SiONx) coating was fabricated according to our previously published protocol (20,26). Briefly, the surface was prepared for the coatings using standard cleaning

procedures using piranha solution (3:1 mixture of sulfuric acid (H_2SO_4, 96%) and hydrogen peroxide (H_2O_2, 30%)) for 10 minutes, and then rinsed in deionized (DI) water for 1 minute. Then, TRION ORION II PECVD/LPECVD system (Trion Technology, Clearwater, FL) was used to deposit a 1000 nm thin film coating of SiONx on silicon wafers. Bare silicon wafers and SiONx-coated wafers were cleaned with 70% ethanol and autoclaved and used as cranial implants.

5.2.3. *In Vivo* Rat Cranial Studies

All surgical modalities, care and treatment plan followed the ethical use of animals' protocol used before (25) and approved by the Institutional Animal Care and Use Committee (IACUC) at The University of Texas at Arlington under IACUC protocol number A18.014. Adult male Sprague Dawley rats, 3-4 months old, weighing about 300g, were used for the procedure. The rats were anesthetized using 5% isoflurane and then maintained at 2-3% isoflurane throughout the procedure. A 1.5 cm long incision was made with a sterile blade on the head, raising the skin and periosteum to expose the underlying cranial bone. A 7 mm X 4 mm +/- 1mm rectangular defect was made using a dental handpiece and round bur on either left or right parietal bone, while the surgical site and surrounding tissues was continuously irrigated with cold saline solution to prevent heating the surrounding bone and to keep the soft tissue moist. The depth of the defect was carefully made, and the loosened bone was carefully removed so as not to damage the dura. A sterile 2" x2" piece of gauze dampened with sterile saline was used to apply firm pressure to prevent excessive bleeding into the site. Implants, either bare or SiONx coated (of the same dimensions as the defect), were then carefully placed and a small gap (<1mm) is maintained. The periosteum and skin (which is kept moist in saline during the surgery) were then closed in layer with a vicryl suture. Analgesia, Buprenorphine SR, was given

to the animals for management of pain and distress right after surgery and repeated, if needed, after 72 hours. After surgery, rats were examined for signs of stress or infection and measured for weight change 2 to 3 times a week during experiments to monitor any changes in weight.

Blood was extracted every week from the rat tail vein using a sterile syringe for serum assays. The experimental endpoint was 4 weeks after the surgery, after which the animals underwent euthanasia (>90% CO2 and monitored until the animal was deceased).

5.2.4. *In Vivo* Rabbit Mandible Study

All animal studies were performed at Dr. Simon Young laboratory at the department of oral and maxillofacial surgery, University of Texas Health Science Center at Houston. All studies were performed on an easily accessible and reproducible, nonhealing alveolar bone defect in the rabbit mandible model established and previously published by the Young laboratory (27). Briefly, mandibular critical size defects (CSDs) were introduced in adult male New Zealand white rabbits (Myrtle's Rabbitry, Thompson Station, TN) by creating 10-mm diameter and full thickness defect with both cortical plates removed the rabbit mandible. Then, bare and SiONx-Ti coated fixation plate were secured with two screws on each side of the defect. Subsequently, the muscle and subcutaneous layers were closed with continuous resorbable 4-0 Vicryl sutures (Ethicon, Somerville, NJ) and the skin closed with interrupted 4-0 Vicryl sutures. After 8 weeks, the hemimandibles and surrounding tissues were harvested with the aid of bone shears and placed in 10% neutral buffered formalin for 48 h, rinsed thoroughly with phosphate-buffered saline (PBS), and placed in 70% (v/v) ethanol solution for further analysis.

5.2.5. X-ray Analysis of Regenerated Bone Layers- Micro-CT

The calvarial bone and the mandibular bone was extracted and analyzed using a 45-Micro-Computer Tomograph 3D imager (μ-CT, Scanco Medical AG, Switzerland). Serial tomographic imaging was taken at 55 kV energy and 145 μA intensity for the samples. The microCT data was further analyzed to determine the bone mineral density and the ratio of BV to TV.

5.2.6. X-ray Absorbance Near Edge Structure Analysis

X-ray Absorbance Near Edge Structure (XANES) analysis coupled with X-ray Fluorescence mapping was used to study the inorganic phase in the bone. XANES spectroscopy was performed at the Canadian Light Source at the University of Saskatchewan in Saskatoon, Saskatchewan, Canada. XANES is a sensitive technique to characterize the local coordination of individual elements using fine structural features at the absorption edge. Calcium (Ca) and phosphorous (P) edges were studied to examine the nature and local coordination of these elements in bone. Using soft X-ray beam-line for the micro-characterization of materials (SXRMB) that operates in the high-energy range from 1700 to 10,000 eV, the Ca K-edge spectra were obtained over energy ranges of 4000–4130 eV, with step sizes of 0.3. Operating at the low energy range between 5-250 eV and a step size of 0.1 eV, Plane Grating Monochromator (PGM) beam-line was used to acquire the P L-edge spectra in the region of 130-155 eV.

5.2.7. Histology

The calvaria samples were extracted and harvested using TechCut preserving the surrounding bone area (of the defect). All samples were fixed using HistoChoice (VWR) for 48 hours and then cut into half. One-half of each sample was decalcified using ethylenediaminetetraacetic acid (EDTA) for 1 week which then was soaked in a sucrose solution

and underwent optimal cutting temperature compound (OCT) embedding for frozen sections. The other half of the samples were dehydrated and used for plastic embedding.

The frozen sections were stained with H&E, ALP activity staining, CD68-ED1 using previously used protocols. The plastic-embedded samples underwent Golder trichrome, and Von Kossa McNeal staining.

5.2.8. Immunohistochemistry

Xylene was used to remove the upper plastic layer for the plastic embedded samples for IHC staining. The samples were rehydrated by descending-grade alcohol and then kept for antigen retrieval using testicular hyaluronidase method. Briefly, samples were kept in prewarmed testicular hyaluronidase solution for 30 mins at 37°C. The samples were then washed 3 times with PBS with 1% tween solution and stained with primary antibodies NRF2/NFE2L2 Polyclonal Antibody (16396-1-AP; Sigma-Aldrich, St. Louis, MO) in 1: 500 dilution overnight at 4°C. The samples were washed again (3X) and stained with secondary antibody Alexa dye 488 Goat anti Rabbit (green fluorescence) (A-11008; Sigma-Aldrich, St. Louis, MO) in 1:500 dilution at room temperature for 1 hour. The samples were washed, mounted, and imaged. Enzyme-linked immunosorbent assay of serum samples: Blood was collected from rat tail vein just before the surgery, at 1 week, 2 weeks and 4 weeks after the surgery. The collected blood was placed in a serum separating gel tube and centrifuged at 5000 rpm for 10 minutes. The supernatant serum was stored in -80ºC until further use. The serum samples were used to measure 4-HNE by a competitive enzyme-linked immunosorbent assay (ELISA) kit and Total ROS/RNS concentration acquired from Cell Biolabs, Inc. The serum samples were also used to detect NRF2 activity by Rat NRF2/NFE2L2 ELISA kit by Aviva Systems Biology using manufacturer protocols.

5.2.9. Nanoindentation

Nano-indentation using Hysitron Ubi-1 Nanoindenter (Hysitron, Minneapolis, MN) was performed to study the mechanical properties of the surrounding and regenerated bones. Bone samples were polished using different grits size and surface was finished with 2000 grit. Then, 3600 μm^2 surface area was scanned using scanning probe microscopy (SPM) and the area of interest was indented with a Berkovich tip. For each sample, 20 nanoindentations were performed on the selected area according to the following loading function: ramped up to 10 mN at a rate of 250 μN/s, held for 10 seconds, and then unloaded at 250 μN/s. The unloading slope of the load-displacement curve was used to calculate the reduced elastic modulus (Er) and the hardness (H) based on the Oliver-Pharr method (28,29).

5.2.10. Serum Analysis

The collected rat serum was tested for NRF2 and reactive oxygen species (ROS) concentrations. NRF2, Total ROS/RNS, and 4-Hydroxynonenal (4HNE) levels in the blood serum were measured to reveal the antioxidant and ROS levels. Enzyme-linked immunosorbent assay (ELISA) kits (Cell Biolabs, Inc., San Diego, CA) were used to measure the NRF2, Total ROS/RNS and 4HNE concentrations in serum using the manufacturer's protocol. The collected rabbit serum was evaluated for osteogenic markers osteocalcin (OCN) and quantitative alkaline phosphatase (ALP), angiogenic marker VEGFA, antioxidant marker SOD1, and 4-Hydroxynonenal (4HNE) lipid peroxidation levels. The ELISA kits were obtained from Cell Biolabs, Inc and evaluated using manufacturer's protocol.

5.2.11. Statistics

Power and statistical analysis were conducted using SPSS. Group comparisons were conducted using analysis of variance (ANOVA) with post-hoc Tukey's t-test for group

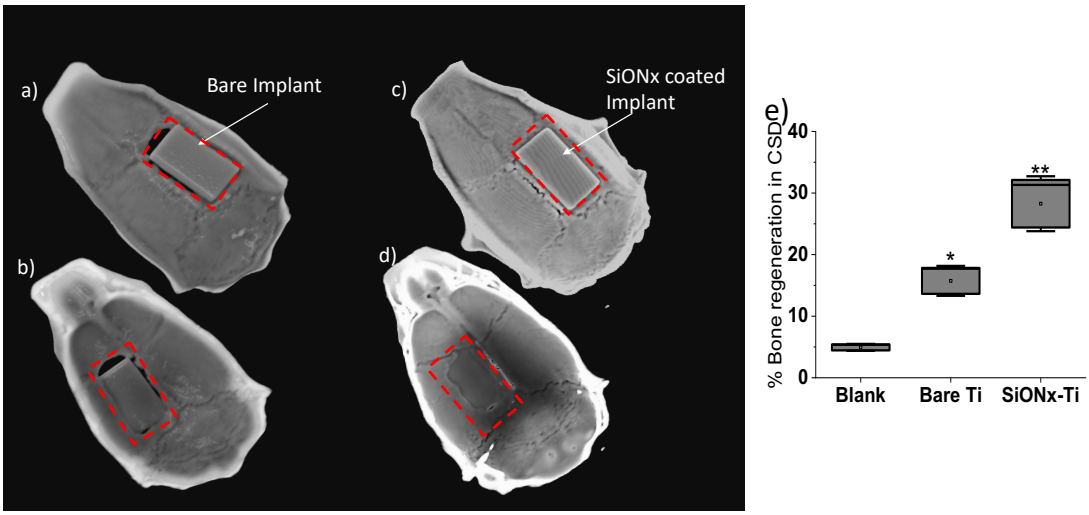

Figure 5.2. MicroCT images shows significantly more healing rate for the SiONx implant as compared to the bare implant. The red dotted line indicates the initial defect size of 8x5mm. (a),(b) showing superior and inferior surfaces of the cranial bone with bare implant and (c), (d) shows superior and inferior surfaces of the cranial bone with SiONx coated implant.

comparisons. Statistical significance was evaluated for group comparisons with $p < 0.05$ used to establish statistical significance.

5.3. RESULTS

5.3.1. Rat Cranial Study

We conducted the microCT imaging for evaluating bone regeneration and the osteointegration of the bone-implant interface. Results revealed that the SiONx-coated implants showed a 2X accelerated healing rate as compared to the uncoated group 4 weeks after surgery. **Figure 5.2**. shows microCT images of SiONx coated implant with significantly more bone growth around the bone-implant interface as compared to the control. Quantitative analysis shows about 30% mineralized tissue formation for the SiONx as compared to 16% for the

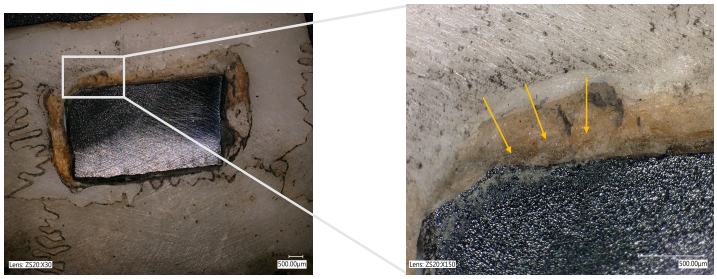

Figure 5.3. Reflective microscopic image of the implant-bone interface showing new bone growth (yellow arrows) on the SiONx coated implant.

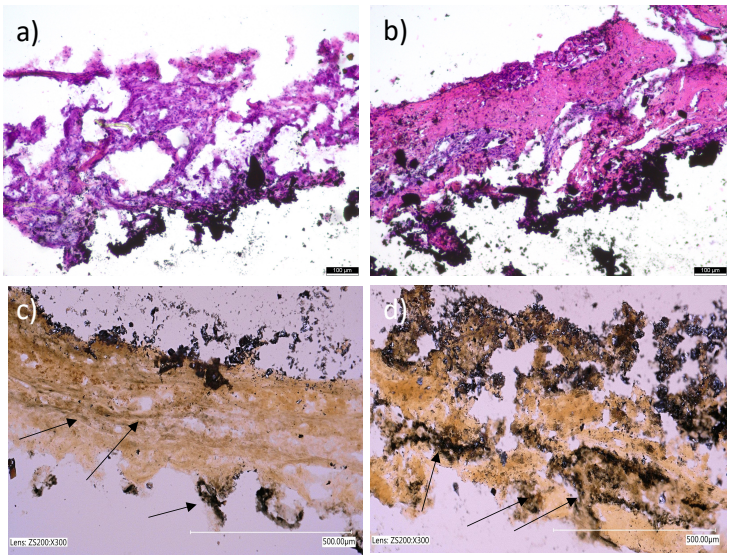

Figure 5.4. shows a more organized ECM matrix structure with significantly more collagen formation stained by H&E in SiONx implant (b) as compared to bare implant (a). (c), (d) shows ALP activity over bare implant (c) and SiONx implant (d). ALP activity is determined by the black reaction product indicated by black arrows.

uncoated group. The reflective microscopic images (**Figure. 5.3**) reveal the tight bone-implant interface and bone in growth in the SiONx coated group.

Histology images shows more organized collagen matrix or extracellular matrix formation for SiONx coated group as compared to the uncoated group as seen in the H&E staining (**Figure 5.4 a, b**) and Goldner Trichrome staining (**Figure 5.5**). The H&E images indicates the formation of significantly more trabecular bone formation along with an increased ALP activity, seen as the black reaction product in **Figure 5.4 (c, d)** when compared to the uncoated group.

McNeal Von Kossa staining (**Figure 5.6**) shows increased number of mass calcium deposits (marked as black arrows) with the SiONx coated group, whereas the uncoated group shows more dispersed calcium deposits. We also observe more mature bone formation with

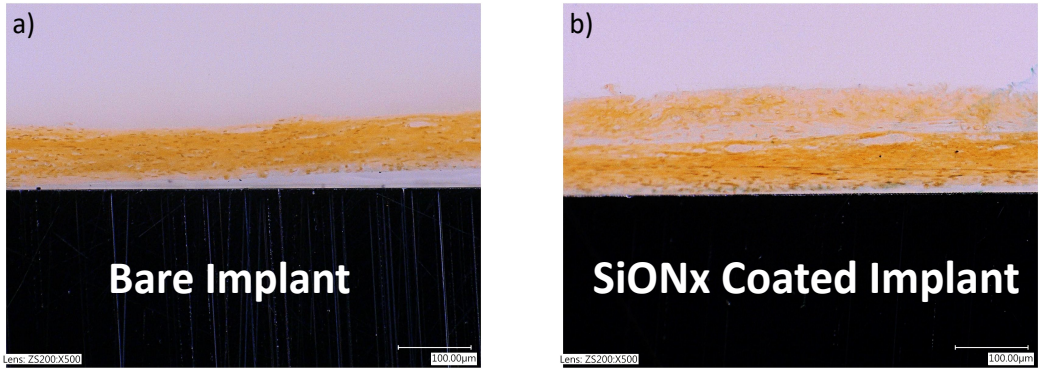

Figure 5.5. (a), (b) shows presence of collagenous matrix stained by Goldner staining on the surface of bare implant and SiONx coated implant respectively.

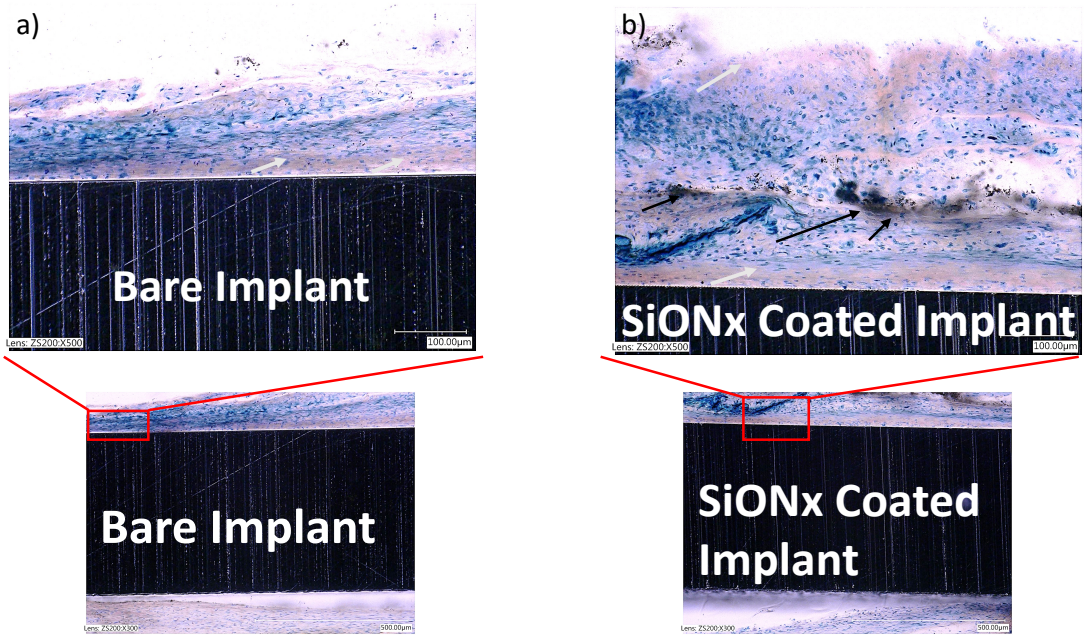

Figure 5.6. (a), (b) shows Von Kossa-McNeal staining on the tissue covering the implant surface on Bare implant and SiONx implant respectively. The black arrows show mass calcium deposits, the grey arrows indicate dispersed calcium deposits. The nucleus is stained blue.

significantly greater number of blood vessels and haversian canals for the SiONx coated implant compared to the uncoated group.

CD68-ED1 stain (**Figure 5.7**) indicates the macrophage invasion (brown staining) in the tissue surrounding the cranial implant. The uncoated implants (a) show significantly more macrophage invasion in the tissue as compared to the SiONx coated implant (b) and sham (d), but less macrophage invasion as compared to the blank defect (c).

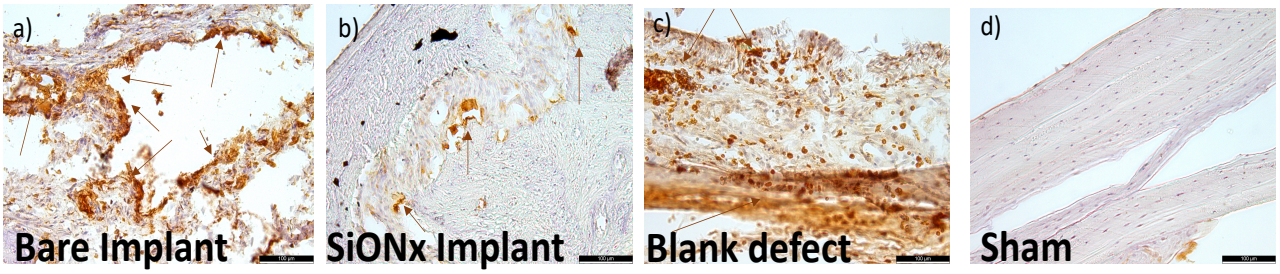

Figure 5.7. shows CD68-ED1 stain indicating the macrophage invasion in the tissue surrounding the cranial implant. The bare implants (a) show significantly more macrophage invasion in the tissue as compared to the SiONx coated implant (b) and sham (d), but less macrophage invasion as compared to the blank defect (c). The brown indicates the macrophage invasion.

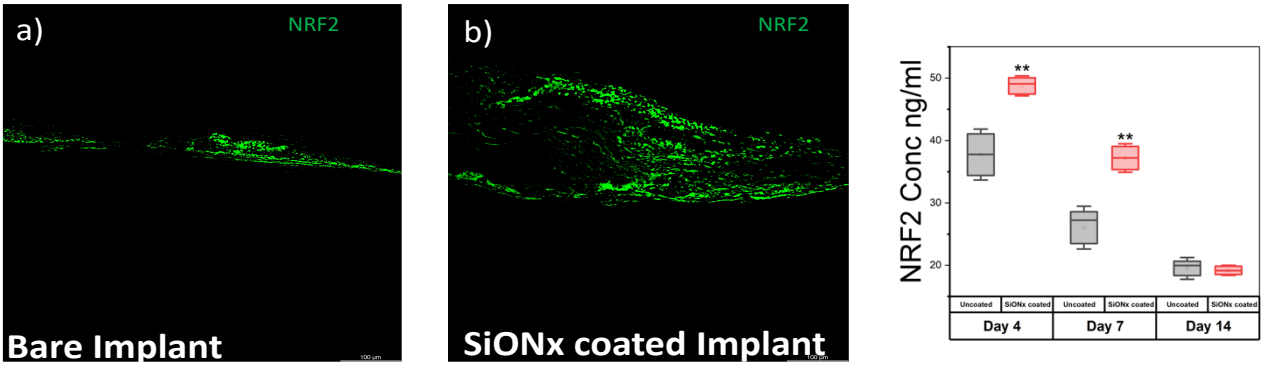

Figure 5.8. Fluorescent staining images for NRF2 indicating significantly more antioxidant activity with SiONx implant (b) as compared to the bare implant (a). (c) ELISA detecting NRF2 concentration in rat blood serum at 4-, 7- and 14-day post-surgery indicating significantly more expression of NRF2 activity in SiONx coated as compared to uncoated group.

We observed localized overexpression of the antioxidant marker NRF2 in the SiONx group as compared to the uncoated group (**Figure 5.8 a, b**). There was also a significant increase in the NRF2 activity in the blood serum analysis done by ELISA at 4-, 7- and 14-day post-surgery indicating an upregulation in the antioxidant activity (**Figure 5.8 c**).

There is a significant (1.5x) reduction in *in vitro* Total ROS/RNS DCF concentration (nM) in the blood serum at 7 and 14 days along with reduced (2x) lipid peroxidation concentration (ug/ml) (4HNE Adduct) in the SiONx group (**Figure 5.9**) indicating a reduction in ROS in the SiONx group as compared to the uncoated.

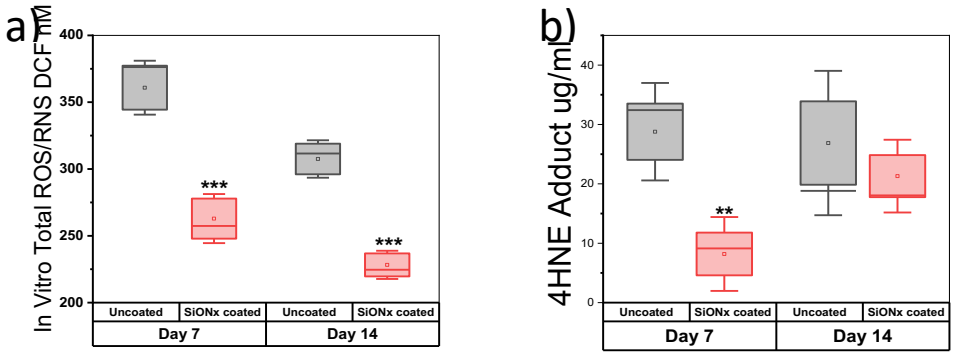

Figure 5.9. (a) In Vitro Total ROS/RNS DCF concentration (nM) and (b) 4HNE Adduct (Lipid peroxidation) concentration (ug/ml) detected in blood serum on uncoated and SiONx coated samples.

5.3.2. Rabbit Mandibular Defect Surgery

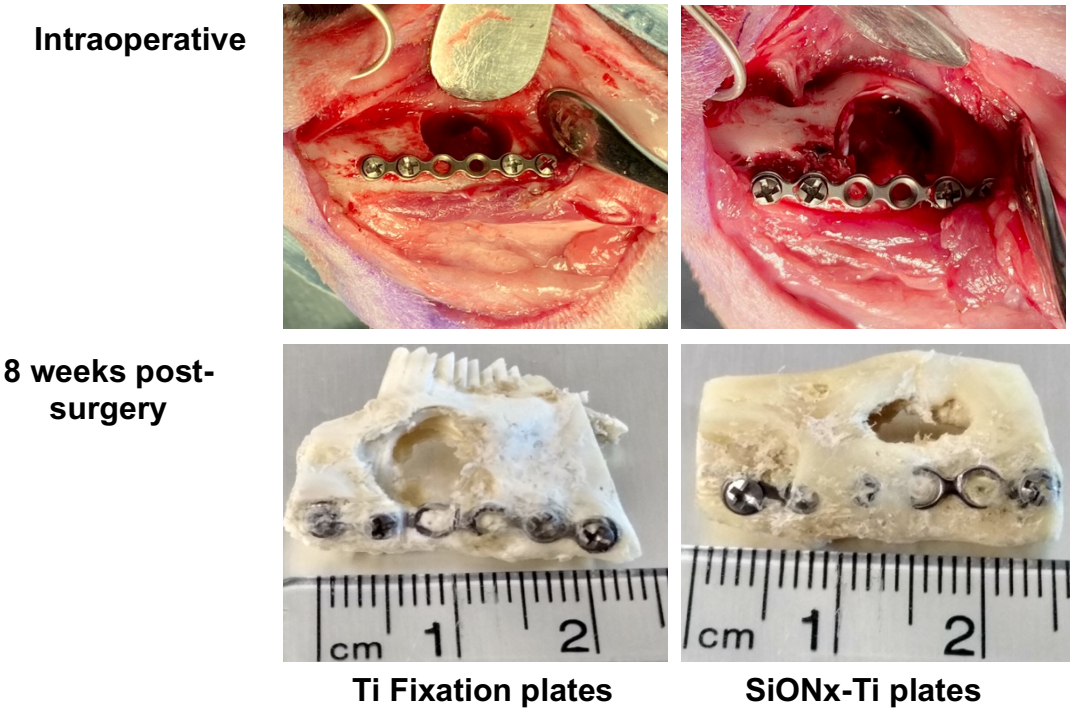

Figure 5.10. Intraoperative photos of the rabbit mandibular alveolar bone showing full thickness defect with both cortical plates removed, and titanium fixation plate secured with two screws on each side of the defect (a, b). (c, d) shows 8-week postoperative rabbit mandibular bone defect.

The rabbit mandibular bone samples were harvested and the effect of SiONx-coated fixative device was compared to the Ti plates. **Figure 5.10** shows the extracted mandible with the bare/uncoated Ti plates and the mandible with SiONx-coated Ti plates. We observe that the SiONx coated group has more regenerated bone around the defect and the defect size was comparatively smaller to the uncoated group. These observations were further confirmed by micro-CT and X-ray imaging as shown in **Figure 5.11.**

The micro-CT images of SiONx-coated implants confirmed the growth of newly formed bone on the surface of the implants indicating implant-bone bonding and enhanced osseointegration. The defect was almost closed with the coated implants that showed less than 30% defect size compared to more than 40% on uncoated implant after 8 weeks. The quality of

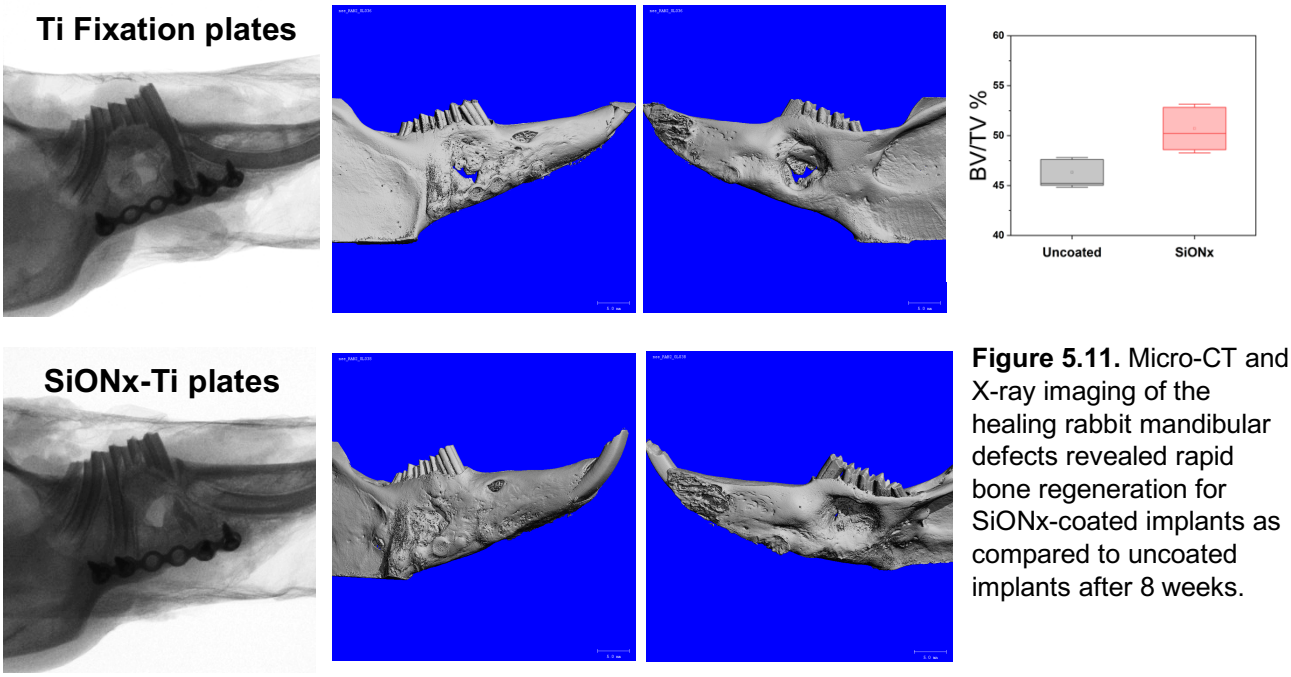

Figure 5.11. Micro-CT and X-ray imaging of the healing rabbit mandibular defects revealed rapid bone regeneration for SiONx-coated implants as compared to uncoated implants after 8 weeks.

regenerated bone was enhanced on the coated implant as confirmed from the X-ray images, while regenerated bone near the uncoated implants had poor quality with low-density bone as confirmed from X-ray (**Figure 5.11**).

Figures 5.12, 5.13 and 5.14 present the chemical structure of the regenerated bone by XANES analysis. The studied bone samples included the 1) bone surrounding the SiONx-coated Ti plates, 2) bone surrounding the uncoated Ti plates, 3) bone from the bone-implant interface (Newly formed bone on the plate) from SiONx coated group and 4) bone from the bone-implant interface (Newly formed bone near the plate) from the uncoated Ti group. **Figure 5.12** show the Ca L edge XANES spectra some standard model compounds and the spectra of the bones. All studied groups indicated the presence of two main spin-orbital related peaks a2 and b2 which appeared at 350.5 and 353.8 eV, respectively. The pre-edge peaks a1 and b1 were located at 349.2 eV and 352.5 eV, respectively, which exactly match the standard model compounds. The b1 peak on both samples of the SiONx-coated plates is similar to the standard nano-hydroxyapatite (Nano-HA) spectra.

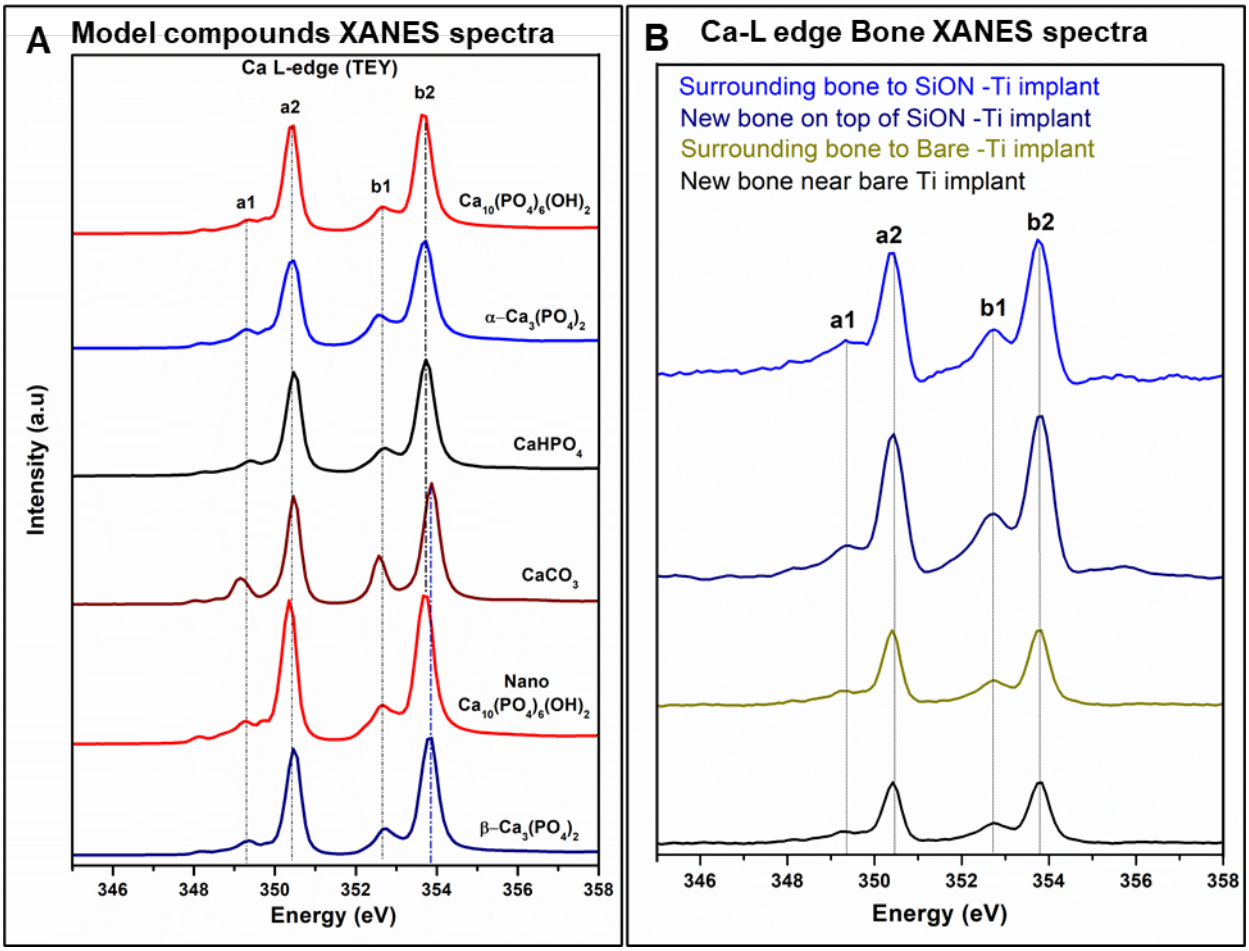

Figure 5.12. Ca L edge TEY XANES spectra of model compounds (A) and extracted mandibular bones after 8 weeks of surgery.

Figure 5.13 represents the P L edge spectra for the studied bone samples compared to standard model compounds. The third pre-edge peak appearing at 136.6 eV in all bone samples reveals the presence of β-tricalcium phosphate (β-TCP) -like structure. We observe an intensity drop in the post-edge shoulder between 139.0 to 142.0 eV for both the bone samples in the uncoated Ti plate group indicating the presence of more soluble phosphate in uncoated group.

Figure 5.14 shows the line scan and X-ray fluorescence mapping of Ca L edge for the regenerated area surrounding the SiONx-coated plate and the defect. The line scan allows the collection of XANES spectra in a straight line for preset points. We scanned 80 points, before the defect area crossing the regenerated bone and defect area reaching the other side of regenerated

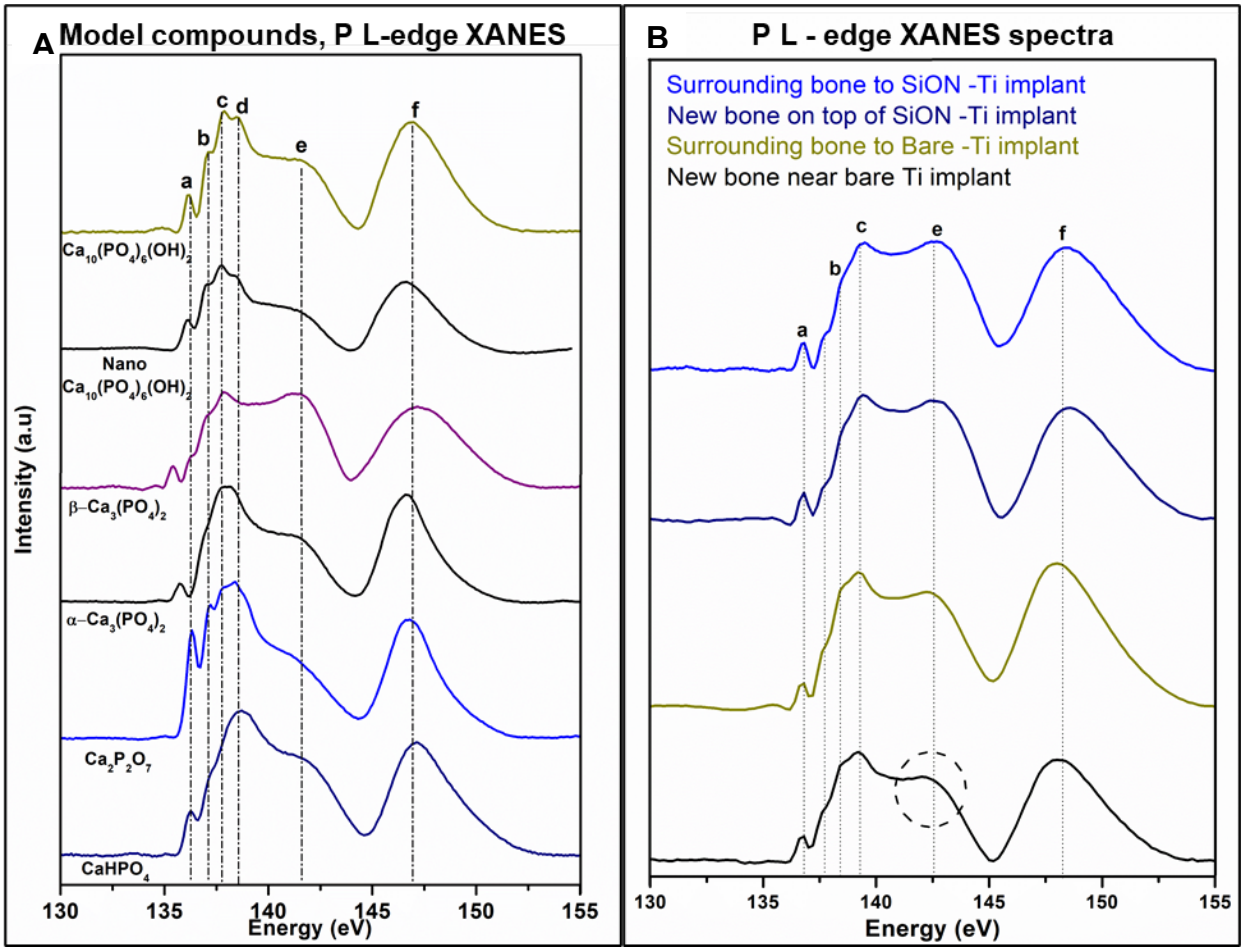

Figure 5.13. P L edge FY XANES spectra of model compounds (A) and extracted mandibular bones after 8 weeks of surgery (B).

bone, to detect the changes in the Ca L-edge in a line. Line scan indicated no Ca exist in the defect area, low Ca spectra intensity in the newly regenerated bone area, and gradual increase in the Ca spectra intensity as passing from the regenerated bone towards the surrounding bone area. **Figure 5.14 B and C** shows the X-ray fluorescence mapping of the extracted rabbit bone on the SiONx-coated plate before and after the Ca L edge. These images indicate the presence of Ca after the edge energy, whereas no Ca distribution is present before the edge.

We evaluated the mechanical properties of the regenerated bone using nano-indentation. **Figure 5.15** shows the load displacement curve of newly formed bone on top of SiONx-Ti coated plate, bone surrounding the coated implant, and bone surrounding the uncoated implant.

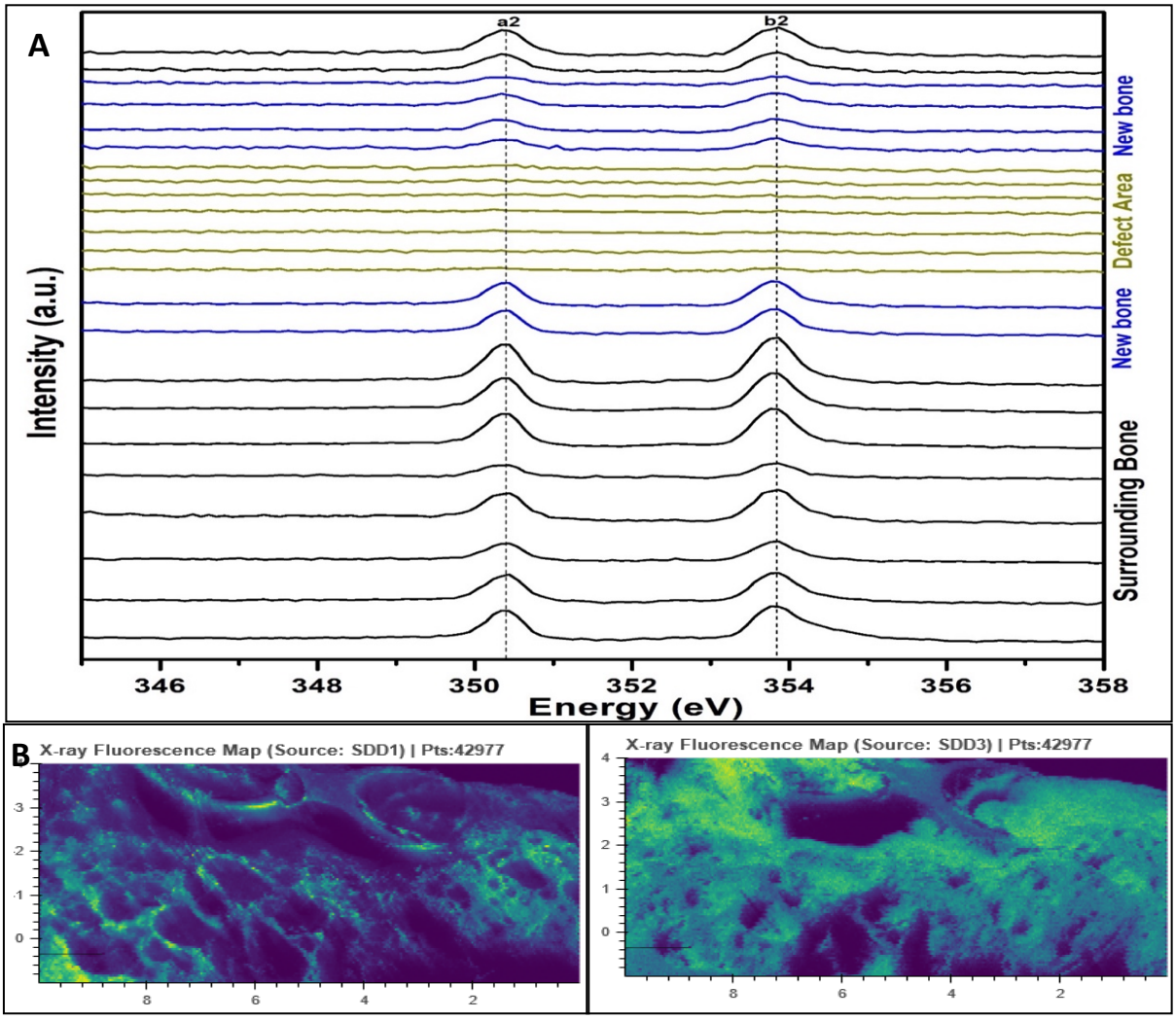

Figure 5.14. Line scan Ca L-edge XANES spectra of the regenerated bone surrounding the coated implant and the defect. From Top, spectra show the presence of the Ca in the surrounding bone (black), developed Ca in newly formed bone (blue), no Ca in the defect area (red), Ca in newly bone past defect area (blue), and Ca in surrounding bone after the defect area (black). X-ray Fluorescence mapping of the extracted rabbit bone on the coated implant before (B) and after (C) Ca L edge shows no Ca distribution before the edge, while presence of Ca (green color) after the edge energy.

We calculated reduced elasticity modulus (Er) and hardness (H) from the nano-indentation data using the Oliver-Pharr method (28,29). Results revealed that the newly formed bone on coated implant has Er = 17.7 ± 1.6 GPa and H = 689 ± 99 MPa, the bone surrounding the SiONx coated Ti has Er = 24.1 ± 2.7 GPa and H=929±169 MPa, and bone surrounding the uncoated Ti has Er = 22.6 ± 2.7 GPa and H = 918 ± 177 MPa. The bone surrounding the uncoated implant has a lower

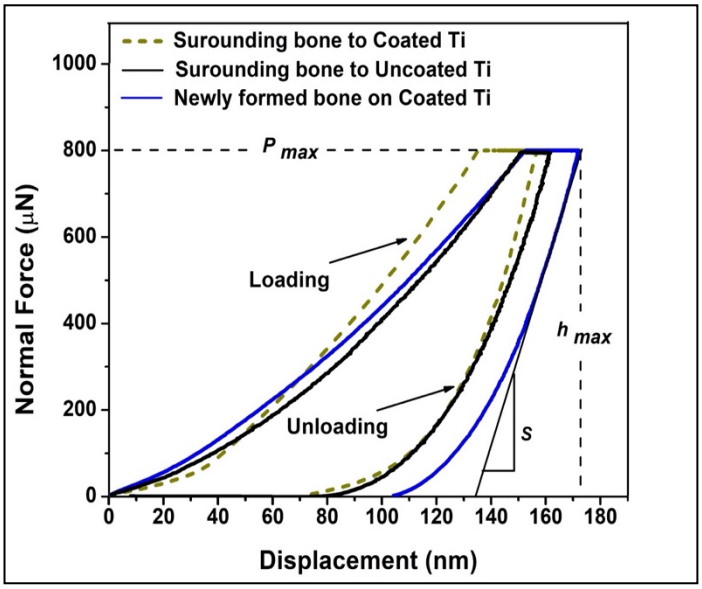

Figure 5.15. Load displacement curve comparing newly formed bone on Ti-implant (Er=17.7±1.6 GPa and H=689±99 MPa) to surrounding bone to coated Ti (Er=24.1±2.7 GPa and H=929±169 MPa) and uncoated Ti (Er=22.6±2.7 GPa and H=918±177 MPa). Er: Reduced Elasticity modulus and H: Hardness.

elasticity modulus compared to the bone near the SiONx-coated implants. Also, the newly formed bone on the top of coated implants has a reduced elastic modulus lower than the normal surrounding bone.

The collected blood serum was screened for bone biomarkers (OCN and ALP), angiogenic marker (VEGFA), antioxidant marker (SOD1) and Lipid peroxidation levels (4HNE). **Figure 5.16** presents the (A) Quantitative ALP assay, (B) OCN activity, (C) VEGFA, (D) 4HNE and (E) SOD1 activity, 1, 2, 4, and 8 weeks post-mandibular defect surgery. We observed significantly higher ALP activity in SiONx implants at all time points ($p<0.05$) compared to the uncoated Ti group. The other osteogenic marker OCN expression and angiogenic VEGFA expression remains nominal in both groups (not statistically different from each other). We also evaluated the lipid peroxidation levels (4HNE) which shows significant reduction at week 2, 4 and 8 with the SiONx coated plate group when compared to the uncoated implants. Antioxidant SOD 1 concentration was elevated for the coated SiONx group at all time points and a significant increase was observed at week 4 (**$p<0.01$) and week 8 (*$p<0.05$) as compared to the uncoated plate group.

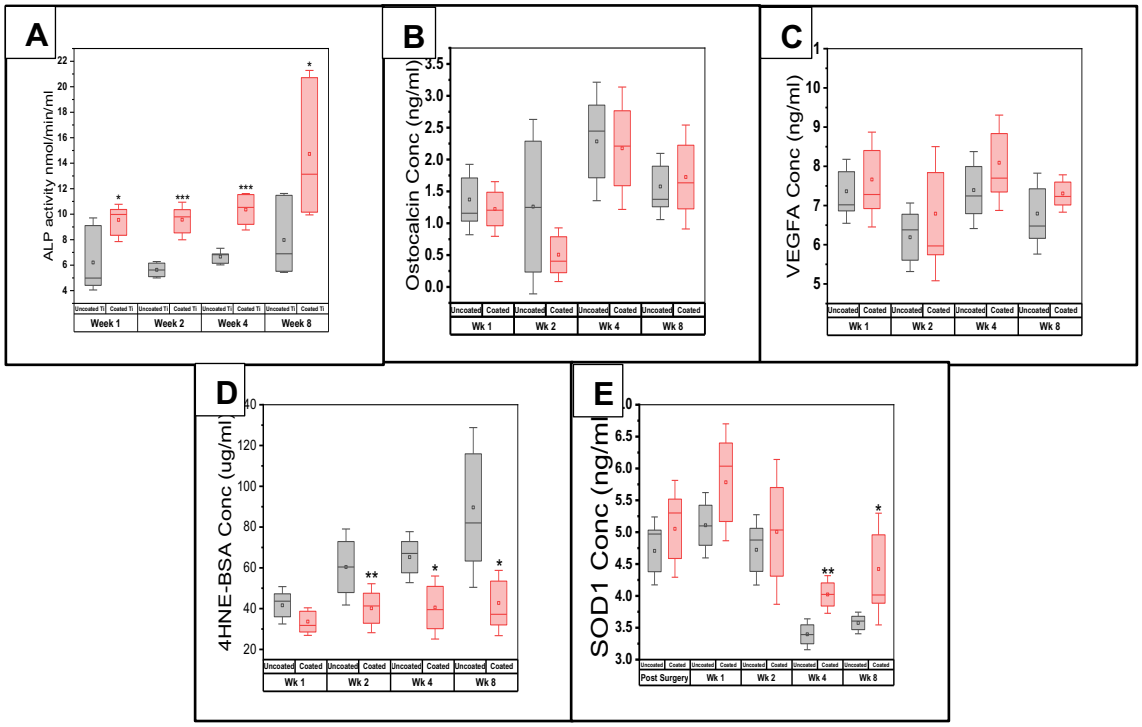

Figure 5.16. Blood serum analysis (ELISA) shows enhanced ALP activity at Week 1, 2, 4, and 8 (A), Osteocalcin expression (B) and VEGFA expression (C) does not show any significant differences. There was significant reduction in lipid peroxidation at week 2, week 4 and week 8 (D) and enhanced antioxidant SOD1 activity with the SiONx-coated implants (E).

5.4. DISCUSSION

Previous studies in our lab have shown 1. The SiONx surface coatings are non-cytotoxic and support cell proliferation and differentiation (23), 2. Si^{4+} and SiONx enhances angiogenic markers (VEGF, HiF1-A, ANG-1, Nes-2), vascular tubule formation, and dense blood vessel formation (24,25), 3. SiONx induces antioxidant marker expression (SOD1, GPX1, NRF2, CAT1) and reduces ROS by cationic reduction (23,30), 4. Increasing the nitrogen to oxygen ratio in the SiONx coatings enhances the antioxidant protective effect against the oxidative stress and enhances osteogenesis, and 5. SiONx induces antioxidant activity by the NRF2 expression (**Chapter 4**). These findings have helped us establish the role and chronology of SiONx in bone healing. In this study, we studied the antioxidant silicon oxynitride PECVD coatings on

craniomaxillofacial titanium fixative devices to enhance localized bone regeneration in two *in vivo*, rat cranial defect and rabbit mandibular critical-sized defect, models.

We have established that the amorphous SiONx coatings induce antioxidant activity and reduce oxidative stress through a sustained release of silicon ions. The sustained leaching of the ions from the bioactive surface coatings can be attributed to the low-temperature vacuum PECVD process (23,31). This low-temperature technique preserves the underlying architecture of the fixative titanium device (as seen in **Figure 5.1**) also leads to a more reductive surface, releasing Si^{4+}, which helps reduce oxidative stress (23,25). The PECVD technique is well-established in the semiconductor industry. Ease of the manufacturing process and repeatability make PECVD a beneficial option for the medical device industry, especially in orthopedic and dental field, to yield good results.

Our previously conducted *in vitro* data (**Chapter 4**) has provided valuable information on the SiONx design and chemistry leading to our hypothesis for this study that SiONx affects key antioxidant markers for the reduction of excessive oxidative stresses in a large bone defect to maximize efficacy for bone healing. We use rat and rabbit models for this study. The rat cranial defect model is a widely used animal model to study bone regeneration studies and also study the biosafety profile of the osteo-conduction process of the implantable material. We see good osteointegration of the fixative device to the bone (microCT image **Figure 5.2**). In our overall observation of all animal subjects (n=6/timepoint), none of the SiONx-coated implants dislocated from the defect area and showed good ingrowth of the bone into the defect area (**Figure 5.3**). There was no/little gap seen between the defect and implant surface (seen on the microCT image from the inferior surface). 2 of the 6 uncoated devices were significantly moved from the defect area, leading to disrupted osteointegration and osteo-conduction processes. Quantitative analysis

for the % bone regenerated showed > 25% of the total defect area regenerated for the SiONx coated devices as compared to about 12-17% total defect area regenerated for the uncoated group in just 4 weeks (**Figure 5.2**). Histological analysis revealed a more organized extracellular matrix (**Figure 5.4**) with SiONx coated group with increased ALP activity and more mineral tissue formation (**Figure 5.6**).

Related to our premise of the study as well as related prior studies conducted (25), we evaluated the NRF2 expression localized to the defect area (immunohistochemistry image **Figure 5.8**) as well as NRF2 expression rat blood serum (ELISA **Figure 5.8**). As expected, we confirm increased NRF2 expression localized to the regenerated tissue surrounding the defect area for the SiONx-coated group compared to the uncoated. We also observe increased NRF2 activity in the rat blood serum at day 4 and day 7. We think that this increased NRF2 systemically is a response to the mitochondrial ROS production after the stress of the surgical defect creation. On the other hand, we saw a significant decrease in the total ROS/RNS concentration in the rat blood serum and lipid peroxidation at day 7 (**Figure 5.9**). This data is in line with our preliminary in-vitro study (23,24) confirming the activation of the master regulator NRF2 for the antioxidant response in regulating the intracellular ROS levels. The regulation of the lipid peroxidation levels in the serum (levels of serum malondialdehyde) (**Figure 5.9**) also indicates the regulation of the osteoclastic activity and balancing out the remodeling process for an organized and faster bone healing process.

The above rat cranial study gives us good insights into the bone osteointegration and osteoconduction process with the SiONx-coated implants (32). We also confirm the data we generated in our former studies conducted *in vitro* and *in vivo*, which minimized our animal use and gave valuable information in a minimum-sized animal model (3,33). Further, we studied the

effect of SiONx-coatings for a more translational plate and screw design popularly used in craniomaxillofacial surgeries as well as orthopedic applications. We use a rabbit mandibular defect model which is an animal model for load bearing bone, that has large defects that mimic that of humans (27). Thus, the rabbit mandibular model has a higher translational potential for traumatic injury defects than do mice or rats for bone. We use this translational model to evaluate the chemical and mechanical structure of the newly regenerated bone structure. The rabbit model is also very popular for immunology studies and hence this model can illustrate how the coating can be used to heal a large and compromised bone defect resulting from the sudden loss of bone due to evulsive trauma (34).

Our rabbit mandibular defect model results are congruent with our rat cranial data. We see %bone volume/ total volume of more than 50% and faster bone regeneration with the SiONx coated group (**Figure 5.11**). In our overall observation, 3 out of the 6 rabbits in the uncoated group showed an iatrogenic fracture, whereas only 1 out of the 6 rabbits in the coated group had an iatrogenic fracture. Subjective visualization of the bone quality seems better in the SiONx-coated group and we observed bone growth on the plate surface along with the osteointegration to the surrounding bone. The uncoated plates had none/ little bone growth on the plate surface, the osteointegration to the surrounding bone was similar to the coated group on the subjective evaluation. On evaluating the chemical structure of the regenerated bone, the Ca L edge revealed that the bone on and surrounding the SiONx coated plates is similar to the standard nano-hydroxyapatite (Nano-HA) spectra as shown from the b1 peak (**Figure 5.12**). The bone surrounding the uncoated titanium plate shows low intensity pre-edge peak a1 suggesting a $CaHPO_4$-like spectra. The P L edge (**Figure 5.13**) also suggests that the SiONx coated groups shows is closer to β-TCP- like spectra and the uncoated group shows more soluble phosphates.

The line scan and X-ray fluorescence mapping confirmed the mineralization growth towards the defect area (**Figure 5.14**). These results combined with the micro-CT and X-ray imaging confirmed the enhanced bone quality and faster osseointegration on the SiONx-coated implants. The mechanical properties (**Figure 5.15**) reveal a lower elasticity modulus for the uncoated group compared to the SiONx-coated. We did not find any relevant literature on the mechanical properties measurements (Er and H) of rabbit mandibular bone, we compared our results to rabbit tibia and cortical bone measurements previously published (35). It has been reported that the reduced elasticity modulus varies between 24 to 35 GPa and the hardness range between 950 to 1200 MPa in rabbit cortical bone depending on the age of the animal (35,36). Our reported Er and H results in this study are in agreement to the above previously reported data. Previous studies have related the reduction in bone elastic modulus and hardness to poor integration after implantation of the dental implants with surrounding bones (37,38). We believe the reduced elastic modulus with the uncoated group compared to SiONx-coated can be attributed to the bone mineralization maturity or poor bone-implant integration between the plate and surrounding bone.

We evaluated osteogenic, antioxidant and serum lipid peroxidation levels to correlate our findings from the above rat cranial defect study. We observe the levels of OCN and VEFGA expression (**Figure 5.16**) in rabbit blood serum remains nominal and not significantly different in both coated and uncoated titanium groups. Osteocalcin is a major biomarker in bone turnover (39). Various pathological conditions including bone metabolic disorders and fracture can increase the OCN activity levels (39,40). Similarly, for the VEGF activity increased in diseased condition and tumor growth (41). We believe that in our study, the surgically induced defect and manipulation of the defect in both test (SiONx coated) and control (uncoated) groups

simultaneously, may increase a localized angiogenic and bone turnover rate and keep the VEGF and OCN expression in the normal range systemically. However, we see an increase ALP activity, a decrease lipid peroxidation and an increase in SOD1 activity (**Figure 5.16**) for the SiONx-coated group compared to the uncoated implants. The increased SOD1 activity can be attributed to the SiONx coatings activating the antioxidant pathway as we see in our results with the rat cranial study (**Figure 5.8**). The enhanced antioxidant activity regulates the intracellular ROS levels and decreases the 4HNE lipid peroxidation levels. The ALP activity is significantly increased in the blood serum with the SiONx plates, although within physiologic levels (42), can be related to the reduction in the 4HNE levels. The enhanced ROS activity has been studied to breakdown the ALP molecules in skeletal abnormalities and pathological conditions (43,44). The ALP concentration in the blood serum for both groups, the SiONx coated as well as uncoated, while remaining in the physiological range, the significantly improved ALP can be attributed to the reduced oxidative stress.

To further explain the antioxidant nature of the SiONx coatings, we learned from our previous study that the release of Si-ions with a higher valance state (+4) increases the charge transfer to the antioxidant and enhances the overall antioxidant production (25). The well-known SOD1 reaction with transition metals (i.e., Cu, Zn, and Mn) produces only one molecule of hydrogen peroxide (H_2O_2) as seen below in equation 1. Then, via Fenton reaction and presence of catalase (45,46), the H_2O_2 is converted to one-water and half-oxygen molecule as in equation 2. In the case of Si^{4+}, the first reaction produces three molecules of H_2O_2 (Equation 3) which is three times higher compared to the normal reaction with transition metals (Equation 1). Then, via Fenton reaction and catalase reduction (45,46), $3H_2O_2$ is converted to $3H_2O$ and one and half-oxygen molecules which is 3-folds compared to the normal reaction. This pronounced

antioxidant activity of Si-ions plays an important role in mitigating the effects of excessive ROS, which was confirmed by the significant reduction is 4HNE concentration (>2-fold reduction). Thus, the enhancement of SOD1 (via Si-ions) reduces oxidative stress (4HNE) and thus improves biocompatibility, osteogenic activity, and osseointegration (47).

$M^{2+}/SOD1 + O_2^- 2H^+ = M^{2+}/SOD1 + H_2O_2$ (Eq. 1)

$Si^{4+}/SOD1 + 3O_2^- 6H^+ = Si^{4+}/SOD1 + 3H_2O_2$ (Eq. 2)

$Fe^{3+}/CAT + H_2O_2 = Fe^{3+}/CAT + H_2O + ½ O_2$ (Eq. 3)

$Fe^{3+}/CAT + 3H_2O_2 = Fe^{3+}/CAT + 3H_2O + 1.5 O_2$ (Eq. 4)

5.5. CONCLUSIONS

To conclude, we demonstrate Silicon Oxynitride coatings promote rapid bone regeneration in rat calvaria bone defects via several key antioxidant and osteogenic markers. We also show Silicon Oxynitride enhances osteointegration and osteogenesis in a translational rabbit mandibular defect model. The amorphous SiONx coating shows a favorable antioxidant-inducing surface modification for critical-sized and compromised bone defect implants for rapid bone healing.

5.6. ACKNOWLEDGEMENTS

The authors want to acknowledge National Institutes of Health /National Institute of Dental and Craniofacial Research (1R56DE027964-01A1-01), the Osteo Science Foundation Peter L. Geistlich Research Grant, Texas STARs award, Departmental Start-up Funds, University of Texas at Arlington (UTA) College of Nursing and Health Innovation, Arlington, TX, for their generous support for this study. The authors would also like to thank UTA College

of Nursing & Health Innovation Bone-Muscle Research Center (UTA-CONHI-BMRC) and Nanotechnology Research Center at Shimadzu center at UTA for their support. Lastly, we want to acknowledge Mr. Matthew Fiedler and Ms. Thy Vo at the Varanasi laboratory, for their contribution towards this study.

5.7. REFERENCES

1. Bone Grafts and Substitutes Market by Product (Allografts, Bone Grafts Substitutes, and Cell-based Matrices), by Application (Spinal Fusion, Long Bone, Foot & Ankle, Craniomaxillofacial, Joint Reconstruction, and Dental Bone Grafting). (2015-2023) [Online]. *Glob. Oppor. Anal. Ind. Forecast*: [date unknown]. https://www.alliedmarketresearch.com/bone-graft-substitutes-market.
2. Craniomaxillofacial Implants Market by Product (Mid Face Implants, Cranial or Neuro Implants, Man-dibular Orthognathic Implants, Distraction Systems, Bone Graft Substitutes, Thoracic Fixation Systems, Total TMJ Replacement Systems, Dural Repair Product. ([Online]. *Glob. Oppor. Anal. Ind. Forecast*: [date unknown]. https://www.alliedmarketresearch.com/craniomaxillofacial-implants-market.
3. **Neovius E**, **Engstrand T**. Craniofacial reconstruction with bone and biomaterials: review over the last 11 years. *J Plast Reconstr Aesthet Surg* 63: 1615–1623, 2010. doi: 10.1016/j.bjps.2009.06.003.
4. **Kwarcinski J**, **Boughton P**, **Ruys A**, **Doolan A**, **Van Gelder J**. Cranioplasty and Craniofacial Reconstruction: A Review of Implant Material, Manufacturing Method and Infection Risk. *Appl Sci* 7, 2017. doi: 10.3390/app7030276.
5. **Rogers GF**, **Greene AK**. Autogenous bone graft: basic science and clinical implications. *J Craniofac Surg* 23: 323–327, 2012. doi: 10.1097/SCS.0b013e318241dcba.
6. **Zanotti B**, **Zingaretti N**, **Verlicchi A**, **Robiony M**, **Alfieri A**, **Parodi PC**. Cranioplasty: Review of Materials. *J Craniofac Surg* 27: 2061–2072, 2016. doi: 10.1097/SCS.0000000000003025.
7. **Chiarello E**, **Cadossi M**, **Tedesco G**, **Capra P**, **Calamelli C**, **Shehu A**, **Giannini S**.

Autograft, allograft and bone substitutes in reconstructive orthopedic surgery. *Aging Clin Exp Res* 25 Suppl 1: S101-3, 2013. doi: 10.1007/s40520-013-0088-8.

8. **Grove, DPM JR**. Autograft, Allograft and Xenograft Options in the Treatment of Neglected Achilles Tendon Ruptures: A Historical Review with Illustration of Surgical Repair. *Foot Ankle J* 1, 2008. doi: 10.3827/faoj.2008.0105.0001.

9. **Albrektsson T**, **Johansson C**. Osteoinduction, osteoconduction and osseointegration. *Eur spine J Off Publ Eur Spine Soc Eur Spinal Deform Soc Eur Sect Cerv Spine Res Soc* 10 Suppl 2: S96-101, 2001. doi: 10.1007/s005860100282.

10. **Thrivikraman G**, **Athirasala A**, **Twohig C**, **Boda SK**, **Bertassoni LE**. Biomaterials for Craniofacial Bone Regeneration. *Dent Clin North Am* 61: 835–856, 2017. doi: 10.1016/j.cden.2017.06.003.

11. **Awad KR**, **Ahuja N**, **Shah A**, **Tran H**, **Aswath PB**, **Brotto M**, **Varanasi V**. Silicon nitride enhances osteoprogenitor cell growth and differentiation via increased surface energy and formation of amide and nanocrystalline HA for craniofacial reconstruction. *Med DEVICES SENSORS* 2: e10032, 2019. doi: 10.1002/mds3.10032.

12. **McEntire BJ**, **Lakshminarayanan R**, **Thirugnanasamb P**, **Seitz-Sampson JW**, **Bock RM**, **O'Brien D**. Processing and Characterization of Silicon Nitride Bioceramics. *Bioceram Dev Appl* 6: 1–9, 2016.

13. **Varanasi VG**, **Saiz E**, **Loomer PM**, **Ancheta B**, **Uritani N**, **Ho SP**, **Tomsia AP**, **Marshall SJ**, **Marshall GW**. Enhanced osteocalcin expression by osteoblast-like cells (MC3T3-E1) exposed to bioactive coating glass (SiO2-CaO-P2O5-MgO-K2O-Na2O system) ions. *Acta Biomater* 5: 3536–3547, 2009. doi: 10.1016/j.actbio.2009.05.035.

14. **Rodrigues CF de S**, **Lima FJC de**, **Barbosa FT**. Importance of using basic statistics

adequately in clinical research. *Brazilian J Anesthesiol (English Ed* 67: 619–625, 2017. doi: https://doi.org/10.1016/j.bjane.2017.01.011.

15. **Davies OG**, **Cox SC**, **Williams RL**, **Tsaroucha D**, **Dorrepaal RM**, **Lewis MP**, **Grover LM**. Annexin-enriched osteoblast-derived vesicles act as an extracellular site of mineral nucleation within developing stem cell cultures. *Sci Rep* 7: 12639, 2017. doi: 10.1038/s41598-017-13027-6.

16. **Pezzotti G**, **Oba N**, **Zhu W**, **Marin E**, **Rondinella A**, **Boschetto F**, **McEntire B**, **Yamamoto K**, **Bal BS**. Human osteoblasts grow transitional Si/N apatite in quickly osteointegrated Si(3)N(4) cervical insert. *Acta Biomater* 64: 411–420, 2017. doi: 10.1016/j.actbio.2017.09.038.

17. **Webster TJ**, **Patel AA**, **Rahaman MN**, **Sonny Bal B**. Anti-infective and osteointegration properties of silicon nitride, poly(ether ether ketone), and titanium implants. *Acta Biomater* 8: 4447–4454, 2012. doi: 10.1016/j.actbio.2012.07.038.

18. **Pezzotti G**, **Bock RM**, **Adachi T**, **Rondinella A**, **Boschetto F**, **Zhu W**, **Marin E**, **McEntire B**, **Bal BS**, **Mazda O**. Silicon nitride surface chemistry: A potent regulator of mesenchymal progenitor cell activity in bone formation. *Appl Mater Today* 9: 82–95, 2017. doi: https://doi.org/10.1016/j.apmt.2017.05.005.

19. **Megat Abdul Wahab R**, **Mohamed Rozali NA**, **Senafi S**, **Zainol Abidin IZ**, **Zainal Ariffin Z**, **Zainal Ariffin SH**. Impact of isolation method on doubling time and the quality of chondrocyte and osteoblast differentiated from murine dental pulp stem cells. *PeerJ* 5: e3180, 2017. doi: 10.7717/peerj.3180.

20. **Kurtz SM**, **Devine JN**. PEEK biomaterials in trauma, orthopedic, and spinal implants. *Biomaterials* 28: 4845–4869, 2007. doi: 10.1016/j.biomaterials.2007.07.013.

21. **Pelletier MH**, **Cordaro N**, **Punjabi VM**, **Waites M**, **Lau A**, **Walsh WR**. PEEK Versus Ti Interbody Fusion Devices: Resultant Fusion, Bone Apposition, Initial and 26-Week Biomechanics. *Clin spine Surg* 29: E208-14, 2016. doi: 10.1097/BSD.0b013e31826851a4.

22. **Torstrick FB**, **Safranski DL**, **Burkus JK**, **Chappuis JL**, **Lee CSD**, **Guldberg RE**, **Gall K**, **Smith KE**. Getting PEEK to Stick to Bone: The Development of Porous PEEK for Interbody Fusion Devices [Online]. *Tech Orthop* 32, 2017. https://journals.lww.com/techortho/Fulltext/2017/09000/Getting_PEEK_to_Stick_to_Bone__The_Development_of.5.aspx.

23. **Tsougeni K**, **Vourdas N**, **Tserepi A**, **Gogolides E**, **Cardinaud C**. Mechanisms of Oxygen Plasma Nanotexturing of Organic Polymer Surfaces: From Stable Super Hydrophilic to Super Hydrophobic Surfaces. *Langmuir* 25: 11748–11759, 2009. doi: 10.1021/la901072z.

24. **Zhang W**, **Huang Z-L**, **Liao S-S**, **Cui F-Z**. Nucleation Sites of Calcium Phosphate Crystals during Collagen Mineralization. *J Am Ceram Soc* 86: 1052–1054, 2003. doi: https://doi.org/10.1111/j.1151-2916.2003.tb03422.x.

25. **Ilyas A**, **Odatsu T**, **Shah A**, **Monte F**, **Kim HKW**, **Kramer P**, **Aswath PB**, **Varanasi VG**. Amorphous Silica: A New Antioxidant Role for Rapid Critical-Sized Bone Defect Healing. *Adv Healthc Mater* 5: 2199–2213, 2016. doi: 10.1002/adhm.201600203.

26. **Buchwald T**, **Kozielski M**, **Szybowicz M**. Determination of Collagen Fibers Arrangement in Bone Tissue by Using Transformations of Raman Spectra Maps. *Spectrosc An Int J* 27: 261487, 2012. doi: 10.1155/2012/261487.

27. **Draper ERC**, **Morris MD**, **Camacho NP**, **Matousek P**, **Towrie M**, **Parker AW**, **Goodship AE**. Novel assessment of bone using time-resolved transcutaneous Raman

spectroscopy. *J bone Miner Res Off J Am Soc Bone Miner Res* 20: 1968–1972, 2005. doi: 10.1359/JBMR.050710.

28. **Tsou H-K**, **Chi M-H**, **Hung Y-W**, **Chung C-J**, **He J-L**. In Vivo Osseointegration Performance of Titanium Dioxide Coating Modified Polyetheretherketone Using Arc Ion Plating for Spinal Implant Application. *Biomed Res Int* 2015: 328943, 2015. doi: 10.1155/2015/328943.

29. **Deng Y**, **Liu X**, **Xu A**, **Wang L**, **Luo Z**, **Zheng Y**, **Deng F**, **Wei J**, **Tang Z**, **Wei S**. Effect of surface roughness on osteogenesis in vitro and osseointegration in vivo of carbon fiber-reinforced polyetheretherketone-nanohydroxyapatite composite. *Int J Nanomedicine* 10: 1425–1447, 2015. doi: 10.2147/IJN.S75557.

30. **Gorth DJ**, **Puckett S**, **Ercan B**, **Webster TJ**, **Rahaman M**, **Bal BS**. Decreased bacteria activity on Si_3N_4 surfaces compared with PEEK or titanium. *Int J Nanomedicine* 7: 4829–4840, 2012. doi: 10.2147/IJN.S35190.

31. **Xiao G**, **Gopalakrishnan R**, **Jiang D**, **Reith E**, **Benson MD**, **Franceschi RT**. Bone morphogenetic proteins, extracellular matrix, and mitogen-activated protein kinase signaling pathways are required for osteoblast-specific gene expression and differentiation in MC3T3-E1 cells. *J bone Miner Res Off J Am Soc Bone Miner Res* 17: 101–110, 2002. doi: 10.1359/jbmr.2002.17.1.101.

32. **Artigas N**, **Ureña C**, **Rodríguez-Carballo E**, **Rosa JL**, **Ventura F**. Mitogen-activated protein kinase (MAPK)-regulated interactions between Osterix and Runx2 are critical for the transcriptional osteogenic program. *J Biol Chem* 289: 27105–27117, 2014. doi: 10.1074/jbc.M114.576793.

33. **Zoch ML**, **Clemens TL**, **Riddle RC**. New insights into the biology of osteocalcin. *Bone*

82: 42–49, 2016. doi: 10.1016/j.bone.2015.05.046.

34. **Hauschka P V**, **Carr SA**. Calcium-dependent alpha-helical structure in osteocalcin. *Biochemistry* 21: 2538–2547, 1982. doi: 10.1021/bi00539a038.

35. **Hoang QQ**, **Sicheri F**, **Howard AJ**, **Yang DSC**. Bone recognition mechanism of porcine osteocalcin from crystal structure. *Nature* 425: 977–980, 2003. doi: 10.1038/nature02079.

36. **Ritter NM**, **Farach-Carson MC**, **Butler WT**. Evidence for the formation of a complex between osteopontin and osteocalcin. *J Bone Miner Res* 7: 877–885, 1992. doi: https://doi.org/10.1002/jbmr.5650070804.

37. **Bal BS**, **Rahaman MN**. Orthopedic applications of silicon nitride ceramics. *Acta Biomater* 8: 2889–2898, 2012. doi: 10.1016/j.actbio.2012.04.031.

38. **Ahuja N**, **Awad K**, **Fiedler M**, **Aswath P**, **Brotto M**, **Varanasi V**. Preliminary study of in-situ 3D bioprinted nano-silicate biopolymer scaffolds for muscle repair in VML defects. *FASEB J* 34: 1, 2020. doi: https://doi.org/10.1096/fasebj.2020.34.s1.03514.

39. **AWAD KR**, **Ahuja N**, **Fiedler M**, **Huang J**, **Brotto L**, **Aswath P**, **Brotto M**, **Varanasi V**. Micro-patterned Bioactive Amorphous Silicon Oxynitride Enhances Adhesion, Growth, and Myotubes and Axon Alignment in Muscle and Nerve Cells. *FASEB J* 34: 1, 2020. doi: https://doi.org/10.1096/fasebj.2020.34.s1.02245.

40. **Monte F**, **Awad KR**, **Ahuja N**, **Kim H**, **Aswath P**, **Brotto M**, **Varanasi VG**. Amorphous Silicon Oxynitrophosphide Coated Implants Boost Angiogenic Activity of Endothelial Cells. .

41. **Varanasi VG**, **Ilyas A**, **Velten MF**, **Shah A**, **Lanford WA**, **Aswath PB**. Role of Hydrogen and Nitrogen on the Surface Chemical Structure of Bioactive Amorphous Silicon Oxynitride Films. *J Phys Chem B* 121: 8991–9005, 2017. doi:

10.1021/acs.jpcb.7b05885.

42. **Awad KR**, **Huang J**, **Brotto L**, **Aswath P**, **Brotto M**, **Varanasi V**. Patterned Silicon Oxynitride (SiONx) Scaffolds Enhance Alignment and Myogenic Differentiation of C2C12 Muscle Cells. *FASEB J* 33: 539.5-539.5, 2019. doi: https://doi.org/10.1096/fasebj.2019.33.1_supplement.539.5.

43. **Ilyas A**, **Lavrik N V**, **Kim HKW**, **Aswath PB**, **Varanasi VG**. Enhanced interfacial adhesion and osteogenesis for rapid "bone-like" biomineralization by PECVD-based silicon oxynitride overlays. *ACS Appl Mater Interfaces* 7: 15368–15379, 2015.

44. **Dimitriou R**, **Jones E**, **McGonagle D**, **Giannoudis P V**. Bone regeneration: current concepts and future directions. *BMC Med* 9: 66, 2011. doi: 10.1186/1741-7015-9-66.

45. **Nauth A**, **Schemitsch E**, **Norris B**, **Nollin Z**, **Watson JT**. Critical-Size Bone Defects: Is There a Consensus for Diagnosis and Treatment? [Online]. *J Orthop Trauma* 32, 2018. https://journals.lww.com/jorthotrauma/Fulltext/2018/03003/Critical_Size_Bone_Defects__Is_There_a_Consensus.2.aspx.

CHAPTER 6

OVERALL CONCLUSIONS AND FUTURE DIRECTIONS

6.1. CONCLUSIONS

Craniomaxillofacial injuries and defects are detrimental, and require urgent attention for a faster and full recovery. Oxidative stresses and complex craniofacial bone physiology complicates bone defect healing. In this dissertation, we hypothesize the use of amorphous silicon oxynitride coating for titanium fixative devices to reduce oxidative stress and enhance angiogenesis and osteogenesis via an enhanced NRF2 antioxidant activity.

In chapter 1, we overview the various treatment strategies used in the craniofacial region. First, we investigate silicon nitride as a fixative device material for craniofacial bone reconstruction (Chapter 2) (1). Silicon Nitride is a ceramic material that is widely used as a spacer in spinal applications for its benefits in bacteriostasis and bioactivity. We compared the osteogenic response of mice pre-osteoblast cells of silicon nitride to titanium and polyether ether ketone (PEEK). The study results concluded that silicon nitride enhances the extracellular matrix deposition as well as support mineral tissue formation of its surface compared to titanium and PEEK (1). However, silicon nitride being a ceramic has low tensile strength lacks the ability of flexure. This is highly significant in the craniomaxillofacial region due to some of the bone structure being load-bearing and may lead to cracking or fracture. This study provided us evidence of the use of the elemental composition of silicon nitride, if used in combination with a more structurally compatible biomaterial can lead to excellent result for the use in craniofacial as well as orthopedic applications.

Further, we examined silicon nitride coatings for angiogenesis in the rat cranial bone defect. The amorphous nanolayered coating of silicon oxynitride is created using a plasma-enhanced chemical vapor deposition (PECVD) method. The high scalability and tunability of PECVD for the silicon oxynitride coatings offers an added benefit along with the antioxidant

benefits from the silicon ions released from the surface. In chapter 3 (2), we investigated the silicon oxynitride coatings with ionic phosphorous added to its chemistry for angiogenic analysis. Results show an upregulation of major angiogenic factors including VEGF, Ang-1 and Hif-1a along with an upregulation in antioxidant biomarkers such as SOD-1, NRF2, GPX1 and Cat1 in vitro and in vivo. Endothelial cells are highly correlated in homeostasis of bone turnover. Hence, these study results are significant and shows great potential of the amorphous silicon oxynitride coating materials for bone regeneration applications (2).

Next, we utilized the benefits of using the PECVD technique to fine tune and optimize the silicon oxynitride coatings to maximally enhance the antioxidant activity and osteogenesis, under oxidative stress conditions. In Chapter 4, we investigate 5 different silicon oxynitride coatings by changing the atomic ratio of nitrogen and oxygen by varying the gas flow rate inside the PECVD chamber. The rationale of this study, being, increasing the nitrogen-to-oxygen atom ratio provides a mix of tetrahedral and trigonal bonds, this decreases the surface energy and creates a surface dipole. The more reductive surface provides us the surface chemistry which provides maximal antioxidant effect. We also study the major transcription factor NRF2, which is involved in the antioxidant response against the oxidative stresses of the injury and is related to maintain bone cell homeostasis. Results reveal the activation of the NRF2 expression and affects the overall antioxidant expression with silicon oxynitride coatings. We conclude that silicon oxynitride coatings enhance NRF2 activity which in turn activates the antioxidant expression which helps reduce oxidative stress and improved osteogenesis.

In Chapter 5, the antioxidant silicon oxynitride coatings on fixative titanium devices is tested using two animal models. The use of the sub-critical sized rat cranial defect model gives us insights to identify the biomarkers for extracellular matrix formation and osteogenesis in the

regenerated bone. Results from this study show silicon oxynitride coatings show increased and organized extracellular matrix formation, and also faster and enhanced bone mineral tissue formation. We also see a reduction in the presence of total ROS/RNS in rat serum for the animals who received the coated implants along with enhanced NRF2 activity locally as well as systemically. We conclude that silicon oxynitride enhances osteogenesis by controlling the excessive ROS production by an antioxidant NRF2 effect, these results are congruent with the above chapters (2, 3, and 4).

Finally, to determine the clinical significance of the silicon oxynitride coatings, we study the rabbit mandibular critical-sized defect model as it is a more translational model. This model helps us conclude the silicon oxynitride antioxidant and osteogenic benefits in an immune-sensitive model. The mandibular defect also translates to the human maxillary or mandibular bone defects, which are most commonly affected in the craniofacial region. We confirm our quantitative bone regeneration x-ray findings of faster and better bone regeneration process with the chemical and mechanical qualitative analysis.

Overall, through the presented work, we can definitely conclude the antioxidant nature of the PECVD Silicon Oxynitride coatings on biomedical devices will reduce the deleterious oxidative stresses and enhance osteogenesis for a faster and complete bone recovery.

6.2. FUTURE DIRECTIONS

This study helps us gets good insights into the use of silica-based biomaterials for the reduction in excessive oxidative stress, for better and faster bone regeneration in the craniofacial region. We believe that the ease of process to make the silicon oxynitride-based coatings, with a reasonable cost associated for manufacturing, makes this an outstanding and easily translational

product. Dental and orthopedic implants, which face similar challenges as the craniomaxillofacial devices, add up to the value for exploring the SiONx chemistry for all bone biomedical applications.

It is now well-established the close connection and crosstalk between bone and muscle tissue. A study conducted by our group shows the positive effect of silicon ions on muscle regeneration (3). However, the treatment of musculoskeletal injury differs from the bone-implants/fixative devices. This inspired the Varanasi Laboratory to develop nanoparticles with silicon oxynitride chemistry using a sol-gel method. The silicon oxynitride- nanoparticles (SiONx-np) can be used in a drug delivery system or combined with a biomaterial for a more targeted and controlled delivery. We evaluated the SiONx-np in methacrylate gelatin (MAG) to evaluate our above hypothesis that silicon oxynitride enhances osteogenesis via enhanced NRF2 antioxidant activity. We first evaluated *in vitro* the optimized nanoparticle concentration in the MAG which can have rheological properties for 3D printing and also enhance mesenchymal stem cell proliferation. From our preliminary findings, we finalized a concentration of 4% SiONx-np with 20% MAG (SiONx-np-MAG). We further compared *in vitro* and *in vivo* the efficacy of SiONx-np-MAG to MAG. We use the material and methods as in Chapter 4 for our *in vitro* study and as in Chapter 5 Rat cranial Study for our *in vivo* analysis. Our results show SiONx-np-MAG supports mesenchymal stem cell proliferation (**Figure 6.1**) and

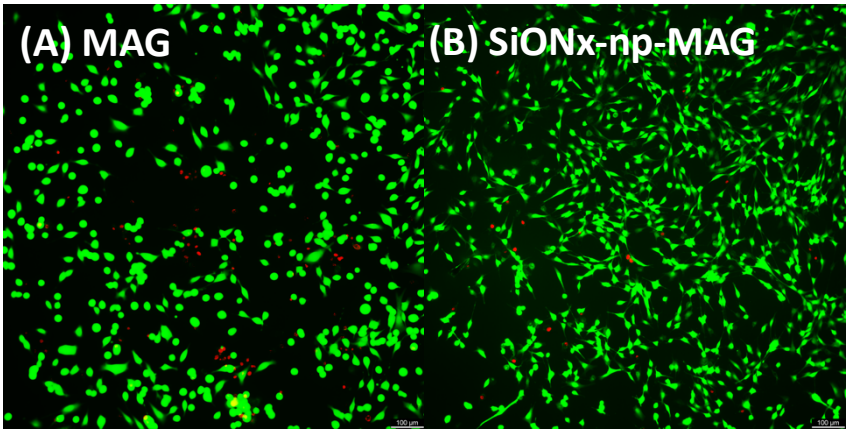

Figure 6.1. Mesenchymal Stem Cell Proliferation on 3D printed methacrylated gelatin (MAG) and 3D printed MAG with silicon oxynitride nanoparticles (SiONx-np-MAG)

differentiation (**Figure 6.2**). We also see significantly enhanced NRF2 activity with the SiONx-np-MAG (**Figure 6.3**). Finally, our preliminary micro-CT findings show enhanced bone regeneration with the SiONx-np-MAG 3D printed scaffolds as compared to the MAG alone (**Figure 6.4**). To our surprise, we notice bone regeneration not just on the edges of the bone defect area, but also in the lattice of the SiONx-np-MAG centrally (**Figure 6.4**). This indicates an osteoinductive nature of the SiONx-np. However, further testing is required to confirm these findings.

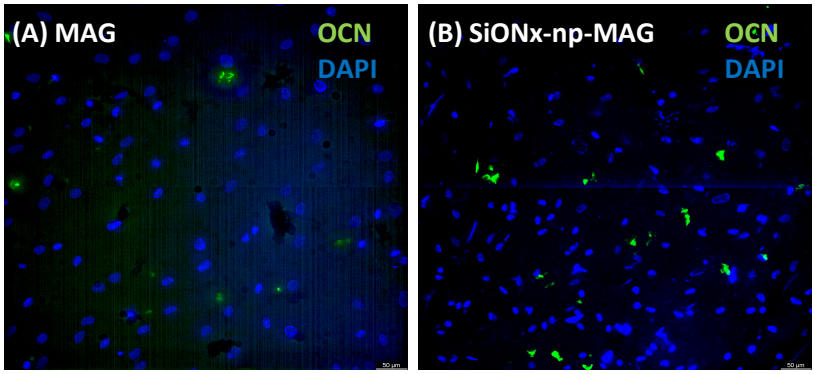

Figure 6.2. Osteocalcin (OCN) expression on MAG and SiONx-np-MAG. (B) shows enhanced osteocalcin activity with SiONx-np-MAG

Overall, results from this dissertation confirm the Osteogenic nature of Silicon Oxynitride. Silicon Oxynitride in combination with a suitable biomaterial shows great potential as an antioxidant small molecule for reduction in oxidative stress. We believe that Silicon Oxynitride implant coatings and nanoparticles can be a holy grail for patients with a compromised bone defect for a faster and physiologic healing.

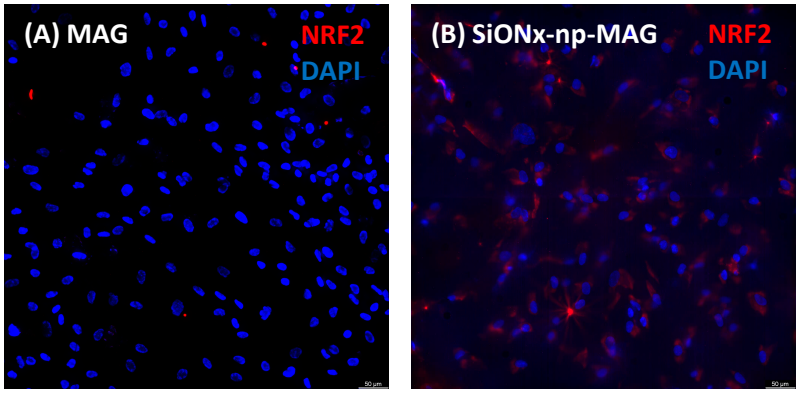

Figure 6.3. NRF2 antioxidant expression on MAG and SiONx-np-MAG. (B) shows enhanced antioxidant activity with SiONx-np-MAG

4 week

12 week

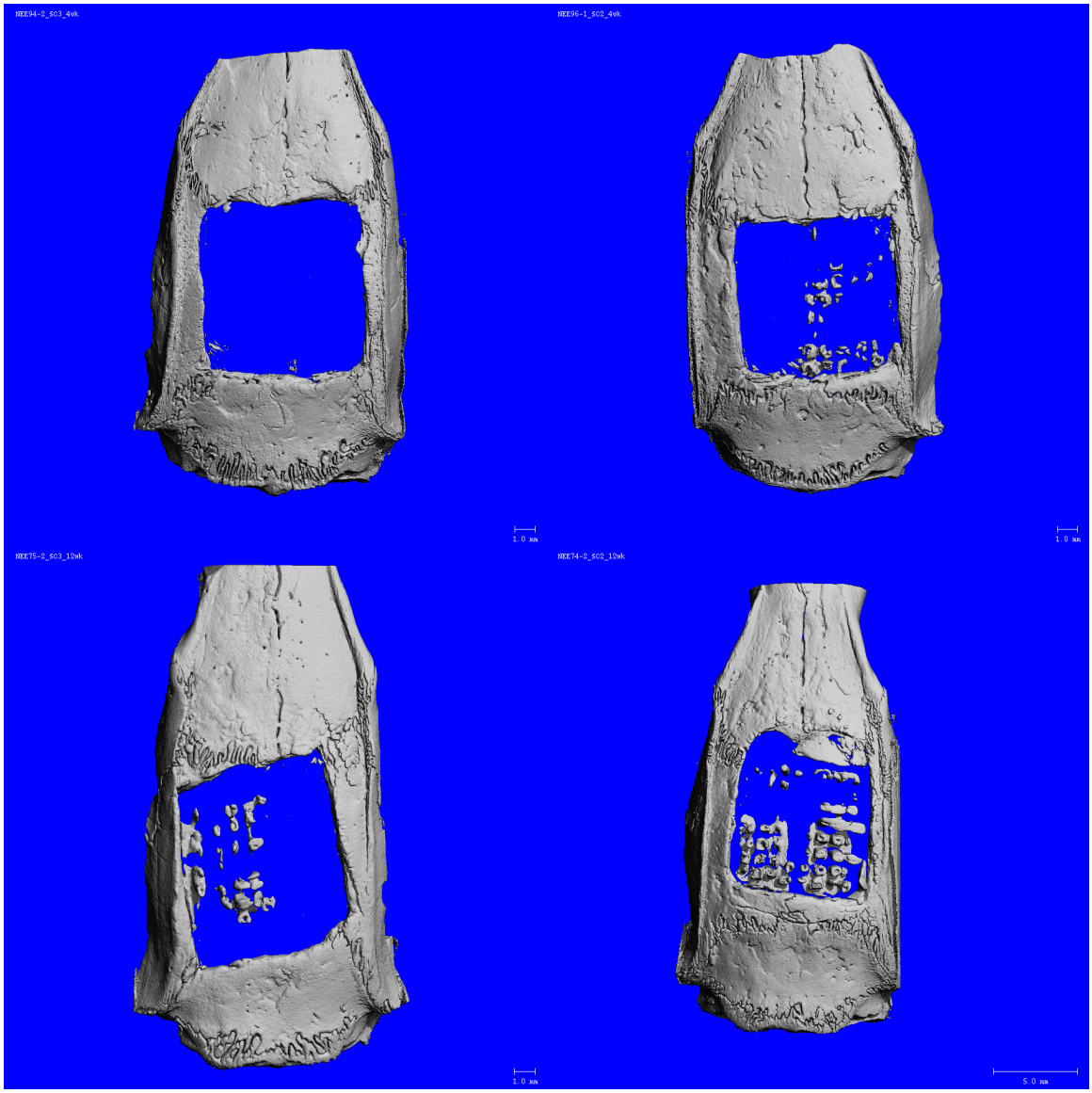

MAG **SiONx-np-MAG**

Figure 6.4. MicroCT images shows enhanced bone regeneration with SiON-np-MAG at early 4-week time-point and late 12-week time-point when compared to MAG.

6.3. REFERENCES

1. **Ahuja N**, **Awad KR**, **Brotto M**, **Aswath PB**, **Varanasi V**. A comparative study on silicon nitride, titanium and polyether ether ketone on mouse pre-osteoblast cells. *Med DEVICES \& SENSORS* 4: e10139, 2021. doi: https://doi.org/10.1002/mds3.10139.
2. **do Monte FA**, **Ahuja N**, **Awad KR**, **Pan Z**, **Young S**, **Kim HKW**, **Aswath P**, **Brotto M**, **Varanasi VG**. Silicon Oxynitrophosphide Nanoscale-Coating Enhances Antioxidant Marker -Induced Angiogenesis During In Vivo Cranial Bone Defect Healing. *JBMR Plus* n/a: e10425, [date unknown]. doi: https://doi.org/10.1002/jbm4.10425.
3. **Awad K**, **Ahuja N**, **Fiedler M**, **Peper S**, **Wang Z**, **Aswath P**, **Brotto M**, **Varanasi V**. Ionic Silicon Protects Oxidative Damage and Promotes Skeletal Muscle Cell Regeneration. *Int J Mol Sci* 22, 2021. doi: 10.3390/ijms22020497.

APPENDIX

This section includes several questions and comments from our committee members and the dissertation defense to help provide future directions and other considerations for future studies.

1. In section 5.2.3., the rat cranial in vivo study, the implants are just placed in the defect without a secondary method for fixation. Why did we not use a secondary fixative method to hold the implants in place?

   Ans: While a tissue adhesive could have been used to hold the implants in place for the primary defect healing, we wanted to study the faster healing rates and the osteointegration with SiONx-coated implants and compare its effect to the uncoated implant without the influence of an additional factor of adhesion.

2. Is there an influence of cerebrospinal fluid leak in the cranial defect in Chapter 5?

   Ans: Craniofacial injuries can lead to a cerebrospinal fluid (CSF) leak which adds an additional challenge to craniofacial bone defect healing. While we don't study the effect of CSF leaks on bone tissue engineering in this study, our results in Chapter 3 show enhanced angiogenic activity which can lead to faster blood vessel regeneration and enhance the overall healing rates of tissue in the localized area which can help overcome the factors related to the CSF leaks as well.

3. In the in vivo study for Rabbit Mandibular Defect Study in Chapter 5, you show an enhanced antioxidant SOD1 activity, however the NRF2 activity which is the hypothesis is not shown.

Ans. After a thorough search, we did not find a suitable NRF2 antibody to perform NRF2 immunohistochemistry assays and imaging, as the NRF2 polyclonal or monoclonal antibodies were usually made in rabbits.

4. What is the next step to confirm the hypothesis for mechanism of action of SiONx works through NRF2 activation especially in vivo?

   Ans: The next step in confirming the NRF2 mechanism of action especially in vivo would be first using the newly regeneration bone from the SiONx-coated plates as well as the uncoated plates to perform an antioxidant mechanism focused RNA sequencing to verify the involvement of all antioxidant pathways. Further, a transgenic model would be used to confirm the involvement of the respective pathways in vivo.